

Development of Long Wave Infrared Detectors
for Space Astronomy

by

Candice Marie Bacon

Submitted in Partial Fulfillment
of the
Requirements for the Degree
Doctor of Philosophy

Supervised by
Professor Judith L. Pipher

Department of Physics and Astronomy
The College
Arts & Sciences

University of Rochester
Rochester, New York

2006

This thesis is dedicated to Robert D. Murphy, physics teacher at White Bear Lake Area High School South Campus, and Dr. Richard Peterson, physics professor at Bethel College, without whom I may never have studied physics, and to my mother Shirley for the amazing woman and mother she was.

Curriculum Vitae

The author was born on October 29, 1976 in St. Paul, Minnesota to Richard and Shirley Bacon. She attended Bethel College from 1995 to 1999, and graduated Summa Cum Laude with a Bachelor of Arts degree in physics and musical studies. She came to the University of Rochester in the summer of 1999 and began graduate studies in detector development/solid-state physics. She pursued her research in detector development/solid-state physics under the direction of Professor Judith L. Pipher and received the Master of Arts degree from the University of Rochester in 2001.

Acknowledgements

We are grateful for support for this program, funded by NASA grants and NASA-Ames grants. Special recognition is given to my advisor, Dr. Judith L. Pipher, for her encouragement, guidance and support throughout my years in graduate school. Her insight, excellent scientific writing skills, and knowledge of the field of infrared detector physics have been invaluable. I also acknowledge Craig McMurtry for his breadth of infrared physics knowledge, excellent experimental skills and continual assistance in the lab. I am grateful to Dr. William J. Forrest for his discussions and ideas which have expanded my understanding of infrared detectors. I am also indebted to James Garnett, Majid Zandian, and Markus Loose of Rockwell Scientific, for their helpful discussions on infrared detector physics, manufacturing techniques and multiplexer design.

I would also like to acknowledge Thomas Allen, Richard Sarkis, Robert Gutermuth and Andrew Moore, for their never-ending assistance in the lab. And finally, grateful thanks to my friends, parents, grandparents, brothers, sisters, nieces and nephews for all their encouragement, prayers and support.

Abstract

This thesis details the research and development of $10\mu\text{m}$ cutoff detector arrays conducted at the University of Rochester in conjunction with Rockwell Scientific. Through my data analysis and theoretical modeling of detector characteristics, processes which prevent the detector arrays from meeting low background astronomical specifications are determined and fed back to the manufacturer. The first set of deliveries were manufactured in a banded format with multiple diode structures. Data analysis indicated that the smallest capacitance diode structure exhibited the lowest dark currents and the highest yield of pixels (28%) meeting the goal of less than $100e^-/\text{s}$ dark current with adequate ($> 45\text{mV}$) well depth. The mechanisms limiting dark current were found to be surface current at lower biases and tunneling (trap-to-band and band-to-band) at higher biases. In order to reduce stress at the junction during hybridization (a leading cause of the observed tunneling current), a proprietary bonding method was developed by Rockwell Scientific. New detector arrays, manufactured with the optimum diode structure and bonded with the new bonding technique to the HAWAII-1RG multiplexer, showed an impressive 75% of pixels exhibiting dark current less than $30e^-/\text{s}$ with sufficient ($> 40\text{mV}$) well depth. Most of these pixels exhibited extremely low dark currents, less than $0.3e^-/\text{s}$. I found that the dark current limiting mechanism at lower biases was still surface current on the front-side, caused by passivation processing techniques. The limiting mechanism at high biases was dislocation-induced early breakdown which took the shape of a screw dislocation (or micropipe) on an I-V curve of dark current, manifesting as a sharp increase in trap-to-band tunneling current. Burst noise was also detected in the source follower unit cell FET of the multiplexer and was fully characterized and explored. It was discovered that the burst noise was a result of oxide trapping of a single charge for most of the observed two-level characteristics. Other, more complicated forms exhibited by some pixels suggested that some multi-carrier traps exist in the bulk silicon close to the channel. With the results presented in this thesis, Rockwell Scientific will again improve their processing and manufacturing techniques on both detectors and multiplexers.

Contents

1	Introduction	1
1.1	Astronomical Motivation	1
1.2	Mercury Cadmium Telluride (HgCdTe)	3
1.3	Photo-diode Operation	6
1.4	Array Readouts and Multiplexers	12
1.5	Space-Based Astronomy Driven Requirements and Expectations	15
1.6	Development Progress	17
2	Theory	23
2.1	Dark Current Theory	23
2.1.1	Diffusion Current	24
2.1.2	Generation-Recombination Current	26
2.1.3	Surface Current	28
2.1.4	Tunneling Current	31
2.1.5	Diode Breakdown	32
2.2	Noise Theory	37
2.2.1	Shot Noise	38
2.2.2	Johnson Noise	39
2.2.3	KTC Noise	39
2.2.4	Clock Feed-Through	40

2.2.5	1/ f Noise	41
2.2.6	Burst Noise	41
3	Test Setup and Preparation	51
3.1	Equipment and Control Electronics	51
3.1.1	The Camera Dewar	51
3.1.2	Array Controller Electronics	54
3.2	Multiplexers: Operation and Calibration	56
3.2.1	Clocking and Sampling	56
3.2.2	NICMOS3 Multiplexer	60
3.2.3	HAWAII-1RG Multiplexer	61
3.2.4	Pedestal Injection and Zero Bias Point (ZBP)	63
3.2.5	DC Gain Calibration	64
4	Phase I: NICMOS3 Deliveries	66
4.1	Pixel Operability Constraints	67
4.2	Diode Calibration: Capacitance	69
4.3	Well Depth	72
4.4	Dark Current Measurements for the NICMOS3 Deliveries	74
4.4.1	Initial Dark Current Tests	74
4.4.2	Temperature and Bias Dependence of Dark Current	77
4.5	Relative Quantum Efficiency	81
4.6	Cutoff Wavelength	82
4.7	Summary of “Lessons Learned” from Phase I Characterization	82
5	Phase II: HAWAII-1RG Deliveries	89
5.1	Diode Calibration	90
5.1.1	Capacitance	92
5.1.2	Non-Linearity	93
5.2	Dark Current and Well Depth	95

<i>CONTENTS</i>	viii
5.2.1 Bias Dependence of Dark Current	100
5.2.2 Temperature Dependence of Dark Current	104
5.2.3 Effect of Forward Bias on Well Depth	107
5.3 Quantum Efficiency	112
5.4 Noise	116
5.5 Burst Noise	117
5.5.1 Testing for Burst Noise	119
5.5.2 Temporal Dependence of Signal Level	121
5.5.3 Burst Noise vs. Temperature	131
5.5.4 Burst Noise vs. Source to Drain Current	138
5.5.5 Burst Noise vs. Gate Voltage	143
5.5.6 Effect of Burst Noise on Future Space Programs	148
5.6 Summary of Phase II Characterization and Conclusions	150
6 Summary and Future Directions	152
Bibliography	156

List of Figures

1.1	Diagrammatic representation of the band transitions of HgCdTe through its crossover composition ($x = 0.16$ at 30K).	5
1.2	Energy band formation of a p - n junction.	7
1.3	Crystal structure close-up of a p - n junction with outer electron bonds shown. Loosely attached extra electrons not forming a bond are shown as a dangling line.	8
1.4	Dark current in a diode as a function of actual bias across the diode. . .	9
1.5	Photo-current in a diode as a function of bias with dark current vs. bias curve of Figure 1.4 shown for reference.	10
1.6	Diagram of Indium bump bonds connecting Silicon circuitry to photodiodes of another material.	11
1.7	Charge transfer in a three phase CCD.	13
1.8	Unit cell schematic for Direct Readout (DRO).	14
1.9	Zodiacal Light emission levels for diffraction limited pixels, quantum efficiency $\eta = 70\%$, optical efficiency 48%, and spectral resolution $R_s = 3$. The diffraction-limited pixel width (here $1.22\lambda/D$) is shown for a $D = 4\text{m}$ telescope.	16
1.10	Mesa and planar DLPH diode structures. Illumination of these devices is through the substrate (back side illumination).	21
2.1	Not-to-scale illustration of the junction regions.	24

2.2	Dark current mechanisms: band-to-band tunneling (2), trap-to-band tunneling (3), thermal assisted trap-to-band tunneling (1, 4), and G-R (5).	31
2.3	Tunneling breakdown energy diagram.	33
2.4	Avalanche multiplication process shown on an energy diagram.	35
2.5	Three dimensional representation of a crystal lattice with a screw dislocation.	36
2.6	Schematic diagram of a MOSFET.	43
2.7	Close up of channel and its dependence on gate voltage ($V_{reset} = V_{gate}$).	46
3.1	Not to scale representation of the camera dewar layout.	52
3.2	Exploded view of the detector mount shown in Figure 3.1 and replicated to the left of the figure.	53
3.3	Signal output diagram for SRP sampling mode.	57
3.4	Signal output diagram for Fowler sampling mode.	58
3.5	Signal output diagram for SUTR sampling mode.	59
3.6	Schematic of one quadrant of NICMOS3.	61
3.7	Read out operation schematic for the H1RG multiplexer.	62
3.8	This is part of the linear portion of the DC Gain measurement for UR008. Both axes are in volts. All four quadrants are shown here and have an average slope (gain) of 0.957.	65
4.1	Image of detector array UR008 with pixels in white that met the constraints for 60mV target well depth (TWD).	68
4.2	Histogram of capacitance for pixels of type A configuration.	70
4.3	Mean signal vs. time for deliverable UR008 at $T=31.7\text{K}$, $V_{bias} = 0\text{mV}$. .	72
4.4	Saturation image for deliverable UR008 at $T = 32\text{K}$, $V_{bias} = 0\text{mV}$. Scale is a black to white gradient from 47.7mV to 79.5mV.	74
4.5	Histogram of the measured saturation values (actual reverse bias and actual well depth) in mV for deliverable UR008 at $T = 30.6\text{K}$, $V_{bias} = 0\text{mV}$.	75

4.6	Mean accumulated dark charge (e^-), vs. itime (s) for each diode type in deliverable UR008 at $T = 32.6\text{K}$, $V_{bias} = 0\text{mV}$, TWD=60mV.	76
4.7	Histograms showing the number of pixels with a given dark charge accumulation from one second to various larger integration times for the selected pixels of type A on deliverable UR008 at $T = 32.6\text{K}$, $V_{bias} = 0\text{mV}$, TWD=60mV.	77
4.8	Top: Dark current of an individual pixel of diode type A at $T=32\text{K}$ as a function of actual reverse bias with surface current dominating. Bottom: Dark current for the same pixel (<i>top</i>) as a function of inverse temperature at $V_{actual_bias} = 75\text{mV}$	84
4.9	Top: Dark current of an individual pixel of diode type A at $T=32\text{K}$ as a function of actual reverse bias with band-to-band tunneling dominating at higher reverse biases. Bottom: Dark current for the same pixel (<i>top</i>) as a function of inverse temperature at $V_{actual_bias} = 63\text{mV}$	85
4.10	Top: Dark current of an individual pixel of diode type A at 32K as a function of actual reverse bias with surface current dominating at lower reverse biases. Bottom: Dark current as a function of inverse temperature for the same pixel (<i>top</i>) at $V_{actual_bias} = 64\text{mV}$	86
4.11	Dark current of an individual pixel of diode type A (same pixel as shown in Figure 4.10, but for the tenth cool-down, see text) at $T=32\text{K}$ as a function of actual reverse bias with trap-to-band tunneling now dominating at higher reverse biases in addition to much higher surface current. . . .	87
4.12	Relative quantum efficiency for deliverable UR008 at $T=33\text{K}$, $V_{bias} = 0\text{mV}$ (TWD=60mV).	88
4.13	Cutoff wavelength map for deliverable UR008 at $T=33\text{K}$ for $V_{bias} = 0\text{mV}$ (TWD=60mV). Units on color bar are in hundredths of a μm	88
5.1	Plot of C_0/C vs. signal for a typical well-behaved pixel from detector HIRG-16-001.	94

5.2	Left: Linear dark charge vs. time plot for SUTR data of a single pixel from detector array H1RG-16-001 with ultra-low dark current ($\sim 0.15e^-/s$) and 62mV ($\sim 41000e^-$) of well depth at $V_{bias} = 0mV$. Right: Non-linear dark charge vs. time curve for SUTR data of a single pixel from detector array H1RG-16-001 with dark current as high as $\sim 7.0e^-/s$ at $V_{bias} = 0mV$	97
5.3	Peak of the dark current histogram for detector array H1RG-16-003. . .	99
5.4	Dark current vs. bias for pixel 1 from detector array H1RG-16-001 which illustrates early reverse bias junction breakdown at 40mV.	102
5.5	Dark current vs. bias for pixel 2 from detector array H1RG-16-001 which illustrates low dark current dominated by surface currents followed by reverse bias junction breakdown.	103
5.6	Dark current vs. bias for pixel 3 from detector array H1RG-16-001 which illustrates low dark current over the entire range of reverse bias.	105
5.7	Dark current vs. temperature for pixel 1 from detector array H1RG-16-001 at $V_{bias} = 0mV$, well depth 25mV.	106
5.8	Dark current vs. temperature for pixel 2 from detector array H1RG-16-001 at $V_{bias} = 0mV$, well depth 40mV.	107
5.9	Dark current vs. temperature for pixel 3 from detector array H1RG-16-001 at $V_{bias} = 0mV$, well depth 60mV.	108
5.10	I-V curves for various photo currents with I_{sc} and V_{oc} indicated for each curve.	109
5.11	This figure shows the difference between the calculated and measured ΔV in mV for pixels with sufficient illumination overlaid with a Gaussian fit. The standard deviation of the Gaussian fit is 0.2mV.	113
5.12	DQE and RQE for selected pixels (as described above) of detector H1RG-16-001.	115
5.13	DQE and RQE for selected pixels (as described above) of detector H1RG-16-002.	115

5.14 DQE and RQE for selected pixels (as described above) of detector H1RG-16-003.	116
5.15 Signal vs. sample number and corresponding histogram for a pixel without burst noise.	120
5.16 Signal vs. sample number and corresponding histogram for a pixel exhibiting two level burst noise below the threshold of detectability in our algorithm.	121
5.17 Signal vs. sample number and corresponding histogram for a pixel exhibiting U-U burst noise.	123
5.18 Signal vs. sample number and corresponding histogram for a pixel exhibiting U-U burst noise with levels relatively close together.	124
5.19 Signal vs. sample number and corresponding histogram for a pixel exhibiting M-U burst noise with a larger scale and indistinct secondary level(s).	125
5.20 Signal vs. sample number and corresponding histogram for a pixel exhibiting S-U burst noise with a larger scale and detectable secondary level very close to the dominant signal level.	125
5.21 Signal vs. sample number and corresponding histogram for a pixel exhibiting M-M burst noise.	126
5.22 Signal vs. sample number and corresponding histogram for a pixel exhibiting S-M burst noise.	127
5.23 Signal vs. sample number and corresponding histogram for a pixel exhibiting S-M burst noise.	127
5.24 Signal vs. sample number and corresponding histogram for a pixel exhibiting S-S burst noise. The dashed line shows the sum of the Gaussians.	128
5.25 Signal vs. sample number and corresponding histogram for a pixel exhibiting S-S burst noise.	128

5.26 Signal vs. sample number and corresponding histogram for a pixel exhibiting multiple level burst noise with S-S superimposed upon U-U. The dashed line shows the sum of the Gaussians. 129

5.27 Signal vs. sample number and corresponding histogram for a pixel exhibiting multiple level burst noise with two defined levels and potentially many undefined levels in-between. 129

5.28 Signal vs. sample number and corresponding histogram for a pixel exhibiting multiple level burst noise with upper and lower secondary levels. 129

5.29 Signal vs. sample number and corresponding histogram for a pixel exhibiting multiple level burst noise. The dashed line shows the sum of the Gaussians. The top two figures are scaled to show the entire range of transition. The bottom two figures show the dominant level. There are many mechanisms involved which result in these various transitions. . . 130

5.30 Percentage of array pixels detected vs. smallest transition size detectable. 132

5.31 Percentage of array pixels detected vs. smallest transition size detectable on a log-log scale. 133

5.32 Maximum burst noise transition amplitude vs. temperature. 134

5.33 Signal vs. sample number at 30K (left) and 37K (right) for a pixel exhibiting burst noise at both temperatures with a level dominance change. 136

5.34 Signal vs. sample number at 30K (left) and 37K (right) for a pixel exhibiting burst noise at both temperatures with a magnitude shift. . . . 136

5.35 Signal vs. sample number at 30K (left) and 37K (right) for two pixels (top and bottom) exhibiting burst noise at both temperatures. 137

5.36 Signal vs. sample number at 30K (left) and 37K (right) for a pixel exhibiting burst noise at both temperatures. 138

5.37 Signal vs. sample number for various currents for a pixel subject to burst noise at 30K. 139

5.38 Signal vs. sample number for various currents for a pixel subject to burst noise at 30K. 140

5.39	Signal vs. sample number for various currents for a pixel subject to burst noise at 30K.	141
5.40	Signal vs. sample number for various currents for a pixel subject to burst noise at 30K.	142
5.41	Signal vs. sample number for various gate voltages (V_{reset}) for a pixel subject to burst noise at 30K.	145
5.42	Signal vs. sample number for various source to drain currents (I_{sd}) of the pixel illustrated in Figure 5.41.	146
5.43	Signal vs. sample number for various gate voltages (V_{reset}) for a pixel subject to burst noise at 30K.	147
5.44	Signal vs. sample number for various gate voltages (V_{reset}) for a pixel subject to burst noise at 30K.	148
5.45	Signal vs. sample number for various source to drain currents (I_{sd}) of the pixel illustrated in Figure 5.44.	149

List of Tables

4.1	Percentage of Pixels Meeting Constraints vs. Diode Type	68
4.2	Capacitances of the various types followed by the number of electrons per ADU (Analog to Digital Unit) for these devices in our system.	71
4.3	Mean Measured Saturation Level (Actual Well Depth) vs. Pixel Type .	73
4.4	Mean dark current for each diode type.	75
4.5	Percentage of Low Dark Current Pixels vs. Target Well Depth at 30.6K	80
5.1	Table showing statistics of capacitance measurements for all three HAWAII- 1RG detectors at $V_{bias} = 0\text{mV}$ (see text).	93
5.2	Table showing mean non-linearity measurements for all three detector arrays for $V_{bias} = 0\text{mV}$	95
5.3	Percentage of saturated pixels in each of the three arrays at 0mV applied bias.	96
5.4	Performance of all three detectors under the constraints of dark current less than the goal of $30e^-/\text{s}$ and well depth greater than the expected well depth (see text).	99
5.5	Parameters used to estimate theoretical dark current contributions for the graphs in Figures 5.4, 5.5, 5.6, and their corresponding dark current vs. temperature graphs (Figures 5.7, 5.8, and 5.9). <i>Note</i> : Reported trap densities are estimated to fit the data and have not been provided or verified by Rockwell Scientific.	101

5.6	This table shows the various amounts of forward bias obtained with different parameters for I_0 and I_{photo}	110
5.7	This table shows the statistics for two pixels which were examined from detector HIRG-16-001. It shows that there could be some well depth unaccounted for for both pixels, although the remaining well depth for Pixel B can be eliminated if the saturation current is reduced to $I_0 = 0.5e^-/s$	111
5.8	This table shows the calculated and measured ΔV for a few sample pixels.	112
5.9	Variations of dual level burst noise.	123
5.10	Percentages of pixels exhibiting burst noise at various temperatures. . .	132
5.11	Percentages of pixels exhibiting burst noise with respect to temperature.	132
5.12	Percentages of pixels exhibiting burst noise with respect to source to drain current at 30K. (Gate voltage at $V_{reset} = 0V$.)	142
5.13	Percentages of pixels exhibiting burst noise with respect to gate voltage (V_{reset}) at 30K. (The current at $V_{reset} = 0V$ and $V_{reset} = 1.35V$ is $I_{sd} = 1.60\mu A$ and $I_{sd} = 1.55\mu A$ respectively.)	148

List of Symbols

Symbol	Description	Units	Page
A	Diode Junction Area	μm	25
A_{jcn}	Diode Junction Area	μm	71
A_{pad}	Contact Pad Area	μm	71
B	Effective Power Bandwidth	Hz	39
c	Speed of Light	m/s	5
c_a	Capture Cross Section	cm^{-2}	43
c_{ao}	Capture Cross Section in High Temperature Limit	cm^{-2}	43
C	Capacitance on the Integrating Node	fF	40
C_n	Capture Coefficient for Electrons in Depletion Region	cm^3/s	27
C_p	Capture Coefficient for Holes in Depletion Region	cm^3/s	27
$C_{source_follower}$	Capacitance of the Source Follower	fF	71
d	Thickness of Active n -type Region	μm	24
d_p	Thickness of p -type Region	μm	24
D	Telescope Diameter	m	16
D_h	Hole Diffusion Coefficient	cm^2/s	25
E	Electric Field Across Depletion Region	V/m	31
E_a	Activation Energy of Dislocation	eV	36
E_c	Critical Electric Field for Avalanche Multiplication	V/m	34
E_g	Energy Gap	eV	4
E_i	Intrinsic Energy Level of the Depletion Region	eV	28
E_o	Height of the Oxide Potential Barrier	eV	44
E_{Si}	Height of the Silicon Potential Barrier	eV	44
E_t	Trap Energy	eV	32
E_{t_gr}	G-R Trap Energy	eV	27
f	Frequency	Hz	41
$G_{external}$	Gain of the External Electronics	unitless	69
G_{mux}	Gain of the Multiplexer	unitless	69

Symbol	Description	Units	Page
$G(z)$	Generation Rate of Charge Carriers in Depletion Region	cm^{-3}/s	26
h	Planck's Constant	Joule·s	5
\hbar	Planck's Constant divided by 2π	Joule·s	5
\bar{I}	Mean Current Flowing Through the Diode	e^-/s	39
I_0	Saturation Current of an Ideal Diode	e^-/s	8
$I_{\text{band-to-band}}$	Band-to-Band Tunneling Current	e^-/s	31
I_{dark}	Dark Current in a Diode	e^-/s	23
I_{dif}	Diffusion Current in a Diode	e^-/s	24
I_{G-R}	Generation-Recombination Current in a Diode	e^-/s	26
$I_{\text{ideal_dark}}$	Dark Current of an Ideal Diode	e^-/s	8
$I_{N_{\text{Shot}}}$	Shot Noise in Current	e^-/s	39
I_{photo}	Photo-current	e^-/s	10
I_{sc}	Short Circuit Current	e^-/s	10
I_s	Surface Current	e^-/s	28
I_{sd}	Source to Drain Current in Unit Cell FET	μA	42
I_{total}	Total Current in a Diode	e^-/s	10
$I_{\text{trap-to-band}}$	Trap-to-Band Tunneling Current	e^-/s	32
I_{tunnel}	Tunneling Current	e^-/s	31
I_λ	Photo-current per unit wavelength	$\text{W}/\text{cm}^3\text{sr}$	15
k_b	Boltzmann's Constant	Joule/K	7
L	MOSFET Gate Length	μm	45
L_h	Minority Carrier Diffusion Length	μm	24
L_t	Effective Trapping Length	nm	47
L_{ts}	Trapping Length for a Scattering Center	nm	47
L_{tp}	Debye Screening Length	nm	47
L_λ	Radiance Per Unit Wavelength	$\text{W}/\text{m}^2\cdot\text{sr}\cdot\text{nm}$	81
m_e	Mass of an Electron	kg	31
m_{eff}	Effective Mass	kg	31
M	Transition Matrix Element	$\text{eV}/\text{cm}^{3/2}$	32
M_{av}	Avalanche Multiplication Factor	unitless	34
\bar{n}	Average Number of Electrons	unitless	69
n_a	Concentration of Charge Carriers	cm^{-3}	43
n_t	Trap Density	cm^{-3}	32
n_{t_d}	Trap Density Added by Dislocation	cm^{-3}	36
n_{t_i}	Initial Trap Density Before Dislocation Activation	cm^{-3}	36
N	Noise in Signal Measurement	unitless	113
N_a	Acceptor Doping Density	cm^{-3}	7
N_c	Conduction Band Effective Density of States	cm^{-3}	27
N_d	Donor Doping Density	cm^{-3}	7
N_t	Density of Trap Centers at E_{t_gr} in Depletion Region	cm^{-3}	27
N_v	Valence Band Effective Density of States	cm^{-3}	27

Symbol	Description	Units	Page
n	Perturbed Electron Concentration within Depletion Region	cm^{-3}	27
n_a	Concentration of Charge Carriers	cm^{-3}	45
n_i	Intrinsic Carrier Concentration	cm^{-3}	8
n_1	Equilibrium Concentration of Electrons	cm^{-3}	27
Δn	Steady State Excess Minority Carrier Concentration	cm^{-3}	25
p	Perturbed Hole Concentration within Depletion Region	cm^{-3}	27
p_1	Equilibrium Concentration of Holes	cm^{-3}	27
q	Charge on an Electron	C	7
Q	Total Charge in the Silicon Channel of a MOSFET	C	47
R	Effective Mean Resistance of the Diode	Ω	39
R_s	Spectral Resolution	unitless	16
$R(z)$	Recombination Rate of Charge Carriers in Depletion Region	cm^{-3}/s	26
s	Effective Maximum Surface Recombination Velocity	cm/s	29
s_0	Velocity Coefficient	unitless	29
S	Number of Collected Electrons	unitless	112
S_0	Number of Incoming Photons	unitless	112
S_{ADU}	Signal Output in ADU	ADU	69
S_n	Surface Recombination Velocity	cm/s	25
t_c	Characteristic Capture Time	s	43
t_{co}	Characteristic Capture Time for Interface Traps	s	44
T	Temperature	K	4
v_{th}	Thermal Velocity	m/s	43
V_{actual_bias}	Actual Bias Across the Diode	mV	8
$V_{av_breakdown}$	Avalanche Breakdown Voltage	V	34
V_{bi}	Built-in Bias Across a p - n Junction	mV	7
V_{bias}	Reverse Bias Applied Across the Detector	mV	63
$V_{breakdown}$	Breakdown Voltage of the Diode	mV	9
V_{gate}	Gate Voltage on Unit Cell FET	mV	42
V_N	Noise Voltage at the junction	μV	69
$V_{N_{diode}}$	Noise Voltage Generated by the p - n Junction	μV	38
$V_{N_{Johnson}}$	Johnson Noise	μV	39
$V_{N_{KTC}}$	KTC Noise	μV	40
V_{N_out}	Measured Noise Voltage	μV	69
$V_{N_{read}}$	Read Noise / Multiplexer Noise	μV	38
$V_{N_{Shot}}$	Shot Noise in Voltage	μV	39
$V_{N_{system}}$	System Noise	μV	38
$V_{N_{total}}$	Total Noise Voltage	μV	38
V_{oc}	Open Circuit Voltage	mV	10
V_{reset}	Reset Voltage / Gate Voltage on Unit Cell FET	mV	42

Symbol	Description	Units	Page
V_s	Source Voltage of Unit Cell MOSFET	mV	47
V_S	Input Referred Signal at the Junction	mV	69
V_{S_out}	Measured Signal Output Voltage	mV	69
V_{ZBP}	Zero Bias Point Voltage	mV	64
W	Depletion Region Width of Diode (e.g. Dark Current)	μm	25
W	Gate Width of MOSFET (e.g. Burst Noise)	μm	45
W_c	Depletion Region Width at Critical Electric Field	μm	34
	E_c		
x	Mole Fraction of Cadmium in HgCdTe	unitless	3
x_s	Surface Mole Fraction of Cadmium in HgCdTe	unitless	29
y_t	Distance from Burst Noise trap from Channel Boundary	nm	43
z	Distance Into n -type Active Region From Depletion Region Doundary	μm	25
β	Ideality Factor in n_i	unitless	29
γ	Scaling Factor for Dislocation Orientation	unitless	36
ε	Relative Permittivity of HgCdTe	unitless	25
ε_s	Relative Permittivity of Silicon	unitless	25
ε_o	Permittivity of Free Space	F/m	25
η	Quantum Efficiency	unitless	10
λ	Wavelength	μm	1
λ_c	Cutoff Wavelength	μm	5
σ	Conductivity of MOSFET Channel	$\Omega^{-1}\text{m}^{-1}$	47
τ_b	Minority Carrier Lifetime	s	25
τ_{no}	Lifetime of Electrons in the Depletion Region	s	27
τ_{po}	Lifetime of Holes in the Depletion Region	s	27
τ_{gr}	Lifetime of Holes and Electrons in Depletion Region	s	27
τ_s	Effective Lifetime of Surface States	s	29
Φ	Photon Arrival Rate	photons/s/pixel	10

Chapter 1

Introduction

1.1 Astronomical Motivation

The infrared wavelength region contains a wealth of information about astronomical objects. Specifically, relatively cool, opaque objects (e.g planets, or enshrouded forming stars) essentially emit temperature-dependent ‘blackbody’ continuum radiation that peaks in the infrared. Since these objects are not perfect blackbodies, their radiation will be modified by the albedo and/or the wavelength dependent emissivity of their ‘atmospheres.’ In particular, the atmospheres of planets and the cool cocoon of dust surrounding enshrouded forming stars exhibit absorption features in the infrared.

The absorption lines generated in the atmosphere of planets are indicative of the composition of the atmosphere. Earth’s atmosphere has absorption lines in the $5\mu\text{m}$ to $10\mu\text{m}$ range corresponding to water and ozone. The existence of these two constituents is essential to life on Earth. If these same absorption lines exist in the absorption spectra of an exo-planet within our Galaxy, it is possible that the planet could also support similar life forms.

Another mechanism by which astronomical infrared emission is generated is through the red-shifting of ultra-violet and visible radiation from the nuclei of distant galaxies because of the expansion of the universe. A measure of the red-shift is given by $z = \Delta\lambda/\lambda$. Currently, the largest measured value of z is 6.4,¹ which red-shifts the $\text{H}\alpha$ line

(656.3nm) to $4.9\mu\text{m}$. There are physical and instrumental limitations that make the detection of objects with large red-shifts extremely difficult. Cooled, large aperture space telescopes such as the planned James Webb Space Telescope (JWST), with very low dark current infrared detector arrays populating the spectrometer focal plane,¹ have a good chance of detecting galaxies with $z \geq 6.4$, back to the first epoch of galaxy formation.

Another application of infrared detector technology stems from the concern that near Earth objects may collide with the Earth and cause devastation. In January 2006, language was inserted into the NASA Authorization Act (H.R. 3070, Sec. 321) to foster a “George E. Brown, Jr. Near- Earth Object Survey”: “NASA will plan, develop, and implement a Near-Earth Object Survey program to detect, track, catalogue, and characterize the physical characteristics of near-Earth objects equal to or greater than 140 m in diameter to 90date of the enactment of this Act.” The Near Earth Object Camera (NEOCAM) has been proposed to meet the need of the above Congressional mandate, which is necessary in order to protect the Earth from the impact of such objects. The NEOCAM will utilize detector arrays with sensitivity to the $6 - 10\mu\text{m}$ wavelength region, in fact the very devices developed for this thesis. Since the surface temperature of an object located approximately 1AU from the Sun (thereby placing it near Earth’s orbit) is $\sim 300\text{K}$, its peak flux will occur near $\sim 10\mu\text{m}$. In addition to this, stars and galaxies are faint compared to asteroids in this wavelength region. Combining information obtained by NEOCAM with visible data from other sources will give a much more accurate breakdown of objects with impact potential than could be obtained without the NEOCAM.

In order to minimize the interference of the Earth and its atmosphere on comprehensive astronomical measurements, infrared detector arrays must be developed for space astronomy. The environmental background radiation for a ground-based observation is orders of magnitude larger than the faint infrared signal from a relatively cool, opaque

¹The focal plane is the plane at which the external image is focused through optics. When that plane is populated with detector arrays, the focused image can be recorded.

object. For the astronomical application of discovering habitable planets, the Earth's atmosphere contains absorption lines from the elements of interest, which can interfere with their detection in extra-solar planet atmospheres via ground-based astronomy. Furthermore, the Earth's atmosphere is turbulent, causing image blurring. Therefore, developing infrared detector arrays for space-based astronomy is a necessity.

Currently, most of the detectors that operate in the 5-10 μm range are constructed of Si:X, where X can be As, Sb, P, etc. Such extrinsic band gap photo-detectors require extensive cooling, e.g. Si:As Impurity Band Conduction (IBC) detectors require cooling to temperatures of $\sim 6 - 8\text{K}$.² This temperature range is achieved by either cryogenics or mechanical coolers which are expensive, massive and/or have a limited lifetime. Detectors which could function at a temperature that can be reached without active cooling would greatly reduce the cost of space-based astronomy missions. The recent development of passive cooling techniques, which will be employed in JWST, has created the possibility of properly designed telescopes which could attain passively cooled focal plane temperatures as low as $\sim 30\text{K}$. Therefore, we have been pursuing development of long wavelength Mercury Cadmium Telluride (HgCdTe) detector arrays that will exhibit low dark current and relatively high quantum efficiencies at a temperature close to this.

1.2 Mercury Cadmium Telluride (HgCdTe)

Mercury Cadmium Telluride is a II-VI ternary compound semiconductor. It is made up of two elements in the II column of the periodic table, Hg and Cd, and one in the VI column, Te. To complete the crystal structure, a II-VI ternary compound semiconductor must have equal parts of II elements and VI elements. Thus, HgCdTe is often referred to as $\text{Hg}_{1-x}\text{Cd}_x\text{Te}$, where x is the mole fraction of Cadmium. Because HgTe is a semi-metal and CdTe is a semiconductor, the carefully tuned mix of these two compounds can create a semiconductor with a very small band gap corresponding to a relatively long cutoff wavelength.

The electron orbitals that contribute to the formation of the conduction and valence

bands are the electrons in the s and p orbitals of the element's outer incomplete shell, also known as valence electrons. Hg and Cd are column II elements, and so have two electrons filling the outer s orbital (spin up and spin down), and none in the three outer p orbitals. Te, as a column VI element, has the outer s orbital filled and two p orbitals filled, leaving only one empty p orbital. In a crystal, these outer electrons are shared, completing the shells for these elements from complementary columns. Due to spin-orbit splitting of these orbitals, each orbital of an individual cell (fundamental unit of structure in a crystal) in a solid built out of N primitive cells ($N \sim 10^{23}$) splits into N orbitals. This results in a large number of very closely spaced orbitals called energy bands.

When molecular bonds are formed between atoms in a crystal, bonding and anti-bonding orbitals are formed from the overlapping s and p orbitals. The overlapping orbitals can be in phase and out of phase which results in a bonding and antibonding orbital respectively. The antibonding orbitals are only accessible through excitation of electrons and thus form the conduction band, leaving the bonding orbitals to form the valence band. The energy gap between the highest bonding p orbital and the lowest antibonding s orbital is known as the energy band gap of the crystal. In the valence band, there are three different bands formed from the three p orbitals, the heavy hole, light hole, and split-off bands. The split-off band has a much lower maximum energy than the other two because of spin-orbit splitting. The eponymous difference in effective masses distinguishes the other two. The four antibonding orbitals (one s and three p) also form conduction bands about different energies, but the one generally referred to as the conduction band in crystals is the lowest energy band of the four, formed by the antibonding s orbital. Likewise, the heavy hole band is referred to as the valence band because it has the highest energy.

The direct band gap energy (in eV) for $\text{Hg}_{1-x}\text{Cd}_x\text{Te}$ as a function of x and temperature in Kelvin, T is given in Equation 1.1.³

$$E_g(x, T) = -0.302 + 1.93x - 0.81x^2 + 0.832x^3 + 5.35 \times 10^{-4}T(1 - 2x) \quad (1.1)$$

The crossover composition is the composition where $E_g = 0$. At $T = 30\text{K}$, the crossover

composition is $x = 0.16$. At a given temperature, $\text{Hg}_{1-x}\text{Cd}_x\text{Te}$ is a semiconductor above and a semi-metal below its crossover composition.

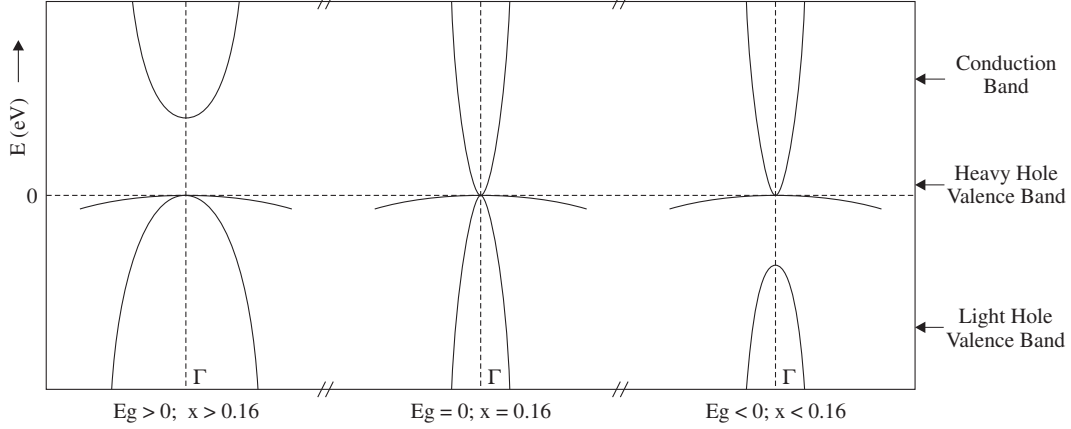


Figure 1.1. Diagrammatic representation of the band transitions of HgCdTe through its crossover composition ($x = 0.16$ at 30K).

Figure 1.1 illustrates the band transitions of HgCdTe as it moves through the crossover composition. The upper curve is the lowest of the conduction bands and the lower two curves are the heavy hole and light hole valence bands. As HgCdTe approaches the crossover composition, the energy bands become less parabolic and eventually the conduction band becomes degenerate with the heavy hole valence band at Γ (a point at the center of the Brillouin zone with high symmetry along each direction passing through it),⁴ causing the fundamental energy gap to be reduced to zero. Spin-orbit coupling forces the light hole valence band to more negative energies and causes it to interchange roles with the conduction band such that the equilibrium population of the valence band is less than the conduction band, giving it an inverted band structure and a negative energy gap.⁵⁻⁸ For compositions with a positive energy band gap, the cutoff wavelength of the material (the longest detectable wavelength) λ_c , is related to the energy band gap by

$$E_g = \frac{hc}{\lambda_c}, \quad (1.2)$$

where h is Planck's constant and c is the speed of light.

The energy band gap is very sensitive to small fluctuations in x around 0.240 (cutoff

wavelength $9.19\mu\text{m}$). For example, a change in x by 0.001 for $x \sim 0.240$ changes the cutoff wavelength via Equation 1.2 by $> 0.1\mu\text{m}$. This makes the actual cutoff wavelength of the fabricated material difficult to control precisely. In addition, the difference in sticking coefficients between Hg and Cd cause Cd to stick to the lattice more readily than Hg, making precise control of composition difficult. As x gets smaller, E_g becomes more sensitive to fluctuations in x , so the longer the cutoff wavelength, the more difficult it is to obtain the desired cutoff wavelength precisely.

Although a smaller band gap will enable detection at longer wavelengths, less energy is required to excite an electron across the gap, leading to larger thermally generated dark currents. This suggests that the lowest functional temperature should be used so that thermal excitation of electrons can be minimized. Since passive cooling can cool focal plane temperatures down to $\sim 30\text{K}$, we aim to create innovative arrays with low dark current at this temperature. Dark current mechanisms will be further discussed in Section 2.1.

1.3 Photo-diode Operation

To understand the operation of a photodiode, one must understand p - n junction diode behavior. A p - n junction is made up of a heterojunction between p -type (doped with a material containing fewer electrons than needed to complete the crystal bonds) and n -type (doped with a material containing more electrons than needed to complete the crystal bonds) material. In n -type material, the Fermi level (the energy below which all states are filled at $T=0\text{K}$) is closer to the conduction band. Similarly, the Fermi level for p -type material is closer to the valence band. When placed in contact, these two materials come to an equilibrium where the Fermi level is the same on both sides of the junction, as shown in Figure 1.2.

This equilibrium is accomplished by the extra electrons from the n -type side filling in the extra holes on the p -type side, thereby completing the crystal bonds within the vicinity of the junction. This microscopic process is illustrated in Figure 1.3, where the nuclei are represented by circles and the p -type and n -type dopants are labeled p and

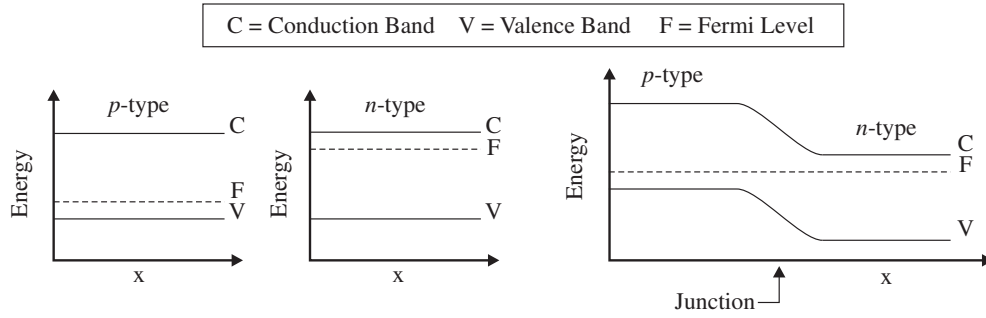


Figure 1.2. Energy band formation of a p - n junction.

n respectively. In the neutral p -type material labeled region (1), of the eight electrons needed to complete the crystal bonds, only seven are shown, representing the lack of an electron. In the neutral n -type material labeled region (4), a weak bond is illustrated by an extra line, indicating a relatively easily freed extra electron. In the depletion region in-between regions (1) and (4), region (2) has p -type nuclei, but the extra electrons from the n -type nuclei of region (3) have completed the missing bonds. Since the n -type and p -type material in this region were charge neutral before this process occurred, the p -type and n -type material have become respectively negatively and positively charged. This causes the process to be self-limiting, for it creates a significant electric field across the junction which resists further carrier diffusion. The region in which the crystal bonds are then complete is called the depletion region, for it is depleted of charge carriers, and consequently has a relatively high resistance. It is also known as the space-charge region, since the charge acquired by the dopants is localized at the dopant sites.

The voltage that becomes ‘built in’ across the junction, as a result of the build-up of charge carriers within the depletion region, can be calculated⁹ by Equation 1.3 and is a function of Boltzmann’s constant, k_b , temperature, T , the charge on an electron, q , the doping density of the p - and n -type region, N_a and N_d , and the intrinsic carrier concentration, n_i , given³ in Equation 1.4, where x is the mole fraction of cadmium.

$$V_{bi} = \frac{k_b T}{q} \ln \left(\frac{N_d N_a}{n_i^2} \right) \quad (1.3)$$

$$n_i = (5.585 - 3.820x + 1.753 \cdot 10^{-3}T - 1.364 \cdot 10^{-3}xT) \times [10^{14} \cdot E_g^{3/4} T^{3/2} \exp(-E_g/2k_bT)] \quad (1.4)$$

This voltage, V_{bi} can also be estimated, assuming the donor and acceptor levels are very close to the conduction and valence band respectively with

$$V_{bi} \simeq \frac{E_g(x, T)}{q}. \quad (1.5)$$

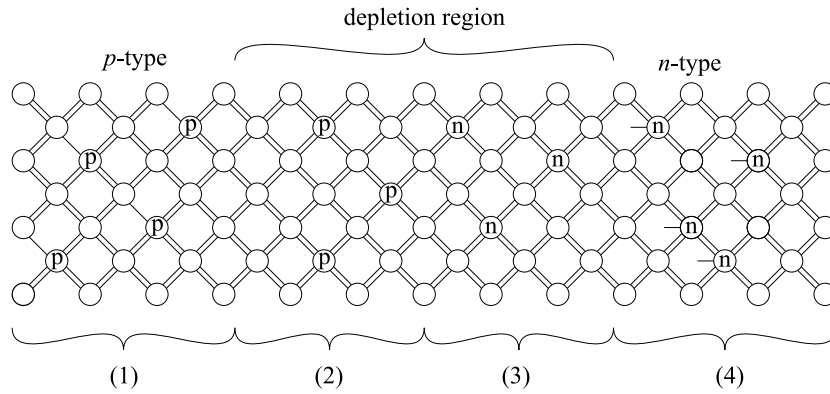


Figure 1.3. Crystal structure close-up of a p - n junction with outer electron bonds shown. Loosely attached extra electrons not forming a bond are shown as a dangling line.

Typical diode behavior depends upon the polarity of the bias applied across it. In forward bias, where the bias polarity opposes the natural diode junction polarity, the diode is strongly conductive, leading to very high currents. In reverse bias, where the bias polarity enhances the natural diode junction polarity, the diode has a relatively stable very small current, I_0 , known as the saturation current (or dark current) of an ideal diode (see Section 2.1). Equation 1.6 describes this behavior for an ideal diode,² which is illustrated in Figure 1.4.

$$I_{ideal_dark} = I_0 \left(e^{\frac{qV_{actual_bias}}{k_bT}} - 1 \right), \quad (1.6)$$

In Equation 1.6, V_{actual_bias} is the actual bias across the diode³ (negative for reverse

²Modeling of an actual diode includes an ideality factor β in the denominator of the exponential.

³The actual bias across the diode is the bias that exists across the terminals of the diode at a given point in time. This bias may oppose or enhance the natural diode junction polarity causing the diode to be forward or reverse biased respectively.

bias), and k_b is Boltzmann's constant.

Figure 1.4 is an I-V curve: a plot of current vs. voltage. In this plot, dark current is shown as a function of actual bias across the diode. In forward bias, the current is exponentially increasing with bias. With increasing reverse bias, the depletion region increases in size (thereby increasing the resistance of the junction) until the bias reaches the breakdown voltage, $V_{breakdown}$, of the diode. At this voltage, the depletion region (and the equation) breaks down, causing exponentially increasing excess current flow. Typically, this breakdown is referred to as avalanche or Zener breakdown. The mechanisms causing these and other forms of breakdown are discussed in Section 2.1.5.

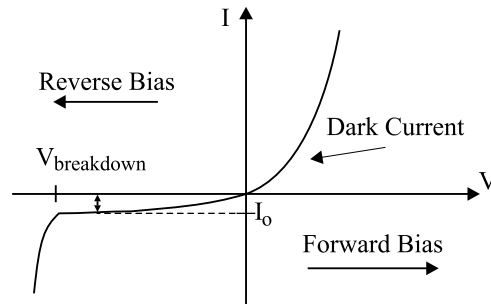


Figure 1.4. Dark current in a diode as a function of actual bias across the diode.

A photodiode consists of a p - n junction, which is typically operated in reverse bias and fabricated with a photo-sensitive material, e.g. semiconductors, such as HgCdTe, InSb, or Silicon (see Figure 1.6). When a photon of energy greater than or equal to the band gap enters the active bulk material, it creates an electron-hole pair close to the incident surface for most responsive wavelengths. Depending on whether the pair was created in p -type or n -type material, the electron or hole respectively diffuses to the depletion region. It is then swept across by the electric field, causing a decrease in bias across the junction. This decrease in bias is measured when the actual bias across the diode is read. The total current in an ideal diode when photon flux is applied is given in Equation 1.7.

$$I_{total} = I_0 \left(e^{\frac{qV}{k_b T}} - 1 \right) - I_{photo} \quad (1.7)$$

For a photoconductive gain of unity, I_{photo} is given by

$$I_{photo} = \eta q \Phi, \quad (1.8)$$

where η is the quantum efficiency and Φ is the photon arrival rate (in photons/s/pixel).

The photo-current depletes the reverse bias across the detector by causing an excess of free charge carriers, which diffuse to the depletion region and are then swept across by the electric field to the other side. This current opposes the natural diode junction polarity, which is represented by the minus sign in Equation 1.7, and illustrated in Figure 1.5.

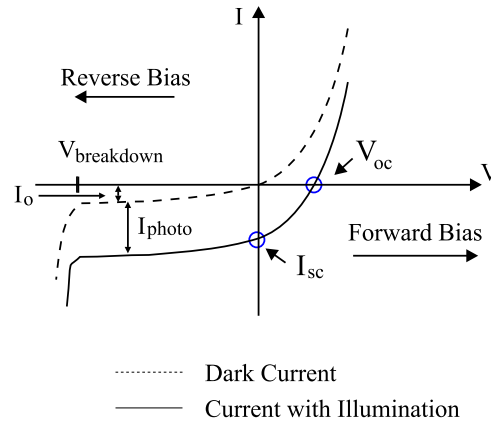


Figure 1.5. Photo-current in a diode as a function of bias with dark current vs. bias curve of Figure 1.4 shown for reference.

For a photodiode, there are a few points of interest on the I-V curves of Figure 1.5: the open circuit voltage, V_{oc} , and the short circuit current, I_{sc} . The open circuit voltage is the voltage when the net current through the diode is zero. This voltage is very important for well depth measurements, as the *measured* well depth of a diode illuminated by photon flux is given by $V_{oc} - V_{actual_bias}$, where V_{actual_bias} is the actual bias on the diode at the beginning of the integration ramp⁴ (negative for reverse bias). Thus, a small I_{photo} is desirable for this measurement in order to minimize V_{oc} . The short

⁴The integration ramp is visible on a signal vs. time plot. As time passes, the signal on the detector increases as long as the detector has not been reset. The beginning of the integration ramp happens immediately after the detector has been reset.

circuit current is also an important parameter. This is the current when there is no net bias across the diode, i.e. purely photo-current in the absence of dark current. This point also marks a significant slope change in the current vs. voltage curve and can indicate where an illuminated diode is switching from reverse bias to forward bias (see Section 5.2.3).

Once the desired wavelength sensitivity and the material for photodiode fabrication have been determined, then the readout circuitry is designed. For most applications, the material of choice is Silicon. Not only is it a semiconductor with wavelength sensitivity in the visible and near infrared, it is also the material with which most circuitry is fabricated. Thus, many devices which require visible sensitivity are fabricated entirely of Silicon and its oxide. Charge Coupled Devices (CCDs) in commercially available digital cameras are one example of this technology. For HgCdTe photodiodes, Indium bump bonds are used to hybridize the photodiodes to the Silicon circuitry as shown in Figure 1.6.

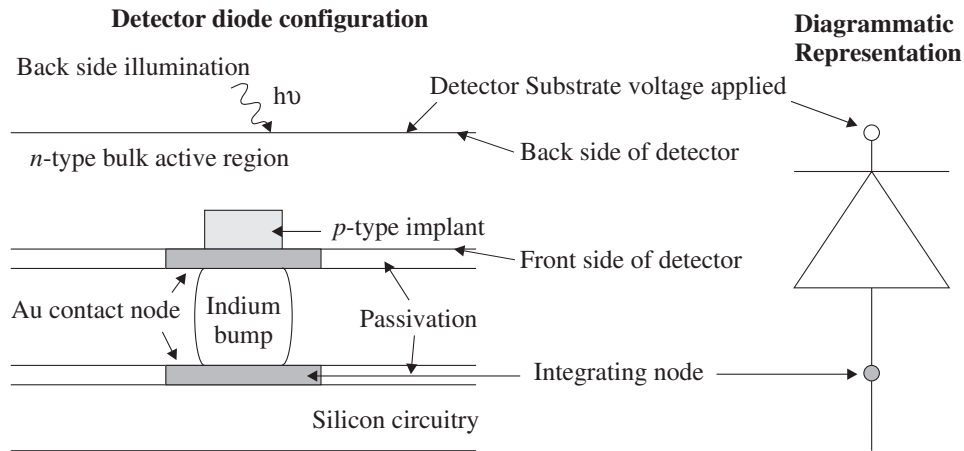


Figure 1.6. Diagram of Indium bump bonds connecting Silicon circuitry to photodiodes of another material.

The bump bond and the integrating node assume the potential of the metallization contact on the front side of the detector (implant side of the diode). Generation of electron-hole pairs in the n -type bulk active region of the diode, due to back side illumination or dark current, debiases the diode as one of the pair is swept to the implant

side of the diode by the electric field in the p - n junction. As the contact on the front side of the detector changes potential due to debiasing of the diode, the integrating node will change potential accordingly. In a CCD readout, the integrating node is electrically isolated from the charge transfer material, causing a build-up of charge in the charge transfer material closest to the integrating node. This build-up of charge, called the electron sea in Figure 1.7, is then multiplexed to the output. In the Direct readout (DRO), the integrating node is not isolated, but rather connected to the gate of a source follower Metal Oxide Semiconductor Field Effect Transistor (MOSFET), which enables multiplexing of voltages, rather than charges, to the output.

1.4 Array Readouts and Multiplexers

Multiplexing voltage (DRO) or charge (CCD) is essential when there is more than one diode to be addressed in a detector array. Multiple elements on a single detector array provide spatial resolution and a wide field of view simultaneously, which is necessary in order to save valuable telescope time. As technology improves, the number of elements on a single detector array continues to increase until it reaches limits set by the maximum size of the substrate on which the material is grown and the minimum pixel pitch possible, which in turn is set by the size of the implants, multiplexer design rules, crosstalk and noise considerations. Even larger composite arrays can be designed with three to four side buttable individual detector arrays employed in a multi-array mosaic.

Since the number of elements (pixels) in a single detector array for wide field astronomical observations continues to increase at a rapid rate, one must be able to measure the output of each pixel quickly and efficiently in order to enable short integration times.⁵ There are a few different types of readouts designed with this goal in mind, two of which I will elaborate on here. First, there is the most familiar one, the CCD readout, made of Silicon, which is itself a semiconductor with a cutoff wavelength of $1.1\mu\text{m}$.

⁵Integration time is the time during which the detector is not reset and collects charge. The detector is usually read at the beginning of this time and at the end. These two reads are subtracted to yield the accumulated charge over the integration time.

Because of this, the CCD can be used by itself for applications requiring sensitivity to visible wavelengths, such as commercial digital cameras. For desired sensitivities to wavelengths longer than $1.1\mu\text{m}$, the CCD readout can be bump-bonded to photodiodes with the desired sensitivity. The CCD readout operates by moving the collected charge from one pixel to the next toward the output, reading each pixel in sequence. One example of this readout is shown in Figure 1.7.

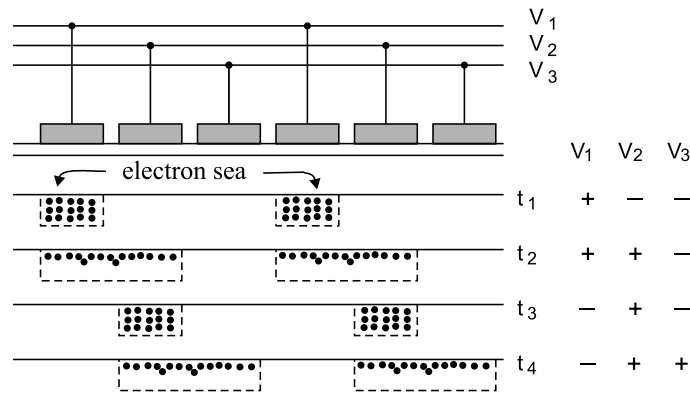


Figure 1.7. Charge transfer in a three phase CCD.

There are many drawbacks to this readout. One drawback is that each read is destructive, allowing only a single sampling of the signal on the array. Another concern is charge transfer efficiency: the quality and maximum speed of the transfer.

A non-destructive readout that multiplexes voltage is the Direct Readout (DRO) which recently utilizes Complementary Metal Oxide Semiconductor (CMOS) technology, as for the devices addressed in this thesis. In this readout, each pixel is addressed individually through clocking, and the voltage is read at the output. This readout requires complex multiplexing circuitry, but provides much more flexibility. Because of its non-destructive nature, pixels can be sampled as many times as desired without resetting, which can yield a much larger signal to noise ratio through Fowler sampling (see page 58 in Section 3.2.1).¹⁰ Alternately, pixels can be sampled multiple times at regular intervals during the integration, allowing Sample Up The Ramp (SUTR) mode (see page 59 in Section 3.2.1), which provides information regarding diode behavior

during integration. In addition, this multiplexer can be programmed to address a single pixel or small subsection of pixels for continuous readout, enabling very short read times.

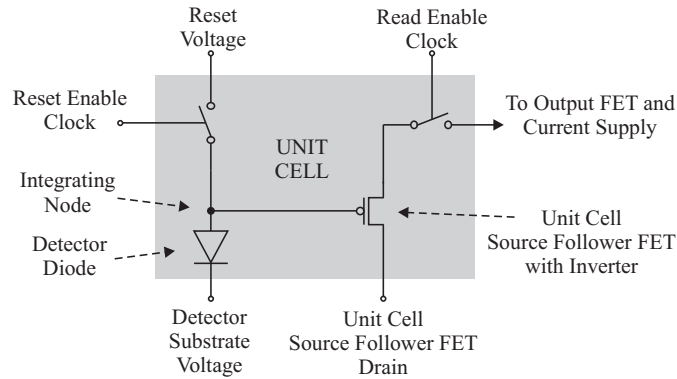


Figure 1.8. Unit cell schematic for Direct Readout (DRO).

Figure 1.8 illustrates the unit cell (UC) operation for DRO. The UC may be individually selected to be read or reset or both simultaneously. When the UC is selected for reset, the Reset Enable Clock connects the Reset Voltage to the Integrating Node. This resets the actual bias across the Detector Diode to the amount determined by the difference between the Reset Voltage and the Detector Substrate Voltage. Once the Reset Enable Clock disconnects the Reset Voltage from the Integrating Node,⁶ the Detector Diode may debias due to photo-current or dark current and the voltage at the Integrating Node will change accordingly.

When the voltage at the Integrating Node is selected for reading, the Read Enable Clock connects the Unit Cell Source Follower (UCSF) Current Supply to the source of the UCSF FET, which in turn enables the current to flow through the UCSF FET. When this happens, the voltage on the integrating node is amplified, first by the UCSF FET, and subsequently by the Output FET, before being read at the output. The gain of the source follower amplifiers (UCSF FET and Output FET) is designed to be

⁶The voltage on the Integrating Node is actually modified when the Reset Voltage is disconnected from it by charge redistribution in the reset line (see Section 3.2.4). The actual bias across the Detector Diode after this redistribution is what debiases by photo-current or dark current, thus changing the voltage at the Integrating Node.

as close to unity as possible. One of the factors that controls this gain is the UCSF current, which must be high enough to keep the gain close to unity, but low enough not to induce amplifier glow. The operational range of this readout design depends upon the threshold voltage and linear range of the amplifiers. For practical multiplexer operation, see Section 3.2.5.

Because the voltage on the Integrating Node is read through a signal chain, any malfunctioning component between the integrating node and the output will cause the measured voltage of any pixel using that component to be incorrect. It is therefore very important to ensure that each component in the signal chain is functioning properly. For the detector array research and development discussed in this thesis, one such problem was encountered. Specifically, some UCSF FETs in the HAWAII-1RG multiplexer have been found to exhibit burst noise, which is extensively discussed in Section 2.2.6. This type of noise manifests by a discrete conductivity change in the UCSF FET, which causes the voltage on the source side of the UCSF FET to fluctuate between distinct levels. Therefore, any measurements of the voltage for pixels that have UCSF FETs exhibiting this noise component have this characteristic. Since this problem was specific to the UCSF FET, its characteristics are specific to each pixel and cannot be removed by a comparative analysis of surrounding pixels. Future multiplexer development will address this issue through characterization of burst noise mechanisms.

1.5 Space-Based Astronomy Driven Requirements and Expectations

The dark current requirements for a space astronomy experiment are driven by background radiation levels. From $3\mu\text{m} < \lambda < 30\mu\text{m}$, the dominant background emission in space is from the zodiacal dust cloud. The zodiacal background radiation was measured by the Cosmic Background Explorer (COBE) experiment. At the south ecliptic pole, where this background is at a minimum, COBE measured $\lambda I_\lambda = 7 \times 10^{-11} \text{W}/\text{cm}^2 \text{sr}$ and $\lambda I_\lambda = 30 \times 10^{-11} \text{W}/\text{cm}^2 \text{sr}$ at wavelengths $5.5\mu\text{m}$ and $10\mu\text{m}$ respectively. The resulting

photo-current per diffraction-limited pixel at spectral resolution $R_s = 3$ ($R_s = \lambda/\Delta\lambda$), is given in Figure 1.9 for the telescope and assumed detector parameters noted in the figure caption. From this figure, we see that for $10\mu\text{m}$ or $5\mu\text{m}$ background-limited⁷ space operation, at $R_s = 3$, we require dark currents $< 2000e^-/s/\text{pixel}$ or $30e^-/s/\text{pixel}$ respectively. Since InSb and $5\mu\text{m}$ cutoff HgCdTe arrays cover the wavelength range out to $5.3\mu\text{m}$ at focal plane temperatures of 30K well, we concentrate here on $10\mu\text{m}$ HgCdTe arrays with dark currents $< 100e^-/s/\text{pixel}$ for the first phase of array development and testing, and $< 30e^-/s/\text{pixel}$ in phase two. Details regarding the two phases of array development and testing will be discussed in Section 1.6.

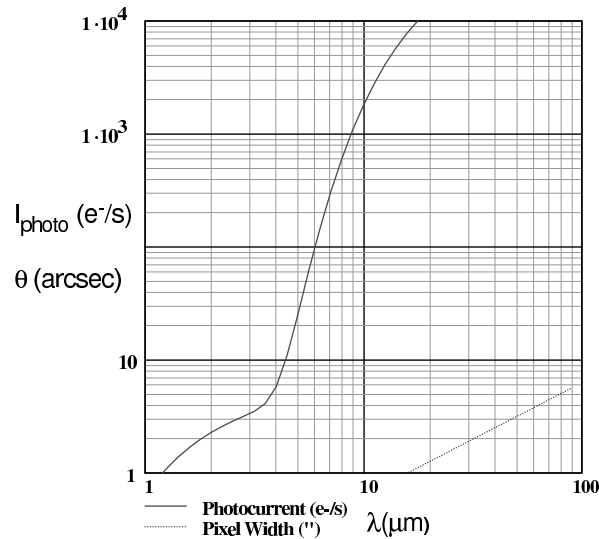


Figure 1.9. Zodiacal Light emission levels for diffraction limited pixels, quantum efficiency $\eta = 70\%$, optical efficiency 48%, and spectral resolution $R_s = 3$. The diffraction-limited pixel width (here $1.22\lambda/D$) is shown for a $D = 4\text{m}$ telescope.

High pixel operability and uniformity are also necessary: an operable pixel will meet the dark current specification, and in addition exhibit adequate quantum efficiency (for comparison, Raytheon Si:As Impurity Band Conduction (IBC) arrays exhibit a detective

⁷Background-limited performance indicates that the noise in the signal is greater than that in the dark current or any other noise source to which the detector is subject. The noise in the signal goes as the square root of the number of incoming photons for Poissonian statistics.

quantum efficiency of $\gtrsim 50\%^2$). The well depth must also be adequate for the scientific application, and the HgCdTe cut-off wavelength can be tailored to that application. Of course, the longer the cut-off wavelength, the higher the limiting thermally generated dark currents for a given array temperature.

1.6 Development Progress

Research on HgCdTe began largely within industry and at national labs for military applications, such as high background (300K) passive thermal imaging (infrared cameras monitoring thermal radiation of surroundings without active feedback or computerized control).¹¹ Not only is HgCdTe sensitive through the mid-infrared region into the long-wave infrared region ($\leq 15\mu\text{m}$) when tuned properly, it is an intrinsic semiconductor, enabling higher temperature operation than extrinsic semiconductor materials. This made HgCdTe a prime candidate for passive thermal imaging, and it has been widely investigated since being reported as a tuneable energy gap semiconductor in 1959.¹¹ Shortly thereafter, astronomers discovered the importance of this material, and in the progress that followed, military and astronomical interests diverged. Whereas military facilities have continued to develop thermal imaging for ground-based operations (high background), astronomy has required very sensitive detectors with ultra-low dark current and noise for detection of faint objects against lower to negligible background.

The University of Rochester has been involved in infrared detector array development since 1982. From 1982 until the present, the near-infrared astronomy lab has received detector arrays manufactured under the guidelines set forth by their research personnel. In particular, they define the specifications that the infrared detector arrays must meet based upon the application. From this information, the contracted company provides a delivery of detector arrays based upon the then current knowledge of how to manufacture a device to meet the defined specifications. After receipt, the research lab carries out extensive testing and characterization, through which processes that prevent the detector from meeting the desired specifications are detected and determined through analysis and theoretical modeling. This new knowledge is shared with the man-

ufacturing company which then modifies processes in order to manufacture new detector arrays better suited for the application. The detector array testing and characterization carried out at the University of Rochester is a crucial step in the development of detector arrays for specific research applications.

The development of $10\mu\text{m}$ HgCdTe detector arrays was assumed by the near-infrared astronomy lab at the University of Rochester in conjunction with Rockwell Scientific (then known as Rockwell International Science Center) in 1995. The original detector material was grown by Liquid Phase Epitaxy (LPE), where the substrate crystalline structure (nearly lattice-matched CdZnTe) is continued by liquid HgCdTe through solidification. Due to the manufacturer's concern about the quality of detector array deliveries, they chose to switch to Molecular Beam Epitaxy (MBE), where epitaxial lattice structures are grown in an ultra-high vacuum⁸ on a nearly lattice-matched substrate. This is accomplished through molecular beams that deposit Hg, Cd, and Te on the substrate. These elements then crystallize in a film on the surface with the same structure and lattice spacing as the substrate on which it is deposited. In this process, the material is grown relatively slowly,⁹ one monolayer at a time, enabling layer thicknesses as low as 10\AA .¹³

One significant benefit to this slow-growth technique is the capability for *in situ* evaluation of crystal growth conditions, which could lead to complete automation of the growth process.¹⁴ Sensors, and in some cases closed-loop feedback control designs, have been developed for HgCdTe alloy composition, substrate temperature, and source fluxes.¹⁵ This substantially increases yield because the growth of HgCdTe is very sensitive and can be affected by temperature fluctuations as small as 1°C and source flux variations as small as 0.1%.¹⁵

MBE has many advantages over Liquid Phase Epitaxy (LPE), one of which is that the material composition can be changed as abruptly as a single monolayer. This makes

⁸Ultra-high vacuum conditions are necessary for MBE so that the surface is kept impurity-free and composition and growth temperature can be carefully controlled.

⁹How slow is slow? According to Cho, 1994, with a 10^{-6} Torr background pressure, one-monolayer-per-second is the rate of growth at the substrate surface.¹²

the process intrinsically flexible and enables the precise heterostructures necessary for ultra-low dark current and noise.^{12–14, 16, 17} A second advantage is that the layers are grown at low temperatures ($\leq 200^\circ\text{C}$), which is essential to achieve compositionally stable, impurity-doped abrupt heterojunctions.¹⁸ The proprietary n - and p -type impurity dopants are shallow donors and acceptors, with low diffusion coefficients in HgCdTe, making them well suited for stable p -on- n junction fabrication.

One of the known detector performance degradation problems that arises during manufacturing is the introduction of dislocations. Even with typical dislocation densities that occur during growth under optimized conditions,¹⁶ resulting dark currents can be too high for statistically significant observations of astronomical objects which are faint in the $5 - 10\mu\text{m}$ region. Dislocations in the substrate will be continued by the deposited HgCdTe and therefore high quality substrates are necessary. Sufficient external stress can cause new defects such as screw dislocations in addition to causing existing dislocations to thread towards the point of greatest stress, such as the misfit threading dislocations discussed in Carmody¹⁹ et al. (2002). This can be a challenging problem to overcome, since physical pressure is used to bond the detector array material to the multiplexer with indium bump bonds. Another problem is growth induced void defects (Hg vacancies on the crystal lattice) due to the different sticking coefficients of the Hg and Cd which comprise the composite structure.²⁰ Steps have been taken to reduce the density of these defects, including substrate choice, buffer layers, and tight temperature control. An analysis of how dislocations affect detector performance following the formalism developed in Chapter 2 will be extensively discussed in Chapter 5.

Surface morphology is another area in which progress has been made. When there are fewer electrons than are needed to complete the bonds in a crystal structure, the unpaired electrons form dangling bonds. While this situation can be desirable in the bulk material (i.e. p -type material), it is undesirable on the surface, since it can result in surface currents. In order to eliminate this problem, the surface must be free from dangling bonds, which is accomplished by the application of another material with a wider band gap to the surface. This process is called passivation. Depending upon

the material used for passivation and the means by which the material is deposited, some surface currents may still be large enough to limit the dark current performance of LWIR diodes at low temperatures.²¹

In order to minimize this problem, two device architectures known as mesa and planar were evaluated by the manufacturer. In each layer deposited on the substrate, *in situ* processes such as doping or passivation can be achieved.¹⁷ However, in order to manufacture multiple diodes on a single substrate, the front side of each diode (*p*-type in our case) must be separated from the rest of the diodes. To accomplish this, the *p*-type material may be etched and passivated between diodes as in the mesa structure, giving it the advantage of in-situ doping. The separation may also be realized by ion implantation of the *p*-type dopant into the wide band gap HgCdTe, resulting in a buried junction.^{14, 16, 17} The second process, developed by Rockwell Scientific for MBE,¹⁴ is known as Double Layer Planar Heterostructure (DLPH) and has the advantage of in-situ passivation which greatly minimizes surface dark currents and is the structure used for deliverables from both phases discussed here. Both structures are schematically shown in Figure 1.10. Even though passivation was implemented on DLPH junctions for both phases of research and development discussed in this thesis, surface current was found to be a low reverse bias limiting mechanism for both through analysis of I-V curves at constant temperature and Arrhenius plots of dark current vs. inverse temperature as discussed in Chapters 4 and 5. It was determined that the process by which passivation is deposited causes the observed surface currents. Therefore, these processes will need to be investigated and improved for future array deliverables.

Progress has been made in detector array fabrication, as well as in improved manufacturing techniques for the production of the HgCdTe material. Earlier work in our lab^{22, 23} determined that 10.6 μ m HgCdTe single pixel devices, with relatively low doping $\sim 9.5 \times 10^{14} \text{cm}^{-3}$, showed excellent performance at 30K where 8 of the 17 single diodes tested exhibited low dark currents¹⁰ (dominated by trap-to-band tunneling) for their size and applied bias. The Rockwell advanced structure junctions (junction area

¹⁰These low dark currents were on the order of $10^5 e^-/s$ for 100mV of reverse bias.

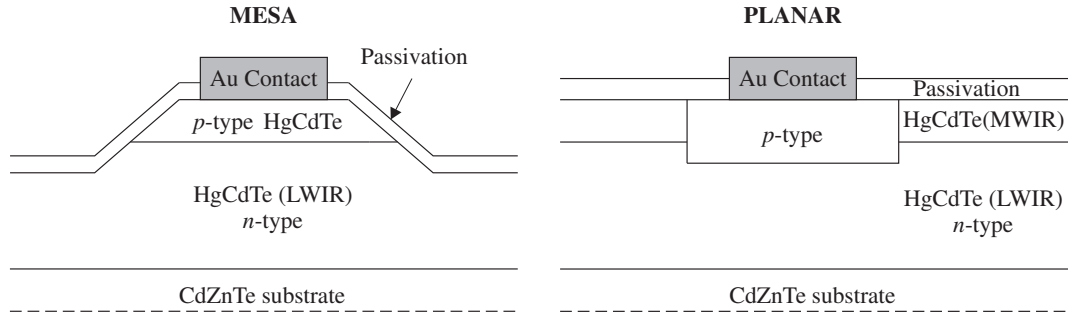


Figure 1.10. Mesa and planar DLPH diode structures. Illumination of these devices is through the substrate (back side illumination).

≪ optical area, so that Generation-Recombination (G-R) currents and capacitance are minimized) were the best performing diodes in the lot.

The first phase of delivered research devices from Rockwell Scientific (see Chapter 4) consisted of seven detector arrays which were manufactured in a “banded” format. This format employed nine different sizes/geometries of diode implants arranged in groupings of four rows for each given type, such that testing of multiple diode structures could be done on one array. These detectors were bonded to engineering grade NICMOS3 multiplexers and had a 256×256 format. The operation of these devices and the lab equipment utilized in testing are detailed in Chapter 3. Results from these devices allowed us to ascertain the optimal diode size and geometry for future research array deliverables (see Chapter 4). However, even the best of these bands of diodes had only 28% of detector pixels meeting the specifications at 60mV reverse bias. Therefore, improvement of diode quality was necessary.

Through the first phase, we confirmed that the diodes with the smallest nodal capacitance had the lowest dark currents ($< 100e^-/s$)²⁴ (see also Section 4.4). Therefore, the research arrays of phase two were manufactured with the diode size and geometry that gave this result. Also, a change in multiplexer was necessary at this time, for the availability of remaining assets was declining. In order to increase yield of detector pixels meeting the desired specifications, Rockwell Scientific developed a proprietary, stress-reducing bonding architecture, which was implemented during hybridization. Thus,

detector arrays with the chosen diode configuration were bonded with the new architecture to the HAWAII-1RG multiplexer for the research arrays manufactured for phase two. The operation of these detector arrays and the equipment utilized in testing them are discussed in Chapter 3. Considerable progress was made in phase two and has been reported^{25,26} at two SPIE meetings: San Diego, 2003 and Denver, 2004. Further progress has been made since that time by the analysis of I-V curves at constant temperature and Arrhenius plots of dark current vs. inverse temperature for individual pixels and is discussed in Chapter 5 using the formalism developed in Chapter 2. This analysis showed that the limiting dark current mechanisms for low and high bias are surface current and dislocation-induced breakdown respectively. The detection and characterization of burst noise discovered in the HAWAII-1RG multiplexer that was reported²⁷ at the SPIE meeting in San Diego, 2005 is also described in Chapter 5 in addition to preliminary analysis of burst noise characteristics as they are affected by operating parameters and temperature. Future directions and a summary of the thesis is given in Chapter 6.

Chapter 2

Theory

In this chapter, dark current and noise theory are presented. These theories will be used in modeling the dark currents obtained with the data given in Chapters 4 and 5. Through this modeling, the limiting dark current mechanisms are identified. Most of the dark current theories presented are derived by other authors. Surface current theory and diode breakdown theory contain, in addition, necessary new components to explain the observations presented in Chapters 4 and 5. The noise theories presented in this chapter are all derived by other authors with the exception of new ideas suggested in the burst noise section, since most existing burst noise theories were not derived for experiments conducted under constant current conditions.

2.1 Dark Current Theory

The dominant sources of dark current in a photodiode under normal operating conditions are thermal generation-recombination in the bulk region (diffusion current), thermal generation-recombination in the depletion region (G-R current), tunneling (band-to-band and trap-to-band), and (front side, see Figure 1.6) surface current. Dark current from each of these mechanisms comprise the total dark current, which can be described as follows:²⁸

$$I_{dark} = I_{dif} + I_{G-R} + I_s + I_{tunnel}, \quad (2.1)$$

where the terms in this equation are diffusion current, G-R current, surface current, and tunneling current respectively. When the detector is exposed to light, the current calculation has an extra term for the photo-current, I_{photo} , given by Equation 1.8. This makes the total current

$$I_{total} = I_{dark} - I_{photo}. \quad (2.2)$$

2.1.1 Diffusion Current

Diffusion current is the ideal dark current mechanism in a diode, and is represented by Equation 1.6. Diffusion current originates in random thermal generation and recombination in the bulk area. Newly generated electrons and holes diffuse to the depletion region and are subsequently separated by its driving electric field. These electron-hole pairs must be generated within one minority carrier diffusion length, L_h , of the depletion region in order to reach the depletion region before recombining. For the n -type region of the photodiode, the majority carrier (or dominant carrier) is the electron, making the hole the minority carrier as indicated by the subscript.

Following the derivation process outlined in Reine et al. (1981),⁹ we make some assumptions in order to determine what quantities comprise the saturation current I_0 (see Equation 1.6). First, we assume that the junction is abrupt, and thus can be divided into three regions with negligible transition space between them. These regions are shown in Figure 2.1, and are the electrically neutral n -type region, the space-charge (depletion) region comprised of partly n - and p -type material, and the electrically neutral p -type region of thicknesses d , W , and d_p respectively. Second,



Figure 2.1. Not-to-scale illustration of the junction regions.

we must assume all of the bias voltage (V_{actual_bias}) is dropped across the space-charge region. Third, we must assume a number of factors about the p -type and n -type regions: they are considered to be electrically neutral and uniformly doped, the low-injection

case is assumed, which means the departure of the minority carrier concentrations from equilibrium is small compared to the majority carrier concentrations. Finally, the carrier distributions are assumed to be non-degenerate so that to first order, $N_a N_d = n_i^2$, where N_a and N_d are the net acceptor and donor concentrations respectively for the active region in thermal equilibrium and n_i is the intrinsic carrier concentration.

Since V_{actual_bias} is dropped across the space-charge region, it affects the width of the depletion region. In fact, the width is given by²²

$$W = \sqrt{\frac{2\varepsilon\varepsilon_o(V_{bi} - V_{actual_bias})}{qN_d}}, \quad (2.3)$$

where ε_o is the permittivity of free space, ε is the relative permittivity of HgCdTe, V_{actual_bias} is the actual bias across the diode (negative for reverse bias) and V_{bi} is given by Equation 1.5.

The steady-state excess minority carrier concentration, Δn , is given by the solution to⁹

$$D_h \frac{\partial^2 \Delta n}{\partial z^2} - \frac{\Delta n}{\tau_b} = 0, \quad (2.4)$$

where D_h is the hole diffusion coefficient in cm^2/s , τ_b is the minority carrier (hole) lifetime in the n -type active bulk material, and z is the distance into the n -type active region from the boundary between it and the space-charge region. The diffusion current I_{dif} is given by

$$I_{dif} = qAD_h \frac{\partial \Delta n}{\partial z}, \quad (2.5)$$

where A is the diode junction area.

To solve this for an active region with a thickness d much less than the diffusion length ($\sim 47\mu\text{m}$ at 77K)²⁹ of the minority carrier L_h , we first use the boundary condition at $z = d$, given by⁹

$$I_{dif}(z = d) = qAD_h \left. \frac{\partial \Delta n}{\partial z} \right|_{z=d} = -qAS_n \Delta n(d), \quad (2.6)$$

where S_n is the surface recombination velocity at the interface between the n -type active region and the substrate or passivation (back side). The solution to Equation 2.4 with

the boundary condition in Equation 2.5 is⁹

$$\Delta n(z) = N_a \left[\exp\left(\frac{qV}{k_b T}\right) - 1 \right] \left[\frac{\cosh\left(\frac{z-d}{L_h}\right) - \beta \sinh\left(\frac{z-d}{L_h}\right)}{\cosh\left(\frac{d}{L_h}\right) + \beta \sinh\left(\frac{d}{L_h}\right)} \right], \quad (2.7)$$

where β is defined as

$$\beta = \frac{S_n}{(L_h/\tau_b)} \quad (2.8)$$

Because HgCdTe is grown by MBE on a nearly lattice-matched CdZnTe substrate, the surface recombination velocity, S_n , is negligible compared to the diffusion velocity, L_h/τ_b . Evaluating Equation 2.5 at $z = 0$ with the condition $\beta \approx 0$, and that for a thin active region ($d \ll L_h$) we obtain

$$I_{dif} = qA \frac{n_i^2 d}{N_d \tau_b} \left[\exp\left(\frac{qV_{actual_bias}}{k_b T}\right) - 1 \right], \quad (2.9)$$

where n_i is the intrinsic carrier concentration (see Equation 1.4), and N_d is the doping density. The exponential term in Equation 2.9 is negligible (in reverse bias) when it is $\ll 1$, which is the case at $T = 30\text{K}$ for $V_{actual_bias} < -12\text{mV}$. For this common case, the diffusion current depends very little upon bias.

2.1.2 Generation-Recombination Current

Generation-recombination (G-R) current is the portion of the dark current caused by generation and recombination in the depletion region. Electron-hole pairs created in the depletion region will be separated by the driving electric field. These pairs must come from trap centers located between the valence and conduction bands. One partner of the pair, however, will be trapped in the generation-recombination trap center.

The equation that must be solved to obtain the trap center generation-recombination current is⁹

$$I_{G-R} = qA \int_0^W G(z) - R(z) dz, \quad (2.10)$$

where $G(z)$ and $R(z)$ are the generation rate and recombination rate respectively of charge carriers in the space-charge region at trap center locations and z is the distance

into the space-charge region from the boundary between it and the n -type active region. The equilibrium concentrations of electrons and holes are given by^{9,30}

$$n_1 = N_c \exp\left(\frac{E_{t-gr} - E_g}{k_b T}\right), \quad (2.11)$$

and

$$p_1 = N_v \exp\left(\frac{-E_{t-gr}}{k_b T}\right), \quad (2.12)$$

respectively, where N_c and N_v are the conduction band and valence band effective densities of states respectively, E_{t-gr} is the trap energy with respect to the valence band and E_g is the band gap energy. The steady-state net recombination rate, $G(z) - R(z)$, through the given G-R trap centers can be calculated by⁹

$$G(z) - R(z) = \frac{n_i^2}{\tau_{po}(n + n_1) + \tau_{no}(p + p_1)} - \frac{np}{\tau_{po}(n + n_1) + \tau_{no}(p + p_1)}, \quad (2.13)$$

where $n = n(z)$ and $p = p(z)$ are the perturbed electron and hole concentrations respectively within the space-charge region, and τ_{no} and τ_{po} are the lifetimes of electrons and holes in the depletion region. The lifetimes are given by

$$\tau_{no} = \frac{1}{C_n N_t}, \quad (2.14)$$

and

$$\tau_{po} = \frac{1}{C_p N_t}, \quad (2.15)$$

respectively, where N_t is the number of trap centers at energy E_{t-gr} per unit volume, and C_n and C_p are the capture coefficients (in cm^3/s) for electrons and holes respectively.

Assuming that the potential varies linearly with distance over the space-charge region, Sah et al. calculate³¹

$$I_{G-R} = \frac{qAn_iW}{\tau_{gr}} \frac{\sinh(-qV_{actual_bias}/2k_bT)}{q(V_{bi} - V_{actual_bias})/2k_bT} f(b) \quad (2.16)$$

with the assumption that $\tau_{gr} = \sqrt{\tau_{po}\tau_{no}}$ and $\tau_{po} = \tau_{no}$, indicating the capture coefficients of electrons and holes are identical. In this equation, τ_{no} and τ_{po} are the lifetime of a hole and an electron in the depletion region respectively. The function $f(b)$ is given by

$$f(b) = \int_0^\infty \frac{dy}{y^2 + 2by + 1}, \quad (2.17)$$

and

$$b = \exp\left(\frac{-qV_{actual_bias}}{2k_bT}\right) \cosh\left(\frac{E_{t_gr} - E_i}{k_bT}\right), \quad (2.18)$$

where E_i is the intrinsic energy level position with respect to the valence band. With a typical mid-gap value for E_i , trap energies close to the center of the gap ($E_{t_gr} \sim E_i$) will be most effective and therefore will contribute most heavily to the G-R current.

2.1.3 Surface Current

When the material composition changes from layer to layer, the interface formed between the layers can contribute to the observed dark current. This comes about due to thermal generation of charge carriers from interface states and is known as surface current. The three interfaces of interest in the HgCdTe detectors can be seen in the planar heterostructure shown on the right side of Figure 1.10.

The first interface is created when the LWIR HgCdTe is deposited onto the CdZnTe substrate. In order to ensure that most carriers generated in the LWIR n -type active region diffuse to the p -type implant before recombining, the n -type active layer is thinner than the minority carrier (hole) diffusion length, L_h . Therefore, in order to contribute to the dark current, any carriers generated at the LWIR HgCdTe and CdZnTe interface would have to diffuse to the depletion region. For this reason, the current generated here would have the same temperature and bias dependence as diffusion current. Because the CdZnTe substrate is nearly lattice matched to the LWIR HgCdTe, this contribution to the dark current is negligible and will not be considered.

At the transition from LWIR HgCdTe to MWIR HgCdTe, another interface is formed. This interface interacts with the p - n junction where it intersects the p -type material along the perimeter of the implant. For this reason, the dark current contribution from charge carriers generated at this intersection would be proportional to the perimeter of the implant and have the same temperature and bias dependence as g - r current.²¹ Because this interface is created *in situ* with MBE, the crystalline structure at this interface is continuous. Therefore, its contribution to the dark current is negligible. MWIR $5.3\mu\text{m}$ HgCdTe detector arrays manufactured by the same process show

dark currents less than $0.006e^-/s$ at 30K.³² This indicates that the contribution of this mechanism is reasonably neglected.

The third interface is between the MWIR HgCdTe and the passivation layer. Passivation is not part of the *in situ* MBE growth process and the MWIR HgCdTe layer undergoes proprietary processing techniques in order to achieve passivation.³³ It is due to this processing that we consider only this interface in modeling the surface current. The surface current at this interface originates in fast surface states (surface traps that can rapidly acquire charge but do not easily release it) and can be given by:^{9,28}

$$I_s = \frac{1}{2}qAn_i s. \quad (2.19)$$

where s is the effective maximum surface recombination velocity associated with the fast surface states at the intrinsic level. The surface recombination velocity depends on the recombination center density per unit area in the surface region. Since the surface region of interest is on the front side of the detector material near the depletion region, the width of the depletion region may affect the surface recombination velocity. We therefore use

$$s = s_0 \frac{W}{\tau_s} \left[\exp\left(\frac{qV_{actual_bias}}{\beta k_b T}\right) - 1 \right], \quad (2.20)$$

where s_0 is the velocity coefficient and τ_s is the effective lifetime of the surface states. In addition, we recognize that the band structure of the HgCdTe material at the surface may not have the same shape as that of the bulk material due to surface boundary conditions. We therefore allow an ideality factor, β , in the exponent of s in Equation 2.20 and n_i (Equation 1.4) for this mechanism such that

$$n_i = (5.585 - 3.820x_s + 1.753 \cdot 10^{-3}T - 1.364 \cdot 10^{-3}x_s T) \times [10^{14} \cdot E_g^{3/4} T^{3/2} \exp(-E_g/\beta k_b T)], \quad (2.21)$$

where x has been changed to x_s to indicate surface composition, which can be modified during passivation processing.³³

Minimizing generation-recombination centers at the interface is accomplished by surface passivation, a technique discussed in Section 1.6. This technique of terminating the dangling bonds on the surface greatly reduces the recombination velocity. As mentioned

previously in this section, the first two interfaces discussed have negligible contributions to the dark current. This is because they are well passivated by the *in situ* modification of layer composition. Specifically, on the back surface, the CdZnTe substrate on which the *n*-type 10 μ m cutoff HgCdTe is grown effectively passivates that surface (and reduces S_n so that $\beta \approx 0$ in Equation 2.8). In addition, the LWIR HgCdTe to MWIR HgCdTe interface is well passivated by the MBE growth of the MWIR HgCdTe on the LWIR HgCdTe surface. The DLPH layers referred to here are illustrated in Figure 1.10.

The passivation applied on the front surface of the MWIR HgCdTe reduces the surface recombination velocity at that surface by completing the dangling bonds left by the termination of the MWIR HgCdTe. Though surface current is greatly reduced in well-fabricated and passivated devices, we continue to reduce G-R current, diffusion, and tunneling through careful control of doping and structure fabrication, and lower temperature operation. Because of this, contemporary methods of passivation may need to be modified in order to keep surface current from being a limiting factor.

The model given here for surface current is not exclusive to any particular form of surface current, such as a current shunt. It utilizes parameters such as the intrinsic carrier concentration n_i , for a given surface composition parameter x_s , allowing for a composition and temperature dependence. It also has a dependence upon the depletion region width, but in the temperature and bias region of interest the width has a negligible effect on the surface current. Increasing β and decreasing x_s have similar effects on the shape of the surface current vs. temperature model. In fact, $x_s = 0.3088$ and $\beta = 5.5$ can fit the data of Figure 4.8 as well as $x_s = 0.210$ and $\beta = 2$, i.e. $E_g/\beta kT$ is the same for both cases. It is likely that some combination of increasing β and decreasing x_s is the proper fit for the data. However, $\beta > 3$ is improbable and proprietary processing techniques employed to passivate can modify the HgCdTe composition parameter on the surface.³³ Therefore, we will concentrate upon fitting the data with a modified x_s , rather than β in both Section 4.4.2, 5.2.1 and 5.2.2.

2.1.4 Tunneling Current

Tunneling current is caused by electrons tunneling from the valence to conduction band either directly (band-to-band) or indirectly (trap-to-band) by using intermediate trap sites. These processes are shown in Figure 2.2. This can be an important mechanism for these devices because of the very small band gap of the ternary material.

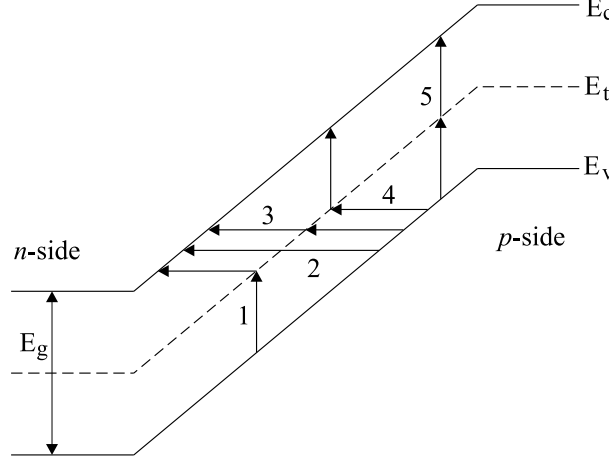


Figure 2.2. Dark current mechanisms: band-to-band tunneling (2), trap-to-band tunneling (3), thermal assisted trap-to-band tunneling (1, 4), and G-R (5).

Band-to-band tunneling has been modeled several ways. One way employs a simple triangular barrier, and has the following form:^{28, 34}

$$I_{band-to-band} = -\frac{q^3 A E V_{actual_bias}}{4\pi^2 \hbar^2} \sqrt{\frac{2m_{eff}}{E_g}} \exp\left(-\frac{4(2m_{eff})^{1/2} E_g^{3/2}}{3q\hbar E}\right), \quad (2.22)$$

where E is the electric field across the junction and m_{eff} is the effective mass of the minority carrier, often given in terms of the mass of the electron m_e . This electric field can be calculated by²⁸

$$E = \sqrt{\frac{2N_d(E_g - qV_{actual_bias})}{\varepsilon\varepsilon_o}}. \quad (2.23)$$

Here, ε is the relative permittivity, which for HgCdTe at 30K is approximately 17.1, and ε_o is the permittivity of free space. This is the form that is used when the diode is free from dislocations. Dislocations may cause the band-to-band potential barrier to be

modified from the ideal case of a triangular barrier to that of a parabolic barrier. For such a case, band-to-band tunneling would assume the form³⁵

$$I_{band-to-band} = -\frac{q^3 A E V_{actual_bias}}{4\pi^3 \hbar^2} \sqrt{\frac{2m_{eff}}{E_g}} \exp\left(-\frac{\pi(m_{eff}/2)^{1/2} E_g^{3/2}}{2q\hbar E}\right). \quad (2.24)$$

For trap-to-band tunneling, the most general equation assumes a parabolic barrier and uniform electric field,³⁶

$$I_{trap-to-band} = n_t W \frac{\pi^2 q A m_{eff} E M^2}{h^3 (E_g - E_t)} \exp\left(-\frac{\sqrt{\frac{m_{eff}}{2}} E_g^{3/2} F(a)}{2qE\hbar}\right), \quad (2.25)$$

where

$$F(a) = \frac{\pi}{2} - a\sqrt{1-a^2} - \arcsin a, \quad (2.26)$$

and

$$a = 2\frac{E_t}{E_g} - 1. \quad (2.27)$$

In the trap-to-band tunneling equations, n_t is the trap density, M is the transition matrix element, and E_t is the energy of the trap level with respect to the conduction band.

2.1.5 Diode Breakdown

Breakdown, either Zener or avalanche, is typically not a limiting mechanism for a diode operated in the low reverse bias region. For the photodiodes on our detector arrays, this type of breakdown is expected to occur at approximately one volt reverse bias. Since normal photodiode operation for these devices is less than 250mV of reverse bias, one would not expect to observe breakdown. However, we have encountered dark currents which increase exponentially with bias at reverse biases ≤ 150 mV. From this, we discovered there is an additional form of breakdown that needs to be considered. This additional form is known as dislocation-induced early breakdown. This breakdown is considered “early” because it occurs at much lower biases than the expected breakdown voltage, $V_{breakdown}$, of avalanche or Zener breakdown. To obtain a complete picture

of the various forms of breakdown, we discuss four such forms here: Zener, avalanche, dislocation-induced, and thermal breakdown.

First is the breakdown due to thermal instability. This results from heat dissipation caused by reverse current that increases the junction temperature, which in turn increases the reverse current.³⁴ The result is junction breakdown which can damage the diode if no current limiting resistor is used. This form of breakdown is negligible at the operating temperatures of our detector arrays.

A second form of breakdown is due to tunneling and is known as Zener breakdown.³⁷ The potential difference between the conduction or valence band of the p - and n -type regions is proportional to $V_{bi} - V_{actual_bias}$, whereas the width of the depletion region is proportional to the square root of the same quantity (see Equation 2.3). Therefore, the height increases faster than the width, narrowing the potential barrier between the valence band of the p -type region and the conduction band of the n -type region as shown in Figure 2.3. This causes the tunneling probability to increase and therefore the current to increase. The actual form of this current is given in Equation 2.22. We will treat Zener breakdown as band-to-band tunneling current, discussed in Section 2.1.4.

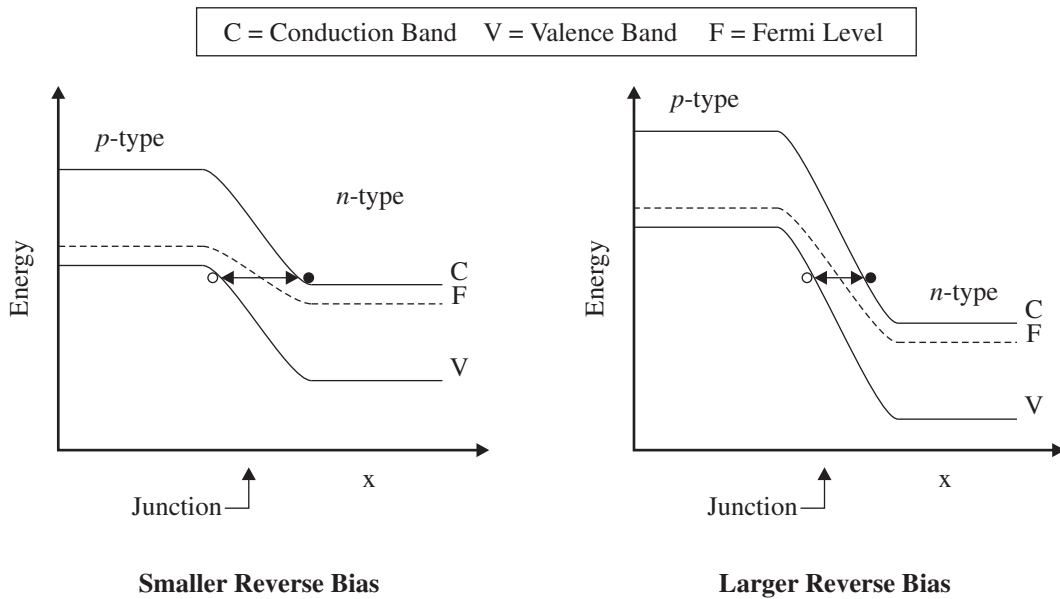


Figure 2.3. Tunneling breakdown energy diagram.

Avalanche multiplication (impact ionization) is a third form of breakdown. If the reverse bias voltage is sufficiently high, a thermally (or otherwise) generated electron-hole pair may gain enough kinetic energy as it moves through the junction due to the electric field that it can transfer its kinetic energy through a collision with the lattice to create another electron-hole pair (impact ionization).³⁴ This process is continued across the junction as illustrated in Figure 2.4. In the figure, the initial hole causing the avalanche is indicated by number one. As hole one moves in the direction of the electric field, it picks up kinetic energy. When it has enough kinetic energy, it collides with an atom, freeing the bound electron in the valence band by transferring its kinetic energy. The electron is freed into the conduction band, leaving a charge carrying hole in the valence band. This newly freed hole and the hole which freed it are accelerated again by the electric field indicated by the number two on the diagram, while the freed electron is accelerated by the same in the opposite direction.

When the two holes acquire enough kinetic energy, they free two more holes, again doubling the number of free holes to four and so on. In addition, the electrons accelerated in the opposite direction may also acquire enough kinetic energy to free more electrons, which in turn frees more holes. Because both charge carriers have high mobility, this results in a large gain and gain dispersion. For extrinsic semiconductor material, where the mobility of the majority carrier is much higher than the ions, the multiplication is limited and can be used to an advantage in photomultiplication devices. For a single initially free hole, multiplication occurs from the n to the p side of the junction, increasing the current with distance through the depletion region.³⁴

If we define M_{av} as the multiplication factor across the junction, it is clear that in the above example (assuming no freed electrons generate more holes at the starting point) $M_{av} = 8$. As $M_{av} \rightarrow \infty$, due to freed electrons generating more holes, avalanche breakdown occurs. The voltage at which avalanche breakdown becomes a dominant process is given for a one-sided abrupt junction by Sze³⁴ as

$$V_{av_breakdown} = \frac{E_c W_c}{2}, \quad (2.28)$$

where E_c is the critical electric field at which avalanche multiplication takes place and

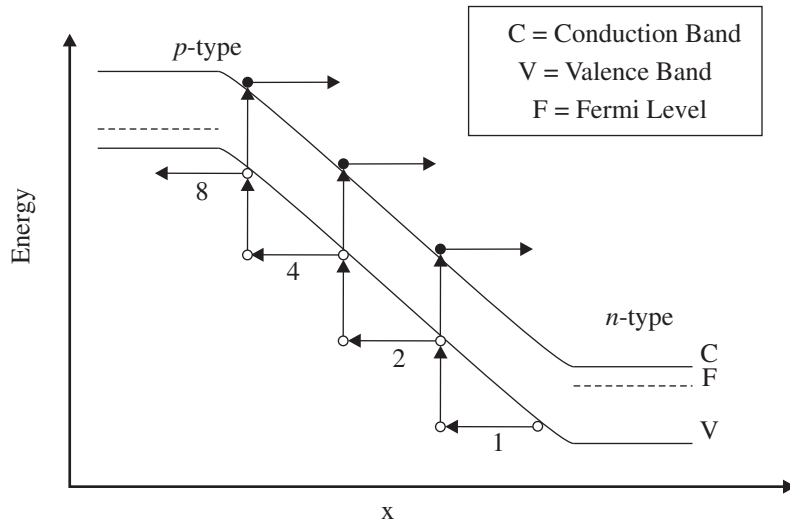


Figure 2.4. Avalanche multiplication process shown on an energy diagram.

W_c is the depletion region width at the critical electric field. For diodes such as these, $V_{av_breakdown}$ is on the order of a volt. Therefore, this form of breakdown does not dominate the dark current in the operating regions considered ($V_{bias} = 0 - 250\text{mV}$).

A final form of breakdown is dislocation-induced early breakdown. The majority of literature that discusses this form of breakdown focuses on silicon carbide (SiC) semiconductor electronic devices, but the resulting effect on the current as a function of actual reverse bias is the same. Specifically, Neudeck et al.³⁸ discuss the effect of elementary screw dislocations on 4H-SiC p^+n junction rectifiers in which they observe localized breakdown indicated on an optical micrograph as a microplasma. The localized breakdown corresponds to a breakdown voltage at a lesser reverse bias than diodes without dislocations (i.e. the tunneling breakdown). In addition, at reverse biases higher than the localized breakdown, they observe a “knee” on the I-V curve (plot of dark current vs. actual reverse bias) where the current does not increase with reverse bias as rapidly as it does initially.

A screw dislocation which forms the beginning of the dislocation line is shown in Figure 2.5. These dislocations are often produced during crystal growth, but can also be a result of mechanical stress.³⁹ Specifically, the dislocation can propagate under

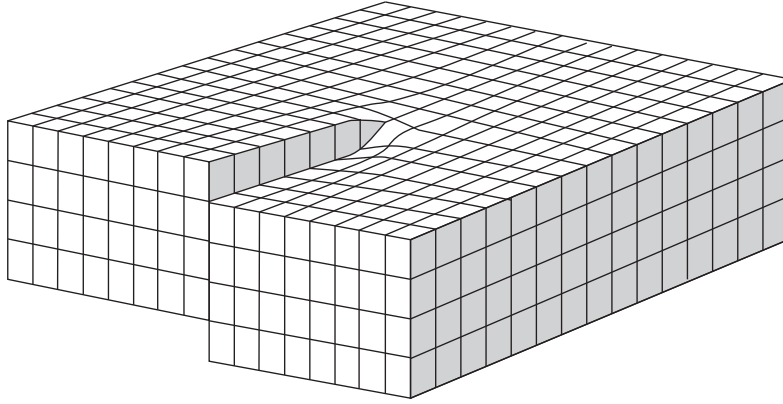


Figure 2.5. Three dimensional representation of a crystal lattice with a screw dislocation.

sufficient stress due to the strong distortion of the lattice at the screw dislocation. The Burgers vector associated with the dislocation indicates the magnitude and direction of the displacement of one part of the crystal with respect to the other as a result of the dislocation.³⁹ For elementary screw dislocations, the Burgers vector should have a magnitude no greater than a lattice constant.⁴⁰ When the magnitude is greater, it often causes more serious distortion of the lattice at the dislocation that can lead to high stress during the growth process. Growth under this kind of stress can cause growth spirals with and without hollow center cores, known as micropipes.^{39,41}

Even elementary screw dislocations when located in the p - n junction can cause early breakdown.³⁸ When this type of defect is activated, the dangling bonds present along the core of the screw dislocation become available trapping centers. This can occur physically if the dislocation is located just outside the p - n junction at lower reverse biases and as the voltage is increased, the depletion region grows so as to include the dislocation. As the ionization energy (qV_{actual_bias}) passes the activation energy with increasing reverse bias voltage, the active trap density in the p - n junction increases from its initial trap density n_{t_i} to

$$n_t = n_{t_i} + \frac{n_{t_d}}{1 + \exp\left(\frac{(E_a + \gamma q V_{actual_bias})}{kT}\right)}, \quad (2.29)$$

where n_{t_d} is the density of traps added by the dislocation, γ is a scaling factor that

pertains to the properties of the dislocation (i.e. orientation)³⁸ and E_a is the dislocation activation energy. Note that V_{actual_bias} is negative for reverse bias. The activation energy is the energy at which the traps associated with the dislocation become active trapping sites and is given for holes by the difference between the trap energy and the valence band. The initial active trap density not associated with the dislocation may have a different trap energy than the dislocation traps. For this reason, the two populations will be considered as separate contributions, both with the formalism of trap-to-band tunneling.

The activation of the traps associated with the dislocation initializes early breakdown which manifests as an abrupt rise in trap-to-band tunneling current. This rise ends as all traps are activated. As this “knee” in the I-V curve is reached, trap-to-band tunneling dominates. In the I-V curves for some pixels, the current continues to rise faster than trap-to-band tunneling with the higher trap density. For these pixels, the subsequent rise can be fit by Equation 2.24, where a parabolic barrier between the valence and conduction bands across the depletion region has replaced the ideal triangular barrier. This is likely a result of the effect of the screw dislocation on the energy bands (i.e. local reduction in band gap).⁴⁰

Since the discussed dark current mechanisms have different temperature and bias dependences, the characteristics of the dark current as a function of temperature and bias will help to determine which mechanism is the primary dark current mechanism in these devices.

2.2 Noise Theory

The total noise of each pixel in an array can be broken down into its components. Although not all components are well understood, each one contributes to the total noise in a pixel, and they add in quadrature. When a noise component is understood, its effect can either be reduced via specific measurement techniques, or minimized (and possibly eliminated) via processing and manufacturing advancements. The total noise in the measured signal of a pixel is given by the quadrature sum of its parts, as shown

in Equation 2.30.

$$V_{N_{total}}^2 = V_{N_{diode}}^2 + V_{N_{read}}^2 + V_{N_{system}}^2 \quad (2.30)$$

The diode noise, $V_{N_{diode}}$, is the noise generated by the p - n junction. If we were able to address the diode directly, we would be limited by $V_{N_{diode}}$. However, we do not address the diode directly, but rather through electronics which multiplexes the signal to an output. The noise in this signal chain is called the read noise, $V_{N_{read}}$. This has also been referred to as multiplexer noise. The output of the multiplexer is not directly addressed either, but rather through a complex system which is able to record the output of many pixels per second. This enables us to work on very short timescales, but is not without its disadvantages. The system used to address the mux adds a finite amount of system noise, $V_{N_{system}}$.

These three noise components are created by multiple noise sources. Shot noise, or Schottky noise, is noise due to current flow and charge quantization. It is present in all three components, but it is the dominant source of noise in $V_{N_{diode}}$. In addition to shot noise, the dominant noise sources in $V_{N_{read}}$ are Johnson noise and the related KTC noise, clock feed-through, $1/f$ noise and burst noise. System noise is dominated by amplifier noise due to the array controller electronics, which is in turn dominated by shot noise, Johnson noise and $1/f$ noise. Following is a discussion of each of the above noise components which dominate $V_{N_{diode}}$, $V_{N_{read}}$, or $V_{N_{system}}$.

2.2.1 Shot Noise

Because free carriers and the source or background photons that produce them (electron-hole pairs) are generated by random uncorrelated processes, a histogram of the number of free electrons generated in a given period of time assumes the shape of a Gaussian and is governed by Poisson statistics. This type of unavoidable noise is commonly known as shot noise (or Schottky noise). Shot noise is a form of “white noise”, meaning that it has a flat frequency spectrum.⁴²

With B as the effective power bandwidth, the noise in the current due to shot noise

is given by⁴³

$$I_{N_{shot}} = \sqrt{2q|I|B}, \quad (2.31)$$

where q is the charge on an electron and $|I|$ is the magnitude of a single current source flowing through the diode. This corresponds to voltage noise

$$V_{N_{shot}} = \sqrt{2qR|V|B}, \quad (2.32)$$

where R is the effective mean resistance of the diode (measured by the inverse slope of a current vs. voltage graph) and $|V|$ is the voltage difference between the integrating node and the substrate. The current flow in the diode is due to either dark current or photocurrent. Dark current is assumed to be Poissonian, thus contributing to shot noise. However, some dark current mechanisms, such as tunneling, may not be completely Poissonian.

2.2.2 Johnson Noise

Johnson noise is another form of “white noise.”⁴² It is exhibited in resistive devices, such as resistors or photo-conductive detectors. It does not apply to ideal or near-ideal ($10^{15}\Omega$) diodes, such as photo-voltaic detectors operated under an externally applied reverse bias, because they are capacitive devices.^{44, 45} Therefore, it does not contribute to the diode noise, but it does contribute to both $V_{N_{read}}$ and $V_{N_{system}}$. At absolute temperature, T , the open-circuit voltage noise generated by resistance R is⁴²

$$V_{N_{Johnson}} = \sqrt{4k_bTRB} \quad (2.33)$$

where k_b is Boltzmann’s constant. At low temperatures, resistive devices are still subject to Johnson noise. At 30K, with an estimated upper limit on the source follower FET source to drain resistance of $10^5\Omega$ and a system bandwidth of 160kHz, $V_{N_{Johnson}} \lesssim 5\mu V$. This is a very small contribution to the overall read noise.

2.2.3 KTC Noise

Another source of read noise is KTC noise, which has a similar form to Johnson noise. The distinguishing factor between these two noises is that KTC noise is for a capacitive

device, whereas Johnson noise is for a resistive device. This noise source was named after the parameters on which it depends:⁴⁶

$$V_{N_{KTC}} = \sqrt{\frac{k_b T}{C}}, \quad (2.34)$$

where C is the capacitance on the integrating node, including diode capacitance, gate capacitance, reset capacitance and the remaining indirect stray capacitances. This type of noise manifests as a reset to reset fluctuation. After the reset switch is turned off (see Section 3.2), each pixel that was reset reaches a voltage on the integrating node determined by C , temperature, and reset voltage. This voltage will not necessarily be the same as that reached after a previous reset, due to variations in the above parameters. The result is a slightly different reset level after each reset. Therefore, if two samples are taken after the same reset (without a reset in-between them) and subtracted, the KTC noise will be effectively subtracted out (see Section 3.2.1), since the voltage level only varies with subsequent resets. This is the normal mode in which the devices are operated, and therefore KTC noise is not an overall dominant source of noise. If, however, the devices were operated such that the samples obtained (single reads of the device) were either uncorrelated or correlated with a reset in-between them, KTC noise may be a large effect.

2.2.4 Clock Feed-Through

Since the multiplexer has a number of input clocks which control FET switches, which in turn enable reset and read lines and select rows and columns, the capacitance between the clock lines and the signal output allows the clock transitions to feed into the output. This manifests as a spike in the output during the transition followed by a slight offset level shift, known as a form of ‘charge dump.’ Level shifting occurs every time a clock level changes. This is especially apparent in the row and column transitions and can contribute to the read noise. This effect is minimized by sampling before or after clock transitions and never during transitions. Therefore, with proper sampling technique (see Section 3.2.1), this noise source is insignificant.

2.2.5 $1/f$ Noise

A noise component that is present in everything from the waves of the ocean to the current in a semiconductor is $1/f$ or flicker noise. It is not well understood, but is found experimentally to have an approximate $(1/f)^\alpha$ dependence. This noise component is unavoidable, and thus affects both the read noise and the system noise. Multiplexers designed with Metal Oxide Semiconductor Field Effect Transistors (MOSFETs) are usually dominated by $1/f$ noise in the low frequency range. Typically, the $1/f$ noise in MOSFETS is orders of magnitude larger than that in Junction Field Effect Transistors (JFETs), strongly suggesting that $1/f$ noise is a surface rather than bulk effect.⁴⁷ It has been postulated, but not confirmed, that $1/f$ noise may result from many superimposed traps or defects of varying capture times and magnitudes which modulate the resistance of a current carrying semiconductor.⁴⁷ While many traps may lead to a $1/f$ spectrum, a single trap or defect leads to burst noise, which has been seen in the HAWAII-1RG and -2RG multiplexers.

2.2.6 Burst Noise

Burst noise is electrical noise that is characterized by rapid conductivity changes manifesting as voltage or current shifts in both the positive and negative directions. It has also been called discrete switching noise, popcorn noise and RTS/RTN (Random Telegraph Signal Noise) or telegraph noise. Various solid state devices, such as p - n junction diodes and transistors, sometimes exhibit this noise component. The conductivity in a device with burst noise varies with respect to time like a step waveform and can be observed by monitoring the current or voltage of the device. In most cases, there are two levels between which the conductivity switches at random times. Less frequently, more complicated waveforms are observed, indicating three or more levels.

Burst noise was originally observed by Pay⁴⁸ in the signal waveform of germanium point contact diodes. Since that time, it has been reported for resistors, p - n junction diodes of various materials in both forward and reverse bias, tunnel diodes, and transistors. While all authors reporting burst noise have attributed it to crystal defects (such

as traps or dislocations) located adjacent to the current carrying region,⁴⁸⁻⁵⁴ the specific defect responsible varies for each theory and each device. Various proposed burst noise mechanisms are line dislocations,⁵¹ G-R recombination centers controlling a region of high conductivity such as a metallic precipitate,⁴⁸ microplasmas associated with dislocations for highly reverse-biased p - n junctions,⁵⁰ or extensive surface defects. In each of the forward-biased cases, the generation or recombination of a charge carrier in a *single* defect or trap either modifies the conductivity of a constrained current channel or reduces the energy barrier between two regions, enabling carriers to tunnel through the barrier more readily. Both of these lead to significant changes in conductivity as a result of a *single* trapped or released charge.

Because of its low-frequency and single event trigger nature, burst noise is usually seen in devices with small dimensions operated at low mean currents. Although larger devices may also exhibit burst noise, it will be much more difficult to detect because of increased Johnson noise and superposition of multiple burst noise mechanisms of varying magnitudes and characteristic transition times.⁴⁹ Many authors have reported observing burst noise in small dimension MOSFETs with gate widths on the order of $1\mu\text{m}$ or less.^{49, 52-56} In these reports, authors concentrate almost exclusively on two-level burst noise (sometimes referred to as a bistable waveform), indicating a single mechanism for the majority of devices exhibiting burst noise. We have narrowed the origin of burst noise observed in the HAWAII-1RG hybridized detector arrays to the Unit Cell Source Follower MOSFET (UCSF FET), by effectively eliminating the detector diode from the circuit of interest (see Section 5.5).

By analyzing the effects of temperature T , source to drain current I_{sd} , and V_{reset} (V_{gate} in Figure 2.6) on the characteristics of burst noise, we can learn much about the crystal defects causing burst noise in the HAWAII-1RG multiplexer. Here we present relations derived by Kandiah⁴⁹ et al. (1989) and Simoen⁵⁶ et al. (1992) for the characteristic transition time and amplitude of burst noise respectively.

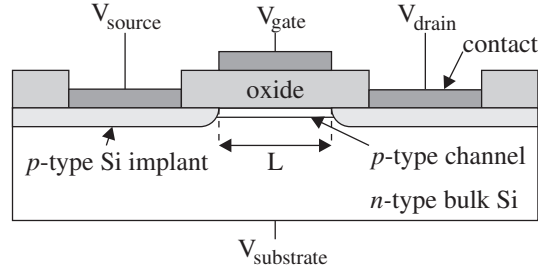


Figure 2.6. Schematic diagram of a MOSFET.

Characteristic Transition Time of Burst Noise

Concentrating on MOSFETs, there are three regions in which traps may reside adjacent to the current carrying channel. The first is in the insulator layer (some form of silicon oxide, possibly SiO_2) between the channel and the gate contact, the second is at the interface between the oxide and the channel and the third is in the bulk silicon on the opposite side of the channel than the oxide. These regions can be seen in the diagram in Figure 2.6. The probability that traps exist in the oxide near the channel surface is much greater than on the bulk side because the crystal is continuous from the channel to the bulk region and there is no change in structure. However, crystal dislocations present near the bulk side of the channel may contribute to the observed burst noise. Here, we will consider oxide and bulk silicon traps within a few Debye screening lengths of the channel or at the interface.

For oxide traps accessible to charge carriers in the adjacent channel by tunneling, Kandiah et al. present an equation for the characteristic time for tunneling of an electron or hole *into* the trap given by

$$t_c = \frac{\exp(2Ky_t)}{4n_a v_{th} c_a}, \quad (2.35)$$

where y_t is the distance from the trap to the silicon-oxide interface and v_{th} is the thermal velocity. The capture cross section is c_a , given by⁵⁵

$$c_a = c_{ao} \exp\left(\frac{-(E_t)}{kT}\right), \quad (2.36)$$

where c_{ao} is the capture cross section high temperature limit, E_t is the energy level of the trap with respect to the conduction or valence band respectively. The concentration

of electrons or holes in the vicinity of the trap respectively is n_a and

$$K = \frac{(2mE_o)^{1/2}}{\hbar}, \quad (2.37)$$

where m is the effective mass of the charge carrier, and E_o is the height of the oxide potential barrier with respect to the conduction or valence band respectively. Interface traps obey the same relationship with $y_t = y_o$, where

$$y_o = \frac{\ln(4)}{2K}, \quad (2.38)$$

such that the characteristic tunneling time becomes the characteristic capture time given by

$$t_{co} = \frac{1}{n_a v_{th} c_a}. \quad (2.39)$$

Interface traps are then defined as those traps between $y_t = 0$ and $y_t = y_o$. For consistency, the tunneling of an electron or hole *out of* the trap will be considered only by the tunneling of the opposite charge carrier *into* the trap, since they result in the same charge state.¹ We apply this same relation to bulk silicon traps where y_t represents the distance from the trap to the bulk side of the channel and E_o is replaced by E_{Si} , the energy barrier between the channel and the bulk silicon.

The temperature controls characteristic transition time through the dependence of the capture cross section in Equation 2.36.² Increasing the temperature increases the capture cross section. This in turn decreases the time the MOSFET remains in either charge state of the trap. The rate at which electron capture time decreases with increasing temperature is different than hole capture time.⁵⁵ Because the rates are different, a change in temperature also causes a change in the relative characteristic transition time of the two levels and may change the dominant level. Increasing the temperature also can enable new higher energy traps, thus adding a new level. The effect of temperature

¹In many situations, either emission or capture dominates except in regions where free carrier densities can be drastically changed by a small change in device parameters. We assume a simple model with capture dominance here.

²Although the thermal velocity is also temperature dependent, replacing n_a with Equation 2.39 solved for n_a , the v_{th} cancels.

on characteristic transition time has been confirmed by many authors^{49, 55, 56} and seems likely to be the case with our data (see Section 5.5.3) although data at more closely spaced temperatures and with better temporal resolution would clinch the argument.

The source to drain current (I_{sd}) controls the concentration of charge carriers, n_a , through the relationship

$$I_{sd} = qn_aWLv_{th}, \quad (2.40)$$

where W and L are the width and the length of the gate respectively. For our situation of a p -type channel and strong inversion operation, holes are the dominant charge carriers flowing through the channel. Therefore, we expect that an increase in I_{sd} current will increase n_a for holes in the p -type channel and the time it takes to capture a hole will decrease. However, increasing I_{sd} will decrease n_a for electrons and the capture time for an electron will increase. Therefore, we expect that an increase in I_{sd} will cause the time the charge state of the MOSFET stays positive and negative to increase and decrease respectively. For the HAWAII-1RG mux, the positive and negative charge state of the trap correspond to the higher and lower voltage output state respectively, since I_{sd} is held constant by a controllable current source. Therefore, an increase in I_{sd} would cause the upper level to be more frequently populated, which we confirm (see Section 5.5.4). The converse is also true.

The voltage applied to the gate of the MOSFET (V_{reset} in Figure 3.7) also has an effect upon burst noise characteristic transition time. As V_{reset} is increased, the channel size decreases and thus resistance in the channel increases. Since the MOSFETs in the unit cell of the HAWAII-1RG multiplexer are being used as source followers, they operate with an external current source. The current from this current source decreases by $0.2\mu\text{A}$ over the entire operable range. This corresponds to $0.05\mu\text{A}$ less current flowing from source to drain through a single source follower unit cell FET operated at $V_{reset} = 1.4\text{V}$ than one operated at $V_{reset} = 0\text{V}$. Therefore, some pixels will show a slight dependence of characteristic transition time on gate voltage as a result of this change in current.

The dependence of characteristic transition time on gate voltage depends upon the location of the trap(s). A trap located in the oxide layer may be affected by the small

change in current discussed above. A trap located on the bulk side of the channel may be affected altogether differently. Taking a closer look at the channel in the MOSFET of Figure 2.6 in Figure 2.7, it can be seen that a trap located on the channel-bulk interface at a gate voltage of $V_{reset} = 0\text{V}$ may be located some distance y_t outside the channel at $V_{reset} = 1.4\text{V}$. This would cause the value for y_t to increase and the characteristic transition time to change accordingly.

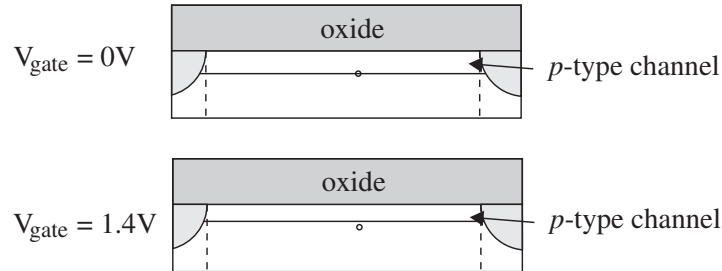


Figure 2.7. Close up of channel and its dependence on gate voltage ($V_{reset} = V_{gate}$).

The widely varying characteristic transition times observed in pixels with burst noise at a given temperature, I_{sd} and V_{reset} indicates a parameter which controls the characteristic transition time that is specific to each trap. This parameter is the product Ky_t . For the same energy, increasing the distance to the trap from the channel boundary increases the characteristic transition time exponentially. Since the transition time is based upon the tunneling probability of a charge carrier from the channel to the trap, this is to be expected. Increasing the barrier height by increasing K will also have the same effect. Therefore, there is likely a wide range of K and/or y_t controlling the wide variety of timings observed at a given temperature and I_{sd} .

Amplitude of Burst Noise

The amplitude of burst noise is also dependent upon I_{sd} current, component temperature, and gate voltage. Amplitude of burst noise in MOSFETs is often characterized by the relative amplitude, given by the change in channel resistance (ΔR) divided by the “reference” resistance (R), where the influence of the trap on the conductivity of

the channel is negligible. For our observations, this corresponds to a change in input referred signal output voltage (ΔV) divided by the voltage upon which this fluctuation occurs (V_s), namely the voltage on the source of the source follower unit cell FET. For a small voltage shift due to an interface trap (between the silicon and the oxide), this is approximately equal to⁵⁶

$$\frac{\Delta R}{R} = \frac{\Delta V}{V_s} \approx \frac{L_t^2}{WL} \frac{\Delta\sigma}{\sigma}, \quad (2.41)$$

where L_t^2 is the area over which a trap affects the charge carriers in the channel, and σ is the conductivity of the channel. The maximum expected transition amplitude corresponds to a completely blocked channel, where $\Delta\sigma/\sigma = 1$. We attempt to understand the temperature dependence of the observed maximum amplitude transition by employing a simple model discussed by Simoen⁵⁶ et al. (1992).

The trapping center may affect the channel conductivity in two ways which we consider here. When a charge carrier is trapped it may become a Coulombic scattering center, causing a decrease in the mobility and hence conductivity in the silicon channel. A simple estimate for the expected trapping length associated with such a center is given by⁵⁶

$$L_{ts} = \frac{2q^2}{4\pi\epsilon_s\epsilon_o kT}, \quad (2.42)$$

where ϵ_s is the relative permittivity of silicon.

The trapping center may also affect the local surface potential over a few Debye screening lengths L_{tp} , where an approximation for a two-dimensional electron gas gives⁵⁶

$$L_{tp} = \sqrt{2} \frac{\epsilon_s \epsilon_o kT L W}{qQ}, \quad (2.43)$$

where Q is the total charge in the channel (assumed distributed along the gate surface).

The actual behavior of the trapping center is some combination of the two, where the smallest of the two lengths dominate. Therefore, an approximation to the effective trapping length is given by⁵⁶

$$L_t = \frac{1}{\frac{1}{L_{ts}} + \frac{1}{L_{tp}}}. \quad (2.44)$$

Substituting for L_t in Equation 2.41 and setting $\Delta\sigma/\sigma = 1$, we arrive at an approximation for the relative amplitude of the maximum transition.

In practice, the observed magnitude of $\Delta V_{max}/V_s$ can be greater than the predicted value as has been noted by other authors, e.g. Simoen⁵⁶ et al. report factors of 10 to 100. There are many possibilities that would lead to a difference between the observed and theoretical values. The ability of the trap to affect the conductivity of the channel depends upon the type of trap (attractive, repulsive, or neutral) and its location.⁵⁵ The relative positioning of the trap between the source and the drain of the MOSFET may affect the amplitude,^{49, 55} since the channel depth and hence density of charge carriers may not be the same along the entire channel. In addition, there is a possibility that two or more correlated traps act together, causing a greater amplitude than expected by a single charge carrier transition. The properties of such a trap are consistent with deep level silicon defects.⁵⁵

Traps that do not completely block the channel will have a relative amplitude somewhat less than the maximum amplitude. An example of such a trap is a trap located some distance into the oxide or into the bulk silicon adjacent to the channel.⁴⁹ Also, a trap located on the perimeter of the channel is not likely to completely block the channel and will have an effectively lower L_t because fewer carriers will pass by the trap,⁵⁵ thereby lowering the amplitude $\Delta V/V_s$.

The component temperature affects the amplitude of the burst noise transitions. Since $L_{tp} \propto T$ and $L_{ts} \propto 1/T$, the magnitude of L_t will first increase with increasing temperature while L_{tp} dominates. As temperature continues to increase, L_{ts} will begin to dominate and the magnitude of L_t will decrease. The dominant mechanism, scattering or local potential modification, for the largest magnitude transitions at a given temperature will be indicated by the shape of the curve $\Delta V_{max}/V_s$ vs. T . The results of such an analysis are discussed in Section 5.5.

Source to drain current also affects the amplitude. The magnitude of Q in Equation 2.43 is controlled by the current. It is given by

$$Q = \frac{I_{sd}}{v_{th}} L. \quad (2.45)$$

Increasing the current increases the total charge between the source and the drain, thereby lowering the magnitude of L_{tp} . This may lower L_{tp} into a region where it dominates, thus causing a reduction in the amplitude. If L_{ts} remains sufficiently smaller than L_{tp} over the range of currents applied, no change in amplitude would be observed.

Altering the voltage applied to the gate of the MOSFET, V_{reset} , can also affect the amplitude. If the trap is located in the bulk silicon adjacent or into the channel, an increase in V_{reset} may decrease the channel depth such that the trap is no longer located within or adjacent to the channel (see Figure 2.7). This would cause a reduction in the amplitude of the observed burst noise, since the farther the trap is away from the channel boundary, the more the trap is screened by the material in-between. Other traps located in the oxide or at the channel-oxide interface would not change position with respect to the channel boundary as a function of gate voltage. The amplitude of these traps would not depend upon gate voltage.

The comparison of the observed burst noise characteristics to the presented theory will provide information about individually analyzed traps. Specifically, it will indicate the location of the traps (bulk silicon or oxide) and the behavior of the traps. This information may reveal the processing step in manufacturing that is causing burst noise to be introduced into the device. As for MOSFETs, there are two process-related aspects in manufacturing that lead to a device with burst noise, namely size of the MOSFET,^{49,52-56} and accessible traps. The biggest concern for devices that utilize MOSFETs exhibiting burst noise is amplitude, which is largely controlled by MOSFET dimensions (see Equation 2.41). Other factors, such as the effectiveness of the trap and number of traps, also influence the amplitude. With a large enough amplitude, burst noise may cause the signal to noise ratio to become too small for low background, small signal astronomy. It is therefore important that the amplitude of burst noise is reduced in future manufacturing efforts. In order to do so, it is necessary to understand the origins of the burst noise. Defects that act as trapping sites may be responsible for the groups of traps that some pixels display. Isolated traps may occur because of the introduction of unwanted impurities into a material. Since the majority of observed

burst noise characteristics indicate a single trapping mechanism (two level burst noise), it is likely that impurities are at the center of this problem. Therefore, in order to eliminate the effect of burst noise on low background astronomical detectors, impurities must be minimized and MOSFET size optimized for the measurement requirements.

Chapter 3

Test Setup and Preparation

3.1 Equipment and Control Electronics

We have a fully outfitted laboratory for measuring the characteristics of two-dimensional detector arrays. The equipment we have consists of a low background camera dewar, in which the array is housed during testing, and Motorola 56001 DSP-based array control electronics.

3.1.1 The Camera Dewar

The liquid helium dewar consists of a number of chambers housed in a high vacuum outer shell as illustrated in Figure 3.1. Attached to the outside of the innermost chamber is a molecular sieve package which keeps the moisture level very low inside the dewar, even when not at high vacuum, by absorbing water molecules. It also absorbs N_2 , O_2 , and CO_2 when it is at or below liquid Nitrogen temperature ($\sim 77K$). The innermost chamber consists of a liquid helium reservoir attached to a cylindrical aluminum radiation shield which provides a cooled controlled environment within which the detector array is mounted. Detector arrays bonded to leadless chip carriers, such as the hybridized NICMOS3 devices, are fastened into a leadless chip carrier socket on a fanout board which is custom designed for each array and includes protection for the gates of the multiplexer (mux) as well as noise reductive RC filters. The gates are protected

by either 15V zener diodes or $1M\Omega$ resistors. The RC filters are on the noise sensitive lines including the Detector Substrate Voltage and the Reset Voltage (see Figure 1.8). Other devices, such as the hybridized HAWAII-1RG devices, have built-in electronic protection and a provided array-specific cable to connect to external array controller electronics. These devices are mounted on a plate made of a material which is chosen to match the coefficient of thermal expansion (CTE) of the HgCdTe. If a fanout board is used, then an array-specific scramble cable is created to connect the fanout board to the dewar wiring. Otherwise the array-specific cable provided with the device is used and a connector board is created to convert between the two wiring systems. This makes changing between multiplexers quite simple and changing detectors trivial, since the wiring inside the dewar is universal.

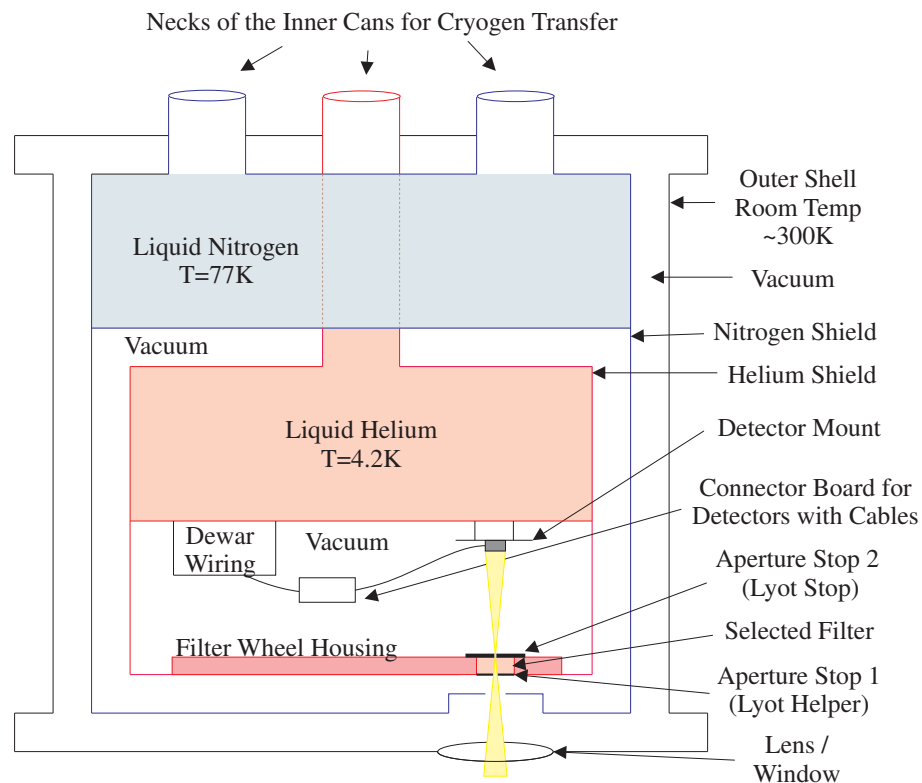


Figure 3.1. Not to scale representation of the camera dewar layout.

The fanout board or mounting plate (either of which, when attached to the detector

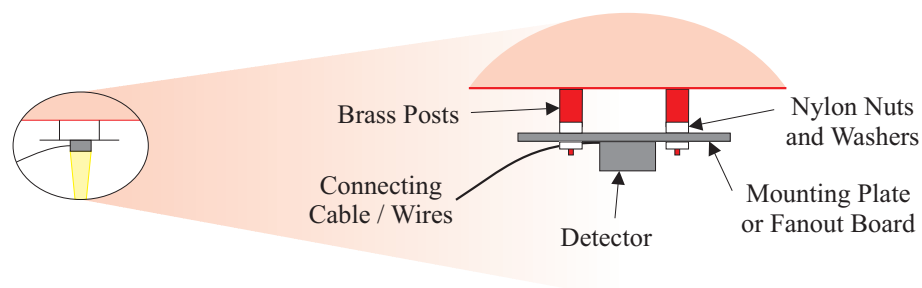


Figure 3.2. Exploded view of the detector mount shown in Figure 3.1 and replicated to the left of the figure.

array, will be referred to as the detector mount) is then attached to the surface of the liquid helium reservoir via brass posts and thermally insulating nylon washers so that we can attain temperatures much greater than 4K (see Figure 3.2). This design allows for some stability in temperature control.¹ In the absence of power to the device, the liquid helium reservoir would hold the detector mount at 4K. During operation, power dissipation of the device raises the thermal equilibrium of the detector mount to a somewhat higher temperature due to the balance between these two thermal sources. However, this is often a much lower focal plane temperature than desired for array operation. Thus, a resistor heater and temperature sensing diode are mounted on the fanout board or mounting plate, and allow us to control the temperature of the device with good stability. The prime temperature range for this control is between 5K and 40K without significant loss of helium. The dewar can also be easily operated at 77K by using liquid nitrogen instead of liquid helium (with fresh desiccant required each cool-down).

Attached opposite the detector array, sealing the bottom side of the liquid helium shield, is the filter wheel. A hole in the bottom side of the filter wheel housing acts as an aperture stop which helps to define the illuminating beam and is known locally as a “Lyot helper.” Employed in this wheel are many commonly used astronomical infrared filters (such as K and L’ band filters at $2.2\mu\text{m}$ and $3.8\mu\text{m}$ respectively) in addition to

¹These arrays are not to be cooled/heated any faster than 1.0K/min and the nylon washers assure this condition.

two long wavelength circular variable filters that combined cover the wavelength region from $4.5\mu\text{m}$ to $14\mu\text{m}$. This wheel is housed in a blackened aluminum enclosure and is held at the temperature which is achieved by the balance between the cooling provided by the liquid helium reservoir and the absorbed radiation emitted by the warmer outer chambers. On the inner side of the filter wheel housing is the changeable Lyot stop which is the final aperture stop for photon flux control.

The liquid nitrogen shield is the middle chamber and consists of a liquid nitrogen reservoir situated on the top of the liquid helium reservoir with an attached aluminum cylinder which surrounds the liquid helium shield. This shield extends the lifetime of the liquid helium in its reservoir by blocking the radiation from the room temperature aluminum outermost housing. It has an aperture in the line of sight between the detector and the BaF_2 window in the outer shell so that the detector can be illuminated by sources external to the dewar (but for typical operation does not define the solid angle viewable by the detector).

The external casing is at room temperature and is designed to block external radiation. Each inner chamber and the super insulation surrounding it allows the dewar to be very light-tight. Measurements have been made showing $< 0.01e^-/s$ light leak with $9.3\mu\text{m}$ cutoff detectors using the cold dark slide filter wheel position, where the array is blocked by a blackened surface on the liquid helium cooled filter wheel. In addition, the outer aluminum shell is designed for high vacuum. This prevents convection from being the dominant source of heat transfer, and protects the detector array from condensation when operating at low temperatures. The dewar wiring which originates within the liquid helium shield emerges via hermetically sealed circular connectors on the top side of the dewar, near the emergence of the necks of the cryogen reservoirs.

3.1.2 Array Controller Electronics

The Digital Signal Processor (DSP) array controller electronics, made up of three different DSP boards, generate clock waveforms and acquire data. One board generates the clocks and the signals to synchronize with the two signal processing DSP boards. The

signal processing boards handle the data from four array outputs (amplified, bandwidth filtered, and converted from analog to digital) at a maximum speed of $2\mu\text{sec}$ per pixel (the minimum time for the A/D converter to convert a signal from analog to digital). The data is recorded in analog to digital units (ADU), which can be converted to mV with the voltage range of the A/D converter divided by 2^{15} ADU. The ADU can also be converted to electrons with a capacitance measurement (see Sections 4.2 and 5.1.1).

Due to limitations during the course of testing, specifically between the NICMOS3 deliveries (phase I of testing) and the HAWAII-1RG deliveries (phase II), the array controller electronics went through a system modification which will be discussed in the description of the ‘black box’ system below. The earlier system, which was used to test the NICMOS3 deliveries is referred to as the “silver box” and our current system, which was used to test the HAWAII-1RG deliveries, the “black box.”

In the silver box, biases, with the exception of the specially filtered applied biases ($V_{detbias}$ and V_{detsub} , see Figure 3.6), and clock on and off levels are adjusted by potentiometers (pots) on bias cards. $V_{detbias}$ and V_{detsub} are set by computer control and are filtered to ensure very low noise on these biases. The silver box is external to the camera dewar and also contains the gain stages for the preamp signal.

The black box, which is the current system and also external to the camera dewar, is an all-inclusive controller. It was developed by A. Moore for the Near Infrared Astronomy Lab at the University of Rochester,⁵⁷ and a complete description can be found in Moore et al. (2003). In the black box system, all of the biases and clock rails are set by computer control and generated within the black box, utilizing an external power supply. The black box also monitors the temperature diode voltage. It allows manual readout of the bias and clock voltages in addition to the currents on each line. Furthermore, it controls the filter wheel motion, set by computer control. It is capable of reading up to four outputs (of which only two are currently enabled) for any array format or size. All of the necessary information is then relayed back in the signal line to the computer for analysis. Together with other improvements, such as the offset being applied before amplifier gain of the signal, the black box is much more versatile than

the silver box.

After the signal is received, the boards accept the data, perform preliminary signal processing determined by the sampling method, and store the resulting image data which is then passed onto the host computer in Flexible Image Transport System (FITS) format for more permanent storage. The data may then be viewed and further analyzed using a FITS image viewing program for astronomy entitled DV² or an image data reduction program, e.g. Interactive Data Language (IDL).

3.2 Multiplexers: Operation and Calibration

3.2.1 Clocking and Sampling

Reading and resetting the device are two necessary operations for using detector arrays. Resetting the device is the process by which the bias across the entire array is re-established. This can be carried out in multiple ways which are referred to as reset modes. During reset in every reset mode, each pixel on the array is connected to the same Reset Voltage (see Figure 1.8). The different reset modes determine the timing in which each pixel is connected.

Three common reset modes are global reset, row by row reset, and pixel by pixel reset. In global reset, each pixel in the array is reset to the Reset Voltage at the exact same time. The second reset mode is row by row reset. In this mode, the array is reset one row at a time where all columns in the row are reset simultaneously. This can be carried out fast or slow. In a fast row by row reset, each row is reset for the minimum amount of time necessary to ensure a full reset before the subsequent row is reset. By this method, reading a row will take longer than resetting it. By contrast, a slow row by row reset resets each row for the same amount of time it would take to read out that row. Therefore, if it would take 4ms to read out a given row, resetting the row would also take 4ms. Finally, the last reset mode is pixel by pixel reset. In this mode, each pixel is reset individually. The timing between the resetting and reading of the device

²DV is a FITS Data Viewer developed by the NASA Infrared Telescope Facility

is determined by the sampling mode by which the device is read.

There are multiple sampling modes in which data were taken, Signal-Reset-Pedestal (SRP) mode, Fowler sampling mode, Sample-Up-The-Ramp (SUTR) mode and Reset On mode. The various sampling modes will be discussed in the subsections below. The reset is measured while the pixel is being reset and the first sample after the reset has been released is known as the pedestal. The signal is obtained after the detector has integrated (collected charge) for the set amount of time (integration time). The difference between the signal and pedestal levels is what is commonly referred to as the signal acquired (dark and photo charge combined) during the integration. The reset to pedestal difference yields the pedestal injection ('charge dump'), which is due to charge redistribution in the reset line when the reset switch is turned off (see Section 3.2.4).

Signal-Reset-Pedestal (SRP) sampling mode

In SRP mode, the entire array is reset pixel by pixel. Then the first pixel is reset (sampled during reset, R1), sampled after the reset switch is turned off, P1, and sampled again at the end of the integration, S1, yielding the reset, pedestal and signal levels respectively as indicated in Figure 3.3.

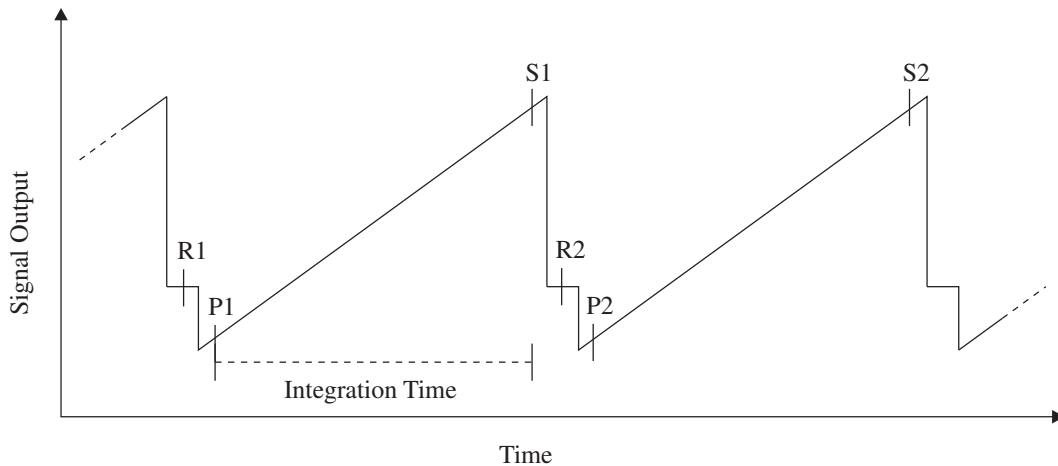


Figure 3.3. Signal output diagram for SRP sampling mode.

The remainder of array pixels are subsequently sampled in this same manner, yield-

ing a correlated triple sample of each pixel in the array. The signal then recorded in a FITS image is given for read n by $(S_n - R_{n+1}) - (P_n - R_n)$. The NICMOS3 data were taken in this sampling mode because it was sufficient for tests run on this device.

Fowler sampling mode

In Fowler sampling¹⁰ mode, multiply sampled images (multiple correlated frame reads) are obtained, which reduces the observed noise in a single image. This is done by resetting the array according to the chosen reset method, then sampling the array n times ($n = 4$ in Figure 3.4) The n samples of each pixel are averaged together, yielding a

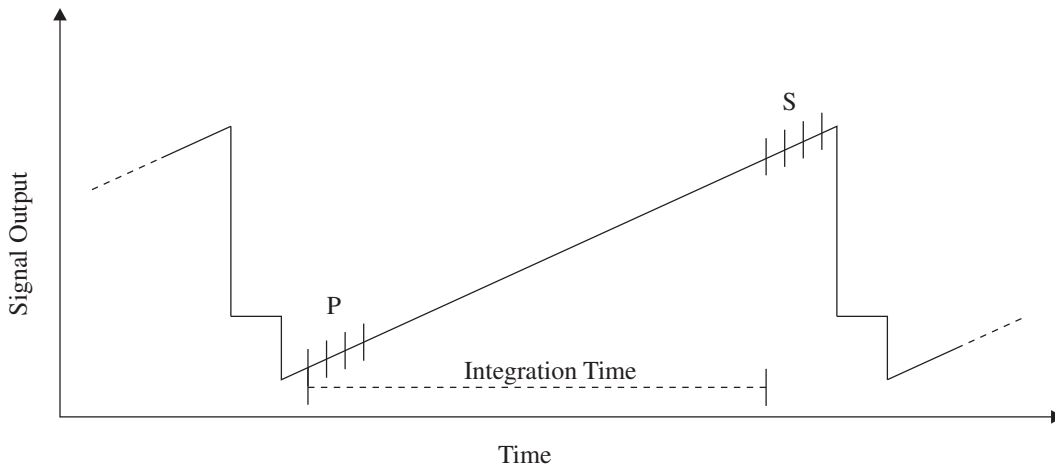


Figure 3.4. Signal output diagram for Fowler sampling mode.

single averaged value for that pixel, which is referred to as the pedestal (P in Figure 3.4). When the desired integration time has passed since the first sample, the next set of n samples begins. These n samples of each pixel are averaged together, yielding a single signal level for that pixel (S in Figure 3.4). The averaged pedestal level subtracted from the averaged signal level gives the signal acquired during integration. This method is known as Fowler- n sampling, where n is the number of sample pairs. Thus the Fowler sampling shown in Figure 3.4 is Fowler-4, and a single Fowler sample pair (Fowler-1) is equivalent to correlated double sampling (CDS).

Sample-Up-The-Ramp (SUTR) sampling mode

Much of the HAWAII-1RG data was taken in sample up the ramp (SUTR) mode in order to obtain many points on the integration ramp. This enabled easier cosmic ray correction in addition to noise characterization. In this mode, the device is reset according to the chosen reset method, which in this case was row by row. Then the first read of the device is recorded, and is referred to as the pedestal. Subsequently, many frames (single reads of the device) were recorded, yielding the signal level at various times during the integration. This is shown in Figure 3.5, where each sample is evenly spaced and the first sample of the array (S0) is also shown as (P), the pedestal. This sampling method yields

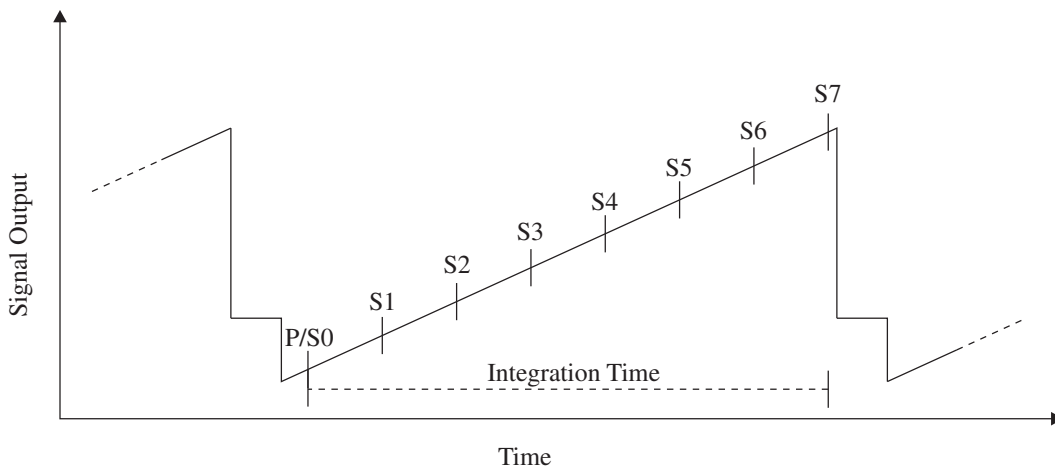


Figure 3.5. Signal output diagram for SUTR sampling mode.

much more information than the signal level minus the pedestal level alone because it can distinguish behavior of the pixel during integration. This is necessary for detection and compensation of burst noise. The signal acquired by a pixel over the integration time from the first to eighth sample of the device is given by the slope of a linear fit to the data of all eight samples multiplied by the integration time. A correlated double sample can be obtained by subtracting the signal of the first sample (the pedestal P/S0) from the eighth sample (S7).

The previous two sampling modes, namely Fowler sampling and sampling up the ramp both employ multiple sampling. For uncorrelated noise in each sample, the aver-

aging of multiple samples reduces the overall noise. For this reason, in read noise limited performance, sampling modes that utilize multiple samples are preferred. Between the two sample modes that employ multiple samples, line fitting to SUTR provides a larger signal to noise ratio by $\sim 6\%$ than optimized³ Fowler sampling.⁵⁸ In background limited performance for non-destructive device readouts, the noise of a subsequent sample is correlated to the noise in the previous sample because the noise of the previous sample is still on the integrating node. In this case, the lowest noise is obtained by a simple correlated double sample.⁵⁸ For data reduction in both limiting regimes, multiple sampling is preferred because the reduction in signal to noise on the background limited pixels is slight compared to the gain in signal to noise on the read noise limited pixels.⁵⁸ For a detailed discussion of the noise reduction capabilities of these sampling techniques, see Garnett and Forrest⁵⁸ (1993).

Reset On sampling mode

Reset On sampling mode can be used with any of the other sampling modes above. It is most often used with SUTR. In this case, the reset switch is always on. Therefore, every sample of the device is a sample of the reset voltage. This is useful when measuring DC Gain (as in Section 3.2.5) and whenever isolated measurement of the multiplexer is necessary (such as in burst noise detection, see Section 5.5).

3.2.2 NICMOS3 Multiplexer

The NICMOS3 multiplexer is a 256×256 pixel ROIC developed for Short Wave InfraRed (SWIR) HgCdTe for the Hubble Space Telescope. This multiplexer is divided into quadrants which share a common detector substrate voltage, V_{detsub} , which is labeled in Figure 3.6 as DETSUB, and ground, Gnd . The schematic of one of these quadrants

³Optimizing Fowler sampling is done by using the best duty cycle. In the read noise limited regime, the best duty cycle is $2/3$, where the pedestal and signal samples of the device occur for $1/3$ of the integration time each.⁵⁸ For a detailed discussion of optimization in any limiting regime, see see Garnett and Forrest⁵⁸ (1993).

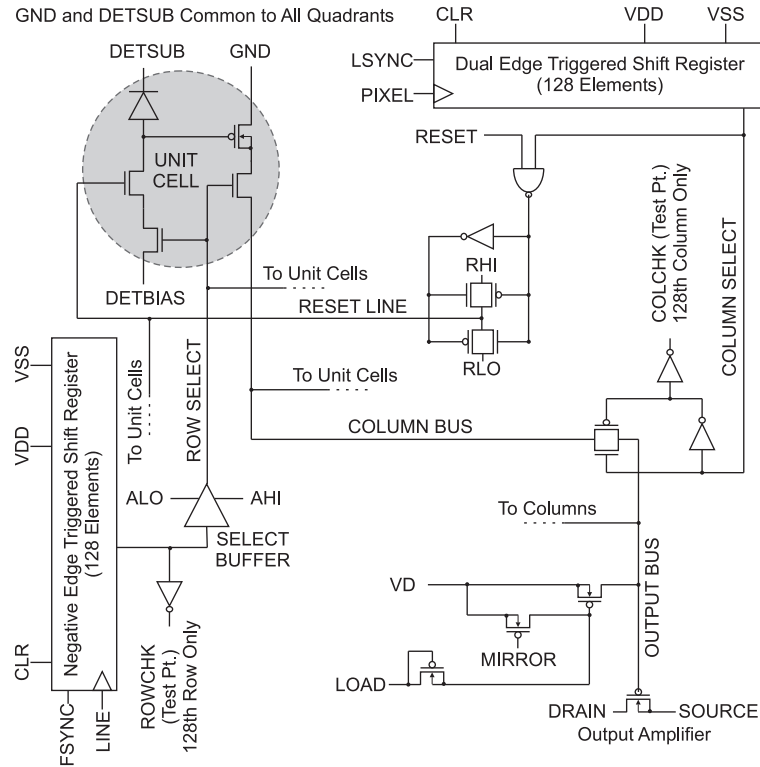


Figure 3.6. Schematic of one quadrant of NICMOS3.

is shown in Figure 3.6. The NICMOS3 was designed only for pixel by pixel reset, and therefore was operated with that reset mode.

3.2.3 HAWAII-1RG Multiplexer

The HAWAII-1RG multiplexer is a 1024×1024 pixel readout integrated circuit (ROIC), with four rows and columns of reference pixels around the perimeter. This leads to 1016×1016 active pixels. It has a selectable number of outputs, plus numerous other features. The HAWAII-1RG is identical in all features and functions to the HAWAII-2RG (see Loose et al. 2003)⁵⁹ except for the pixel format (1024×1024 vs. 2048×2048) and number of selectable outputs (1, 2, 16 vs. 1, 4, 32).

The HAWAII-1RG was operated in two-output “normal readout mode”⁴ with 100

⁴“Normal readout mode” is a method of reading out the device, which is detailed in the HAWAII-1RG User’s Manual. It involves resetting the entire device row by row, then reading the pedestal and

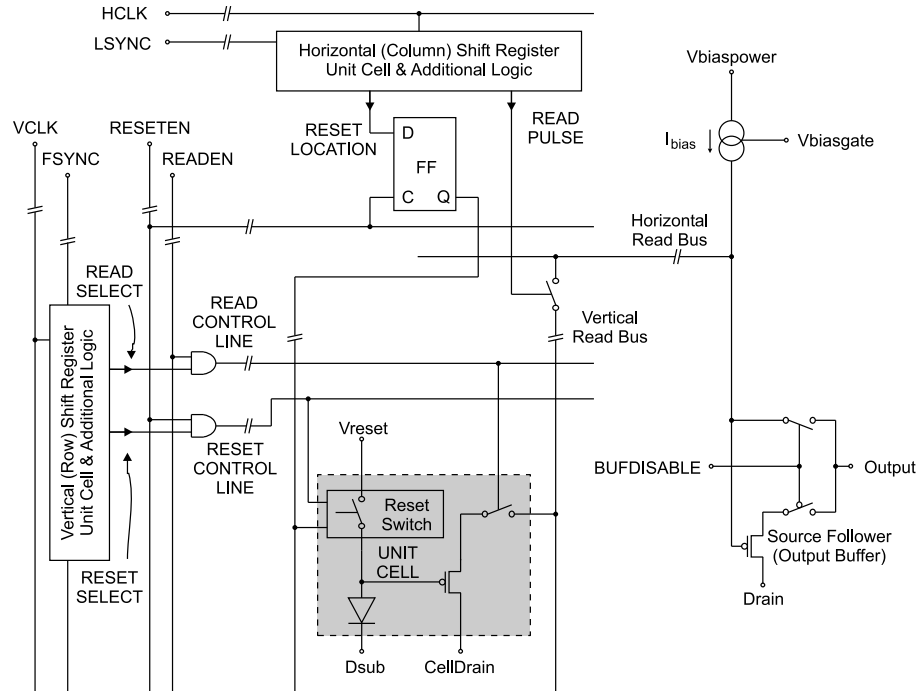


Figure 3.7. Read out operation schematic for the H1RG multiplexer.

kHz pixel read rate. We used a fast row by row reset followed by either partial or full array reads. Because we were concerned that this readout mode might lead to variable amounts of debias because the reset to pedestal delay increased from the first to the last pixel read (i.e. for a full frame read this corresponds to an increase in reset to pedestal delay time from 1.5ms to 1.57s), we were careful to employ experimental methods which took this concern into account. These methods will be described in Section 5.2. Pixel by pixel reset and the HAWAII-1RG enhanced clocking mode⁵ would have made dark current characterization at early integration times much easier, although we had not implemented that clocking scheme at the time the data were obtained.

While the HAWAII-1RG has an $18\mu\text{m}$ pixel pitch designed for SWIR and Mid-Wave InfraRed (MWIR) HgCdTe, we desire a $36\mu\text{m}$ pixel pitch for LWIR HgCdTe. Thus the LWIR HgCdTe detector array was bonded to every other pixel of the HAWAII-1RG, subsequent frames.

⁵This clocking mode enables integration times shorter than a frame time during a full frame read.

resulting in an effective array size of 512×512 (508×508 active) pixels.

3.2.4 Pedestal Injection and Zero Bias Point (ZBP)

The reset line is enabled for a given unit cell, shown by the grey circle and square in Figure 3.6 and 3.7 respectively, when the reset switch is closed to allow Reset Voltage connection (see Figure 1.8). In order for this to happen, the input voltage lines which control the reset switch must be high (3.3V and 0V are high and low respectively). These lines correspond to the reset line and row select in the NICMOS3 devices (see Figure 3.6) and the reset control line and output of the reset location flip flop circuit (toggle switch) shown by the rectangle with ‘FF’ in the center in Figure 3.7. When this occurs, the applied bias across the detector is re-established.

The Reset Voltage, $V_{detbias}$ or V_{reset} for the NICMOS3 or HAWAII-1RG multiplexer respectively, is the voltage applied to the front side of the detector during reset. The front side of the detector is the side to which the electronics are bonded. The other side is known as the back side of the detector. These detector arrays are back side illuminated, which means that the radiation does not pass through the electronics before entering the detector material. The transparent contact on the back side of the detector is held at the Detector Substrate Voltage (see Figure 1.8), V_{detsub} or V_{Dsub} for the NICMOS3 or HAWAII-1RG multiplexer respectively. This voltage is determined by the reset voltage plus the applied reverse bias across the detector, V_{bias} . (A convention note: For V_{bias} , a positive voltage corresponds to reverse bias and a negative voltage to forward bias.)

When the reset switch is turned off, charge redistribution in the reset line modifies the voltage on the integrating node(see Figure 1.6 in Section 1.3 and Figure 1.8 in Section 1.4). This results in an actual bias that differs from the applied bias, where the difference is the pedestal injection. In both the NICMOS3 devices and the HAWAII-1RG devices, this ‘charge dump’ adds to the well depth. On other devices, such as the Raytheon CRC-744 InSb arrays, the pedestal injection subtracts from the well depth, causing a zero applied bias to put the diode into forward bias. For example, most of the tests on detector UR008 were done at $V_{bias} = 0\text{mV}$. The well depth measurement,

however, showed an average actual reverse bias of 61mV at the beginning of the integration ramp ($V_{actual_bias} = -61\text{mV}$). The zero bias point (ZBP) is determined by the amount of applied bias that is needed to achieve an actual bias of 0mV, and is given by the negative of the pedestal injection. If 0mV applied bias gives 61mV actual reverse bias (a pedestal injection of 61mV), then 61mV applied forward bias would give 0mV actual bias. Therefore, on average for detector UR008 V_{ZBP} is -61mV. Thus, $V_{actual_bias} = V_{bias} + V_{ZBP}$ or $V_{actual_bias} = V_{bias} - V_{pedestal_injection}$. Note, however, that these voltages are averages. Due to differing capacitances, the resulting voltage on the integrating node is different for each pixel.

3.2.5 DC Gain Calibration

As mentioned in Section 1.4, the two source follower amplifiers preceding the output should have a gain close to unity. One of the first measurements made on a mux (whether it is hybridized or not) is that of the source follower gain. This is important to ensure the mux is working properly and to make sure the operating point is within the linear region giving the maximum well depth possible to the detector. This measurement is made by comparing the output signal (reset minus ground level) to the input reset voltage. The gain measurement for detector UR008 (a NICMOS3 device) is shown in Figure 3.8. A similar gain measurement would be seen for the other operational NICMOS3 multiplexers or the HAWAII-1RG devices.

The gain curve when taken to its extremes shows a lower limit and an upper limit on the range of the multiplexer output. The lower limit is reached when either amplifier enters saturation or is ‘railed.’ The upper limit is therefore reached when the voltage at the gate of either amplifier is below the amplifier’s threshold. For complete dynamic range, the initial level of the detector should be above the lower limit and the saturated level of the detector should be below the upper limit. For the detector UR008, the gain was measured to be 0.957 (averaged between four boxes, one per quadrant) over a range from -1V to 1V $V_{detbias}$, the applied reset voltage. The detector was subsequently operated at 0V $V_{detbias}$ and had an average actual well depth of 61mV (corresponding

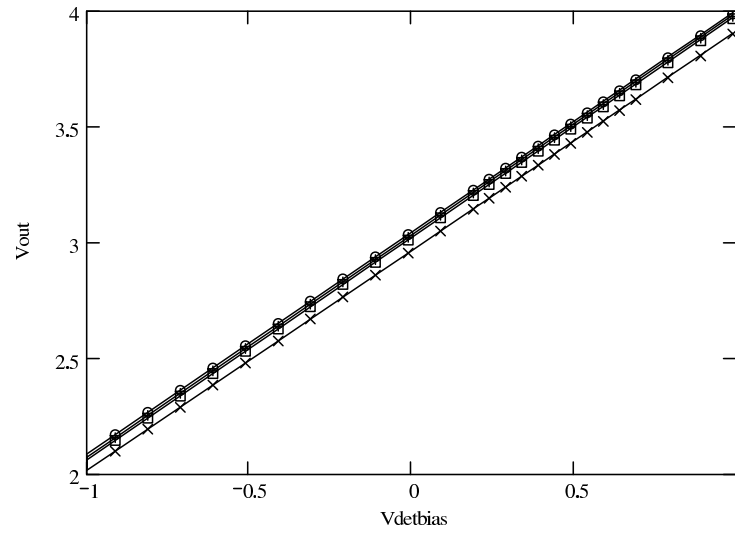


Figure 3.8. This is part of the linear portion of the DC Gain measurement for UR008. Both axes are in volts. All four quadrants are shown here and have an average slope (gain) of 0.957.

to 0mV applied bias), which was well within the range of the multiplexer. V_{reset} had a lower limit slightly below 0V in the HAWAII-1RG muxes, and they were subsequently operated at a reset voltage of 0V.

Chapter 4

Phase I: NICMOS3 Deliveries

In the first phase of LWIR array development, we received seven detector arrays from Rockwell Scientific (then known as Rockwell Science Center) which the University of Rochester had manufactured in a “banded” format. This format employed nine different sizes/geometries of diode implants arranged in rows, such that multiple diode structures could be investigated on one array. These diode types will be referred to as type A through I. The array is manufactured beginning with type A for four rows and then type B for four rows and so on until type I, after which the pattern starts over again with type A. This leads to 8192 pixels of type A and 7168 pixels of all subsequent types. The goal in testing these detector arrays was to ascertain which diode type had the lowest average dark current and the largest percentage of pixels meeting our dark current goal, which for this phase was less than $100e^-/s$.

These detectors were bonded to engineering grade NICMOS3 multiplexers in a 256×256 format. Phase one concentrated on one of those arrays, UR008,¹ a $9.3\mu\text{m}$ wavelength cut-off device (at 30K), with relatively high doping ($1.6 \times 10^{15}\text{cm}^{-3}$) and hence lower G-R current (see Equation 2.16), all other parameters remaining the same. The testing of this device enabled us to ascertain the optimal diode choice for future array development.

¹Tests concentrated on this array because many of the others had defects, extremely low well depth, were non-responsive to illumination or were non-operational. The array UR008 was the best performing array of the lot and had the most operational pixels for analysis.

Results for this array were reported at the SPIE conference for Astronomical Telescopes and Instrumentation in 2002.²⁴

4.1 Pixel Operability Constraints

Because pixel properties, such as dark current and well depth, varied greatly from pixel to pixel in detector array UR008, it became necessary to select a group of pixels with similar properties to concentrate on for characterization. Thus, we developed criteria which would ensure that the results would be appropriate for all of the selected pixels. The first of these criteria that the pixel must meet is our low dark current goal of $< 100e^-/s$ in a bias frame subtracted 100 second integration frame. Inclusion of high dark current pixels would make the signal with respect to time non-linear, even at low integration times. This would make capacitance measurements (see Section 4.2), which require low photon flux and short integration times, difficult to properly obtain.

In order to distinguish between the well depth of a single pixel and that which is an average of the whole array, three terms for well depth are defined. First, the *actual well depth* for a given pixel is determined by the signal the pixel reaches in a saturation image. The *useful well depth* for a that same pixel is given by the subtraction of a one second dark from the *actual well depth*. Third, the average of all useful well depths (see Section 4.3) is the *target well depth* (TWD). From this, the second criterion is that the pixel must show a *useful well depth* of at least 0.75 times the *target well depth*. This ensures that the low dark current pixels selected by the first criterion have adequate well depth and are at approximately the same actual reverse bias at low integration times. Third, the pixel must have filled less than half its useful well depth at 300s integration time (itime) with no illumination. This prevents pixels with signals in the regime where the diode capacitance has significantly changed from the capacitance at full well depth (see Section 5.1.2) from being included in the dark current measurement. Those pixels meeting the low dark current goal for 60mV target well depth and satisfying the above constraints are white in the pixel mask shown in Figure 4.1,² and the corresponding

²Artifacts of the engineering muxes are also apparent: e.g. see the vertical black bar.

percentages are given in Table 4.1.

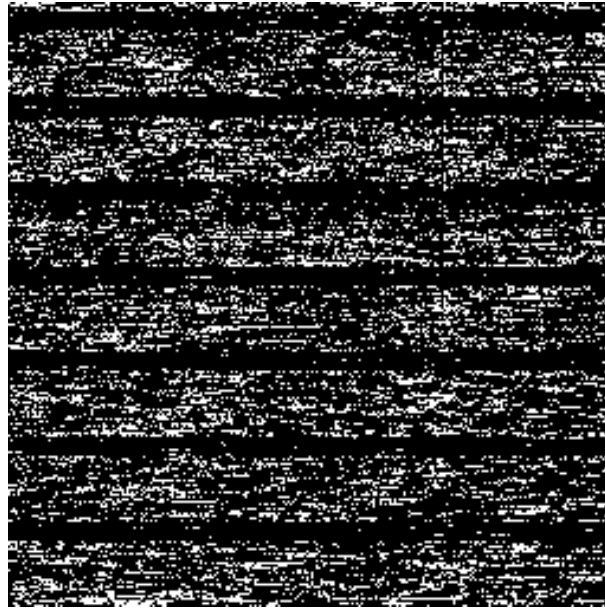


Figure 4.1. Image of detector array UR008 with pixels in white that met the constraints for 60mV target well depth (TWD).

Table 4.1. Percentage of Pixels Meeting Constraints vs. Diode Type

Type	Number of Pixels	Total Available	Percentage
A	2309	8192	28
B	1569	7168	22
C	1749	7168	24
D	1672	7168	23
E	1560	7168	22
F	1407	7168	20
G	1430	7168	20
H	126	7168	1.8
I	116	7168	1.6

The only pixels included in characterization and used in the following graphs, tables and figures, are the pixels that are shown in white on Figure 4.1. As indicated by Table 4.1, types H and I have less than 2% of available pixels that met these constraints and correspond to the black horizontal bands in Figure 4.1 . Because of their extremely

poor performance, they will not be examined further. From the percentages shown in Table 4.1, it is clear that array non-uniformity is an issue to be tackled in future development.

4.2 Diode Calibration: Capacitance

The first step to determining the capacitance is by the noise squared vs. signal method.⁶⁰ This method determines capacitance through a measurement of the input referred signal and shot noise, assuming Poisson statistics. For the NICMOS3 deliveries, the input referred signal voltage at the junction (V_S) was related to the measured signal in ADU (S_{ADU}) by

$$V_S = S_{ADU} \times \frac{10V}{2^{15}ADU}. \quad (4.1)$$

The signal voltage at the junction, V_S , is also equal to the total signal collected (charge) divided by the capacitance (C),

$$V_S = \frac{\bar{n}q}{C}. \quad (4.2)$$

The total charge is given by the average number of electrons, \bar{n} , times the electron charge, q . The measured signal voltage output, V_{S_out} , is related to the voltage at the junction by

$$V_{S_out} = V_S \times G_{mux} \times G_{external}, \quad (4.3)$$

where G_{mux} is the gain of the multiplexer (0.957), and $G_{external}$ is the gain stage of the external array controller electronics (see Section 3.2.5 and Section 3.1 respectively).

The noise voltage at the junction, V_N , is proportional to the rms of the fluctuation in the number of generated electrons (Δn),

$$V_N = \frac{\sqrt{\Delta n^2}q}{C}. \quad (4.4)$$

Likewise, the measured noise voltage is given by

$$V_{N_out} = V_N \times G_{mux} \times G_{external}, \quad (4.5)$$

Squaring Equation 4.5, dividing by Equation 4.3, rearranging and using the Poisson relation $\overline{\Delta n^2} = \bar{n}$, we obtain the equation that relates the measured quantities of signal and noise voltage to capacitance,

$$C = \frac{qV_{S_out}G_{mux}G_{external}}{V_{N_out}^2}. \quad (4.6)$$

Using this form of the capacitance, data were taken and a value was found for each pixel.³ Since there was a spread in measured capacitances for each pixel diode configuration, a histogram of measured capacitances was created for each type. The histogram for pixels of type A is shown in Figure 4.2.⁴

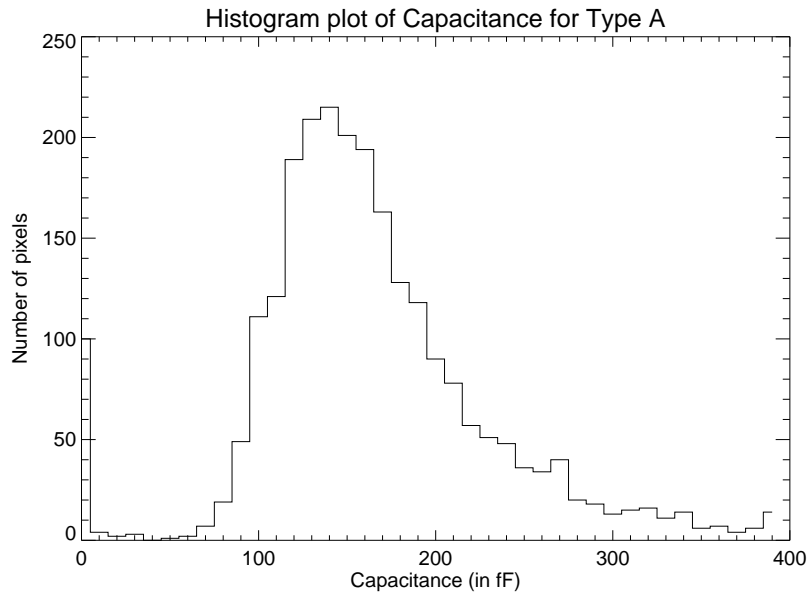


Figure 4.2. Histogram of capacitance for pixels of type A configuration.

For each subsequent type, the width of the peak increased, and the number of pixels capable of giving a good capacitance measurement decreased. Thus, the uncertainties

³The values reported here are only appropriate if there is no interpixel capacitance. Since interpixel capacitance has been encountered on the HAWAII-1RG multiplexers,⁶¹ these values are overestimates of the true capacitance.

⁴Not all pixels of each type were plotted and used in these histograms. Only the pixels that were capable of giving a good capacitance measurement were included. For more information on those pixels, see Section 4.1.

in the mean capacitance for the latter types are even greater than that for type A. The following model of known capacitative components given by Rockwell Scientific was fit to the midpoints of the full width at half max of each histogram:

$$C = A_0(A_{pad} - A_{jcn}) + 0.317A_{jcn} + C_{source_follower}, \quad (4.7)$$

where the three terms are that of the pad capacitance,⁵ the junction capacitance, and the source follower capacitance respectively, all in units of fF, A_{jcn} is the junction area in square microns, and A_0 is the fitting parameter. The junction capacitance was determined theoretically by

$$C = \frac{\epsilon\epsilon_0}{W}A_{jcn}, \quad (4.8)$$

where W is the depletion region width, given by Equation 2.3. The variable parameters were fixed by the fit, and the capacitances, as determined by this equation, as well as the e^-/ADU for our system are given in Table 4.2.⁶

Table 4.2. Capacitances of the various types followed by the number of electrons per ADU (Analog to Digital Unit) for these devices in our system.

Type	Capacitance (fF)	e^-/ADU
A	140	27.7
B	144	28.6
C	150	29.7
D	160	31.8
E	173	34.3
F	194	38.4
G	225	44.7

⁵Because the junction is small, the metal pad that the indium bump sits on overlaps the n -type bulk of the detector. They are separated by the passivation layer. Because the n -type bulk is conductive, a capacitance exists between the metal pad and the overlap with the n -type bulk. This is not negligible here because the p -type junction is not a large fraction of the pad area.

⁶In the earlier presentation of these results in SPIE Proceedings Vol. 4850,²⁴ the capacitances were estimated based upon assumptions and not measured.

4.3 Well Depth

The mean well depth in electrons for each diode type was determined based upon the capacitance (see Table 4.2) of the particular geometric configuration of the diode. In order to minimize the degree of forward bias at saturation, a small photo-signal was used to integrate to saturation (see Section 5.2.3). Assuming the open circuit voltage $V_{oc} = 0$ (see Figure 1.5 and Section 1.3, no forward bias on the detector diodes at saturation), the actual well depth or saturation level corresponds to the actual reverse bias across the diode at the beginning of the integration ramp.

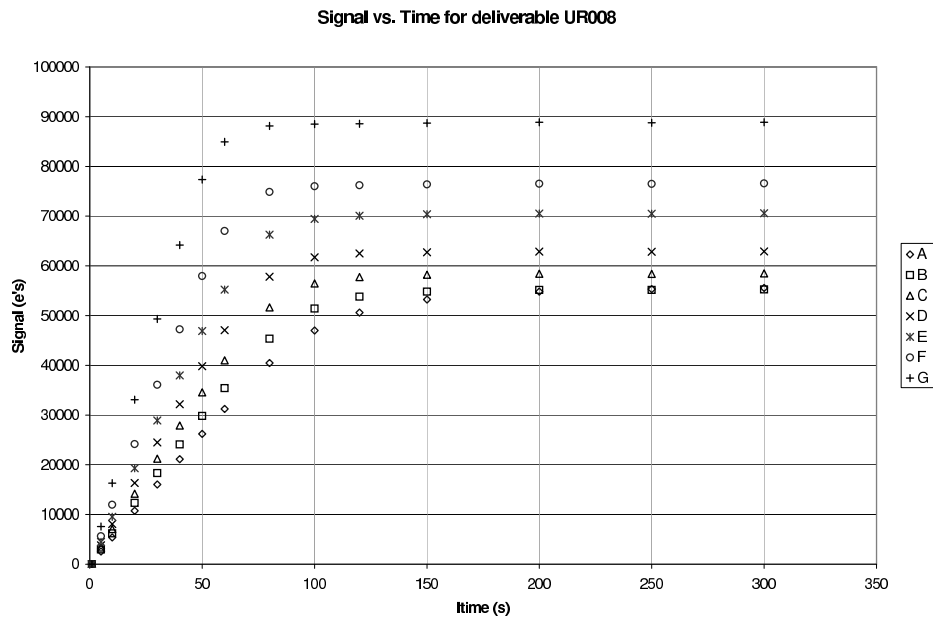


Figure 4.3. Mean signal vs. time for deliverable UR008 at $T=31.7\text{K}$, $V_{bias} = 0\text{mV}$.

Figure 4.3 shows the mean photo-signal (and dark charge) vs. time for the selected pixels on detector array UR008 as the array integrates to saturation at an applied bias of 0mV at 31.7K . The mean measured saturation level of the selected pixels for each type, i.e. the average amount of actual reverse bias across the diodes at the beginning of the integration ramp, is shown in Table 4.3. The actual reverse biases shown correspond to the *actual well depths* (see Section 4.1). Since these actual reverse biases correspond to 0mV applied bias, they give the average pedestal injection for each pixel type. These

values are not corrected for non-linearity because the non-uniformity in dark current and variation in photon flux across the array caused the dark current to affect the linearity measurement (see Section 5.1.2).

Table 4.3. Mean Measured Saturation Level (Actual Well Depth) vs. Pixel Type

Type	Mean Measured Saturation Level		
	ADU	e^-	mV
A	2116	58600	67.3
B	2031	58100	64.6
C	2079	61700	66.1
D	2104	66900	66.9
E	2188	75100	69.6
F	2158	82800	68.6
G	2157	96400	68.6

Figure 4.4 shows the variation in the measured saturation level across the array at 32K for 0mV applied bias. Because the image is not characteristic of an illumination pattern, the observed variation in saturation level cannot be explained by different amounts of forward bias at saturation (see Section 5.2.3). It is also unlikely that high dark current is influencing the measured saturation level, because these data were taken in SRP mode. Therefore, the spread in saturation levels is likely due to a spread in Zero Bias Point (ZBP, see Section 3.2) across the array. A histogram of the measured saturation levels for $T = 30.6\text{K}$ and 0mV applied bias is shown in Figure 4.5. The peak of the histogram is around 64mV, but the distribution is broad. The half ‘power’ points occur at 48mV and 73mV respectively, indicating that the distribution is not entirely Gaussian. This is due to the fact that the upper right-hand quadrant has on average a higher saturation level than the other three quadrants. The non-uniformity of the diodes makes any reasonable measurement of a detector characteristic difficult. It also makes the uncertainties large for any measurement with averages of more than one pixel. Since our goal is to have a full array operational for space astronomy missions, it is imperative to obtain a more uniform array, which was realized in our second phase deliveries.

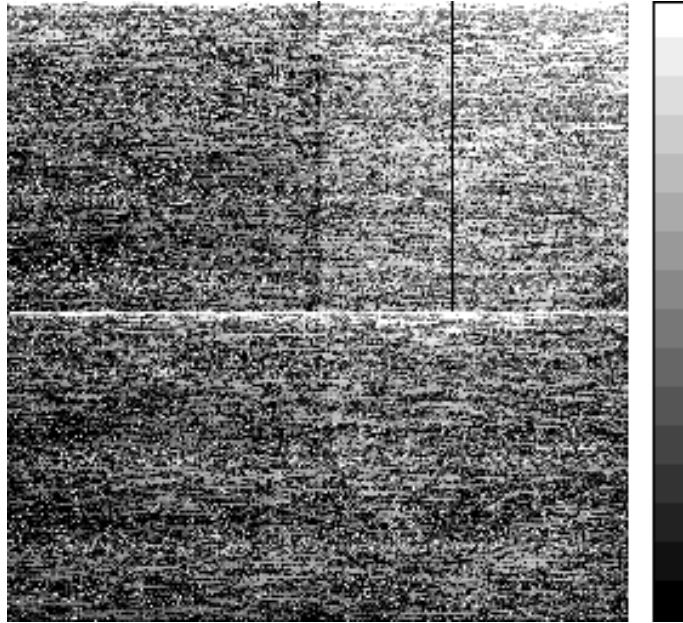


Figure 4.4. Saturation image for deliverable UR008 at $T = 32\text{K}$, $V_{bias} = 0\text{mV}$. Scale is a black to white gradient from 47.7mV to 79.5mV .

4.4 Dark Current Measurements for the NICMOS3 Deliveries

4.4.1 Initial Dark Current Tests

The dark current goal for this set of detectors was $< 100e^-/s$ at a focal plane temperature of $T \sim 30\text{K}$. We employed SRP (see Section 3.2.1) mode to obtain these measurements with external light blocked by a liquid helium cooled, blackened aperture stop. The measurements were taken at an applied bias of 0mV , corresponding to a target well depth (TWD) of 60mV . Figure 4.6 shows the *mean* dark charge vs. integration time for each pixel type at $T = 32.6\text{K}$. Even though the applied bias is the same for every pixel in the array, the actual reverse bias on each pixel of a given type after reset is different. Therefore, each datum corresponds to an average of dark charge accumulated over the given amount of time for an average well depth of 60mV (target well depth). An appropriate one second bias frame value has been subtracted from each datum.

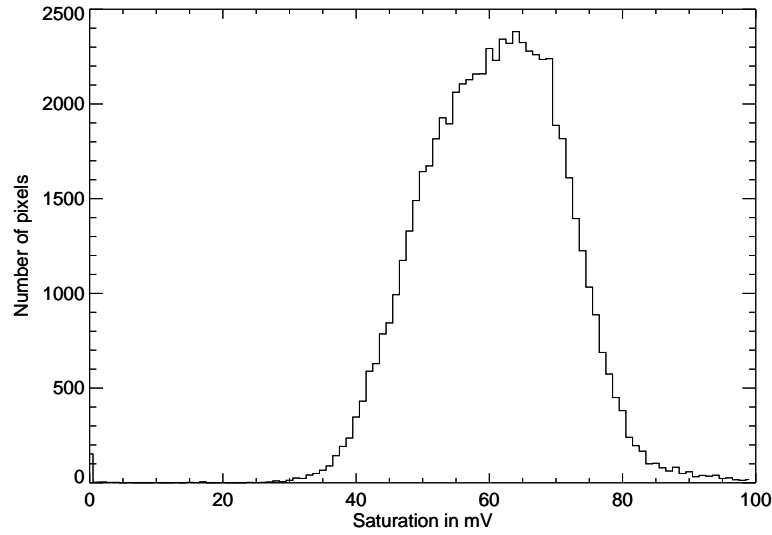


Figure 4.5. Histogram of the measured saturation values (actual reverse bias and actual well depth) in mV for deliverable UR008 at $T = 30.6\text{K}$, $V_{bias} = 0\text{mV}$.

Table 4.4. Mean dark current for each diode type.

Type	A	B	C	D	E	F	G
Dark Current (e^-/s)	9	14	14	15	18	19	22

The dark current can be determined by the slope of the linear region of the dark charge vs. time graph. Fitting from 100 seconds to 300 seconds integration time in Figure 4.6 gives the slope (dark current) reported in Table 4.4. The dark charge data are non-linear at short integration times, even for pixels with low dark current, due to settling in the mux. We therefore concentrate on the longer integration times to determine the low dark current values. From Table 4.4, we find diode type A provides the best dark current performance. In order to understand the limiting mechanisms for the best diode type, we focus on type A pixels.

Since the mean dark current for the good pixels for all of these pixel types is much less than the goal, and the pixels included can have any dark current up to the goal, this implies that the vast majority of the included pixels have small dark currents. Histograms of bias-subtracted dark charge images (only including the selected pixels

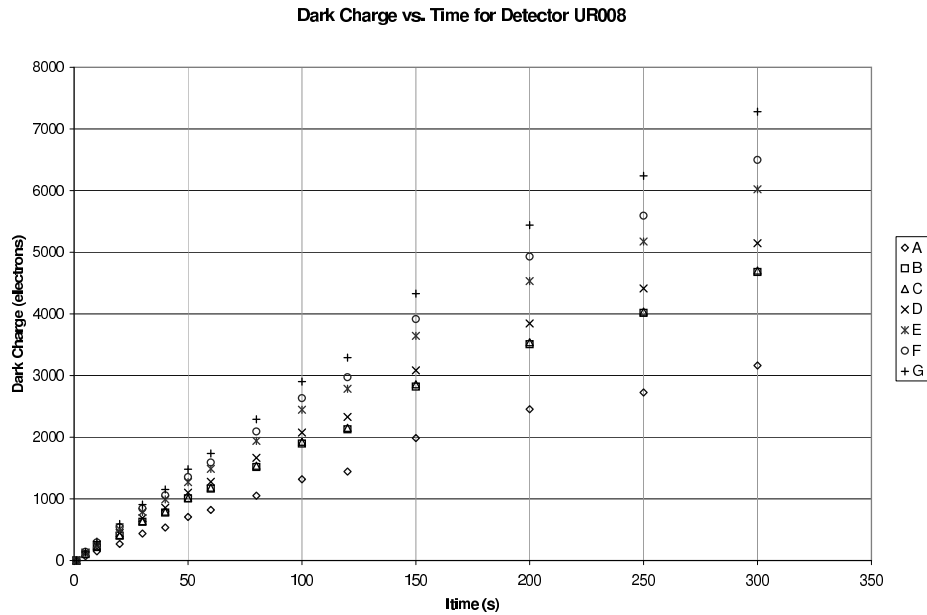


Figure 4.6. Mean accumulated dark charge (e^-), vs. itime (s) for each diode type in deliverable UR008 at $T = 32.6\text{K}$, $V_{bias} = 0\text{mV}$, $\text{TWD}=60\text{mV}$.

of a specific type) confirm this, exhibiting a nearly perfect Gaussian at low integration times with an increasingly prominent high-end tail as the integration time increases as can be seen in Figure 4.7.

Even for a given diode type, there is a large variation in dark current within the allowed range as is apparent in Figure 4.7. Because of this, at 300 seconds, a pixel with an average dark current of $100 e^-/\text{s}$ (the maximum allowable dark current) will have acquired a charge of 30000 electrons, while a pixel with an average dark current of $1 e^-/\text{s}$ will acquire only 300 electrons. Because it is likely that two pixels with these characteristics have different dominant dark current mechanisms, we examine the dark current of individual pixels rather than focusing on an average of a grouping of pixels. This will help us to ascertain where improvement is necessary as we proceed with further development.

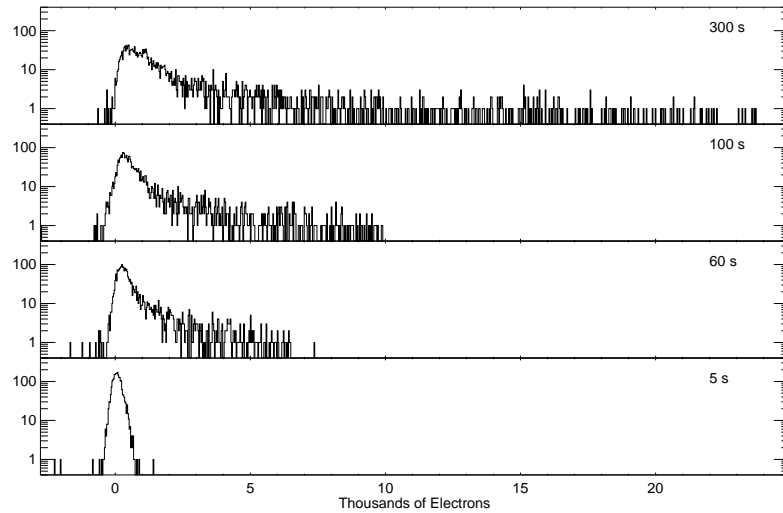


Figure 4.7. Histograms showing the number of pixels with a given dark charge accumulation from one second to various larger integration times for the selected pixels of type A on deliverable UR008 at $T = 32.6\text{K}$, $V_{bias} = 0\text{mV}$, $\text{TWD}=60\text{mV}$.

4.4.2 Temperature and Bias Dependence of Dark Current

The various dark current mechanisms discussed in Section 2.1 have different dependences on temperature and bias. Diffusion and G-R current depend strongly on temperature, whereas tunneling has a strong bias dependence. In the following, we analyze and model the data with the sum of the theoretical dark currents in order to ascertain the dominant mechanism for a given condition.

In order to fit the data with the theoretical dark current mechanisms given in Section 2.1 for various individual pixels, a range of parameters was necessary. The active layer thickness of $10.38\mu\text{m}$, doping density of $\sim 1.6 \times 10^{15}\text{cm}^{-3}$, and the junction area (proprietary) were provided by Rockwell Scientific. For the pixels modeled, the following parameter ranges were used: Lifetime of minority carriers, taken to be $1 \times 10^{-8}\text{s}$ in the bulk region and on the surface and $1.5 \times 10^{-7}\text{s}$ in the depletion region, doping density from $1.35 \times 10^{15}\text{cm}^{-3}$ to $1.75 \times 10^{15}\text{cm}^{-3}$, x parameter from 0.2385 to 0.2400, based upon the cutoff wavelength of the given pixel,⁷ G-R trap level centers from 34meV

⁷We expect some variation in composition parameter x because of the difficulty in process control

to 53meV, tunneling trap level centers at 44meV, density of trap-to-band tunneling centers from $8 \times 10^5 \text{cm}^{-3}$ to $3.9 \times 10^9 \text{cm}^{-3}$, effective mass from $0.09E_g m_e$ to $0.10E_g m_e$, ideality factor $\beta = 2$ indicating a G-R process controls the surface current, $x_s = 0.210$, and surface velocity coefficient from 3.0×10^{-7} to 3.5×10^{-5} . These parameters are on the order of the values cited in many relevant articles.^{9, 21, 22, 28, 31, 36, 62–65} The higher dark current pixels may stretch these ranges even further. This emphasizes the non-uniformity of the array, much of which is due to the difficulty in obtaining uniform composition and doping of $\text{Hg}_{1-x}\text{Cd}_x\text{Te}$ for all pixels. Because of this non-uniformity, we now consider individual pixels.

The dark current has been measured at intervals between 31K and 54K. This dark current corresponds to the initial dark current after the reset switch is opened and is obtained by the initial slope of a fit to the dark charge vs. time data. The dark current has also been measured with respect to voltage from data taken at the target well depths of 30mV, 60mV, 110mV, and 160mV, corresponding to -30mV, 0mV, 50mV, and 100mV of applied bias respectively, at a focal plane temperature 32K. Current-voltage curves were created from these data for individual pixels by subtracting the voltage remaining on the diode at the second sampling from the first and then dividing by the time between samples to obtain the current, and using the mean of the two voltages.⁸ When the currents became low enough that the signal difference between two subsequent data points had a poor signal to noise ratio, the whole data set was used to determine the current and the voltage. The dark current mechanism models were fit to the data, using the highest possible current contribution from each mechanism. All dark current mechanism contributions (see Section 2.1) are modeled to fit the data, although only mechanisms that have magnitudes within the graph limits will be apparent.

The first pixel we examine is a pixel with low dark current at all biases at an operating temperature of 32K. The upper graph in Figure 4.8 shows the bias dependence of this pixel. The dark current appears to be nearly constant with bias, showing only

(see Section 4.6).

⁸Because the dark current was not constant with bias, it strongly affected the non-linearity measurements. Therefore, these data were not linearized.

the slightest increase at the highest bias. This constant dark current can be modeled by diffusion, G-R or surface current, with the appropriate parameter values, since they have very little bias dependence. At the higher actual reverse biases, band-to-band tunneling contributes to the dark current. Looking at the temperature dependence of this pixel in the lower graph of Figure 4.8 makes it clear that surface current, in some form, is dominant at the lower temperatures and nearly all measured biases. At the higher temperatures, a best fit to the data shows that diffusion current is starting to take over as the dominant mechanism, although the lack of data significantly departing from the modeled surface current contribution makes the determination unclear.

The second pixel we examine has nearly constant dark current with bias until the higher biases are reached. Then the dark current exhibits a much stronger bias dependence. Modeling this pixel shows surface current dominating at the lower biases, as for the first pixel, and band-to-band tunneling current dominating at the higher biases, as seen in the upper graph of Figure 4.9, and hinted at for the pixel shown in Figure 4.8. The lower graph again shows surface current dominating at the lower temperatures and potentially diffusion dominating at the highest measured temperature. Like the first pixel, there are not enough data points significantly deviating from the modeled surface current to accurately determine the diffusion contribution.

The last pixel we examine is dominated by surface current at lower biases and by band-to-band tunneling at the highest measured bias as seen in the upper graph of Figure 4.10. The lower graph of Figure 4.10 shows the dark current as a function of inverse temperature at 63mV actual reverse bias. This pixel, unlike the other two, shows a strong dependence on G-R current at the higher temperatures.

Each time the dewar is cooled down to 30K and tests taken, some pixels may undergo damage due to the contracting and expanding process of the cool-down and warm-up. Such damage would cause the dark current to increase from one cool-down to the next. For the majority of pixels, this does not seriously impact the dark current, since the cooling/warming process is carefully controlled to be no faster than 1K/min. For a small subsection of formerly good pixels, however, there is a dramatic change. The bias

dependence data shown for the pixel in Figure 4.10 were taken in the first cool-down. Bias dependence data were also taken in the tenth cool-down (the cool-down following the temperature dependence data), and are shown in Figure 4.11. Although we do not have an exact number of pixels damaged by each cool down, the manual analysis of a representative group of pixels indicates that only a select few pixels are affected by thermal cycling damage in any given cool down. As shown in this figure, the dark current is now dominated by trap-to-band tunneling at the higher reverse biases, with a much stronger surface current than Figure 4.10 at the lower reverse biases. This indicates that the damage to the pixel caused an increase in the trap density in addition to surface defects, possibly pointing to the propagation of a dislocation or other defect into the region near the p - n junction of the pixel (see Sections 2.1.3 and 2.1.5).

Since dark current changes with bias, the percentage of accepted pixels also changes with bias, as can be seen in Table 4.5. Although the percentage of all the pixels is

Table 4.5. Percentage of Low Dark Current Pixels vs. Target Well Depth at 30.6K

Target Well Depth (mV)	Percentage of All	Percentage of Type A
30	19.2	24.0
60	18.0	28.3
110	12.4	23.3
160	5.4	12.8

greater, type A has fewer acceptable pixels at 30mV target well depth than 60mV. This is due to the well depth requirement we imposed (see Section 4.4.1).

For the best performance of type A pixels in a laboratory setting, we note two considerations. As the operating temperature is increased, the percentage of accepted pixels will decrease, indicating that lower temperature operation is preferable. In addition, preliminary analysis suggests that minimizing the number of thermal cycles, and hence thermal cycling damage, is desired.

4.5 Relative Quantum Efficiency

The relative quantum efficiency as a function of wavelength was obtained by measuring the response of the selected detector pixels as a function of wavelength from $8\mu\text{m}$ to approximately $12\mu\text{m}$. The transmitted wavelength was defined by a cold circular variable filter of $\sim 1.54\%$ spectral resolution. The array was illuminated by a blackened metal plate on the liquid nitrogen shield of the dewar through a liquid helium cooled Lyot stop of 2mm diameter, and the signal, which consisted of photo-charge and dark charge, was then dark subtracted to yield the photo-signal. This was compared against the expected grey-body signal from the liquid nitrogen ($T \sim 80\text{K}$) cooled black plate, assuming the emissivity at these wavelengths was unity and wavelength independent.⁹

The expected photon flux is calculated using Planck's radiation law for blackbodies and multiplied by the emissivity to obtain the grey-body signal. Planck's radiation law for radiance per unit wavelength (in $\text{W}/\text{m}^2\cdot\text{sr}\cdot\text{nm}$) is given by

$$L_\lambda(\lambda) = \frac{2hc^2}{\lambda^5 (e^{(hc/\lambda k_b T)} - 1)}, \quad (4.9)$$

where λ is the central wavelength at which the radiance is being calculated, and T is the temperature of the blackbody source. For each position of the circular variable filter, we calculate $L_\lambda(\lambda)$ at the central wavelength, multiply by the bandwidth for the given wavelength, the transmission of the liquid helium cooled filter (4K) at that wavelength, and the emissivity of the grey-body in order to obtain the radiance on the detector side of the Lyot stop.

This value is then multiplied by the detector pixel area and the solid angle field of view of the pixel and divided by the photon energy to obtain the photon flux (photon arrival rate) incident upon the detector for the central wavelength, Φ . Rearranging Equation 1.8, we obtain

$$\eta = \frac{I_{photo}}{q\Phi}, \quad (4.10)$$

⁹Since the relative quantum efficiency is not affected by the emissivity as long as the emissivity is wavelength independent, the actual value of the emissivity is irrelevant to this calculation.

where η is the responsive quantum efficiency (RQE), I_{photo} is the measured photocurrent, and Φ is the incident photon flux, we calculate the responsive quantum efficiency (see Section 5.3 for further discussion).

Because there is uncertainty in the temperature of the black plate, the value of the assumed grey emissivity, and the optical area of the pixels, only the relative quantum efficiency has been measured and is shown normalized to unity in Figure 4.12.

4.6 Cutoff Wavelength

The cutoff wavelength for this device is defined as the half-power point of the detector response. This point is reached at about $9.3\mu\text{m}$ for a focal plane temperature of 30K, based upon the relative quantum efficiency (see Figure 4.12).

The relative quantum efficiency data were also examined pixel by pixel and fit with a logistic curve $QE = [(A_1(A_2)^\lambda + A_3)]^{-1}$ with variable parameters A_1 , A_2 , and A_3 . The initial parameters were $A_1 = 2.51 \times 10^{-19}$, $A_2 = 100$, and $A_3 = 1$. When the data for a pixel were fit and the fitting parameters returned, the curve was then examined to find the wavelength at which the relative quantum efficiency dropped to 0.5. This wavelength was then determined to be the cutoff wavelength for that pixel. This was done for the entire array and the resulting map shows a slight gradient in cutoff wavelength across the array, as can be seen in Figure 4.13.

4.7 Summary of “Lessons Learned” from Phase I Characterization

From the testing on the NICMOS3 deliveries, it has been determined that type A, or the diode structure with the smallest nodal capacitance, shows the most promise for low dark current, high uniformity arrays. Thus, future work will concentrate on arrays made with a small nodal capacitance diode structure. Even amongst pixels of diode type A, there were significant non-uniformity issues in the dark current. It was determined that the pixels exhibiting larger dark currents were affected by stress-induced defects

caused by hybridization.¹⁹ Therefore, proprietary processing and bonding techniques were implemented to reduce the density of stress-induced defects in the deliveries for Phase II. This also warranted a change in multiplexer to Rockwell Scientific's HAWAII-1RG.

Although efforts to improve the quantum efficiency were not made in Phase II, future work will definitely include polishing of the back surface, antireflective coatings and other design changes, such as a smaller pixel size or microlensing to improve optical collection efficiency.

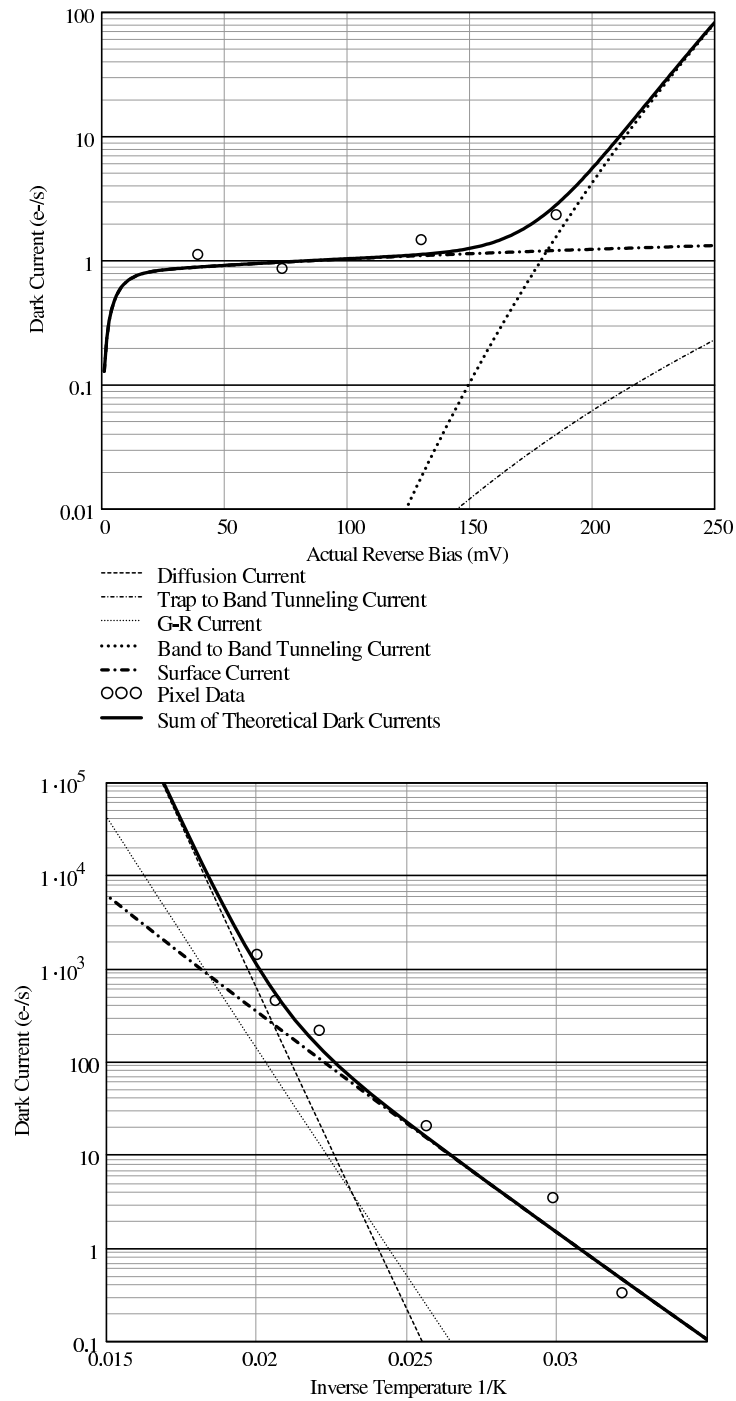


Figure 4.8. Top: Dark current of an individual pixel of diode type A at $T=32\text{K}$ as a function of actual reverse bias with surface current dominating. **Bottom:** Dark current for the same pixel (*top*) as a function of inverse temperature at $V_{actual_bias} = 75\text{mV}$.

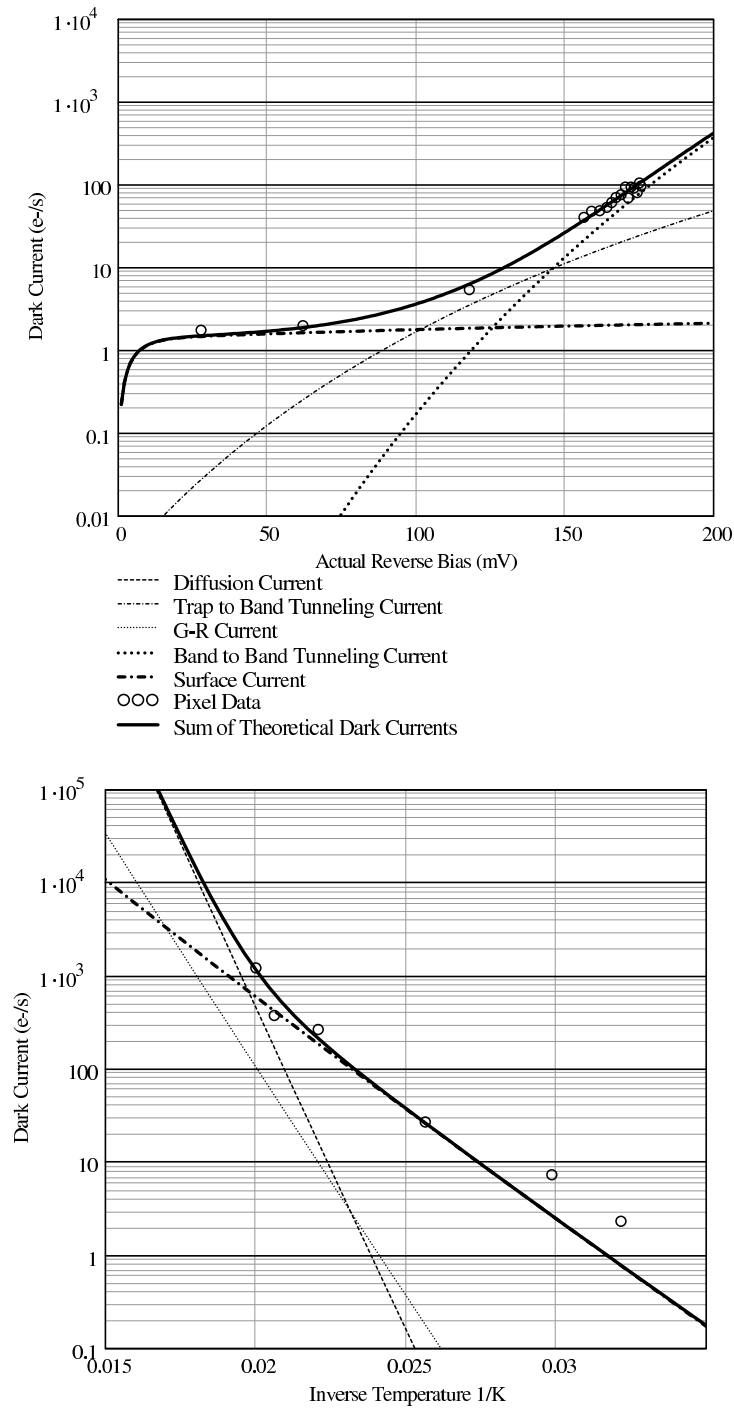


Figure 4.9. Top: Dark current of an individual pixel of diode type A at $T=32\text{K}$ as a function of actual reverse bias with band-to-band tunneling dominating at higher reverse biases. **Bottom:** Dark current for the same pixel (*top*) as a function of inverse temperature at $V_{actual_bias} = 63\text{mV}$.

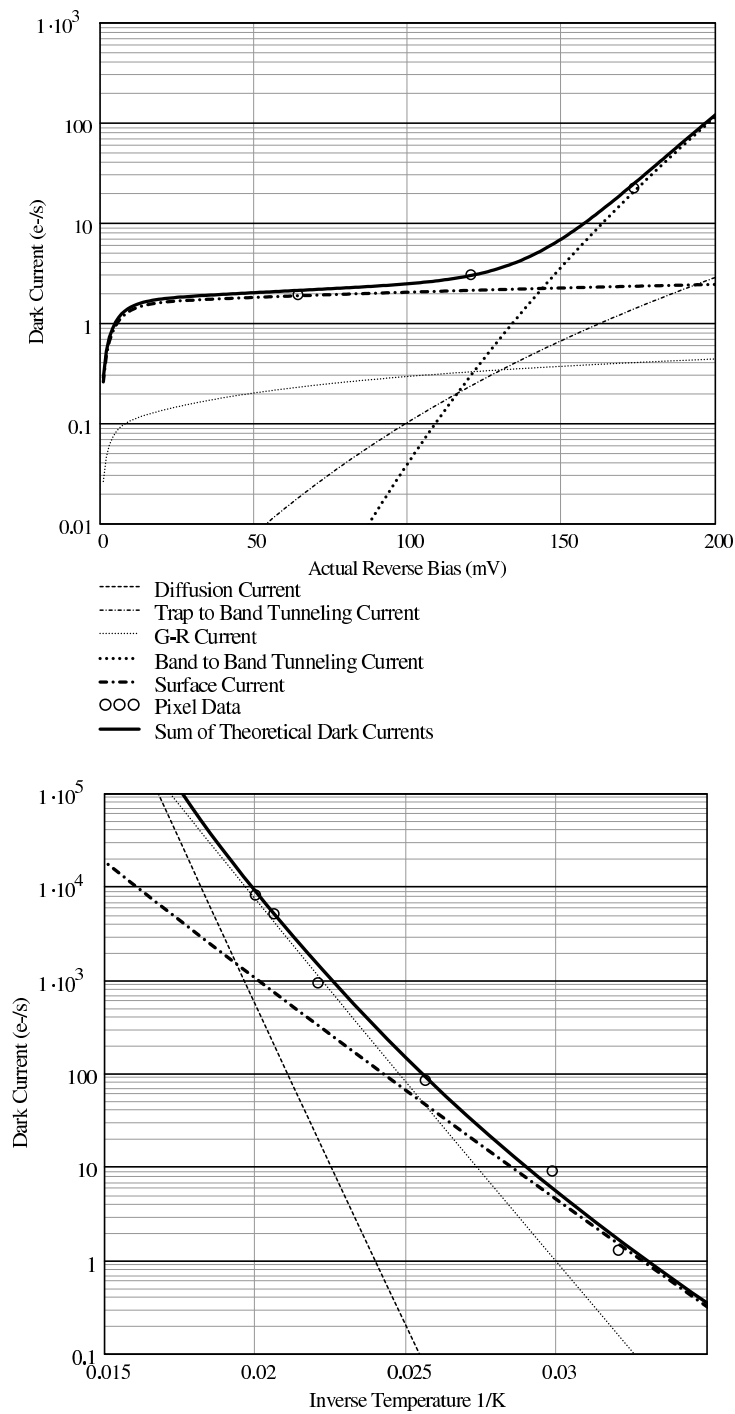


Figure 4.10. Top: Dark current of an individual pixel of diode type A at 32K as a function of actual reverse bias with surface current dominating at lower reverse biases. **Bottom:** Dark current as a function of inverse temperature for the same pixel (*top*) at $V_{actual_bias} = 64\text{mV}$.

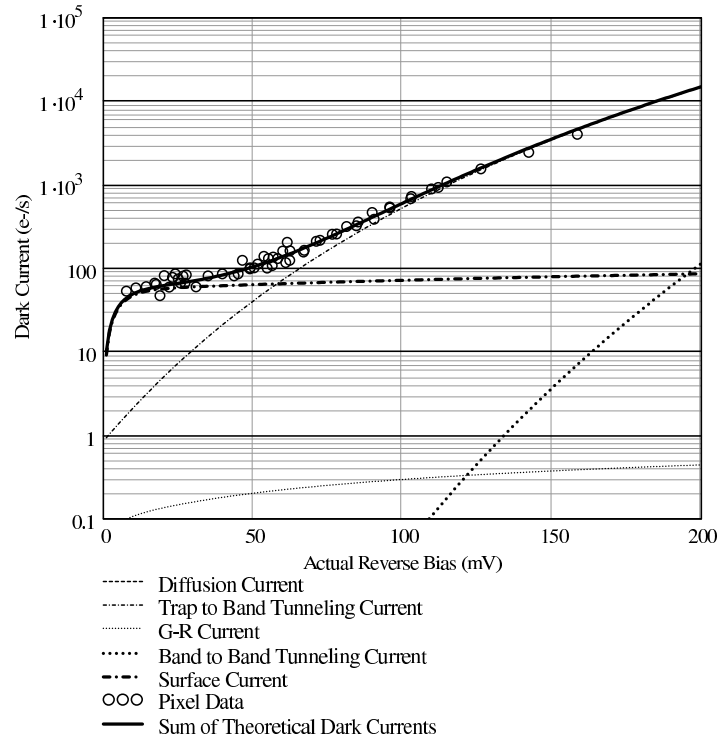


Figure 4.11. Dark current of an individual pixel of diode type A (same pixel as shown in Figure 4.10, but for the tenth cool-down, see text) at $T=32\text{K}$ as a function of actual reverse bias with trap-to-band tunneling now dominating at higher reverse biases in addition to much higher surface current.

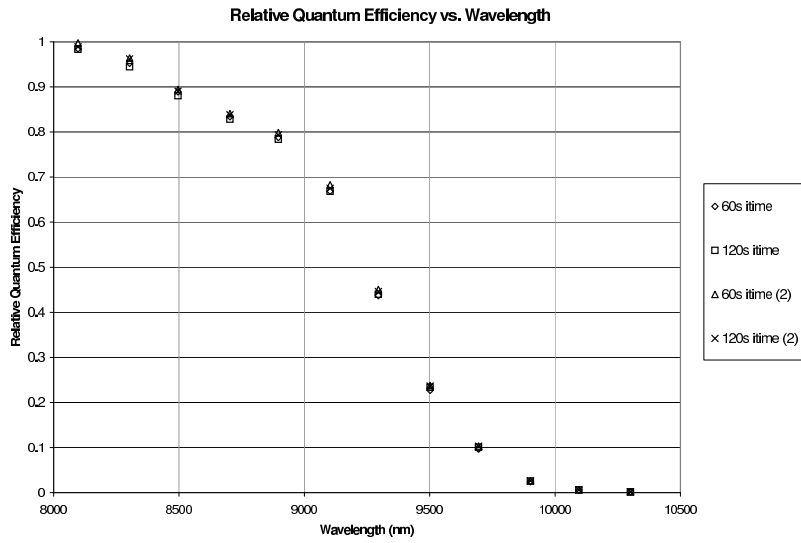


Figure 4.12. Relative quantum efficiency for deliverable UR008 at $T=33\text{K}$, $V_{bias} = 0\text{mV}$ (TWD=60mV).

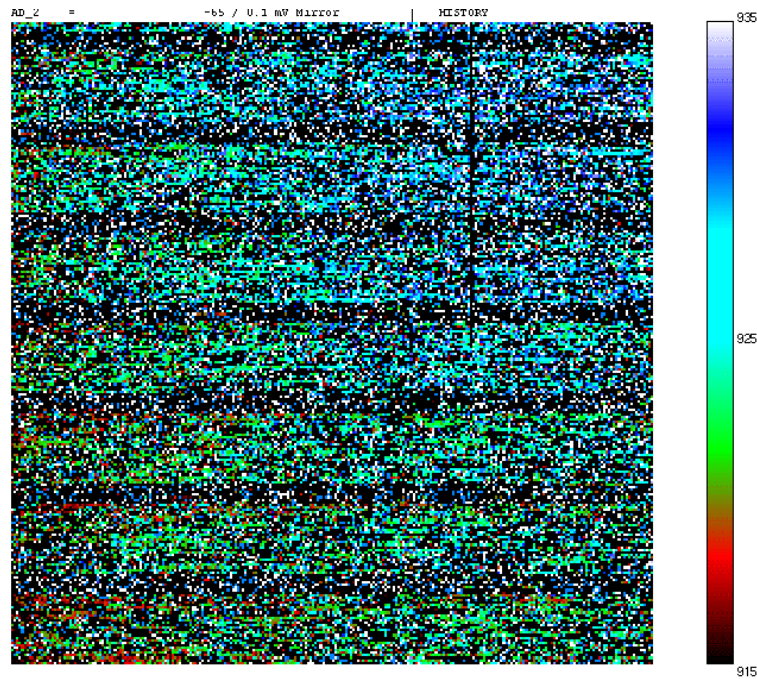


Figure 4.13. Cutoff wavelength map for deliverable UR008 at $T=33\text{K}$ for $V_{bias} = 0\text{mV}$ (TWD=60mV). Units on color bar are in hundredths of a μm .

Chapter 5

Phase II: HAWAII-1RG

Deliveries

Based upon the lessons learned in the Phase I development and testing, the University of Rochester specified the detector parameters and architecture to be employed in Phase II deliveries in order to address some of the concerns raised in Phase I. The first thing addressed in Phase II was the diode structure. Since the best diode structure was determined from the Phase I deliveries, Phase II deliveries were not manufactured in a “banded” structure (see the introduction to Chapter 4). Instead, they were manufactured completely with the diode structure with the smallest nodal capacitance from the Phase I deliveries.

Another concern addressed was the choice of multiplexer. The choice for Phase II deliveries was considered carefully. The slower readout capability of the NICMOS readout and the declining availability of remaining assets, combined with the advantages of the HAWAII-1RG multiplexer, led to the choice of the HAWAII-1RG readout for detector array deliverables in phase II. This increased the grade of the multiplexers we received and granted us more readout flexibility, including faster integration times and sub-frame readouts. The HgCdTe diodes were designed for a $36\mu\text{m}$ pixel pitch and were therefore bump-bonded to every other unit cell of the HAWAII-1RG, resulting in an effective array size of 512×512 . Bonding to the HAWAII-1RG also allowed for proprietary

bonding techniques which reduced stress-induced defects caused by hybridization.

This leads to the non-uniformity concerns in dark current and well depth. Primarily because of the reduction in hybridization defects, the dark current on the resulting devices was dramatically reduced. Because of this, we reduced our dark current goal to the lowest desirable dark current for a 5-10 μ m mission. According to Figure 1.9, the maximum allowable dark current in order to be background rather than detector limited is $30e^-/s$. Even reducing the maximum allowable dark current, the percentage of pixels meeting this goal for a reasonable well depth more than doubled from the Phase I result for $V_{bias} = 0mV$ (target well depth 60mV): compare Tables 4.5 and 5.4. The much lower dark current of the HAWAII-1RG arrays enabled non-linearity correction (see Section 5.1.2) of the diodes, but the addition of burst noise (see Section 5.5) due to the HAWAII-1RG multiplexer made capacitance measurements much more difficult.

Through all that was learned from Phase I LWIR detector array development for low background space astronomy, great strides were made in Phase II manufacturing processes. We now discuss tests of Phase II deliverables, beginning with a discussion of calibration followed by dark current, well depth, quantum efficiency, and ending with burst noise characterization. Through Phase II we again learn much which will enable significant progress in manufacturing potentially flight quality detector arrays in the next research phase.

5.1 Diode Calibration

In order to calibrate the diodes in the HAWAII-1RG arrays, a number of tests were required, with information derived from each test deriving the ranges of consideration in the others. The necessary data sets for calibration allow capacitance, non-linearity, dark current, and well depth to be determined. Many of these tests demand extremely low signal levels. Hence the overall stability of the system will also be addressed.

The HAWAII-1RG multiplexers are equipped with reference pixels as mentioned in Section 3.2.3. They are designed to be in every way similar to the detector pixels, but with a capacitor in place of the detector diode. Therefore, if the output voltage of a

detector pixel is affected by anything other than the detector diode, the reference pixels should similarly be affected, and through calibration data reduction techniques, correction should be possible. Some examples of correctable behaviors are minor temperature fluctuations (which manifest as offset drifts), bias drifts and row noise. The reference pixels were used to correct all data for the above mentioned correctable behaviors except those data which were used for capacitance and well depth (see below). The method by which this was accomplished is detailed below.

For data involving SUTR (see Section 3.2.1) signal vs. time, the first frame (the pedestal) was subtracted from all subsequent frames, and the reference pixel values in the difference images were extracted. Due to our clocking scheme (see Section 3.2.3), there were four useful reference pixels in each row. For each difference image, the four reference pixel values in each row were averaged and the resulting string of values corresponding to row averages for all 512 rows were convolved with a smoothing filter.⁶⁶ The smoothed reference value for each row was subtracted from the entire row of the frame used to make the difference image. This technique subtracted out frame-to-frame fluctuations in addition to row noise. The capacitance data were not reference-average-subtracted because the frame-to-frame noise in individual pixels was of interest. It was not necessary to reference-average-subtract well depth data because the signals were so much higher than the frame or row noise. For Fowler sampling (see Section 3.2.1), each Fowler image was also reference-average-subtracted. For burst noise data (see Section 5.5), a similar subtraction scheme was used, where every pixel was treated like a reference pixel.

Even after the reference pixel subtraction, some low frequency drift, sometimes lasting throughout the duration of the measurement (an hour and a half), remained in the detector pixels' data. Because of the characteristics of this drift, it is unlikely that the drift is temperature-stabilization related. In fact, while operating a bare multiplexer at a stabilized temperature for four hours, it will exhibit this drift consistently throughout operation with temporary intervals of stability. It is unclear why this drift still remains, but it affects low signal measurements by causing a small erroneous positive or nega-

tive signal. We have observed slightly negative drifts on low dark current pixels (up to $-0.6e^-/s$ on a dark charge vs. time graph, see Section 5.2.1) and for a given low dark current ($< 10e^-/s$) pixel, multiple measurements of dark current under identical conditions yield different dark current results consistent with a small, varying pixel drift.

Of the calibration measurements still to be addressed, measurement of pixel capacitance, expressed as the number of electrons per ADU for our system, as well as the pixel non-linearity, will be discussed first because both are needed to characterize quantum efficiency, noise, and dark current.

5.1.1 Capacitance

Using the noise squared vs. signal method,⁶⁷ the capacitance and e^-/ADU were determined (see Section 4.2 for a description of this method). Forty Fowler-1 *images* (sample pairs) for each of 6 integration times were taken. These data were obtained by viewing an external blackbody source through a cold, narrow band $3.3\mu m$ filter for H1RG-16-001 and H1RG-16-002 and through the K ($2.23\mu m$) filter for H1RG-16-003. An 8×6 grid of boxes was used, each of size 20×20 pixels in the central portion of each array. The mean and median capacitance for each box was determined as follows. (Higher dark current, poorly illuminated and small well depth pixels were excluded from this measurement by a pixel mask in software, discussed in Section 5.2.)

For each box and pair of *images* (20 pairs per integration time), the signal and noise (assumed Poissonian) were determined for a variety of fluences. The signal is given by the mean value of each pair of images for the accepted pixels within each box. The noise was determined by what we call a “spatial” noise measurement. This method assumes that all selected pixels are similar enough in characteristics to be considered identical, so the standard deviation (divided by the square root of two) of the difference frame of the selected pixels’ signals is interpreted as the noise. This is in contrast to a “temporal” noise measurement, where each pixel is measured repeatedly under identical conditions, and the standard deviation of the measured signals gives a noise measurement for each pixel individually. We have found that the two methods yield comparable results, on

average.

The noise squared was plotted vs. signal for each box for a variety of fluences, with each pair of images yielding one point on the plot. The inverse slope of the resulting line fit when both noise and signal are given in ADU is the number of e^-/ADU for our system and hence capacitance⁶⁷ by the relationship

$$C = \text{slope}^{-1} q \frac{2^{15} \text{ADU} \times G_{\text{mux}} \times G_{\text{external}}}{10\text{V}}, \quad (5.1)$$

where the final fraction corresponds to the conversion factor between ADU and volts. The capacitances and e^-/ADU for all boxes were examined and the statistics for those 48 boxes are given in Table 5.1. Of those boxes, the majority gave very similar results. A few, however, gave results very different than the rest, perhaps due to burst noise. For this reason, the *median* values are used in subsequent data reduction.

Table 5.1. Table showing statistics of capacitance measurements for all three HAWAII-1RG detectors at $V_{\text{bias}} = 0\text{mV}$ (see text).

Capacitance and e^-/ADU				
Detector	<i>Statistic</i>	<i>Mean</i>	<i>Median</i>	<i>Std Dev</i>
-001	<i>Capacitance (fF)</i>	97.8	101.4	14.24
	e^-/ADU	4.07	4.22	0.59
	$e^-/\mu\text{V}$	0.61	0.63	0.09
-002	<i>Capacitance (fF)</i>	106.8	106.2	12.47
	e^-/ADU	4.44	4.42	0.52
	$e^-/\mu\text{V}$	0.67	0.66	0.08
-003	<i>Capacitance (fF)</i>	105.8	103.9	13.5
	e^-/ADU	4.4	4.32	0.56
	$e^-/\mu\text{V}$	0.66	0.65	0.08

5.1.2 Non-Linearity

Detector response under constant photon flux is non-linear with increasing exposure time, because the device debiases with increasing fluence, as discussed in Section 1.3. Given C is the nodal capacitance, the signal rate is proportional to $1/C$. The normalized signal rate is therefore given by C_0/C , where C_0 is the capacitance at zero signal. An

effective means of measuring the non-linearity is by calculating the slope of the plot of normalized signal rate (C_0/C) vs. signal (Wu et al.).⁶⁸ Non-linearity was determined by using the same data that were used to measure well depth (see Section 5.2). The pixel mask described in Section 5.2 was used in order to concentrate on pixels with similar dark current and well depth, and for these pixels, normalized signal rate was plotted vs. signal.

The signal rate was obtained by dividing the signal by the integration time. Since these data were obtained with SUTR sampling mode, the first frame was subtracted from all subsequent frames to remove the individual pixel offset present in the pedestal frame. Each image obtained from this subtraction corresponded to a different integration time, and therefore the signal of each pixel in each image was divided by the integration time of that image. The signal rate was then normalized by dividing by the signal rate of the first subtracted image. The normalized signal rate was then plotted vs. signal and a non-linearity curve was obtained for each pixel. At low signal, the normalized signal rate is near 1.0. A completely linear pixel would remain at 1.0 as the signal increases until saturation is reached. This is in contrast to actual pixel behavior, such as that shown in Figure 5.1.

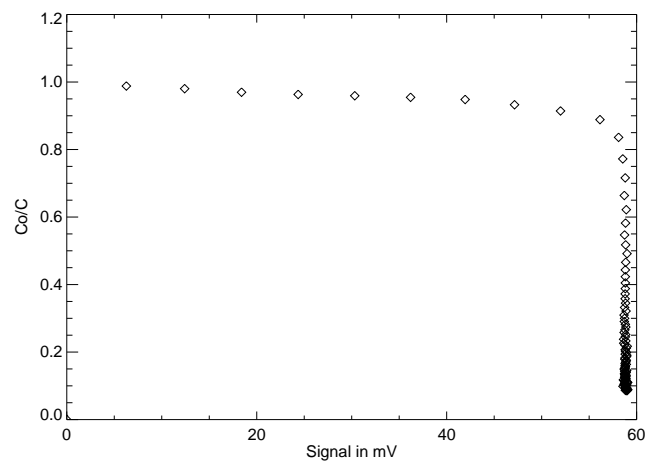


Figure 5.1. Plot of C_0/C vs. signal for a typical well-behaved pixel from detector H1RG-16-001.

The plots of C_0/C vs. signal exhibited a range of non-linearity for the pixels in each array. Some pixels showed extremely flat behavior while others had relatively steep negative slopes. Still, others had slight positive slopes for various possible reasons (such as a significant first frame effect⁶⁹). In addition, there are many behaviors displayed by these detector pixels (related and unrelated to the diode) which can interfere with the non-linearity measurement. One such behavior is burst noise in the multiplexer, as discussed in Section 5.5. Burst noise appears as a false increase or drop in signal, thus causing the signal per unit time to be erroneously small or large. High initial dark current is another behavior which often causes the non-linearity curve to be improperly deduced.

Of the pixels which do not have these behaviors, there is still a range of non-linearity due to the varying construction of each individual diode. For these pixels, the slopes of linear fits to C_0/C vs. signal data, from 20% to 80% of saturation, were plotted in a histogram. The resultant distribution was Gaussian with a high-end tail. The mean of the Gaussian, and the corresponding deviation from linearity at saturation is shown in Table 5.2. The non-linear behavior of a typical well behaved pixel from detector H1RG-16-001 can be seen in Figure 5.1.

Table 5.2. Table showing mean non-linearity measurements for all three detector arrays for $V_{bias} = 0\text{mV}$.

Detector	Mean Slope of C_0/C vs. Signal in $1/e^-$	Percent Non-Linearity at Saturation
H1RG-16-001	-2.6×10^{-6}	8.2%
H1RG-16-002	-1.9×10^{-6}	7.2%
H1RG-16-003	-1.0×10^{-6}	4.4%

5.2 Dark Current and Well Depth

Dark currents were obtained on a pixel by pixel basis *as soon after the reset* as practicable. Many partial array frames were combined into a full array frame in order to

minimize the reset to pedestal delay times for each pixel (see Section 3.2.3 for further explanation). These combined frames will be referred to as *composite* frames. In addition to this, actual full array frames were also taken in sample up the ramp (SUTR) mode, and these will be referred to as *full* frames.

We found percentages of saturated, high dark current ($> 30e^-/s$), low dark current ($< 30e^-/s$), and ultra-low dark current ($< 1e^-/s$) pixels in our dark current characterization of these devices (see Tables 5.3 and 5.4). These pixels are randomly distributed throughout the arrays.

Table 5.3. Percentage of saturated pixels in each of the three arrays at 0mV applied bias.

	H1RG-16-001	H1RG-16-002	H1RG-16-003
Saturated Pixels	8.5%	7.6%	7.2%

Although all ultra-low dark current pixels with sufficient well depth (see Table 5.4) exhibited linear dark charge vs. time curves, some pixels with relatively low dark current can exhibit a non-linear dark charge vs. time curve. Both graphs in Figure 5.2 show dark charge vs. time in SUTR mode for an individual pixel from detector array H1RG-16-001 at $V_{bias} = 0mV$. The pixel illustrated in the *left* graph has approximately 62mV ($\sim 41000e^-$) of well depth and ultra-low dark current ($\sim 0.15e^-/s$ in addition to exemplifying a linear dark charge vs. time curve (where $R = 0$ in Equation 5.2). By contrast, the pixel illustrated in the *right* graph has dark current as high as $\sim 7.0e^-/s$ near the beginning of the integration ramp (low integration times). Because the dark charge appears to be reaching a maximum level after 3000 seconds, it appears as though this pixel is reaching saturation (see Section 5.1.2). However, since the measured well depth is 32mV ($\sim 21000e^-$), the observed behavior is not likely to be saturation. A possible explanation is that the curve observed here is actually due to a form of junction breakdown (see Section 5.2.1 for further discussion). The fit shown in the graphs of Figure 5.2 was created by the method described below.

In order to measure and accurately characterize the various ranges of dark current, two sets of data were taken: composite data (15 to 20 frames 100ms apart in SUTR

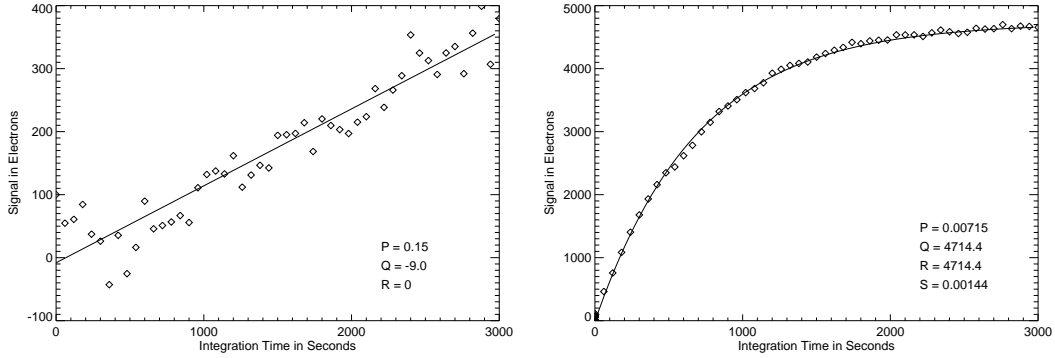


Figure 5.2. Left: Linear dark charge vs. time plot for SUTR data of a single pixel from detector array H1RG-16-001 with ultra-low dark current ($\sim 0.15e^-/s$) and 62mV ($\sim 41000e^-$) of well depth at $V_{bias} = 0mV$. **Right:** Non-linear dark charge vs. time curve for SUTR data of a single pixel from detector array H1RG-16-001 with dark current as high as $\sim 7.0e^-/s$ at $V_{bias} = 0mV$.

mode) and full frame data (52 frames 60 seconds apart in SUTR mode). The first composite frame in the series is referred to as the composite pedestal, since it is the first frame read after the reset. We plot the dark charge, $F(t)$, vs. t , the actual time after the pedestal for each data point, and subsequently fit with the empirical function in Equation 5.2, where P , Q , R and S are fitting parameters. At any point in time on the dark charge vs. time fit, the dark current is given by the time derivative, $F'(t)$, of Equation 5.2. The functional form of Equation 5.2 was chosen to accurately represent the linear and non-linear behaviors over the range of integration times observed.

$$F(t) = Pt + Q - Re^{(-St)} \quad (5.2)$$

For each pixel, the recorded dark current is $F'(0)$, the dark current at the time ($t = 0$) the pedestal was read. To complement the dark current measurement for each pixel, we measured the corresponding well depth (i.e. at $t=0$).

The well depth was determined by illuminating the detector array with a relatively low photon flux so that the degree of forward bias at saturation is at a minimum. We took full frame data in SUTR mode (110 frames 2 to 4 seconds apart), and ensured that the pixels were indeed saturated after 110 frames. We found the maximum value reached

(in ADU) in that time for each pixel and created a saturation map, then determined actual well depth by subtracting the dark composite pedestal frame from the saturation map. The data were then linearized. There is a range of actual well depths after linearization, but a histogram of well depths peaks around the expected value,¹ given by the addition of the applied bias to the pedestal injection of approximately 50mV (e.g. an applied bias of 50mV corresponds to an expected well depth of 100mV), for each applied bias.

In Table 5.4, we report percentages of pixels with at least the minimum well depth shown and dark current less than the maximum dark current shown at the given applied bias. The minimum well depth requirement in this table is 80% of the expected well depth. An example of the distribution of dark currents for pixels with greater than 40mV of well depth at 0mV applied bias is shown in Figure 5.3. Pixels meeting these requirements are randomly distributed throughout the array. It can be seen here that the goals set forth at the beginning of this phase of testing were met and far exceeded for the majority of detector pixels on this array.

We obtained a statistical sample of well depth and dark current for arrays H1RG-16-002 and H1RG-16-003, by analyzing sub-array boxes, for two reasons. First, the arrays were not fully illuminated in our dewar. Second, there were defects on each of the two arrays that increased in size with increasing bias. Thus the boxes were chosen to exclude both the vignetted portions of the illumination and the defects at all applied biases for the dark current and well depth analysis. All boxes chosen for other analyses in this paper exclude the defects for the biases at which the data were taken.

In order to fully understand the dark current limiting behavior of these diodes, we analyze not only the pixels which meet the constraints in Table 5.4, but also pixels with higher dark currents and/or lower well depths. The results we obtained through this analysis will be fed into the next research phase (late-2006).

¹We could not use the *target* well depth (the average value of a saturation image taken in SRP mode, see Section 4.1) for the HAWAII-IRG devices, because the array was not operated in SRP mode. Instead, we use the *expected* well depth, given by the addition of the applied bias to the pedestal injection. The mean actual well depth of the low dark current pixels at 0mV applied bias is the pedestal injection.

Table 5.4. Performance of all three detectors under the constraints of dark current less than the goal of $30e^-/s$ and well depth greater than the expected well depth (see text).

Detector Performance					
Applied Bias (mV)	Well Depth Greater Than (mV)	Dark Current Less Than (e^-/s)	-001	-002	-003
0	40	30	75.0%	76.2%	74.4%
		1	67.4%	69.9%	72.2%
50	80	30	50.9%	68.1%	69.4%
		1	27.9%	25.0%	55.7%
100	120	30	25.0%	53.8%	55.4%
		1	10.8%	5.92%	37.6%
200	200	30	2.07%	16.4%	24.3%
		1	0.30%	0.71%	10.6%

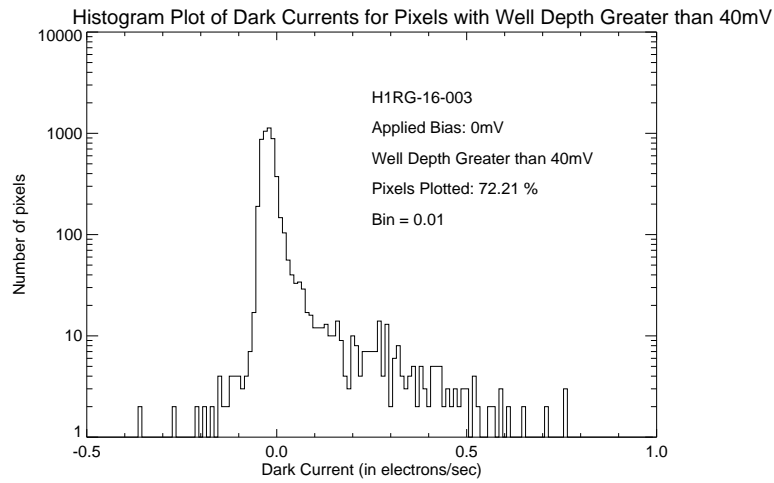


Figure 5.3. Peak of the dark current histogram for detector array H1RG-16-003.

Since trap-to-band and band-to-band tunneling current is primarily dependent upon bias while G-R, diffusion, and surface current are primarily dependent upon temperature, the simultaneous fit of the behavior of a single pixel with respect to bias and temperature should give us a good understanding of the limiting dark current mechanism. However, in analyzing the behavior of many pixels, it is apparent that the limiting mechanism for the bias dependence of dark current is not tunneling as we had expected

based upon previous research, but rather surface current (at low bias) and “breakdown” (at high bias), which may include tunneling microdiodes. Microdiodes are formed unintentionally in regions of the larger diode structure (outside the depletion region), when an effectively p -type region of material forms next to an effectively n -type region. The surface current limiting mechanism for the temperature dependence of dark current requires a significant modification of the material composition (discussed later in this section).

5.2.1 Bias Dependence of Dark Current

Dark charge vs. integration time was investigated at $T = 32\text{K}$ for multiple applied biases. The resultant dark current vs. bias plot is normally called the diode I-V curve. There are virtually no pixels with high dark current at the lower applied biases which have any significant amount of well depth. This is because the high dark current pixels are associated with defect-assisted, localized and early reverse bias junction breakdown. When resetting a pixel to a reverse bias which is greater than its early breakdown voltage, higher dark current and in some cases a change in well depth is observed.²

In the I-V curves below, we highlight three different pixels, one with extremely early breakdown (Figure 5.4), one with moderately early breakdown (Figure 5.5) and one with no breakdown over the range of biases applied (Figure 5.6). When the dark current is low and linear, the dark charge vs. time data for a given reverse bias are fit by Equation 5.2 and the dark current (linear slope of the equation P) is shown as a single point on the graph. (This same method is used for the dark current vs. temperature data.) For higher, non-linear dark currents, the slope of a small subset of points (2-10 points on average) from the dark charge vs. time graph is shown for various regions of the graph (instead of the instantaneous slopes of the fit). Because of this, the latter points have higher uncertainty.

²A change in well depth is observed when the applied bias is much greater than the early breakdown voltage. This causes the I-V curve to follow a different path which leads to a smaller effective well depth.

On the I-V curves in Figures 5.4 through 5.6 and their corresponding dark current vs. temperature graphs (Figures 5.7 through 5.9), theoretical estimates of the dark current (see Section 2.1) are overplotted. The parameters that were used in the theoretical estimates are shown in the first column of Table 5.5, where the value used for each figure is given in the subsequent columns. All dark current mechanisms were considered simultaneously for a given pixel and its dark current vs. bias and dark current vs. temperature data. The parameters were chosen (within reasonable ranges) to give the largest possible contribution from each mechanism limited only by the data. However, only those with sufficiently large contribution are visible on the graphs are shown.

Table 5.5. Parameters used to estimate theoretical dark current contributions for the graphs in Figures 5.4, 5.5, 5.6, and their corresponding dark current vs. temperature graphs (Figures 5.7, 5.8, and 5.9). **Note:** Reported trap densities are estimated to fit the data and have not been provided or verified by Rockwell Scientific.

Parameter	Figures		
	5.4, 5.7	5.5, 5.8	5.6, 5.9
τ_b	2×10^{-7} s	2×10^{-7} s	2×10^{-7} s
N_d	0.59×10^{15} cm ⁻³	0.59×10^{15} cm ⁻³	0.59×10^{15} cm ⁻³
E_{t-gr}	0.032eV	0.032eV	0.032eV
τ_{gr}	1.5×10^{-7} s	1.5×10^{-7} s	1.5×10^{-7} s
x	0.2402	0.2402	0.2402
x_s	0.18	0.18	0.18
τ_s	2×10^{-7} s	2×10^{-7} s	2×10^{-7} s
β	2	2	2
s_0	2×10^{-10}	2.5×10^{-10}	1.5×10^{-10}
n_t	N/A	N/A	3.9×10^5 cm ⁻³
n_{t_i}	1×10^9 cm ⁻³	1×10^7 cm ⁻³	N/A
n_{t_d}	2×10^{10} cm ⁻³	2×10^8 cm ⁻³	N/A
E_t	0.067eV	0.067eV	0.067eV
E_a	0.052eV	0.069eV	N/A
γ	1.233	0.562	N/A
m_{eff}	$0.09 \frac{E_g}{eV} m_e$	$0.083 \frac{E_g}{eV} m_e$	$0.09 \frac{E_g}{eV} m_e$

In Figure 5.4, only one data point exhibits dark current that is not in reverse bias junction breakdown, namely at ~ 30 mV actual reverse bias. (The first applied reverse bias for pixel 1 in Figure 5.4 gave a ‘negative dark current’ (see Section 5.1) of $-0.2e^-/s$

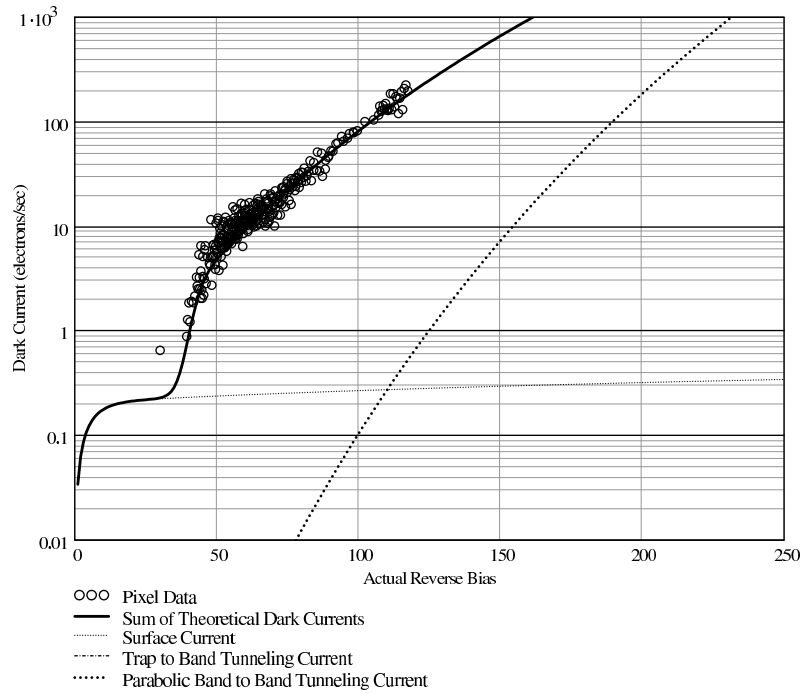


Figure 5.4. Dark current vs. bias for pixel 1 from detector array H1RG-16-001 which illustrates early reverse bias junction breakdown at 40mV.

at 16mV actual reverse bias. This negative value is attributed to an uncompensated drift and is not displayed.) Considering only the bias range where the pixel is not in breakdown, this pixel shows a small well depth. The active trap density is initially 10^9cm^{-3} . This rises to $2 \times 10^{10} \text{cm}^{-3}$ as the activation energy of 0.042eV is passed by the ionization energy in Equation 2.29. When all the traps associated with the dislocation are activated, the increase in active trap density ceases, but trap-to-band current is still the dominant mechanism, due to the relatively large trap density. Band-to-band tunneling current for an assumed parabolic barrier is also shown in the figure and does not contribute significantly because the trap density is high. However, as band-to-band current increases with increasing reverse bias at a faster rate than trap-to-band current, it is expected that band-to-band tunneling current will eventually dominate.

Other pixels exhibit very low dark current, well below our goal, for a range of actual reverse bias, after which they exhibit breakdown characteristics. In Figure 5.5,

we show this for one such pixel, where we observe low, $\sim 6e^-/s$ dark current until approximately 100mV of reverse bias. At this point, the dark current increases rapidly until approximately 120mV reverse bias, where it then bends and begins to increase less rapidly, in a similar manner to pixel 1.

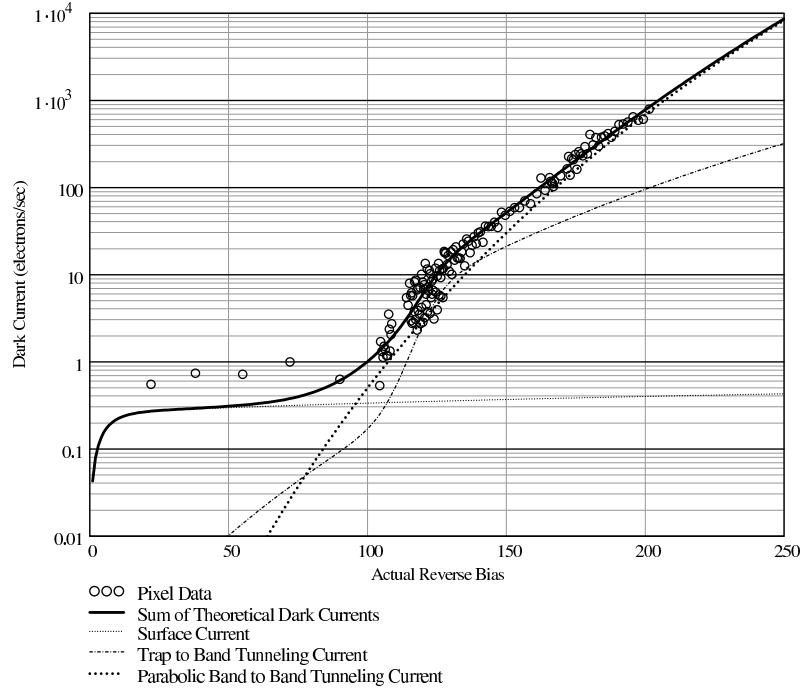


Figure 5.5. Dark current vs. bias for pixel 2 from detector array H1RG-16-001 which illustrates low dark current dominated by surface currents followed by reverse bias junction breakdown.

The trap density for this pixel is two orders of magnitude lower than that of pixel 1, indicating that the trap density in general is very low. In order to fit the breakdown characteristics for this pixel, a combination of band-to-band tunneling through a parabolic barrier and trap-to-band tunneling with a grouping of traps being activated in a dislocation was necessary. It is apparent in Figure 5.5 that the two mechanisms begin to dominate at nearly the same voltage, causing band-to-band tunneling to dominate at the majority of the higher measured reverse biases. It is likely that the presence of the dislocation alters the energy band structure such that band-to-band tunneling is best modeled with a parabolic barrier.

The sum of theoretical dark currents exhibits a similar shape to the observed points for actual reverse bias $\leq 100\text{mV}$, but the data are a factor of two higher than the theoretical surface current curve. The theoretical dark currents in this region are constrained by the dark current vs. temperature data (see Section 5.2.2) and the offset of the dark current vs. bias point from the dark current vs. temperature data in Figure 5.8 at these low dark currents suggests that uncompensated drift (see Section 5.1) may be the cause of the measured dark current in excess of the theoretical estimate in Figure 5.5. Most detector pixels on these arrays exhibit similar behavior to this pixel with early breakdown commencing between 100mV and 200mV .

There are also a select few pixels with low dark current over the entire tested range, up to 200mV applied bias. These pixels do not exhibit any breakdown characteristics, even at actual reverse biases as high as 200mV . Figure 5.6 shows one such pixel. The dark current appears to be decreasing with increasing reverse bias in Figure 5.6 between 30mV and 110mV reverse bias: since there is no known mechanism that causes this behavior, it is likely that there is a detector pixel drift which is not properly compensated for by reference pixel subtraction. Offsets such as noted above are therefore not unexpected.

Regardless of the mechanism causing the low dark currents, the usefulness of these detector array pixels is limited by their breakdown voltage. In order to manufacture space quality detector arrays, we must identify the dislocation which is causing premature breakdown and prevent it in the manufacturing process.

5.2.2 Temperature Dependence of Dark Current

Now that the dominant dark current mechanism causing high dark currents with applied bias has been determined for these three pixels, we examine the temperature dependence of dark current for these same pixels at 0mV applied bias, in order to identify the dominant low dark current mechanism. The graphs shown in Figures 5.7, 5.8, and 5.9 display the initial dark current from a fit to the data taken for each focal plane temperature. The corresponding actual reverse bias well depth is given in each figure caption. All

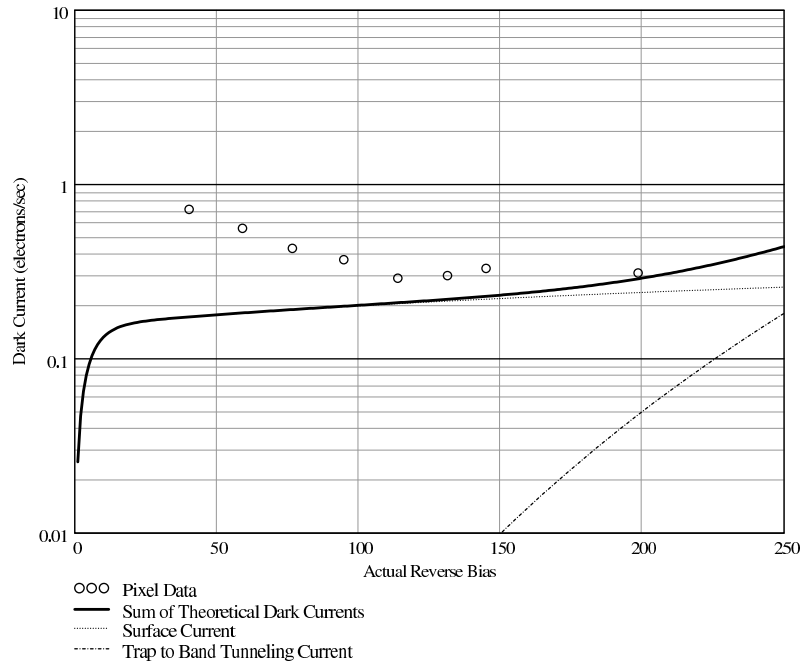


Figure 5.6. Dark current vs. bias for pixel 3 from detector array H1RG-16-001 which illustrates low dark current over the entire range of reverse bias.

three pixels show similar dark current vs. temperature behavior. This indicates that where breakdown occurs has little to no effect on the dark current temperature dependence. Since the data were taken at 0mV applied bias, none of the pixels were in breakdown. Figures 5.7, 5.8, and 5.9 show the dark current vs. temperature for the same pixels examined in Figures 5.4, 5.5, and 5.6 respectively. The data point from the dark current vs. bias graphs is shown on each graph. Since the data for the dark current vs. bias plot were taken in a separate cool-down at a different time, pixel drift is likely to have caused a higher value for dark current than expected from these dark current vs. temperature data.

For all three graphs, the higher dark currents at higher temperatures appear to follow the predicted shape of G-R current. More data at higher temperatures would have clinched the argument. At lower temperatures, the shallower slopes are not indicative of tunneling as we had expected from previous work. Since tunneling is strongly dependent

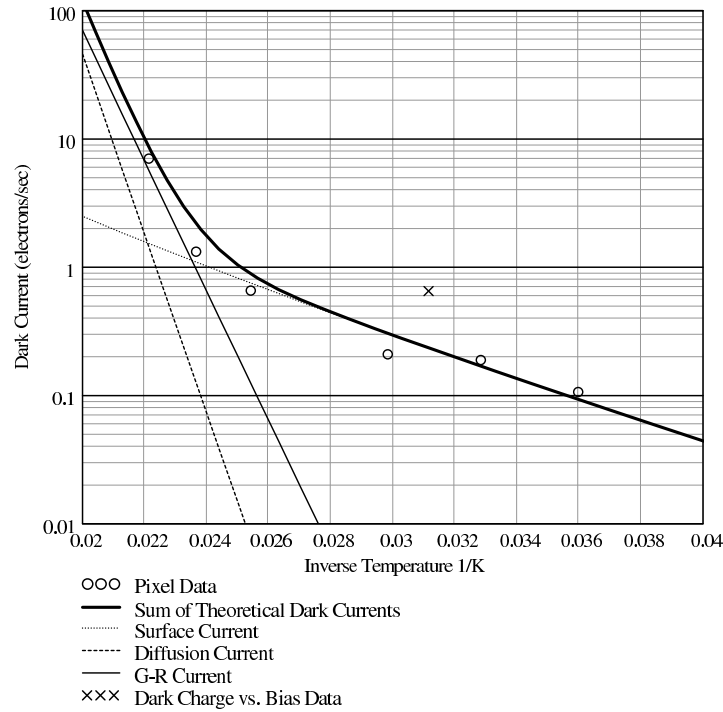


Figure 5.7. Dark current vs. temperature for pixel 1 from detector array HIRG-16-001 at $V_{bias} = 0\text{mV}$, well depth 25mV .

upon bias, see Figures 5.4, 5.5 and 5.6 models, we exclude tunneling as the primary mechanism at low bias. In order to understand the dominant dark current mechanism, we need a mechanism that is not strongly dependent upon bias or temperature. This could be fit by a surface current (or other similarly modeled mechanism) for diodes with a cutoff wavelength of nearly $36\mu\text{m}$, where the composition parameter on the surface, $x_s = 0.18$, may indicate that the surface mechanism causing the dark current lies within a region of higher mercury concentration. Proprietary processing effects³³ on the front side surface of the device (see Section 2.1.3) reasonably require such an adjustment to the composition. This mechanism has also been modeled by shunt leakage³³ (current associated with a voltage applied across a resistance), but the formalism presented here gives insight into the cause of the leakage. Although the very low dark current caused by this mechanism is well below our goal, we believe further work on this mechanism is

indicated.

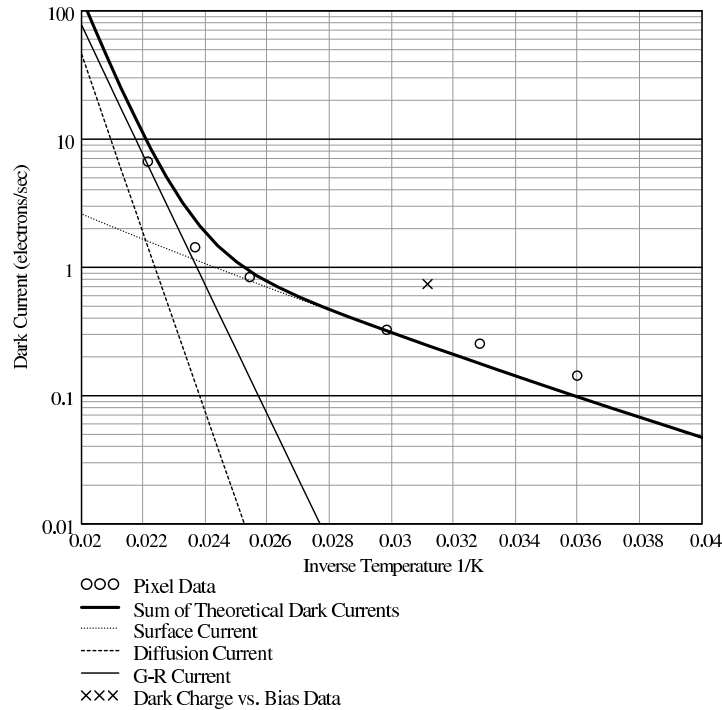


Figure 5.8. Dark current vs. temperature for pixel 2 from detector array H1RG-16-001 at $V_{bias} = 0\text{mV}$, well depth 40mV.

In order to isolate pixels with similar dark current and well depth which are not in breakdown, the remainder of the data reduction was done only on the pixels that meet our dark current goal of $< 30e^-/s$ and fit the well depth requirement in Table 5.4. Thus, a pixel mask was created in software for each array to select only these pixels for the remaining analyses.

5.2.3 Effect of Forward Bias on Well Depth

In Figure 5.10 we schematically present I-V curves for several photo-current levels. It is apparent that increasing the photon flux not only increases the short circuit current, I_{sc} , but also the open circuit voltage, V_{oc} . The short circuit current and open circuit voltage occur when there is no net voltage across the diode and no net current across

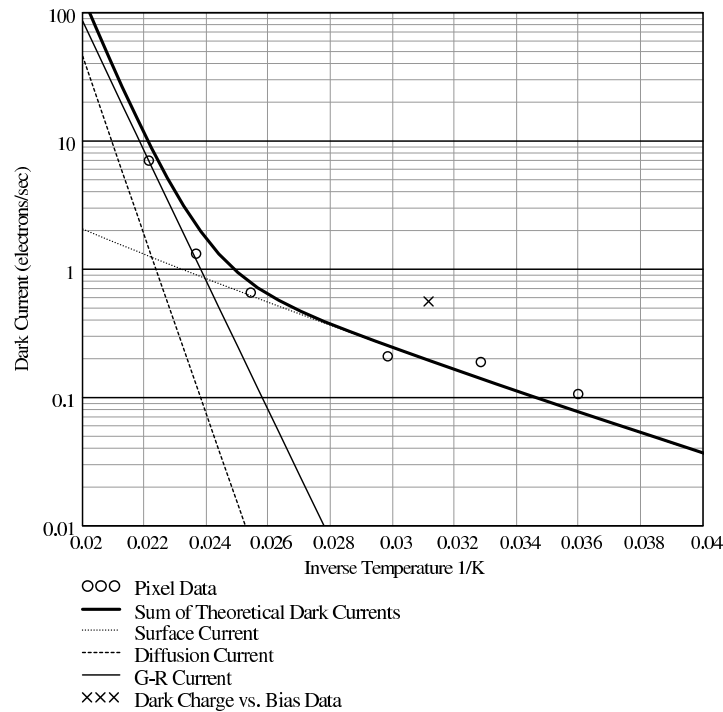


Figure 5.9. Dark current vs. temperature for pixel 3 from detector array H1RG-16-001 at $V_{bias} = 0\text{mV}$, well depth 60mV.

the diode respectively. When the detector diode is reset to a specific reverse bias, the amount of bias across it is given by V_{actual_bias} , shown at an arbitrary reverse bias voltage in Figure 5.10. This voltage is with respect to $V = 0$. In practice, however, the measured bias is with respect to the value of V where the current goes to zero, V_{oc} . With no illumination, these two voltages are the same because $V_{oc} = 0$. In the presence of photon flux, however, $V_{oc} > 0$ and therefore the measured well depth (referred to in previous sections as actual well depth and given by the difference between the voltage at saturation and that immediately after reset), erroneously includes a forward bias contribution. The amount of forward bias can be substantial relative to the applied bias used. It may seem logical to integrate to saturation in the dark to avoid this contribution, but since many of the HAWAII-1RG pixels have very low dark current, they cannot be integrated to saturation in the dark in readily measurable times under

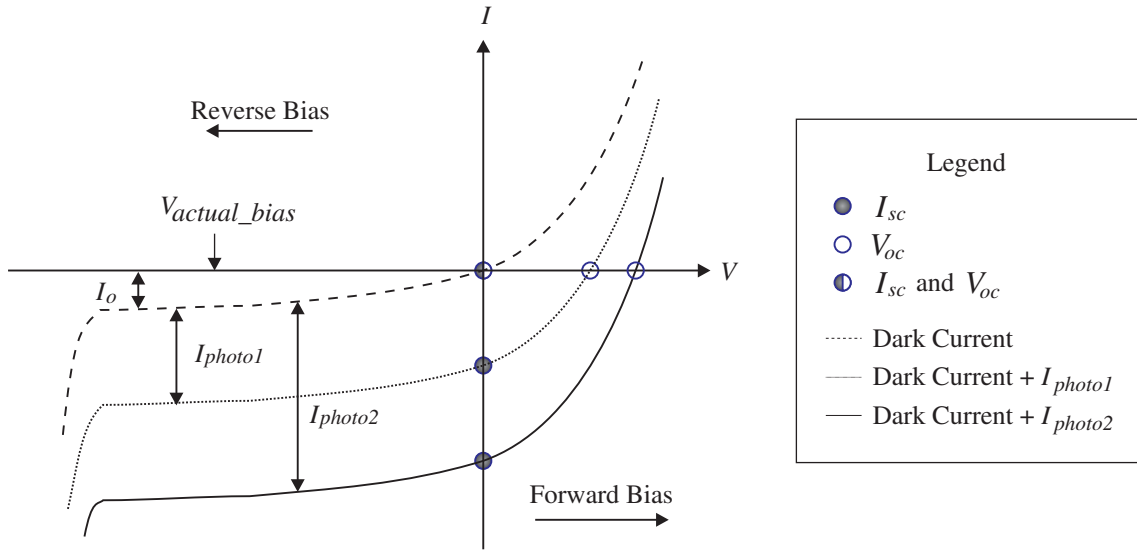


Figure 5.10. I-V curves for various photo currents with I_{sc} and V_{oc} indicated for each curve.

stable conditions. Therefore, the amount of photon flux applied to the detector to determine well depth is small in order to minimize the amount of forward bias on the detector at saturation.

Calculation of Expected Forward Bias

Following is a calculation of the amount of forward bias at saturation. First, we begin with the diode equation given in Equation 1.7,

$$I_{total} = I_0 \left(e^{\frac{qV}{kT}} - 1 \right) - I_{photo}, \quad (5.3)$$

where I_{total} is the net current through the photodiode, I_{photo} is the photo-current, I_0 is the saturation current under reverse bias (the dark current), q is the charge on an electron, V is the bias on the diode, k is Boltzmann's constant, and T is the temperature of the diode. The amount of forward bias when the net current goes to zero (saturation) is given by the open circuit voltage (see Figure 1.5), where $I_{total} = 0$, i.e. when the photon current exactly balances the dark current. Solving for V under this condition gives

$$V_{I_{total}=0} = \frac{kT}{q} \cdot \ln \left(\frac{I_{photo} + I_0}{I_0} \right). \quad (5.4)$$

Utilizing this equation at 30K, we find the ranges of forward bias for the corresponding I_0 and I_{photo} in Table 5.6. Here, I_0 is selected to be on the order of the maximum expected dark current for the majority of the pixels ($1e^-/s$), and a more common value ($0.1e^-/s$).

Table 5.6. This table shows the various amounts of forward bias obtained with different parameters for I_0 and I_{photo}

I_0	I_{photo}	$V_{I=0}$
$1e^-/s$	$1000e^-/s$	17.8mV
$1e^-/s$	$100e^-/s$	11.9mV
$1e^-/s$	$10e^-/s$	6.2mV
$0.1e^-/s$	$1000e^-/s$	23.8mV
$0.1e^-/s$	$100e^-/s$	17.8mV
$0.1e^-/s$	$10e^-/s$	11.9mV
$0.01e^-/s$	$1000e^-/s$	29.7mV

The measured well depths for our $\sim 10\mu\text{m}$ HgCdTe detector arrays are on the order of 60mV for 0mV applied bias, which implies up to half of the total measured well depth can be in forward bias. This is a foreign regime for more typical photo-voltaic detector operation, since the well depths are typically on the order of 300mV or more with utilized signals below 80% of saturation, thus avoiding the forward bias regime entirely.

Higher Dark Current Pixels

Some of the higher dark current pixels appeared to saturate in the dark as indicated in Figure 5.2 and related text, but when the well depth was measured, it was found to be much higher than the apparent saturation in the dark would indicate. We then investigated whether forward bias could compensate for the difference. For some sample pixels, a few representative quantities were obtained. The well depth obtained under illumination was compared to the apparent well depth in the dark. If forward bias could compensate for the difference, then that implies that the diode may indeed be

saturating in the dark. Table 5.7 shows the diagnosis for two pixels. Keep in mind that the possible forward bias is extremely dependent upon the saturation current, I_0 , which is not easily obtained for these higher dark current pixels, since their dark charge does not vary linearly with time.

Table 5.7. This table shows the statistics for two pixels which were examined from detector H1RG-16-001. It shows that there could be some well depth unaccounted for for both pixels, although the remaining well depth for Pixel B can be eliminated if the saturation current is reduced to $I_0 = 0.5e^-/s$.

Quantity	Pixel A		Pixel B	
Total Well (light)	$40,164e^-$	60.5mV	$17,988e^-$	27.1mV
I_{photo}	$1178e^-/s$	1.78mV/s	$672e^-/s$	1.01mV/s
I_0	$0.6e^-/s$		$\sim 1e^-/s$	
Calculated Forward Bias	$13,080e^-$	19.7mV	$11,146e^-$	16.8mV
Well Depth (dark)	$7,000e^-$	10.6mV	$3,750e^-$	5.7mV
Well Depth Unaccounted For	$20,084e^-$	30.3mV	$3,090e^-$	4.7mV

As can be seen, the remaining well depth left to account for (30mV) on Pixel A is substantial. In fact, by no reasonable means can one explain this by uncertainty in the saturation current. Consequently, for this pixel, there must be some other reason why the dark current is dramatically lower at the bias at which it appears to saturate in the dark. A possible explanation is that the pixel may be coming out of early breakdown (see Section 2.1.5), since the breakdown characteristics discussed in Section 5.2.1 manifest as an exponential increase in reverse current at higher reverse biases. The other pixel's remaining well depth could be explained by uncertainty in the saturation current, since $1e^-/s$ was only an estimate. Some of the pixels that appear to saturate in the dark may do so. However, it is clear that *not all* of those pixels are actually saturating, and that a mechanism such as early breakdown (illustrated in Figure 5.4) is in play.

Confirmation of Forward Bias Calculation

With detector array H1RG-16-003 we find different saturation levels obtained with exposure to different photon fluxes. By comparing two different saturation levels to the difference expected from their respective fluxes, we test the validity of the forward bias

explanation above. Let I_{photo1} and I_{photo2} be the photo-current due to two different photon fluxes. The quantities I_{photo1} and I_{photo2} correspond to forward bias levels V_1 and V_2 respectively via Equation 5.4. Therefore, the expected difference between V_1 and V_2 is given by

$$\Delta V \simeq \frac{kT}{q} \cdot \ln \left(\frac{I_{photo1}}{I_{photo2}} \right), \quad (5.5)$$

where $\Delta V = V_1 - V_2$, assuming $I_{photo} \gg I_0$.

Table 5.8 compares the calculated ΔV to the measurement (which is obtained from $V_{sat,3.3\mu m} - V_{sat,2.2\mu m}$, where the photon flux levels at $3.3\mu m$ and $2.2\mu m$ are given by I_{photo1} and I_{photo2} respectively) for a few sample pixels. The calculated ΔV was com-

Table 5.8. This table shows the calculated and measured ΔV for a few sample pixels.

Pixel	I_{photo1}	I_{photo2}	$\Delta V_{calculated}$	$\Delta V_{measured}$
P1	$2747e^-/s$	$460e^-/s$	4.61mV	4.96mV
P2	$1799e^-/s$	$386e^-/s$	3.97mV	3.94mV
P3	$887e^-/s$	$473e^-/s$	1.62mV	1.45mV
P4	$556e^-/s$	$408e^-/s$	0.80mV	0.66mV

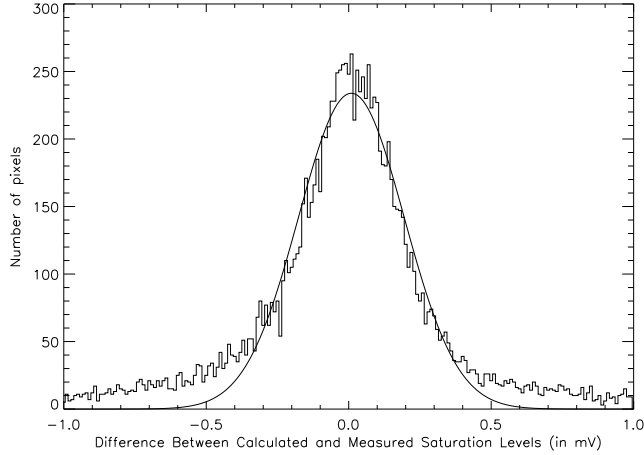
pared to the measured ΔV for all pixels with sufficient illumination, and the result was plotted in a histogram. The histogram featured a Gaussian centered around zero, with a full-width half max of 0.43mV (see Figure 5.11). This confirms the hypothesis that the detector is going into forward bias by the amount predicted.

5.3 Quantum Efficiency

In Section 4.5 responsive quantum efficiency (RQE) was discussed. Here, we also desire a detective quantum efficiency (DQE) measurement. Assuming that photoconductive gain and gain dispersion are both unity, RQE is given by

$$\eta = \frac{I_{photo}}{q\Phi} = \frac{I_{photo}t}{q\Phi t} = \frac{S}{S_0}, \quad (5.6)$$

Figure 5.11. This figure shows the difference between the calculated and measured ΔV in mV for pixels with sufficient illumination overlaid with a Gaussian fit. The standard deviation of the Gaussian fit is 0.2mV.



where S is the number of collected electrons and S_0 is the number of incoming photons, DQE is given by⁴⁶

$$\eta = \frac{\left(\frac{S}{N}\right)^2}{S_0}, \quad (5.7)$$

where N is the noise in the signal measurement. A photoconductive gain greater than unity can cause RQE to be greater than DQE. Photoconductive gain can occur when a generated electron or hole obtains enough kinetic energy from the photon to create an additional electron-hole pair. This can lead to more than one electron-hole pair being generated for each photon that is detected. This can make the measured RQE artificially high, which can lead to reported RQEs greater than 100%.

The quantum efficiency for all three detectors was determined using a circular variable filter and a calibrated thermal illumination source. The data were taken with a Lyot stop of $50\mu\text{m}$. There were 8 Fowler-1 *images* taken at each wavelength so that a DQE measurement could be obtained in addition to the RQE measurement. As with the capacitance data, the pixel mask described in Section 5.2 was used. Signals from

the mask-selected pixels within a user defined box³ were averaged. The average signal obtained (S) was then compared to the expected signal from incoming photons for 100% quantum efficiency (S_0), calculated assuming an emissivity of unity for the illuminating source) to determine responsive quantum efficiency⁴⁶ as illustrated in Equation 5.6 (see Section 4.5 for calculation of Φ).

A “spatial” noise (N) measurement (see Section 5.1.1 for further explanation) was obtained from the standard deviation (divided by the square root of two) of masked pixels in the difference of two of the aforementioned images. Since there were eight images, the median noise of the four difference images was used. Likewise, the median signal of the four averaged images was used. The signal (determined as described above) to noise ratio compared to the expected signal in incoming photons yielded detective quantum efficiency,⁴⁶ as in Equation 5.7.

The results are shown in Figures 5.12, 5.13, and 5.14. Defining the cutoff wavelength to be the half power point of detector response, the cutoff wavelength is determined to be $9.1\mu\text{m}$, $8.5\mu\text{m}$, and $8.4\mu\text{m}$ for detectors H1RG-16-001, -002, and -003 respectively. It can also be seen that between $8\mu\text{m}$ and $9\mu\text{m}$ in Figures 5.12 and 5.14, the DQE appears to be greater than the RQE. Since this is unphysical, it is attributed to uncertainty in the measurement or incorrect noise determination. Pain and Hancock⁷⁰ report that proximity of the signal to saturation can cause errors in the noise determination. This can consequentially cause DQE to be measured greater than RQE for a given wavelength region.

It can also be seen that the RQE is greater than the DQE by a significant amount at wavelengths below $5\mu\text{m}$. Although this could imply photoconductive gain, this conclusion is premature because of uncertainties⁴ in the deduced QEs. In Figure 5.14, it is apparent that the QE of this device is significantly lower than that of the other two

³For these data, the box used was the same for all three arrays and centered in the illumination. The box had dimensions of 15×59 . This not only avoided the vignetted regions, but since we were using a circular variable filter, it helped to ensure we were reporting values for the central selected wavelength.

⁴As discussed in Section 5.5, an unexpected, temporal noise source appeared which affected all noise measurements.

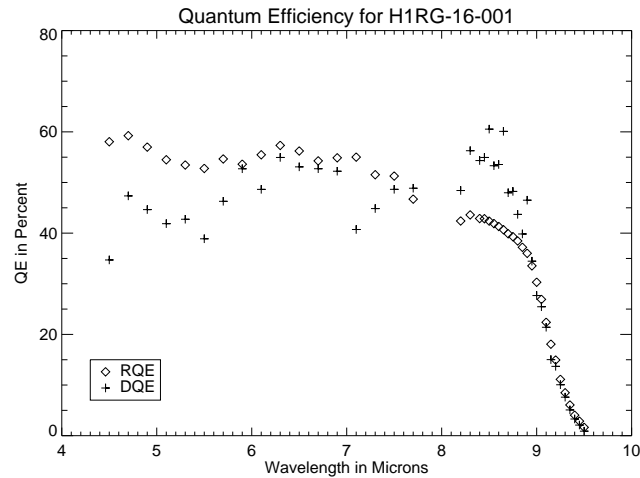


Figure 5.12. DQE and RQE for selected pixels (as described above) of detector H1RG-16-001.

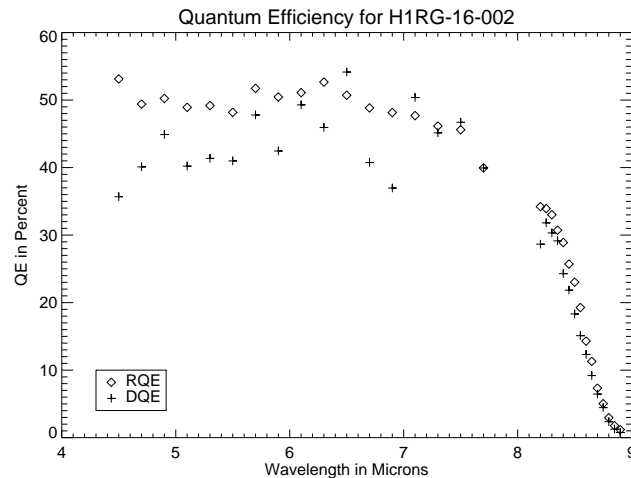


Figure 5.13. DQE and RQE for selected pixels (as described above) of detector H1RG-16-002.

devices. This may be related to noticeable irregularities on the surface of the device.

Even though these devices are neither anti-reflection coated nor polished, the measured quantum efficiency (QE) was substantial (see Figures 5.12, 5.13 and 5.14). The QE can be no greater than 70 percent, due to reflection loss, and we expect that poor lateral diffusion may also contribute to the lower measured QE. We therefore intend to use antireflective coatings, reduce pixel size and possibly employ microlenses in order to improve the quantum efficiency for space applications.

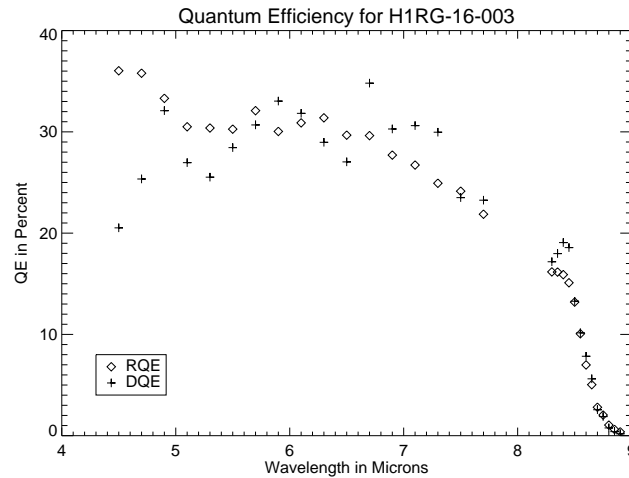


Figure 5.14. DQE and RQE for selected pixels (as described above) of detector H1RG-16-003.

5.4 Noise

As stated in Section 2.2, the measured noise of any given pixel includes diode noise, read noise, and system noise. Although the University of Rochester did not specify a noise requirement for this phase of testing, the measured pixel noise was expected to be within the range of readily available published values on product information sheets from Rockwell Scientific. Although the noise was found to be quite low on average, we were surprised to discover an additional noise component, burst noise, which will be discussed in Section 5.5. First, we will address the other noise components.

The system noise was measured to be $15.7\mu\text{V}$ and $23.3\mu\text{V}$ (input referred) for outputs one and two respectively in our black box (see Section 3.1.2). This was measured by disconnecting the signal cable from the dewar, shorting all of the signal return lines together on the signal cable that leads to the black box, and attaching all of the signal lines to their respective return line with 2k resistors. Then two Fowler-1 (CDS) images were obtained and subtracted from one another. The standard deviation of each output was divided by the square root of two and converted to input referred μV . For the capacitance of H1RG-16-001 pixels, the system noise corresponds to approximately $10.4e^-$ and $15.4e^-$ respectively.

The read noise of the HAWAII-1RG multiplexer is found in our analysis of burst noise data taken in SUTR sampling mode, where we effectively removed the detector diode from the circuit in order to focus noise characterization on the multiplexer. For a description of the data taking method used, see Section 5.5. Figure 5.15 shows a histogram of signal measurements with the reset enabled for a pixel with no burst noise. The standard deviation of this histogram corresponds to the CDS read and system noise combined of a typical pixel and was measured to be approximately $32\mu\text{V}$ (input referred) for a typical pixel of output one. This corresponds to approximately $21e^-$ of system plus read noise, therefore leaving the read noise alone to contribute $27.9\mu\text{V}$ or $18.5e^-$ of noise.

Finally, the diode noise depends upon the signal of the pixel. Since diode noise is dominated by shot noise, we expect to acquire a noise that varies as the square root of the number of photons which have arrived at the pixel. Since only those photons which are captured contribute, we will concern ourselves only with the number of electrons, and thus the signal on the diode (including any dark current, which is also assumed to be Poissonian).

At low signal, the most significant source of noise in a majority of pixels is the read noise. Burst noise, since it originates in the HAWAII-1RG multiplexer, can be a significant fraction of the read noise. Since a typical pixel which does not exhibit burst noise has very low noise indeed, burst noise needs to be eliminated or reduced, if possible.

5.5 Burst Noise

The information that follows through Section 5.5.2 regarding burst noise was presented at the SPIE meeting at San Diego in August of 2005. This material was included in the SPIE proceedings from that meeting.²⁷

We first encountered burst noise while refining the algorithm I created to characterize dark current data from these phase II devices. With data taken in sample up the ramp (SUTR) mode, we expect that the slope of the data ramp will be continuous with the

exception of cosmic ray hits. During the evaluation of individual pixels we noticed that some pixels exhibited what appeared to be positive and negative cosmic ray hits of varying magnitudes. Investigation revealed that the source of this phenomenon was not cosmic rays at all, but rather burst noise, since cosmic rays do not suddenly decrease the signal on a pixel. Burst noise can also be indicated by unusually noisy pixels. A typical pixel has noise corresponding to a σ about the mean of $32\mu\text{V}$ (input referred). However, some pixels have uncharacteristically larger standard deviations than that of a typical pixel. The extra noise in these pixels is often due to burst noise. For example, if a pixel has burst noise with transitions smaller than our detection limit, defined in Section 5.5.1, the pixel will merely appear to be slightly noisier than other pixels.

Burst noise, also known by other names such as popcorn noise and RTS/RTN (Random Telegraph Signal/Noise), is a phenomenon that is understood to be a result of defects in the vicinity of a current carrying region (see Section 2.2.6). It is characterized by rapid conductivity changes manifesting as voltage or current level shifts in both positive and negative directions and can have varying magnitudes. For an integrated circuit, such as the HAWAII-1RG multiplexer, a current change in any component in the signal chain results in a change in voltage at the signal output.

Because this noise was seen both in forward and reverse detector bias, as well as in reference pixels (no detector), all of which were capable of producing very large magnitude transitions (on the order of mV), the burst noise is attributed to the multiplexer.²⁵ Since some pixels exhibit this noise while others do not, the origin of the noise must be within the affected unit cells of the multiplexer, with the most likely candidate being the source follower unit cell MOSFET. Other authors⁷¹ have also detected burst noise in the HAWAII-1RG and HAWAII-2RG, but not, to our knowledge, in other multiplexers. The reason for this may be the $0.25\mu\text{m}$ design rules employed by Rockwell Scientific in multiplexer manufacturing, which are a factor of two smaller than that used by other detector vendors. Specifically, Rockwell Scientific previously used $0.5\mu\text{m}$ design rules for the HAWAII-1, and those arrays do not show evidence for burst noise. However, the foundry was changed at the same time as the switch to $0.25\mu\text{m}$ design rules. Therefore,

the processes employed by the specific foundry used by Rockwell Scientific may also contribute to the existence of burst noise in the above multiplexers.

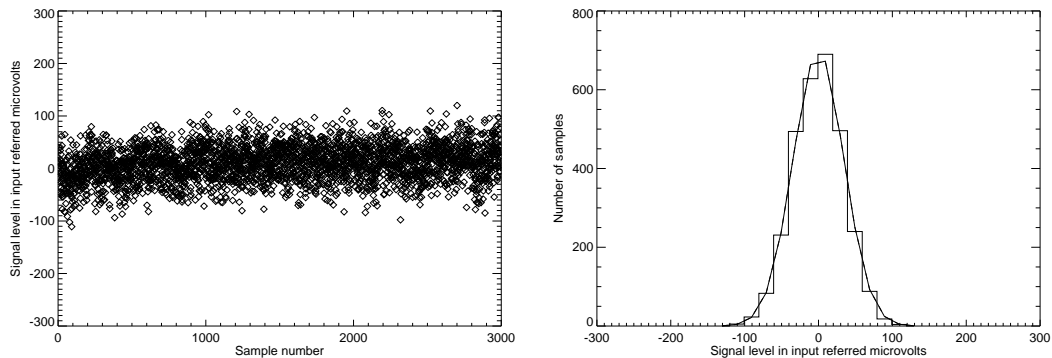
Several authors have reported observing burst noise in small dimension MOSFETs.^{49, 52–56} In these reports, authors concentrate almost exclusively on two-level burst noise (sometimes referred to as a bistable waveform), indicating a single mechanism for the majority of devices exhibiting the phenomenon. To further investigate burst noise, on the assumption that the source follower unit cell FET was the origin, a testing method was devised to eliminate the HgCdTe diode contribution to the noise.

5.5.1 Testing for Burst Noise

To test for burst noise in the HAWAII-1RG multiplexer, the following procedure was used. First, the reset clock is always on, causing V_{reset} to be applied to every pixel during each read throughout the entire integration. Also, the bias across the detector is set to zero ($V_{reset} = 0$ and $V_{Dsub} = 0$). This eliminates the effects of the HgCdTe diode on the output (such as dark current). Other global voltage fluctuations are subtracted off with a single frame average of the reference pixels, leaving only the fluctuations due to the FETs within the unit cell.

The data are taken in SUTR mode, 3000 samples per integration, each sample two seconds apart (which is near the minimum frame read time at 100kHz operation). The integration is thus 6000 seconds long. Over the hour and 40 minutes of each integration, peculiar fluctuations are seen on some pixels, but not others. Samples of these fluctuations are shown in Section 5.5.2.

Integrations were obtained at three temperatures, 30K, 37K, and 77K. These data were reduced using an IDL (Interactive Data Language) program that I wrote to detect burst noise. For a pixel without burst noise, it is expected that the average signal level (with respect to the global signal level) does not change over the entire integration. This is in fact what well behaved pixels show. Figure 5.15 shows the signal as a function of sample number and the corresponding histogram for a pixel that does not have burst noise. This figure and all following figures are for data taken at 30K, although similar

Figure 5.15. Signal vs. sample number and corresponding histogram for a pixel without burst noise.

figures can be found for each of the temperatures at which data were taken. The signal is shown in input referred microvolts, and the peak of the Gaussian distribution is centered at zero. (The average value of the dominant level is subtracted from the data to place its peak at zero.)

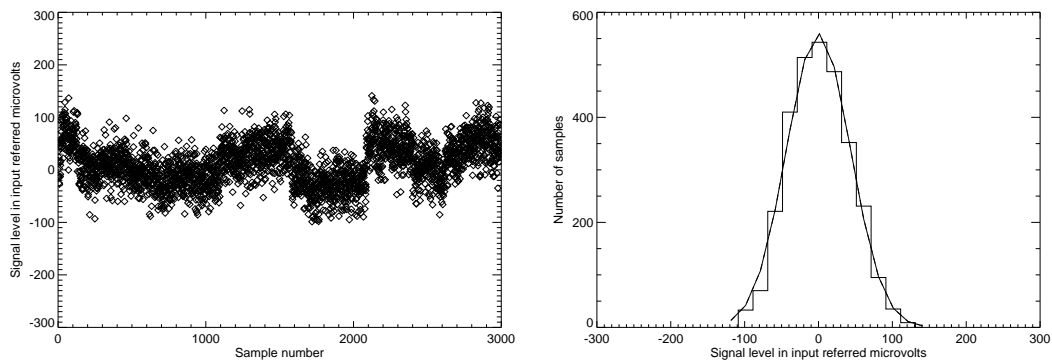
In a pixel with burst noise, the average signal level over one period of time during the integration may not be the same as that over another, leading to the appearance of multiple levels. To detect these various levels, a histogram is plotted, indicating number of samples vs. signal level. A pixel without burst noise displays a single Gaussian around a single signal level as shown on the right of Figure 5.15. On the other hand, a pixel with burst noise displays multiple Gaussians, each around a different signal level. The detection of more than one Gaussian in a single histogram indicates a pixel that exhibits burst noise.

The minimum distinguishable separation between Gaussians determines the detectability of burst noise (by this algorithm) in pixels, where parts of the multiple Gaussians overlap. To determine this separation, we used a modified version of the Rayleigh criterion for multiple Gaussians with varying sizes. In short, in order to distinguish between two Gaussians, the sum of the two individual Gaussians had to at least form a saddle point between them. If more than one Gaussian was fit concurrently, they were required to have the same standard deviation, since the noise around a given

level represents the total pixel noise in the absence of burst noise (see the discussion of read noise in Section 5.4).

The characteristic time for a given level may also affect its detectability. If the levels overlap and a pixel spends equal time in each level, then the resultant histogram may indicate a single Gaussian. Therefore, the burst noise detectability of a pixel depends on its total noise excluding burst noise in addition to the time spent in each level. Figure 5.16 shows a pixel with two very close levels which overlap. These close, nearly equally occupied levels result in a single Gaussian which makes the burst noise in this pixel undetectable by our algorithm. Even so, the width of the Gaussian in this histogram is slightly larger than that of Figure 5.15, indicating more noise.

Figure 5.16. Signal vs. sample number and corresponding histogram for a pixel exhibiting two level burst noise below the threshold of detectability in our algorithm.



5.5.2 Temporal Dependence of Signal Level

For pixels whose mean signal level changes with respect to time indicating burst noise, there are many variations in observed temporal behavior. Considering the various degrees of stability of the levels between transitions leads to a quantification of the observed behavior. The degree of stability is defined by the total time the pixel output remains in the same level before transitioning to another level. These levels can be stable (S), on average 1000 seconds or more, unstable (U), 10 seconds or less, or metastable (M),

i.e. somewhere in-between stable and unstable. For some pixels, the transitions happen so frequently, that it is unclear whether the pixel is actually remaining in the level in which it is measured, or whether the pixel level is merely undersampled, yielding an approximation of a much faster behavior. These levels will be considered unstable, reserving the term metastable for levels in which a pixel clearly remains for a period of time.

Because the minimum frame time for reading out 512^2 pixels on the HAWAII-1RG multiplexer with 100kHz operation is on the order of two seconds, burst noise transitions that happen more frequently than two seconds will be undersampled. The subjective determination of burst noise variation outlined below is constrained by the minimum frame time of two seconds. To determine oversampled levels with this constraint, a level must remain occupied for at least 10 seconds (5 samples) each time it is accessed. Therefore, levels occupied for less than this amount of time are undersampled and are therefore considered unstable in this analysis. If the entire array was read (1024^2 pixels), the minimum frame time would be eight seconds and the minimum level occupation time for a metastable state would have to be adjusted accordingly.

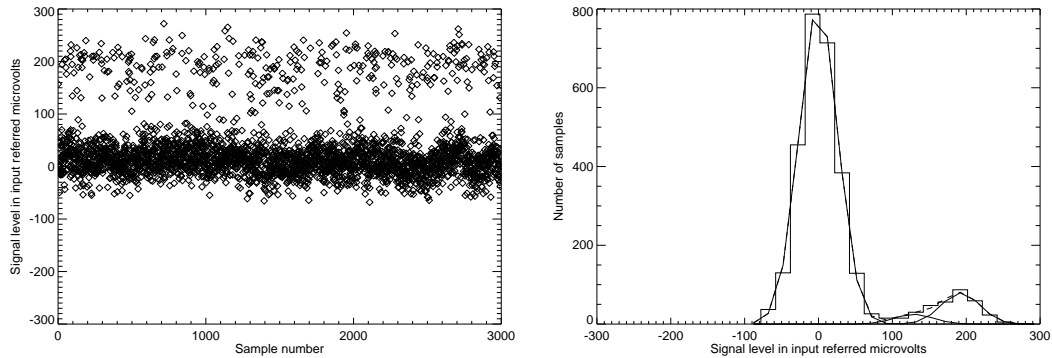
For two level burst noise, the most common case, the three degrees of stability (stable (S), metastable (M), and unstable (U)) make 6 unique variations. Table 5.9 details the possible variations. Each of these variations have been seen in HAWAII-1RG pixels, with some variations more common than others. In the figures that follow, the data for an individual pixel is plotted signal vs. time. Next to that graph is plotted the histogram analysis performed by our algorithm, where the Gaussian fits are overlaid with solid lines. A dashed line (most apparent between Gaussians) shows the sum of the Gaussians.

The U-U variation is apparent when the pixel exhibits any level at any time. This variation can come about from undersampling as described above, and is the most common variation. One such pixel exhibiting this variation with two levels is shown in Figure 5.17. This particular pixel shows a preference for the lower level. Other pixels may show a preference for the upper level or may spend equal time in both levels.

Table 5.9. Variations of dual level burst noise.

Variation	Level 1	Level 2
S-S	Stable	Stable
S-M	Stable	Metastable
S-U	Stable	Unstable
M-M	Metastable	Metastable
M-U	Metastable	Unstable
U-U	Unstable	Unstable

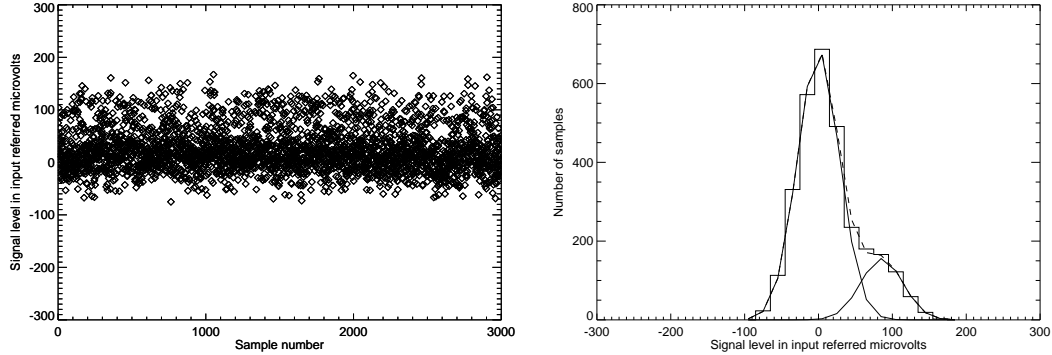
Notice that this pixel also has the preferred level centered at $0\mu V$ with approximately the same spread as Figure 5.15, but also has another distinct level where a Gaussian forms centered at $\sim 200\mu V$, leading to a ‘peak to peak’ separation of $\sim 200\mu V$.

Figure 5.17. Signal vs. sample number and corresponding histogram for a pixel exhibiting U-U burst noise.

As the ‘peak to peak’ separation between neighboring Gaussians is decreased, it becomes harder to distinguish the burst noise with the eye, because the pixel merely appears noisier than usual. However, when the Gaussian fits are performed on the data, it becomes clear that the data are representative of more than one signal level relatively close together. One example of this proximity is shown in Figure 5.18. Here the ‘peak to peak’ separation is less than $100\mu V$.

When the frequency of transitioning to the secondary level decreases, the burst noise variation moves from U-U to M-U, and eventually to S-U. In the same manner, the num-

Figure 5.18. Signal vs. sample number and corresponding histogram for a pixel exhibiting U-U burst noise with levels relatively close together.



ber of data points from a pixel in the secondary level decreases, making it increasingly more difficult to detect the secondary level when they are very close together. In addition, even levels greater than 4σ apart can be difficult to detect when the unstable level has only a few data points, since more than one data point in a $20\mu\text{V}$ bin is required for a detection. Therefore, many pixels with close levels or very infrequent transitions that have M-U and S-U remain undetected by our burst noise detection algorithm.

Two pixels, exhibiting M-U and S-U respectively with larger, easily detectable transitions are shown in Figures 5.19 and 5.20. Figure 5.19 does not show a clear second level. However, in this case, more than one transition to approximately the same level enables burst noise detection. The samples that are not at the dominant average signal level may be mid-transition, or this may indicate multiple unstable levels. In addition, the wider Gaussian on the dominant signal level in Figure 5.19 could indicate burst noise on an undetectable level, similar to the detectable burst noise in the dominant signal level of Figure 5.20.

Although one or more unstable levels is by far the most common variation of burst noise that has been detected in the HAWAII-1RG pixels, there are definitely cases where each level is at least metastable. This leaves the last three variations, M-M, S-M, and S-S. Although they appear to be the least common, they are the variations that traditional

Figure 5.19. Signal vs. sample number and corresponding histogram for a pixel exhibiting M-U burst noise with a larger scale and indistinct secondary level(s).

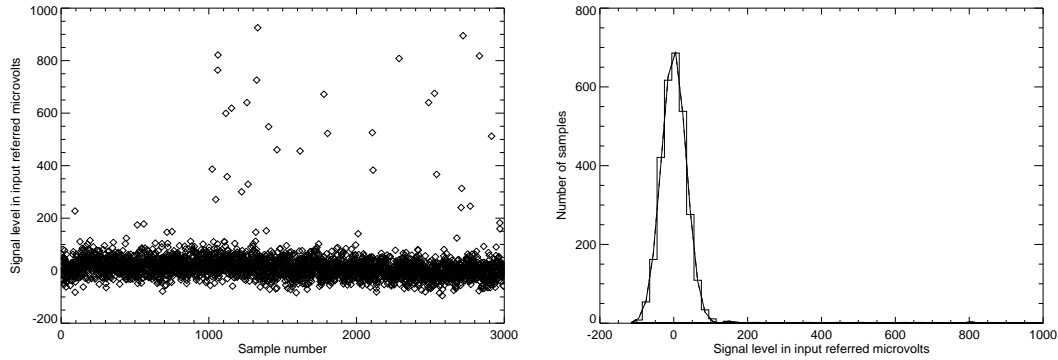
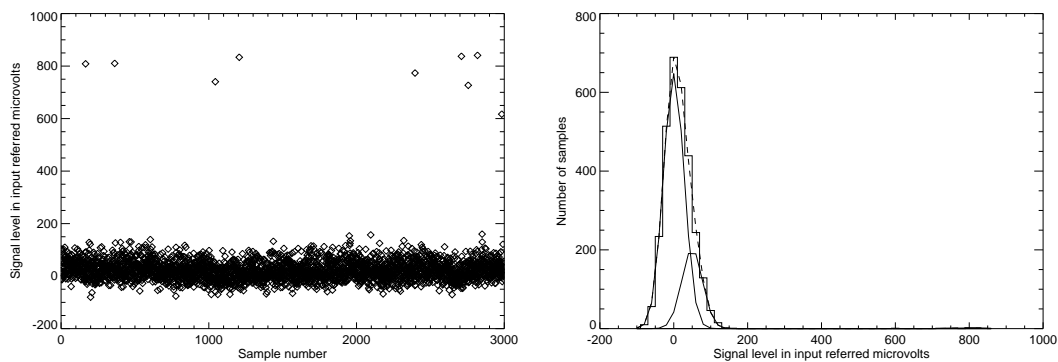


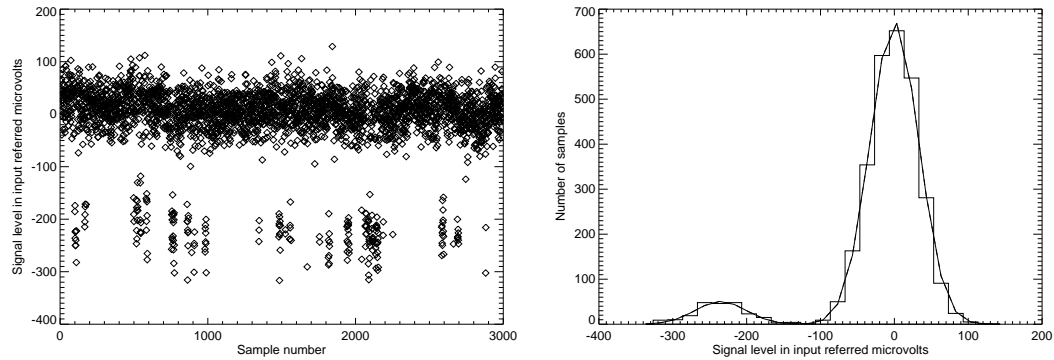
Figure 5.20. Signal vs. sample number and corresponding histogram for a pixel exhibiting S-U burst noise with a larger scale and detectable secondary level very close to the dominant signal level.



burst noise detection algorithms detect.⁷¹ Similar to the U-U variation, a pixel can show a preference for one level over the other, or have no preferred level. One example of the M-M variation is shown in Figure 5.21. (Figure 5.16 also shows the M-M variation, but is not above the threshold of detectability by the Rayleigh criterion in our algorithm.) In Figure 5.21, one of the metastable states is much less preferred than the other, but it still exhibits the less preferred state for a significant amount of time before returning to the dominant state. The S-M variation can be seen in Figures 5.22 and 5.23.

On a much slower timescale we have the least common of all variations, the S-S varia-

Figure 5.21. Signal vs. sample number and corresponding histogram for a pixel exhibiting M-M burst noise.



tion. Since these pixels can exhibit one transition in over an hour and a half integration, it is very likely that many of these pixels are overlooked in a single integration. In fact, Kandiah et al. (1989) reports observing transitions with a characteristic time spent in a single level of 20 hours. Two examples of this variation are shown in Figures 5.24 and 5.25.

In less common circumstances (less than twenty percent of pixels identified with burst noise), a pixel may be detected with more than one additional level or many indistinguishable levels. Some examples of this are shown in Figures 5.26, 5.27, 5.28, and 5.29 as well as Figures 5.19 and 5.20.

Figure 5.22. Signal vs. sample number and corresponding histogram for a pixel exhibiting S-M burst noise.

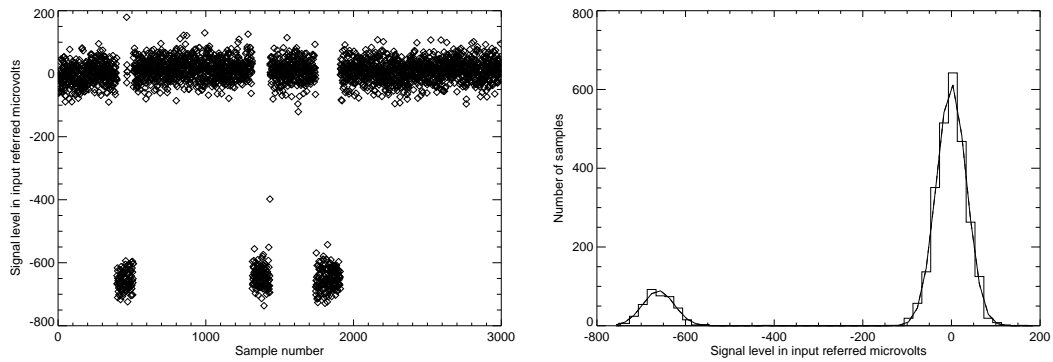


Figure 5.23. Signal vs. sample number and corresponding histogram for a pixel exhibiting S-M burst noise.

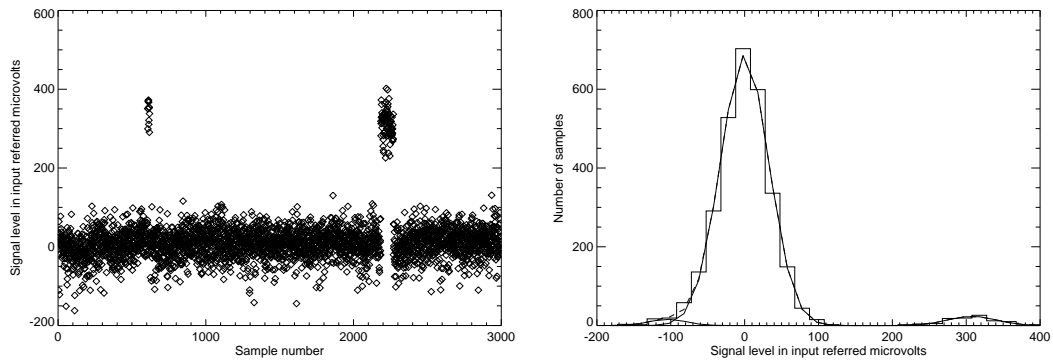


Figure 5.24. Signal vs. sample number and corresponding histogram for a pixel exhibiting S-S burst noise. The dashed line shows the sum of the Gaussians.

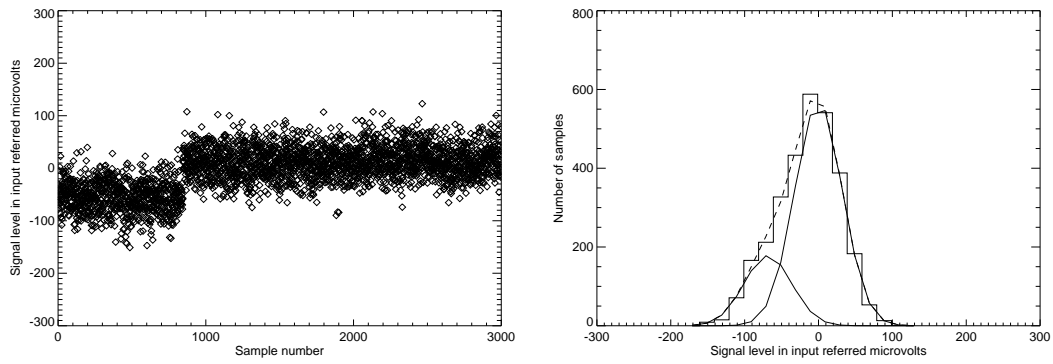


Figure 5.25. Signal vs. sample number and corresponding histogram for a pixel exhibiting S-S burst noise.

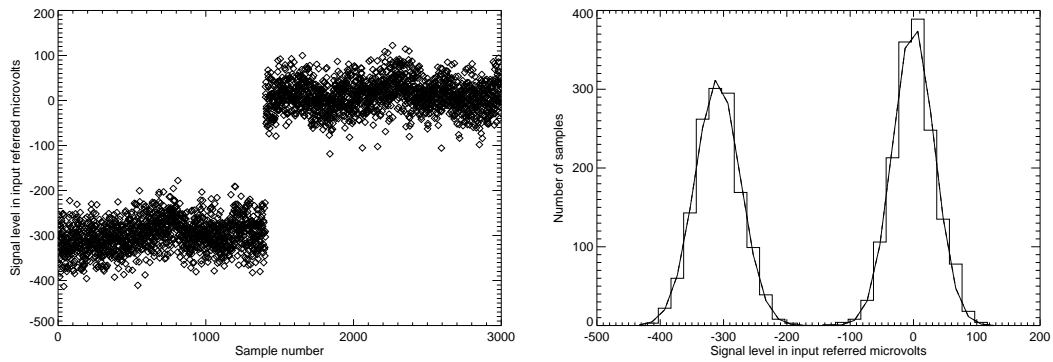


Figure 5.26. Signal vs. sample number and corresponding histogram for a pixel exhibiting multiple level burst noise with S-S superimposed upon U-U. The dashed line shows the sum of the Gaussians.

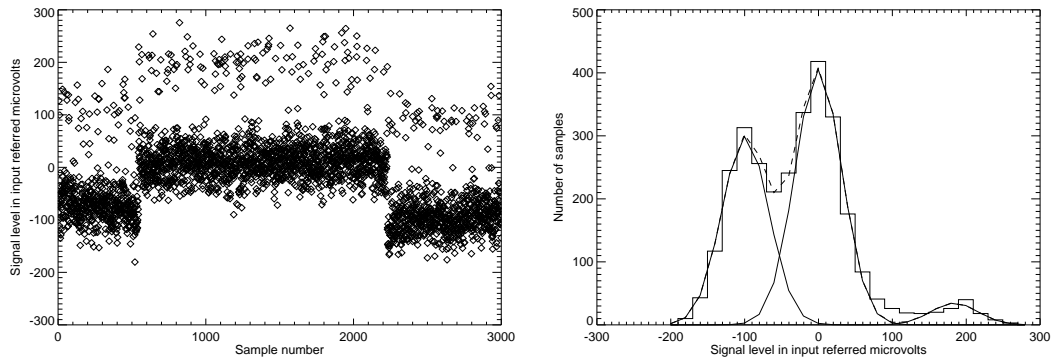


Figure 5.27. Signal vs. sample number and corresponding histogram for a pixel exhibiting multiple level burst noise with two defined levels and potentially many undefined levels in-between.

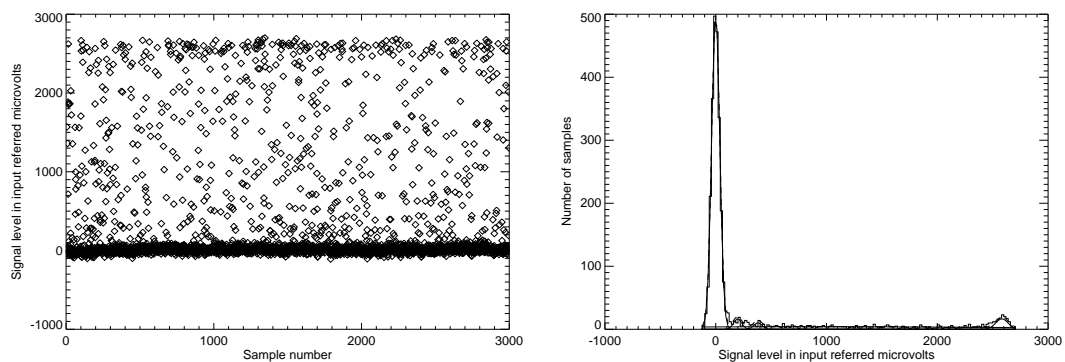


Figure 5.28. Signal vs. sample number and corresponding histogram for a pixel exhibiting multiple level burst noise with upper and lower secondary levels.

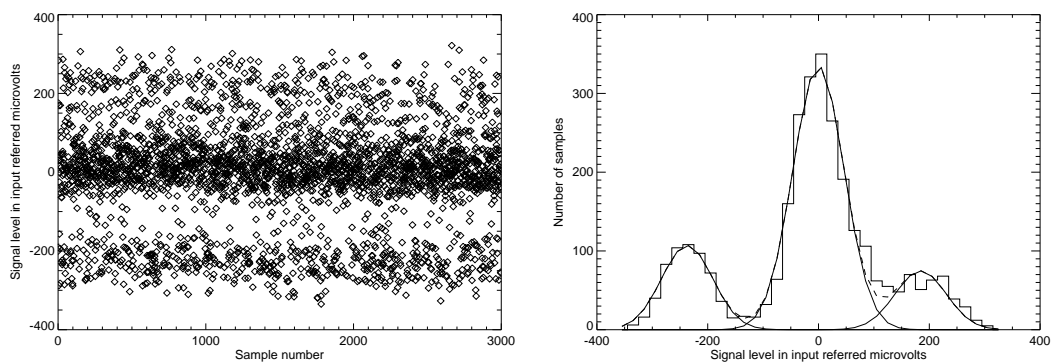
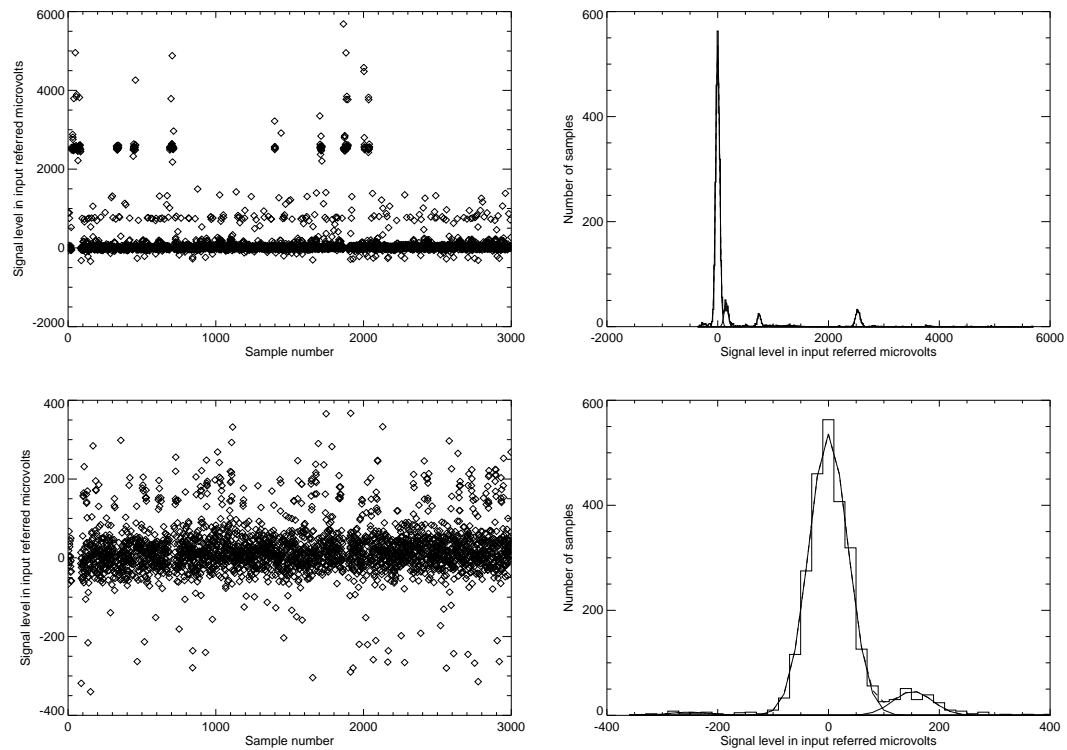


Figure 5.29. Signal vs. sample number and corresponding histogram for a pixel exhibiting multiple level burst noise. The dashed line shows the sum of the Gaussians. The top two figures are scaled to show the entire range of transition. The bottom two figures show the dominant level. There are many mechanisms involved which result in these various transitions.



5.5.3 Burst Noise vs. Temperature

All of the different variations seen in Section 5.5.2 contribute to the total percentage of pixels affected by burst noise. This percentage was measured as a function of temperature using the resolution criteria given in Section 5.5.1, and the largest detected ‘peak to peak’ transition for each temperature is given in Table 5.10. These percentages do not change if the electronics are on or off during cool-down, and similar percentages were found for pixels which were and were not connected to the HgCdTe material.

For 37K data, there are only 2000 samples used in data reduction because of a significant non-global drift that occurred in the first 1000 seconds which created false positives. Percentages computed using only the last 2000 samples are given for 30K and 77K for comparison. The reduction algorithm removes less significant drift exhibited by the 30K and 77K data.

Although the percentage of pixels exhibiting some form of detectable burst noise remains approximately the same for all three temperatures, the largest detected transition decreases with increasing temperature. In addition, the percentage of pixels identified with burst noise that exhibit three or more distinct levels decreases with increasing temperature. However, pixels that were detected with burst noise at one temperature were not the same as those detected at other temperatures, see Table 5.11. In fact, some pixels which exhibit one burst noise variation at 30K may exhibit a totally different variation or no detectable burst noise at all at 77K, leading to a larger percentage of pixels containing burst noise mechanisms than are being detected at any one temperature. However, when tested more than once at the same temperature, pixels will consistently exhibit the same behavior.

The percentage of array pixels with detectable burst noise increases as the sensitivity of detection increases. This relation between the smallest transition size detectable and the percentage of array pixels detected with burst noise is shown in Figures 5.30 and 5.31.

Table 5.10. Percentages of pixels exhibiting burst noise at various temperatures.

Temperature (K)	Number of samples used	Percentage of Pixels	Largest Transition
30	3000	13.4	10.6mV
30	2000	11.7	10.5mV
37	2000	11.1	7.7mV
77	3000	15.2	2.5mV
77	2000	13.5	2.5mV

Table 5.11. Percentages of pixels exhibiting burst noise with respect to temperature.

Condition	Number of Pixels	Percentage
All three temperatures	5372	2.0%
Any two temperatures	29371	11.2%
Any single temperature	74654	28.5%

Figure 5.30. Percentage of array pixels detected vs. smallest transition size detectable.

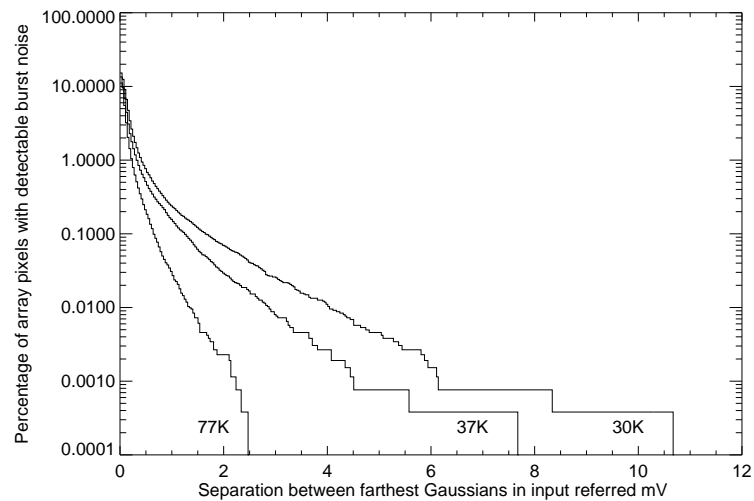
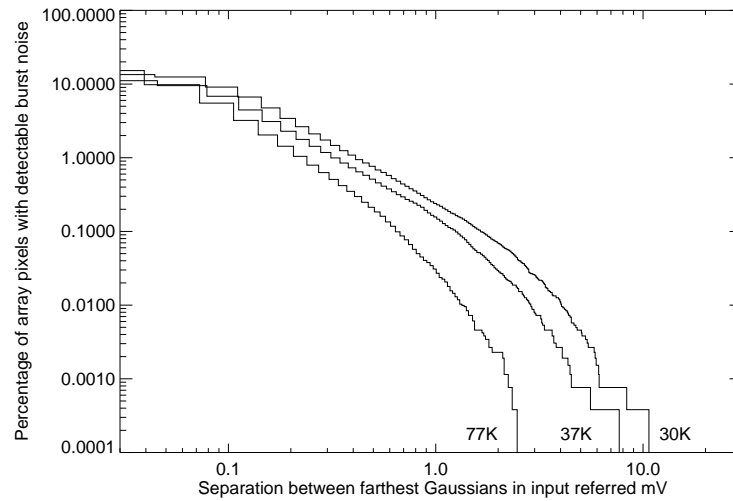
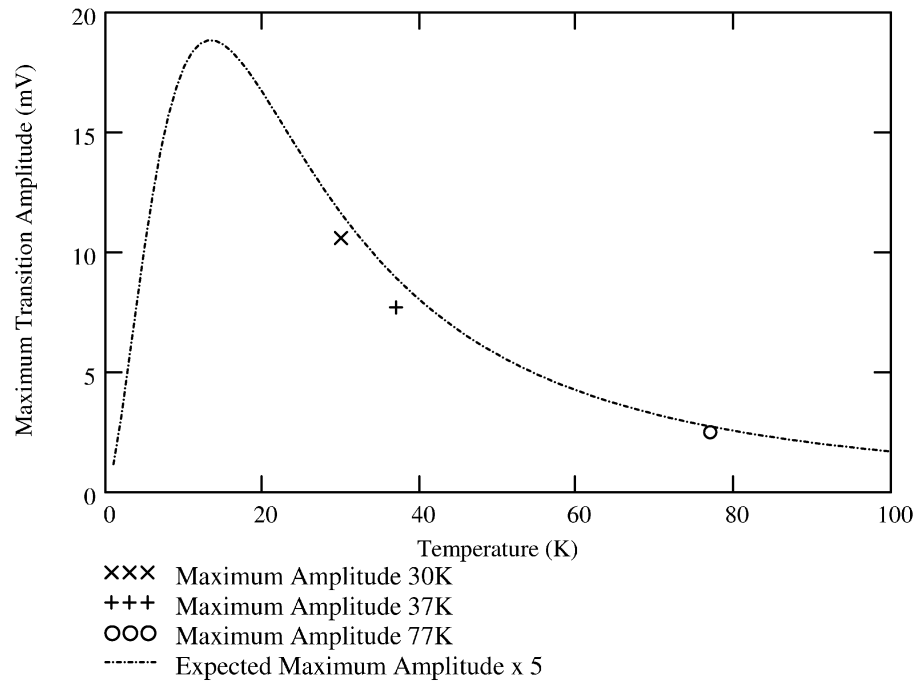


Figure 5.31. Percentage of array pixels detected vs. smallest transition size detectable on a log-log scale.



For the experimental situation described, we find that between 11 and 15% of pixels exhibit burst noise at a single focal plane temperature between 77K and 30K. This percentage is a lower limit set by the limitations of our burst noise detection algorithm. The largest transition for detector -001 at each temperature as laid out in Table 5.10 is plotted vs. temperature in Figure 5.32. In order to fit the data, it was necessary to multiply the theoretical curve (Equation 2.41) by five. The theoretical curve employed reasonable values for the MOSFET gate dimensions and other parameters, but the charge in the channel contribution, Q in Equation 2.43, was decreased by a factor of two to obtain the proper shape.

Figure 5.32. Maximum burst noise transition amplitude vs. temperature.



Although the predicted amplitude was a factor of five lower than observed, the shape of the curve at the high temperature side of the maximum is in good agreement with the three data points. The difference between observed and theoretical magnitudes could be due to any of the possibilities discussed in Section 2.2.6. The shape of this curve

determines the behavior of the trapping center at the origin of the observed burst noise. As discussed in Section 2.2.6, two ways in which the trapped charge carrier affects the conductivity in the silicon channel are by becoming a Coulombic scattering center and modifying the local surface potential. The temperature dependence of the trapping length determines the shape of a plot of $\frac{\Delta R}{R}$, as in equation 2.41.

The trapping length of scattering and local surface potential modification is proportional to $1/T$ and T respectively (see Equations 2.42 and 2.43). Through comparison of Figure 5.32 to these dependences, it was determined that the change in conductivity for the greatest magnitude transitions was dominated by scattering. At temperatures lower than 15K, the voltage fluctuation is dominated by a modification of the local surface potential caused by the trapping center.

Varying the temperature not only changes the amplitude of the maximum transition observed amongst all pixels in the array, it also changes the time between and magnitude of individual pixel transitions. It was observed that approximately 60% of pixels that exhibit detectable burst noise at 30K also exhibit detectable burst noise at 37K. From 30K to 37K it was found that often the characteristic time to transition out of each of the two levels changed in opposing manners and the majority of pixels had a change in level dominance as illustrated in Figure 5.33. The plotting procedure centers the dominant level at zero. Although the dominance moves to the lower level in Figure 5.33 as the temperature is increased, it is just as common to see a dominance shift to the upper level. About half of the examined traps had an observable change in magnitude between the two temperatures, and of those that changed, the majority had a magnitude that increased with increasing temperature as illustrated in Figure 5.34, indicating the trapping center acted to shift the local surface potential rather than behaving as a scattering center (see Section 2.2.6). This is in contrast to the observation that the maximum amplitude transition decreases with increasing temperature. The difference may mean that the maximum amplitude transitions are dominated by scattering centers and the majority of other transitions are related to a change in local surface potential. In many of the pixels exhibiting burst noise at both temperatures, an additional level was

Figure 5.33. Signal vs. sample number at 30K (left) and 37K (right) for a pixel exhibiting burst noise at both temperatures with a level dominance change.

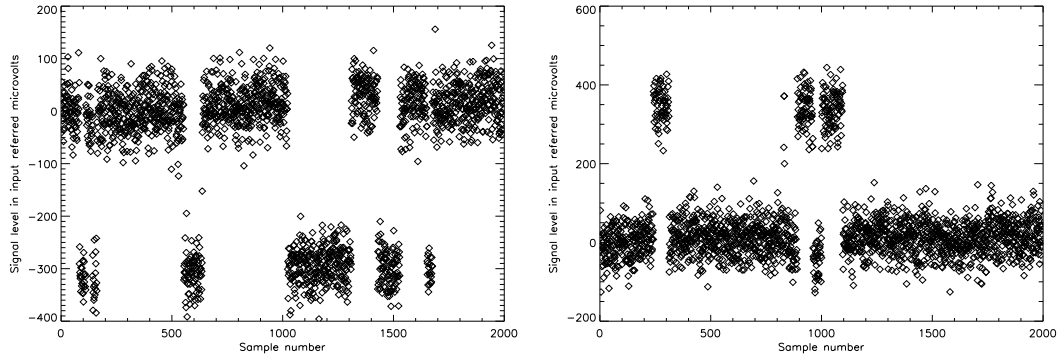
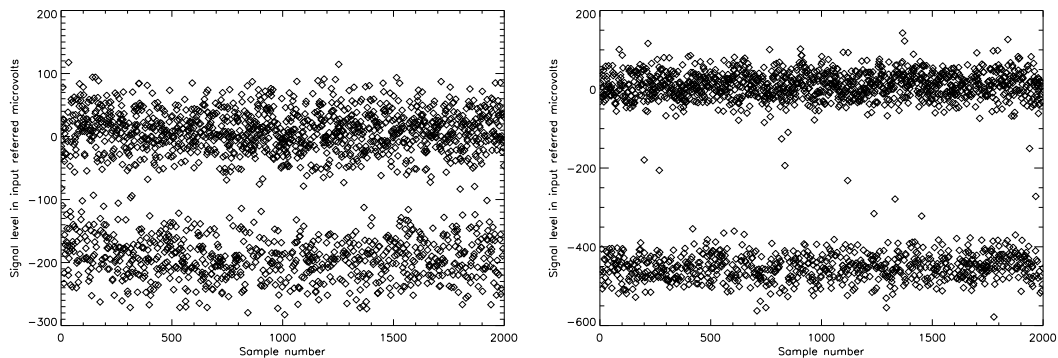


Figure 5.34. Signal vs. sample number at 30K (left) and 37K (right) for a pixel exhibiting burst noise at both temperatures with a magnitude shift.

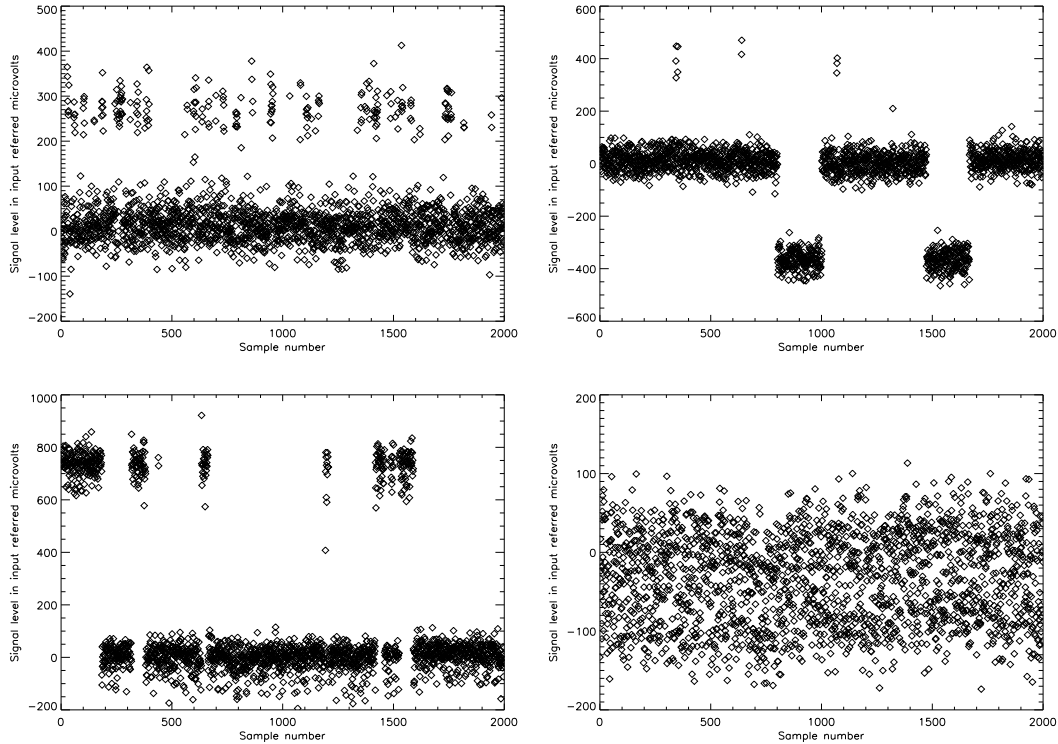


observed at one of the two temperatures that was unobserved at the other temperature, such as that in Figure 5.35.

As one can see, the graphs on top in Figure 5.35 indicate an additional level in the 37K data whereas the graphs on the bottom indicate an additional level in the 30K data. The additional levels indicate a trap that is accessible at one temperature but not the other. An additional level can occur at 37K because the thermal energy at 30K is not sufficient for a charge carrier to populate the trap.

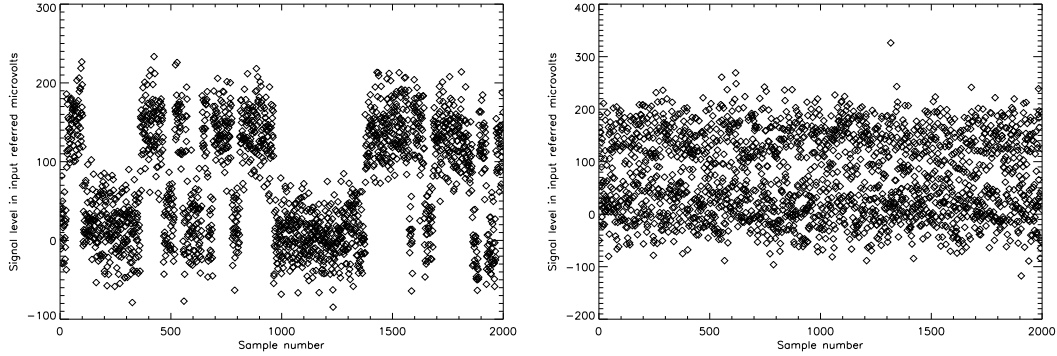
The shift in characteristic transition time between the two temperatures was diffi-

Figure 5.35. Signal vs. sample number at 30K (left) and 37K (right) for two pixels (top and bottom) exhibiting burst noise at both temperatures.



cult to discern for the majority of pixels because at 30K the most commonly observed variation of burst noise is that of unstable levels, where the levels are undersampled (see beginning of Section 5.5.2). When comparing the characteristic transition time of 30K and 37K data for pixels that exhibit burst noise at both temperatures, it was found that the variation with unstable levels at 30K also exhibited variations with unstable levels at 37K. This indicates that both temperatures are undersampled with two seconds per sample temporal resolution. Therefore, the only discernable difference between the two is the change in dominance between the levels and magnitude of transitions (if any). Those pixels that do have longer characteristic times can follow the expected trend of decreasing characteristic times with increasing temperature. An example of one such pixel is shown in Figure 5.36. As illustrated in Figure 5.33, it is clear that not all pixels

Figure 5.36. Signal vs. sample number at 30K (left) and 37K (right) for a pixel exhibiting burst noise at both temperatures.



follow that trend.

In order to verify the expected behavior for undersampled pixels, it is necessary to use a much finer temporal resolution than two seconds. For this, continuous sampling of an individual pixel is necessary and will be done in future work. This combined with data at more closely spaced temperatures may provide a basis for a good understanding of burst noise characteristics exhibited by the HAWAII-1RG and -2RG multiplexers.

5.5.4 Burst Noise vs. Source to Drain Current

Another set of tests that would benefit future work in this area is finding the dependence of the characteristic transition time and amplitude of the burst noise displayed by a single pixel on the source to drain current through the FET, and on the FET gate voltage. Comparing such results to those of other authors^{49,56} and discerning how trap characteristics correspond to observed behaviors may provide information which, when fed back to Rockwell Scientific, could lead to elimination of the problem through improved processing. To that end, we have conducted preliminary tests on detector H1RG-16-003 for burst noise while varying the gate voltage and the current flowing through the unit cell source follower FET.

Changing the source to drain current, I_{sd} , noticeably affects burst noise charac-

teristics. Increasing I_{sd} increases the characteristic trapping time t_c for electrons (see Section 2.2.6) and decreases t_c for holes. This reduces the time between subsequent transitions to the upper level and increases the time the pixel remains in that level as is expected by the dependence of t_c on I_{sd} discussed in Section 2.2.6. With enough current, the upper level becomes dominant. Increasing the current further can cause another trap to become accessible, introducing an even higher level into the transition characteristics. Lowering the current has the exact opposite effect by making the lower level dominant, reducing the time between subsequent transitions to the lower level and increasing the time the pixel remains in the lower level. Further lowering the current can introduce another previously unobserved lower level. In addition, varying the current may increase or decrease the amplitude of the transitions. A few representative pixels are shown in Figures 5.37 through 5.40.

Figure 5.37. Signal vs. sample number for various currents for a pixel subject to burst noise at 30K.

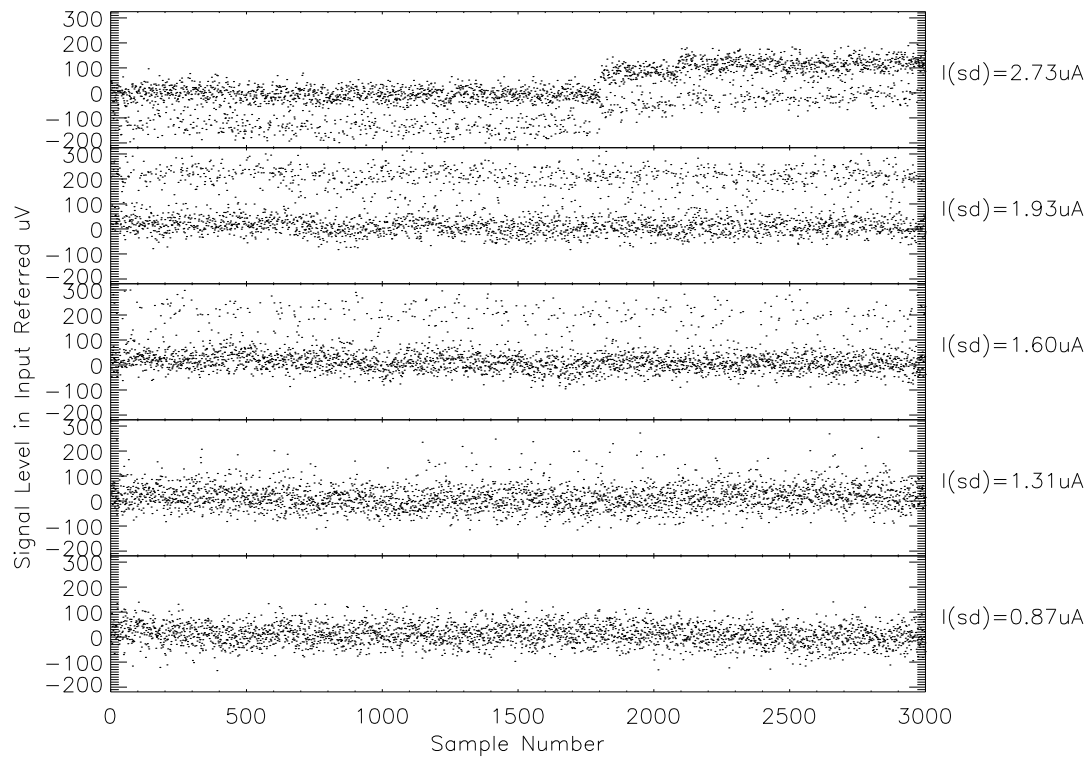
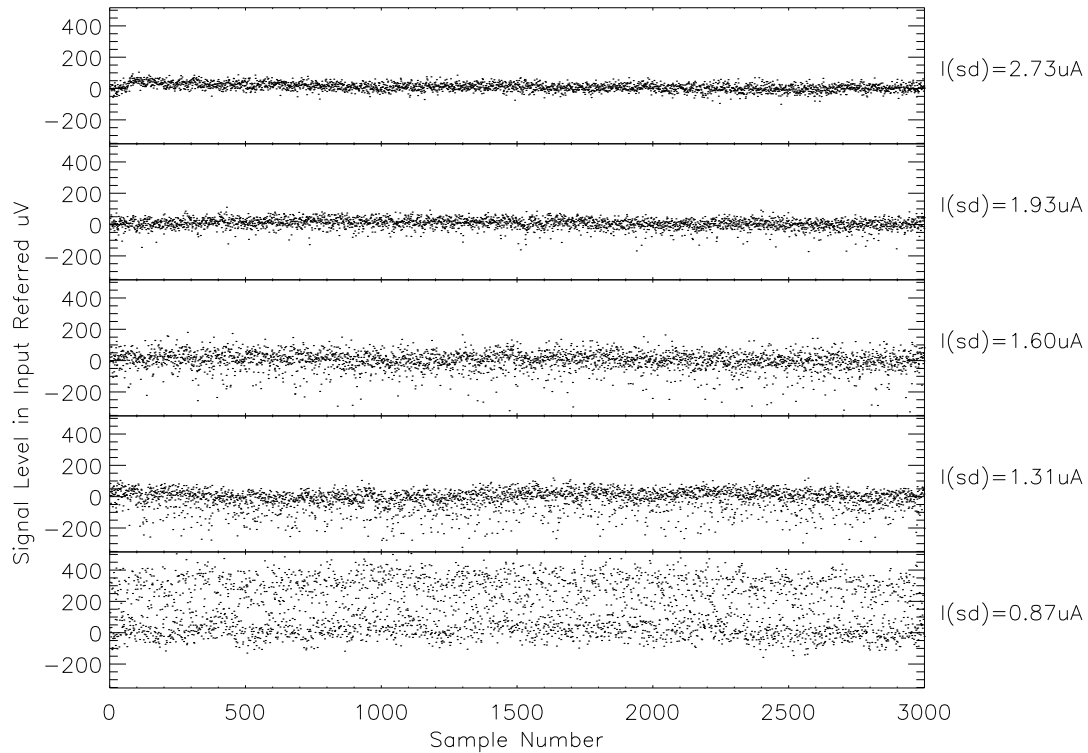
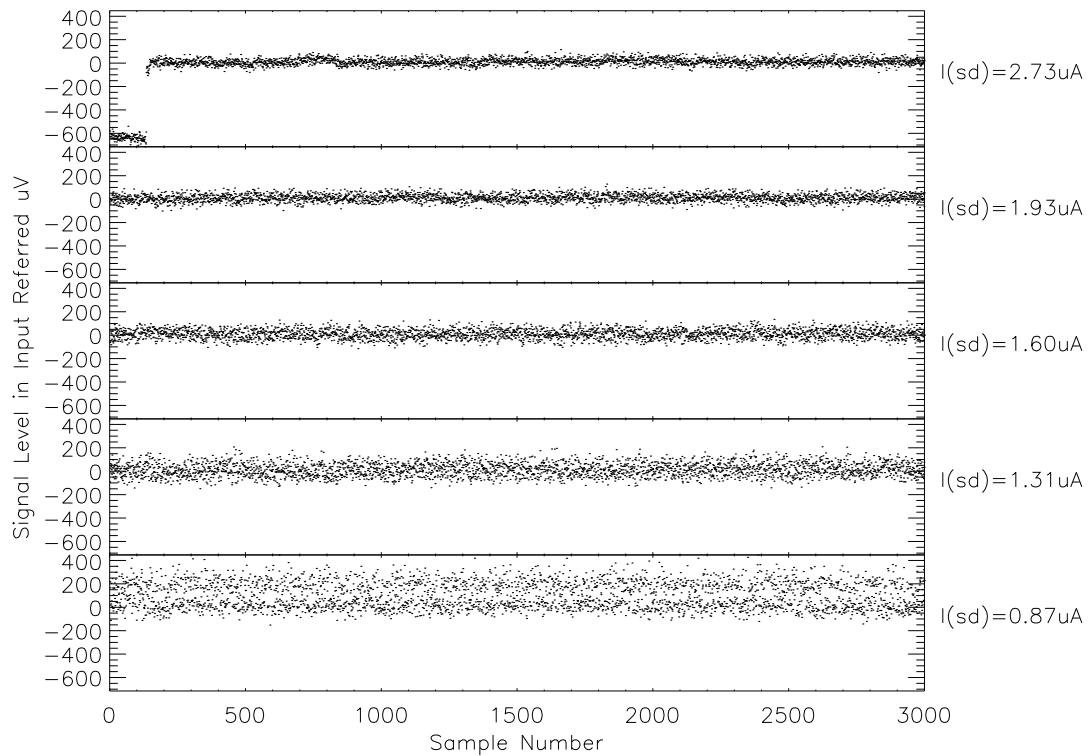


Figure 5.38. Signal vs. sample number for various currents for a pixel subject to burst noise at 30K.

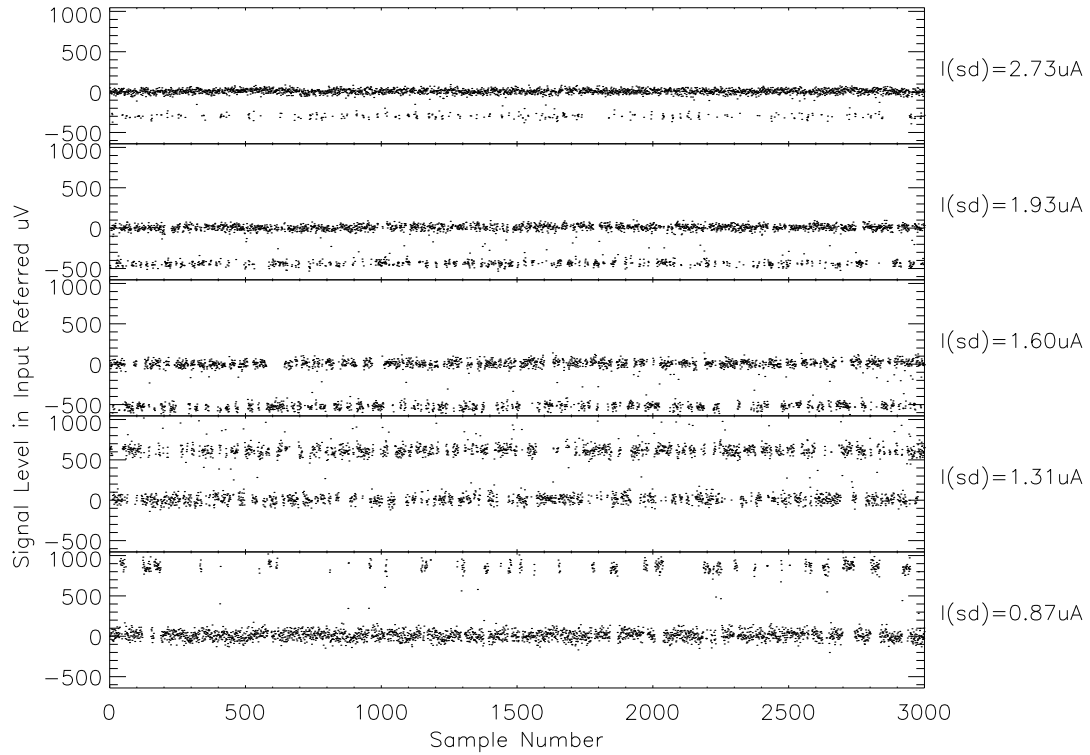
Figures 5.37 through 5.40 show pixels whose burst noise characteristics (characteristic transition time/amplitude) change with current. Notice that in all figures the level deemed by the program to be the dominant one is centered by the program at zero signal. Figure 5.37 shows a pixel that begins to populate an upper level as the current is increased from $0.87\mu A$ to $2.73\mu A$. Since the upper level indicates hole capture (lower conductivity), the probability of hole capture is increased as the current is increased and the probability of electron capture is decreased. We therefore observe a shift in signal level dominance to the upper level as the current is increased. For this pixel, the optimal operating current is the lowest one, since burst noise is undetectable at this current. A similar case, but with burst noise characteristics observable at the lower current levels and not at the upper current levels is shown in Figure 5.38.

Figure 5.39 shows the burst noise characteristics for a pixel which has detectable

Figure 5.39. Signal vs. sample number for various currents for a pixel subject to burst noise at 30K.

burst noise at the highest and lowest currents, but not in the middle. The top graph ($I_{sd} = 2.73\mu\text{A}$) has upper level dominance, but the graph directly underneath ($I_{sd} = 1.93\mu\text{A}$) shows no burst noise. Since throughout the other graphs we see that the level dominance shifts to the lower level as current decreases, it is likely that the graph for ($I_{sd} = 1.93\mu\text{A}$) is in the lower level of the two shown in the top graph ($I_{sd} = 2.73\mu\text{A}$). There is a significant difference in current between the upper two graphs in the figure, making it possible that the transition of dominance to the lower level happens in the intermediate currents (not shown). Both behaviors represented by Figures 5.37 and 5.38 are more common than that shown in Figure 5.39. To illustrate the effects, the percentage of pixels exhibiting detectable burst noise for various currents at 30K are shown in Table 5.12.⁵ The typical operating current (for $V_{bias_gate} = 2400\text{mV}$) is

⁵The percentage reported for $2.73\mu\text{A}$ current is a lower limit because there was some uncompensated

Figure 5.40. Signal vs. sample number for various currents for a pixel subject to burst noise at 30K.

1.60 μA at 30K. Notice that the percentage of pixels exhibiting burst noise is higher for currents higher and lower than the typical operating current.

Table 5.12. Percentages of pixels exhibiting burst noise with respect to source to drain current at 30K. (Gate voltage at $V_{reset} = 0\text{V}$.)

I_{sd}	Percentage
2.73 μA	> 14.3 %
1.93 μA	12.9 %
1.60 μA	13.1 %
1.31 μA	14.2 %
0.87 μA	19.8 %

drift within the first 1000 samples for some pixels in that data set. The percentage is quoted for the latter 2000 samples.

Lastly, Figure 5.40 represents a large population of burst noise pixels whose burst noise characteristics change from one current to another, but at no examined current does the burst noise disappear altogether. It is possible, however, that at higher and lower currents than those examined, the trap(s) indicated by the burst noise characteristics may become occupied or unoccupied on timescales as long as the 6000 seconds over which these samples were taken. There is no indication, however, that there will not be another accessible trap at a higher or lower energy that will be ‘turned on’ by increasing or decreasing the current respectively.

Even if one could increase the current enough to make the upper level solely occupied, this will increase the power dissipation of the readout integrated circuit. Since infrared space telescopes operate at low temperatures, their power dissipation requirements are very strict. Specifically, passively cooled space telescopes rely on very low power dissipation in order to achieve and maintain temperatures as low as 30K. On the other hand, decreasing the current so that the lower level is solely occupied (if it were possible) is impractical. Output voltage rise time is dependent upon source follower current and lowering the current causes the rise time to increase. This is undesirable. If the current gets too low, the source follower unit cell FET can turn off, which would cause the multiplexer to become inoperable.

5.5.5 Burst Noise vs. Gate Voltage

Preliminary experiments on the HAWAII-1RG multiplexer have shown most pixels exhibit little to no discernable change in burst noise characteristics when the gate voltage is varied. This indicates that the majority of traps contributing to burst noise are located within the oxide (see Section 2.2.6). A notable difference between these experiments and those conducted by other authors, i.e. Uren⁷² et al. (1985), is that the MOSFET under investigation in the unit cell is being operated as a source follower and therefore has an external current source. When other authors report a change in characteristics with gate voltage,⁵⁵ current is not kept constant. The change in characteristics they observe may therefore be a result of this changing current, similar to the changes discussed in

Section 5.5.4.

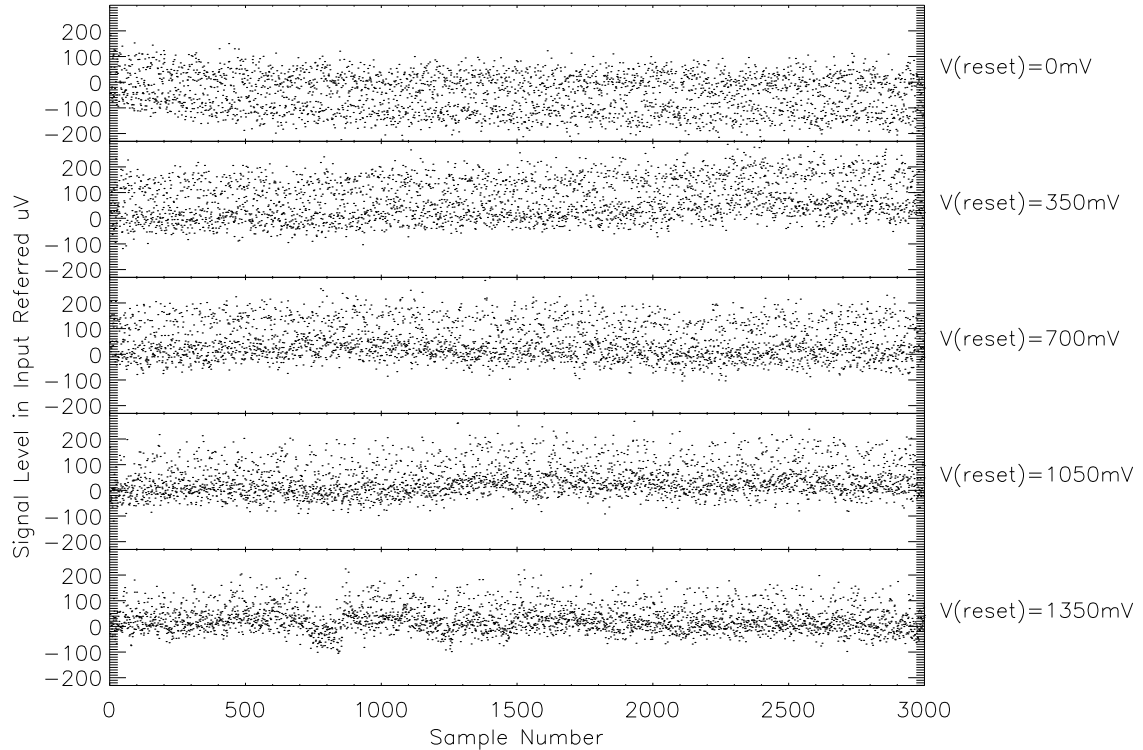
The voltages applied to V_{reset} (the unit cell source follower MOSFET gate voltage⁶) for burst noise analysis are within and span the entire operable range. At $V_{reset} < 0\text{mV}$ or $V_{reset} > 1350\text{mV}$, the device reaches the lower and upper limit respectively of the source follower output amplifiers as discussed in Section 3.2.5. Therefore, the burst noise variations observed from 0mV to 1350mV are the variations that would be observed during normal operation of the device. Over a change in V_{reset} from 0V to 1.35V , the current supplied by the external current source decreases by $0.05\mu\text{A}$ through each enabled source follower unit cell MOSFET. This is a small amount as compared to the current change illustrated in Section 5.5.4 and would cause a slight shift in preference to the lower level. One such pixel is illustrated in Figure 5.41.

A shift towards the lower level for increasing gate voltage can be seen in Figure 5.41. The current at $V_{reset} = 0\text{V}$ and $V_{reset} = 1.35\text{V}$ is $I_{sd} = 1.60\mu\text{A}$ and $I_{sd} = 1.55\mu\text{A}$ respectively. This particular source follower MOSFET changes characteristics rapidly with current. Figure 5.42 shows the behavior of the same MOSFET at $V_{reset} = 0\text{V}$ as current is changed. Comparing Figure 5.42 to Figure 5.41 it can be seen that the range of characteristics observed over an increase from $V_{reset} = 0\text{V}$ to $V_{reset} = 1.35\text{V}$ correspond to a current change from $I_{sd} = 1.60\mu\text{A}$ to somewhere in-between $I_{sd} = 1.60\mu\text{A}$ and $I_{sd} = 1.31\mu\text{A}$. Since the expected current change over the given increase in voltage (from $I_{sd} = 1.60\mu\text{A}$ to $I_{sd} = 1.55\mu\text{A}$) falls within this range, it follows that this pixel is responding to the change in current. The majority of pixels exhibiting burst noise at 30K exhibit this behavior.

Other pixels that do not change characteristics as rapidly with current show a much smaller or no discernable change with gate voltage. One such example is shown in Figure 5.43. As can be seen in Figure 5.43, at no value of V_{reset} applied to the integrating node does burst noise become undetectable. Thus, for this pixel and the many others

⁶It is important to note that in this testing scheme, V_{reset} is always connected to the integrating node and therefore, the gate voltage and V_{reset} are one and the same. During normal operation of the device, the voltage on the integrating node at any point in time will be determined by the actual bias across the diode and the detector substrate voltage, V_{Dsub} as discussed in Section 3.2.4.

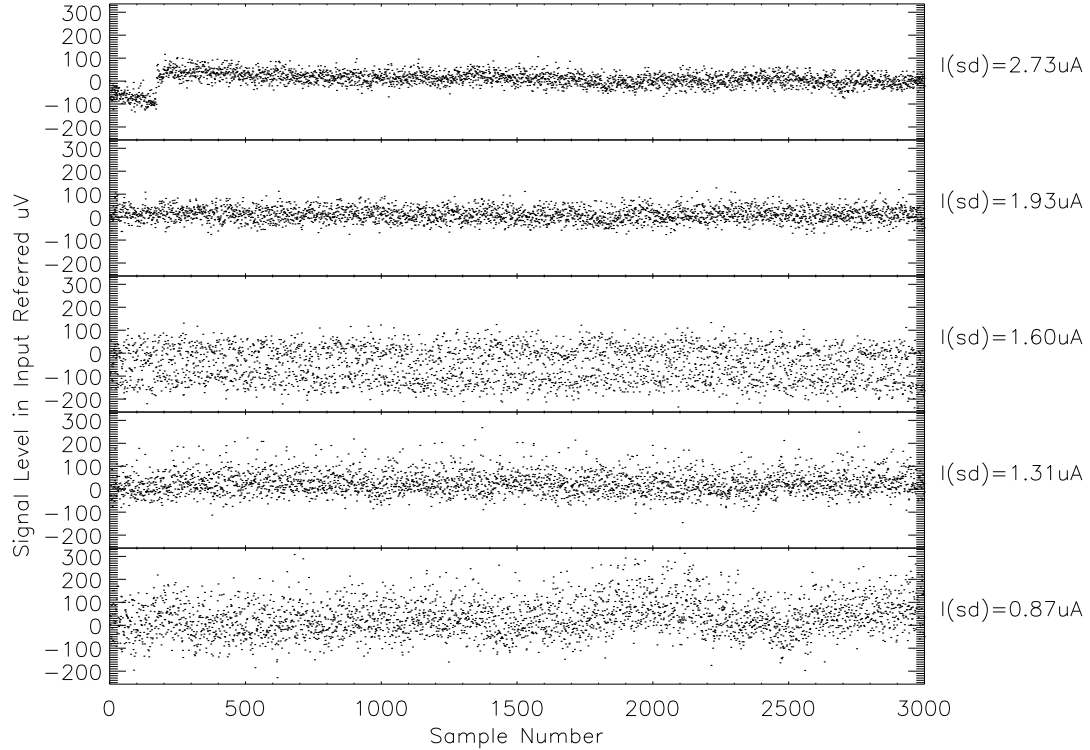
Figure 5.41. Signal vs. sample number for various gate voltages (V_{reset}) for a pixel subject to burst noise at 30K.



like it, burst noise characteristics can not be altered by a change in gate voltage. Pixels that exhibit a small (or no) change in characteristics with gate voltage are likely to have traps located in the oxide (see Section 2.2.6). The majority of these pixels do not exhibit burst noise at 77K, which points towards a much more localized energy distribution, possibly corresponding to an impurity or single trap.

Figure 5.44 illustrates signal vs. sample number for a pixel whose characteristics change with gate voltage more than the corresponding change in current would suggest. Comparison of Figure 5.44 to Figure 5.45 shows that this MOSFET's characteristics change in the opposite direction of a decrease in current. The notable features of Figure 5.44 are the undefined levels, decreasing amplitude with increasing voltage, and an apparent shift in dominance to the upper level. The majority of pixels with these

Figure 5.42. Signal vs. sample number for various source to drain currents (I_{sd}) of the pixel illustrated in Figure 5.41.

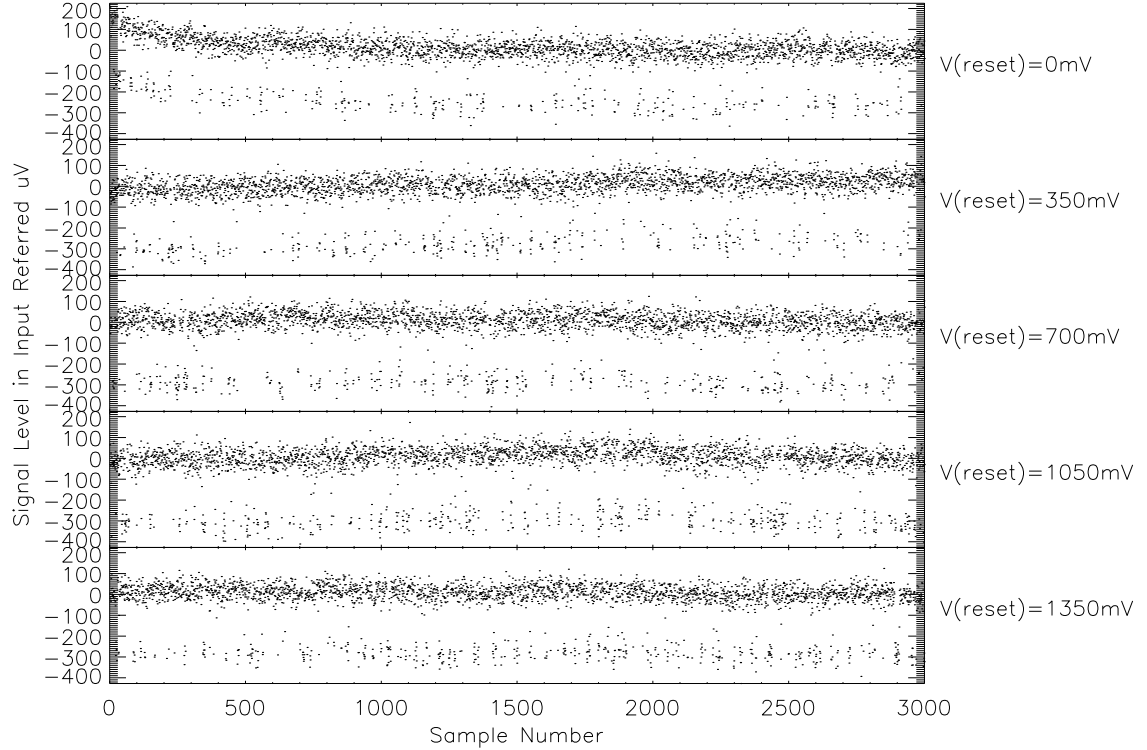


features exhibit burst noise at all three measured temperatures, 30K, 37K, and 77K and contain, on average, the highest magnitude transitions. These features indicate a different type of trap than the ones causing burst noise in Figures 5.41 and 5.43. In fact, as per the discussion in Section 2.2.6, they indicate dislocations or traps within the bulk silicon that are close enough to the channel to significantly affect channel conductivity at low biases and less at higher biases. Multi-electron trapping is possible in dislocations as there may be many trapping sites available within Angstroms from each other.

Shown in Table 5.13 is the percentage of pixels exhibiting burst noise in detector H1RG-16-003 at 30K with respect to gate voltage (V_{reset}).⁷ It can be seen that at the

⁷The percentage reported for 0mV is a lower limit because there was some uncompensated drift within the first 1000 samples for some pixels in that data set. The percentage is quoted for the latter 2000 samples.

Figure 5.43. Signal vs. sample number for various gate voltages (V_{reset}) for a pixel subject to burst noise at 30K.



higher reset voltages, the percentage of pixels exhibiting burst noise increases. This is due to the constraining of the current channel at the source of the MOSFET as it reaches the upper limit of its dynamic range. This could also indicate that a grouping of traps exist near the source of the MOSFET. The data for other analyses presented in this thesis were taken at $V_{reset} = 0\text{mV}$. Since the percentage indicated in Table 5.13 is a lower limit for $V_{reset} = 0\text{mV}$ and traps exhibiting burst noise with the characteristics of Figure 5.44 have their maximum amplitude at $V_{reset} = 0\text{mV}$, this indicates that the percentage of pixels exhibiting burst noise at $V_{reset} = 0\text{mV}$ is likely larger than $V_{reset} \sim 350\text{mV}$. Therefore, in order to have the smallest percentage of pixels exhibiting detectable burst noise, the detector should be operated with $V_{reset} \sim 350\text{mV}$ and $I_{sd} \sim 1.93\mu\text{A}$. This will by no means, however, eliminate the burst noise or make it insignificant.

Figure 5.44. Signal vs. sample number for various gate voltages (V_{reset}) for a pixel subject to burst noise at 30K.

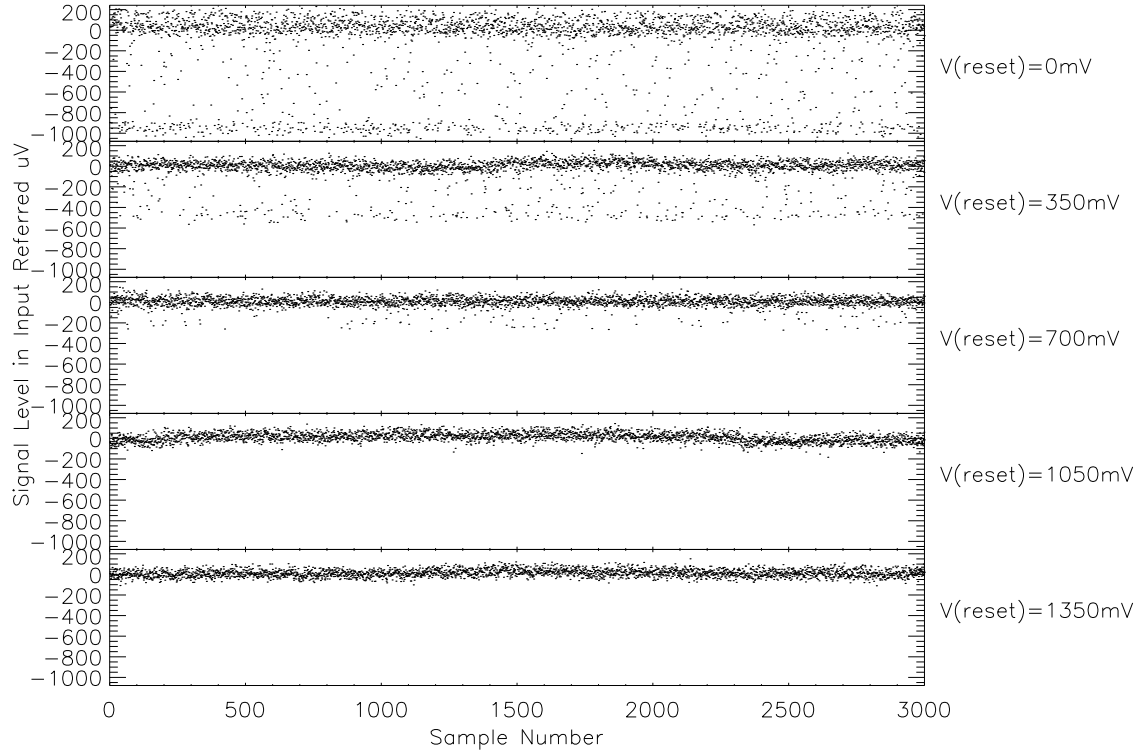


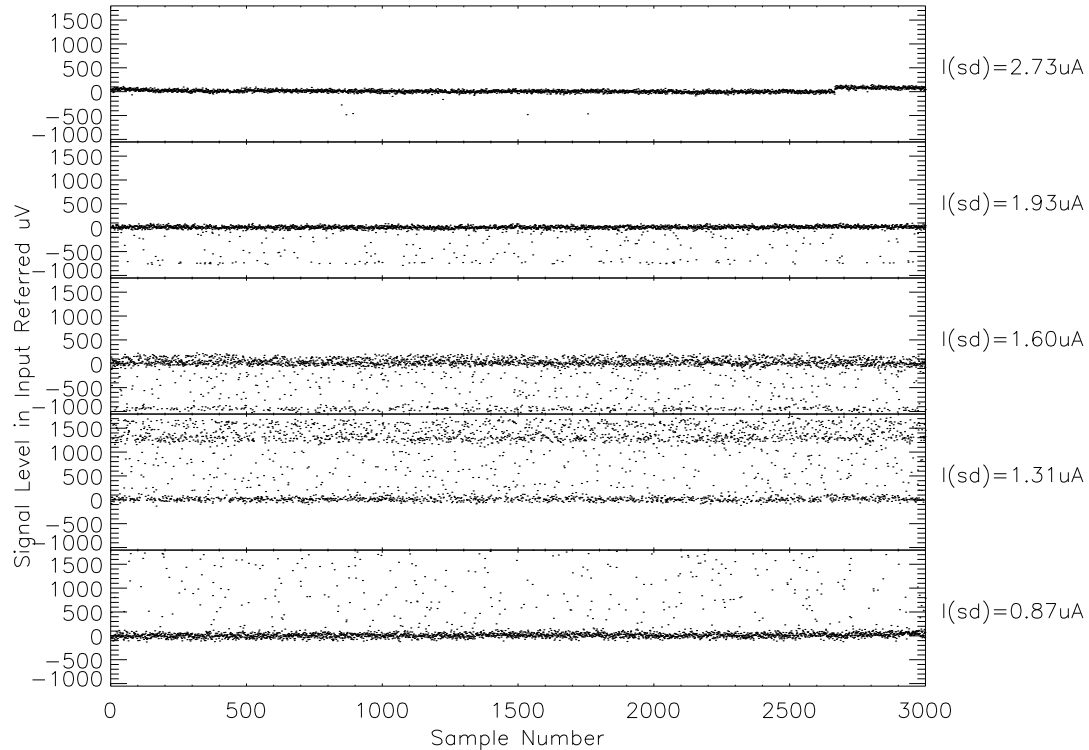
Table 5.13. Percentages of pixels exhibiting burst noise with respect to gate voltage (V_{reset}) at 30K. (The current at $V_{reset} = 0V$ and $V_{reset} = 1.35V$ is $I_{sd} = 1.60\mu A$ and $I_{sd} = 1.55\mu A$ respectively.)

V_{reset}	Percentage
0mV	> 12.8 %
350mV	14.1 %
700mV	14.6 %
1050mV	16.5 %
1350mV	29.2 %

5.5.6 Effect of Burst Noise on Future Space Programs

Unfortunately, at this time there does not appear to be a way to fully compensate for burst noise in the present HAWAII-1RG muxes by varying mux operating parameters once burst noise already exists in the mux, since modifying the current may introduce

Figure 5.45. Signal vs. sample number for various source to drain currents (I_{sd}) of the pixel illustrated in Figure 5.44.



yet another level, changing gate voltage appears to have no effect, and practical considerations limit the range of operating parameters. Therefore, burst noise may continue to be a challenging effect for low background applications that require very low noise multiplexers, unless Rockwell Scientific can change the process affecting the channel-oxide interface to eliminate trap formation. In order to experimentally determine the physical location or origin of a burst noise generating trap, isolated MOSFETs with individually controlled gate, source, drain and substrate voltages, manufactured with the same specifications under identical conditions as the current HAWAII-1RG multiplexers, designed specifically for such an analysis are necessary. Further research on such devices is necessary to characterize the traps causing burst noise in order to provide the required feedback to Rockwell Scientific.

For proposed space programs focusing on low background infrared detection that employ the HAWAII-2RG, such as JWST, WISE and NEOCam, it may be necessary to develop ways to deal with burst noise. Researchers on JWST are developing software routines to detect and compensate for burst noise, such as implementing the sampling technique of Fowler Up The Ramp developed by Offenber⁷³ et al. (2005). Craig McMurtry re-analyzed the data presented in this thesis to ascertain its effect on the WISE mission, an all sky survey mission that covers $3.5\mu\text{m}$ to $23\mu\text{m}$. WISE will utilize nine consecutive samples and will therefore observe burst noise on $\sim 70\%$ of the pixels which would exhibit burst noise in a 3000 sample analysis. NEOCam, the Near Earth Object Camera designed to detect asteroid threats to life on Earth, is still under development and will likely utilize a similar sampling method to WISE. NEOCam will develop software routines similar to those used to detect cosmic rays in order to exclude pixels exhibiting burst noise. By far the largest effect will be felt by those missions which require very sensitive low signal operation.

5.6 Summary of Phase II Characterization and Conclusions

Extensive characterization of three Rockwell Scientific LWIR HgCdTe detector arrays bonded to a HAWAII-1RG mux has led to the following conclusions: The majority of the detector pixels exhibit exceedingly low dark currents, well below our goal of $30e^-/s$ while maintaining adequate well depth at lower applied biases. The limiting dark current mechanism at higher applied bias ($\geq 100\text{mV}$) is defect-assisted localized junction breakdown, whereas the limiting dark current mechanism at low temperature and low bias is a form of surface current. These same pixels also exhibit varying degrees of non-linearity. The average quantum efficiency per pixel of these detector arrays varies from 30% to 55%, which could be increased with the addition of anti-reflection coatings. In addition, microlenses can be used to focus optical collection and pixel pitch can be reduced to improve lateral diffusion.

In the multiplexer, burst noise can significantly affect the pixel noise power. Elimination of the source of burst noise would make the HAWAII-1RG and -2RG even lower noise multiplexers than they already are. In addition, a way to mitigate the burst noise that currently exists in the multiplexer would be to bump-bond multiple unit cells to the same detector diode. Aside from the increase in capacitance, this will help provide multiple reads of the same diode and with only approximately 25% of pixels exhibiting any form of detectable burst noise, four unit cells bump-bonded to the same detector diode should provide, on average, three burst-noise-free unit cells per diode.

With the proprietary technological advancements demonstrated in these detector arrays, future space astronomy missions employing passively cooled $10\mu\text{m}$ cutoff HgCdTe detector arrays are now possible. In future work we intend to obtain detector arrays with even longer cutoff wavelengths. A modification in format that may eliminate the need for microlenses and anti-reflection coatings will be applied to improve the average RQE.

The area in greatest need of improvement is the high dark current tail, which needs to be eliminated. Since the mechanism causing high dark currents in these devices is dislocation-induced early breakdown, the density of such defects needs a vast reduction. In addition, any defects that exist in the substrate, especially screw dislocations, will continue into the material applied on the substrate. Thus, it is very important to have substrate materials as free of defects as possible. By addressing the high dark current tail, future arrays will be significantly closer to space quality.

Chapter 6

Summary and Future Directions

In this thesis, the first two phases of development of low background space-based $\sim 10\mu\text{m}$ HgCdTe detector arrays were discussed. First, the astronomical motivation behind this research was described in Section 1.1, followed by a discussion of molecular beam epitaxy of HgCdTe and its crystalline structure. Then photodiode design and operation were described, as well as bonding to multiplexers, readout structures and design. Next, the requirements on these devices for space-based astronomy were laid out as well as diagnostic tests made by the University of Rochester to provide the device manufacturer, Rockwell Scientific, with specific paths for improvement.

In the second chapter, the theory of dark current and noise were outlined, with specific focus on the mechanisms most pertinent to phase I and phase II deliveries: surface current, localized junction breakdown and burst noise. The third chapter elaborated on the equipment utilized by the University of Rochester to carry out the testing and characterization, followed by a description of the multiplexers and their operation.

In Chapter 4, Phase I research on the NICMOS3 deliveries was discussed. For this phase, the University of Rochester had $\sim 10\mu\text{m}$ HgCdTe detector arrays bonded to the NICMOS3 multiplexer in a “banded” format, where nine different diode structures were tested on a single array. Through this analysis, the best performing diode structure (with the highest percentage meeting the dark current and well depth goals and with the lowest mean dark current) was determined to be the one with the smallest nodal

capacitance. This diode structure was used in phase II deliveries.

The low reverse bias dark current limiting mechanism on the NICMOS3 deliveries of phase I was surface current, which was a result of processing prior to passivation. This knowledge was obtained after the HAWAII-1RG deliveries of Phase II, so no processing advancements were developed and implemented between the two phases regarding this result. The high reverse bias dark current limit was tunneling, specifically that induced by dislocations that threaded to the junction while stresses were applied to the device during hybridization. In fact, it was assumed that the 70% of pixels with higher dark current and/or lower well depth than the constraints were most likely due to stress-induced defects. This information prompted Rockwell Scientific and the University of Rochester to come up with ways to reduce the density of such defects. As a result, proprietary processing and bonding techniques were implemented in the manufacturing process of detector arrays for phase II.

Finally, Chapter 5 detailed Phase II development and research on the HAWAII-1RG deliveries. The mean dark current performance of the detector diodes was improved by over two orders of magnitude due to the processing advancements made based upon the results of phase I. The temperature and bias dependence of dark current enabled determination of the dominant dark current mechanisms. It was discovered that the dominant low temperature and low bias dark current mechanism in these Phase II arrays was still surface current on the frontside surface. These currents were a result of processing techniques which modified the composition parameter x to a lower number.³³ This caused higher surface currents than expected. With low temperature and high bias (200mV) conditions, the dominant dark current mechanism for many pixels was screw dislocation assisted localized breakdown. The shape of the I-V curve for this mechanism is very distinctive, manifesting as a sharp increase in the trap density and hence trap-to-band tunneling. These pixels also have a modified energy band structure, which leads to band-to-band tunneling modeled best with a parabolic barrier. At higher temperatures (45K), G-R current dominates.

A noise feature exhibited by these arrays which had not been seen in previous devices

was burst noise. Burst noise is characterized by rapid signal level changes in the positive and negative directions. It was observed when characterizing the dark current of individual pixels and was determined to originate in the source follower unit cell MOSFET. The trapping or releasing of a single charge carrier in the oxide of the MOSFET caused a conductivity change in the silicon channel. This manifested as an output voltage shift. The magnitude and timing of the transitions are affected by source to drain current, gate voltage and temperature. However, there is no operating temperature, gate voltage or source to drain current at which burst noise was not seen. Modifying operating parameters does not eliminate burst noise. However, characterization of existing burst noise as it depends upon operating parameters has suggested the location and nature of traps in the unit cell source follower FET. This information, in addition to the IDL code I developed to detect burst noise, has been fed back to Rockwell Scientific and may lead to changed processes in the manufacturing of the multiplexers and consequently elimination of burst noise.

In conclusion, there has been a significant amount of progress already made up to this point, but there is much more that can be done. One of the first endeavors stemming from the presented Phase I and Phase II research will be individual pixel burst noise characterization with fine temporal resolution. In order to determine the characteristic time a pixel remains in a given level, the pixel needs to be sampled such that multiple samples are detected in the same level every time the pixel transitions to it. In the analysis presented in Section 5.5, most pixels were undersampled, such that the condition above was not met. Therefore, the level timing of these pixels is unknown. Since the influence of varying detector parameters on burst noise timing can provide information regarding the location and nature of the defects causing it, it is important to be able to monitor even the fastest characteristic times. Utilization of a faster sampling technique will yield this missing information, providing a better understanding of burst noise mechanisms.

Another research focus is the characterization of a $10.2\mu\text{m}$ cutoff device which will jumpstart the proposed NEOCam space mission. Because the NEOCam mission will

be passively cooled and observe with a single bandpass from $6\mu\text{m}$ to $10\mu\text{m}$, the detectors developed for phase II presented in this thesis already meet most of the mission requirements. The steps remaining to realize the necessary devices are to increase the cutoff wavelength past $10\mu\text{m}$, bond devices to every pixel of a HAWAII-2RG multiplexer utilizing a modification of the proprietary bonding techniques used in Phase II deliveries, and antireflective coat the surface to increase quantum efficiency, all while maintaining sufficient well depth and low dark current for over 90% of pixels on the array. The first step has been achieved in the $10.2\mu\text{m}$ cutoff device, which has already been delivered to the University of Rochester for characterization. This device will determine if recent improvements to processing techniques at Rockwell Scientific have improved device quality. It will also determine the direction of detector development during NEOCam's phase B.

Finally, the main goal of future research endeavors will be to reduce the high dark current tail at higher biases and well depths. This will involve modifications of existing processing and bonding techniques in order to further reduce stress-induced defects. In addition, substrate material of superior quality will be necessary in order to ensure that dislocations are not introduced into the HgCdTe by the substrate. The result of such efforts will be space quality $10\mu\text{m}$ cutoff wavelength arrays with low dark current and sufficient well depth for over 90% of detector array pixels, suitable for many space astronomy applications.

Bibliography

- [1] X. Fan, M. A. Strauss, D. P. Schneider, R. H. Becker, R. L. White, Z. Haiman, M. Gregg, L. Pentericci, E. K. Grebel, V. K. Narayanan, Y. Loh, G. T. Richards, J. E. Gunn, R. H. Lupton, G. R. Knapp, Ž. Ivezić, W. N. Brandt, M. Collinge, L. Hao, D. Harbeck, F. Prada, J. Schaye, I. Strateva, N. Zakamska, S. Anderson, J. Brinkmann, N. A. Bahcall, D. Q. Lamb, S. Okamura, A. Szalay, and D. G. York, “A Survey of $z > 5.7$ Quasars in the Sloan Digital Sky Survey. II. Discovery of Three Additional Quasars at $z > 6$,” *The Astronomical Journal* **125**, pp. 1649–1659, Apr. 2003.
- [2] A. D. Estrada, G. Domingo, J. D. Garnett, A. W. Hoffman, N. A. Lum, P. J. Love, S. L. Solomon, J. E. Venzon, G. R. Chapman, K. P. Sparkman, C. R. McCreight, M. E. McKelvey, R. E. McMurray, J. A. Estrada, S. Zins, R. McHugh, and R. Johnson, “Si:As IBC IR focal plane arrays for ground-based and space-based astronomy,” in *Proc. SPIE, Infrared Astronomical Instrumentation*, A. M. Fowler, ed., **3354**, pp. 99–108, Aug. 1998.
- [3] G. L. Hansen and J. L. Schmit, “Calculation of intrinsic carrier concentration in $\text{Hg}_{1-x}\text{Cd}_x\text{Te}$,” *Journal of Applied Physics* **54**, pp. 1639–1640, Mar. 1983.
- [4] J. Callaway, *Energy Band Theory*, Academic Press, New York, NY, 1964.
- [5] W. M. Coderre and J. C. Wooley, “Normal-Inverted Band Transitions with Temperature in $\text{InAs}_x\text{Sb}_{1-x}$ Alloys,” in *The Physics of Semimetals and Narrow-Gap Semiconductors*, D. L. Carter and R. T. Bate, eds., pp. 535–542, 1971.
- [6] H. Overhof, “A Model Calculation for the Energy Bands in the $\text{Hg}_{1-x}\text{Cd}_x\text{Te}$ Mixed Crystal System,” *Phys. Stat. Sol. (b)* **45**, pp. 315–321, 1971.
- [7] S. H. Groves, “Recent Experiments on Zero Gap Semiconductors,” in *The Physics of Semimetals and Narrow-Gap Semiconductors*, D. L. Carter and R. T. Bate, eds., pp. 447–460, 1971.
- [8] G. M. Minkov, A. V. Germanenko, V. A. Larionova, and O. E. Rut, “Tunneling Studies of Two-Dimensional States in Semiconductors with Inverted Band Struc-

- ture: Spin-Orbit Splitting, Resonant Broadening,” *Phys. Rev. B* **54**, pp. 1841–1852, 1996.
- [9] M. B. Reine, A. K. Sood, and T. J. Tredwell, “Photovoltaic infrared detectors,” *Semiconductors and Semimetals* **18**, pp. 201–311, 1981.
- [10] A. M. Fowler and I. Gatley, “Noise reduction strategy for hybrid IR focal-plane arrays,” in *Proc. SPIE, Infrared Sensors: Detectors, Electronics, and Signal Processing*, T. S. Jayadev, ed., **1541**, pp. 127–133, Nov. 1991.
- [11] P. W. Kruse, “The Emergence of $Hg_{1-x}Cd_xTe$ as a Modern Infrared Sensitive Material,” *Semiconductors and Semimetals* **18**, pp. 1–20, 1981.
- [12] A. Cho, ed., *Molecular Beam Epitaxy*, AIP Press, 1993.
- [13] A. Cho, “Molecular beam epitaxy,” in *Molecular Beam Epitaxy*, A. Cho, ed., pp. 3–37, AIP Press, 1993.
- [14] J. M. Arias, J. G. Pasko, M. Zandian, S. H. Shin, G. M. Williams, L. O. Bubulac, R. E. Dewames, and W. E. Tennant, “Planar p-on-n HgCdTe heterostructure photovoltaic detectors,” *Applied Physics Letters* **62**, pp. 976–978, Mar. 1993.
- [15] T. J. de Lyon, R. D. Rajavel, J. A. Roth, J. E. Jensen, G. L. Olson, P. D. Brewer, A. T. Hunter, T. S. Williamson, S. L. Bailey, J. W. Bangs, A. Buell, G. Chapman, A. C. Childs, E. Gordon, M. D. Jack, S. M. Johnson, K. Kosai, K. D. Maranowski, E. A. Patten, J. Peterson, L. Pham, W. A. Radford, V. Randall, J. B. Varesi, and J. A. Wilson, “Advances in HgCdTe-based infrared detector materials: the role of molecular-beam epitaxy,” in *Proc. SPIE, Materials for Infrared Detectors*, R. E. Longshore, ed., **4454**, pp. 47–59, Nov. 2001.
- [16] J. M. Arias, J. G. Pasko, M. Zandian, J. Bajaj, L. J. Kozlowski, R. E. Dewames, and W. E. Tennant, “Molecular beam epitaxy (MBE) HgCdTe flexible growth technology for the manufacturing of infrared photovoltaic detectors,” in *Proc. SPIE, Producibility of II-VI Materials and Devices*, H. K. Pollehn and R. S. Balcerak, eds., **2228**, pp. 210–224, July 1994.
- [17] J. D. Benson, J. H. Dinan, J. R. Waterman, C. J. Summers, R. G. Benz, B. K. Wagner, S. D. Pearson, A. Parikh, J. E. Jensen, O. K. Wu, R. D. Rajavel, G. S. Kamath, K. A. Harris, S. R. Jost, J. M. Arias, L. J. Kozlowski, M. Zandian, J. Bajaj, K. Vural, R. E. Dewames, C. A. Cockrum, G. M. Venzor, S. M. Johnson, H.-D. Shih, M. J. Bevan, J. A. Dodge, and A. Simmons, “MBE flexible manufacturing for HgCdTe focal plane arrays,” in *Proc. SPIE, Infrared Technology and Applications XXII*, B. F. Andresen and M. S. Scholl, eds., **2744**, pp. 126–133, June 1996.

- [18] J. M. Arias Cortes, “Molecular-Beam Epitaxy of HgCdTe for Electro-Optical Infrared Applications,” in *II-VI Semiconductor Compounds*, M. Jain, ed., pp. 509–535, World Scientific Press, 1993.
- [19] M. Carmody, D. Lee, M. Zandian, J. Phillips, and J. Arias, “Threading and Misfit Dislocation Motion in MBE Grown HgCdTe Epi-layers,” Apr. 2002.
- [20] J. M. Arias, M. Zandian, J. G. Pasko, L. O. Bubulac, S. H. Shin, and R. E. DeWames, “MBE HgCdTe growth-induced void defects and their effect on infrared photodiodes,” in *Proceedings of the 1993 U.S. Workshop of the Physics and Chemistry of HgCdTe and Other IR Materials*, **24**, May 1995.
- [21] P. H. Zimmermann, M. B. Reine, K. Spignese, K. Maschhoff, and J. Schirripa, “Surface passivation of HgCdTe photodiodes,” *Journal of Vacuum Science and Technology A* **8**(2), pp. 1182–1184, 1990.
- [22] J. Wu, *Development of Infrared Detectors for Space Astronomy*, *PhD Thesis*, University of Rochester, Rochester, NY, 1997.
- [23] R. B. Bailey, J. M. Arias, W. V. McLevige, J. G. Pasko, A. C. Chen, C. Cabelli, L. J. Kozlowski, K. Vural, J. Wu, W. J. Forrest, and J. L. Pipher, “Prospects for large-format IR astronomy FPAs using MBE-grown HgCdTe detectors with cutoff wavelength $> 4\mu\text{m}$,” in *Proc. SPIE, Infrared Astronomical Instrumentation*, A. M. Fowler, ed., **3354**, pp. 77–86, Aug. 1998.
- [24] C. M. Bacon, J. L. Pipher, W. J. Forrest, C. W. McMurtry, and J. D. Garnett, “Diode Characterization of Rockwell LWIR HgCdTe Detector Arrays,” in *Proc. SPIE, IR Space Telescopes and Instruments*, J. C. Mather, ed., **4850**, pp. 927–934, Mar. 2003.
- [25] C. M. Bacon, C. W. McMurtry, J. L. Pipher, W. J. Forrest, J. D. Garnett, D. Lee, and D. D. Edwall, “Characterization of Rockwell Scientific LWIR HgCdTe Detector Arrays,” in *Proc. SPIE, Focal Plane Arrays for Space Telescopes*, T. J. Grycewicz and C. R. McCreight, eds., **5167**, pp. 313–319, Jan. 2004.
- [26] C. M. Bacon, C. W. McMurtry, J. L. Pipher, W. J. Forrest, J. D. Garnett, D. Lee, and D. D. Edwall, “Further Characterization of Rockwell Scientific LWIR HgCdTe Detector Arrays,” in *Proc. SPIE, Infrared Detectors and Focal Plane Arrays VIII*, E. L. Dereniak and R. E. Sampson, eds., **5563A**, 2005.
- [27] C. M. Bacon, C. W. McMurtry, J. L. Pipher, W. J. Forrest, and J. D. Garnett, “Burst Noise in the HAWAII-1RG Multiplexer,” in *Proc. SPIE, Focal Plane Arrays for Space Telescopes II*, T. J. Grycewicz and C. J. Marshall, eds., **5902**, 2005.
- [28] M. A. Kinch, “Metal-insulator-semiconductor infrared detectors,” *Semiconductors and Semimetals* **18**, pp. 313–378, 1981.

- [29] J. Wenus, J. Rutkowski, and A. Rogalski, "Two-Dimensional Analysis of Double-Layer Heterojunction HgCdTe Photodiodes," *IEEE Transactions on Electron Devices* **48**(7), pp. 1326–1332, 2001.
- [30] A. S. Grove, *Physics and Technology of Semiconductor Devices*, John Wiley & Sons, 1967.
- [31] C. T. Sah, R. N. Noyce, and W. Shockley, "Carrier generation and recombination in p-n junctions and p-n junction characteristics," *Proc. of the IRE* **45**, pp. 1228–1243, 1957.
- [32] J. D. Garnett, M. Farris, S. Wong, M. Zandian, D. N. B. Hall, S. Jacobson, G. Lupino, S. Parker, D. Dorn, S. Franka, E. Freymiller, and S. McMudroch, "2Kx2K molecular beam epitaxy HgCdTe detectors for the James Webb Space Telescope NIRCам instrument," *Proc. SPIE, Optical and Infrared Detectors for Astronomy* **5499**, pp. 35–46, 2004.
- [33] Private communication with M. Zandian.
- [34] S. M. Sze, ed., *Physics of Semiconductor Devices*, John Wiley & Sons, 1969.
- [35] J. L. Moll, *Physics of Semiconductors*, McGraw-Hill, New York, NY, 1964.
- [36] M. A. Kinch, J. D. Beck, and W. T. Zwirble, "Dark Current Limitations in P-Type HgCdTe MIS Devices," *IEEE: 1980 IEDM Technical Digest*, pp. 508–511, 1980.
- [37] I. F. McLuckie, "Investigation of Zener and Avalanche Diode Characteristics," *Physics Education* **23**, pp. 251–254, 1988.
- [38] P. G. Neudeck, W. Huang, and M. Dudley, "Breakdown Degradation Associated with Elementary Screw Dislocations in 4H-SiC p⁺ n Junction Rectifiers," *Solid State Electronics* **42**(12), pp. 2157–2164, 1998.
- [39] G. Busch and H. Schade, *Lectures on Solid State Physics*, Pergamon Press, Oxford, 1976.
- [40] P. G. Neudeck, W. Huang, and M. Dudley, "Study of Bulk and Elementary Screw Dislocation Assisted Reverse Breakdown in Low-Voltage (< 250V) 4H-SiC p⁺n Junction Diodes - Part I: DC Properties," *IEEE Transactions on Electron Devices* **46**(3), pp. 478–484, 1999.
- [41] M. Xianyun, "Superscrew dislocations in silicon carbide: Dissociation, aggregation, and formation," *Journal of Applied Physics* **99**(063513), pp. 1–6, 2006.
- [42] P. Horowitz and W. Hill, *The Art of Electronics*, Cambridge University Press, Cambridge, UK, 1989.

- [43] R. H. Kingston, *Optical Sources, Detectors, and Systems: Fundamentals and Applications*, Academic Press, San Diego, CA, 1995.
- [44] J. D. Vincent, *Fundamentals of Infrared Detector Operation and Testing*, John Wiley & Sons, New York, NY, 1990.
- [45] A. Rogalski, *Infrared Photon Detectors*, SPIE, Bellingham, WA, 1995.
- [46] G. H. Rieke, *Detection of Light from the Ultraviolet to the Submillimeter*, Cambridge University Press, Great Britain, 1994.
- [47] M. J. Buckingham, *Noise in Electronic Devices and Systems*, John Wiley & Sons, New York, NY, 1983.
- [48] S. T. Hsu and R. J. Whittier, "Physical Model for Burst Noise in Semiconductor Devices," *Solid-State Electronics* **13**, pp. 1055–1071, 1970.
- [49] K. Kandiah, M. O. Deighton, and F. B. Whiting, "A physical model for random telegraph signal currents in semiconductor devices," *Journal of Applied Physics* **66**, pp. 937–948, July 1989.
- [50] D. Wolf and E. Holler, "Bistable Current Fluctuations in Reverse-Biased p - n Junctions of Germanium," *Journal of Applied Physics* **38**(1), pp. 189–192, 1967.
- [51] P. M. Campbell, E. S. Snow, W. J. Moore, O. J. Glembocki, and S. W. Kirchoefer, "Light-Activated Telegraph Noise in AlGaAs Tunnel Barriers: Optical Probing of a Single Defect," *Physical Review Letters* **67**, pp. 1330–1333, Sept. 1991.
- [52] B. Dierickx and E. Simoen, "The decrease of "random telegraph signal" noise in metal-oxide-semiconductor field-effect transistors when cycled from inversion to accumulation," *Journal of Applied Physics* **71**(4), pp. 2028–2029, 1992.
- [53] Y. Dai, Y. Li, and J. Xu, "Discussion on Physical Models for Burst Noise in a Forward Biased P-N Junction and Their Experimental Validation," *Microelectronics Reliability* **38**(4), pp. 671–675, 1998.
- [54] J. Sikula, J. Pavelka, V. Sedlakova, M. Tacano, S. Hashiguchi, and M. Toita, "RTS in Submicron MOSFETs and Quantum Dots," *Proc. SPIE, Noise and Information in Nanoelectronics, Sensors, and Standards II* **5472**, pp. 64–73, 2004.
- [55] M. J. Kirton and M. J. Uren, "Noise in solid-state microstructures: A new perspective on individual defects, interface states and low-frequency ($1/f$) noise," *Advances in Physics* **38**, pp. 367–468, Nov. 1989.
- [56] E. Simoen, B. Dierickx, C. L. Claeys, and G. J. Declerck, "Explaining the Amplitude of RTS Noise in Submicrometer MOSFETs," *IEEE Transactions on Electron Devices* **39**(2), pp. 422–429, 1992.

- [57] A. C. Moore, Z. Ninkov, G. S. Burley, W. J. Forrest, C. W. McMurtry, and L. E. Avery, "Operation and test of hybridized silicon p-i-n arrays using open-source array control hardware and software," in *Proc. SPIE, Sensors and Camera Systems for Scientific, Industrial, and Digital Photography Applications IV*, R. J. M. Morley M. Blouke, Nitin Sampat, ed., **5017**, pp. 240–253, 2003.
- [58] J. D. Garnett and W. J. Forrest, "Multiply sampled read limited and background limited noise performance," *Proc. SPIE, Infrared Detectors and Instrumentation* **1946**, pp. 395–404, 1993.
- [59] M. Loose, M. C. Farris, J. D. Garnett, D. N. B. Hall, and L. J. Kozlowski, "HAWAII-2RG: a 2k x 2k CMOS multiplexer for low and high background astronomy applications," in *Proc. SPIE, IR Space Telescopes and Instruments.*, J. C. Mather, ed., **4850**, pp. 867–879, 2003.
- [60] L. Mortara and A. Fowler, "Evaluations of Charge-Coupled Device / CCD / Performance for Astronomical Use," in *Proc. SPIE, Solid State Imagers for Astronomy*, **290**, pp. 28–+, 1981.
- [61] A. C. Moore, Z. Ninkov, and W. J. Forrest, "Interpixel capacitance in nondestructive focal plane arrays," in *Proc. SPIE, Focal Plane Arrays for Space Telescopes.*, T. J. Grycewicz and C. R. McCreight, eds., **5167**, pp. 204–215, Jan. 2004.
- [62] P. S. Wijewarnasuriya, M. D. Lange, S. Sivanathan, and J. P. Faurle, "Carrier recombination in indium-doped hgcdte(211)b epitaxial layers grown by molecular beam epitaxy," *Journal of Applied Physics* **75**(2), pp. 1005–1009, 1994.
- [63] J. V. Gumenjok-Sichevskaya and F. F. Sizov, "Currents in narrow-gap photodiodes," *Semiconductor Science and Technology* **14**, pp. 1124–1131, 1999.
- [64] F. F. Sizov, J. V. Gumenjok-Sichevskaya, Y. G. Sidorov, V. Vasilev, A. G. Golenkov, V. V. Zabudsky, V. P. Reva, Y. P. Derkach, and V. V. Tetyorkin, "Dark current transport mechanisms in narrow-gap heterojunctions for IR arrays," in *Proc. SPIE Vol. 4454, p. 123-134, Materials for Infrared Detectors, Randolph E. Longshore; Ed.*, R. E. Longshore, ed., pp. 123–134, Nov. 2001.
- [65] F. F. Sizov, V. Vasilev, D. G. Esaev, V. N. Ovsyuk, Y. G. Sidorov, V. P. Reva, Y. P. Derkach, A. G. Golenkov, and J. V. Gumenjok-Sichevskaya, "Properties of 2x64 linear HgCdTe MBE-grown LWIR arrays with CCD silicon readouts," in *Proc. SPIE Vol. 4288, p. 345-353, Photodetectors: Materials and Devices VI, Gail J. Brown; Manijeh Razeghi; Eds.*, G. J. Brown and M. Razeghi, eds., pp. 345–353, June 2001.
- [66] B. J. Rauscher, D. F. Figer, M. W. Regan, L. E. Bergeron, J. Balleza, R. Barkhouser, G. Greene, S. Kim, S. McCandliss, E. Morse, R. Pelton, T. Reeves,

- U. Sharma, P. Stemmiski, H. Stockman, and M. Telewicz, "Ultra-Low Background Operation of Near-Infrared Detectors Using Reference Pixels for NGST," *Proc. SPIE, IR Space Telescopes and Instruments* **4850**, pp. 962–970, 2003.
- [67] L. Mortara and A. Fowler, "Evaluations of CCD: Performance for Astronomical Use," *Proc. SPIE, Solid State Imagers for Astronomy* **290**, pp. 28–30, 1981.
- [68] J. Wu, W. J. Forrest, and J. L. Pipher, "Development of infrared focal plane arrays for space," *Review of Scientific Instruments* **68**(9), pp. 3566–3578, 1997.
- [69] J. L. Hora, G. G. Fazio, S. P. Willner, M. L. Ashby, J. Huang, S. T. Megeath, J. R. Stauffer, E. V. Tollestrup, Z. Wang, W. J. Glaccum, J. L. Pipher, W. J. Forrest, C. R. McCreight, M. E. McKelvey, W. F. Hoffman, P. Eisenhardt, J. A. Surace, W. T. Reach, S. H. Moseley, R. G. Arendt, K. P. Stewart, and F. D. Robinson, "Calibration and performance of the Infrared Array Camera (IRAC)," *Proc. SPIE, Infrared Spaceborne Remote Sensing VIII* **4131**, pp. 13–25, 2000.
- [70] B. Pain and B. Hancock, "Accurate Estimation of Conversion Gain and Quantum Efficiency in CMOS Imagers," *Proc. SPIE, Sensors and Camera Systems for Scientific, Industrial, and Digital Photography Applications IV* **5017**, pp. 94–103, 2003.
- [71] B. J. Rauscher, D. F. Figer, M. W. Regan, T. Boeker, J. Garnett, R. J. Hill, G. Bagnasco, J. Balleza, R. Barney, L. E. Bergeron, C. Brambora, J. Connelly, R. Derro, M. J. DiPirro, C. Doria-Warner, A. Ericsson, S. D. Glazer, C. Greene, D. N. Hall, S. Jacobson, P. Jakobsen, E. Johnson, S. D. Johnson, C. Krebs, D. J. Krebs, S. D. Lambros, B. Likins, S. Manthripragada, R. J. Martineau, E. C. Morse, S. H. Moseley, D. B. Mott, T. Muench, H. Park, S. Parker, E. J. Polidan, R. Rashford, K. Shakoorzadeh, R. Sharma, P. Strada, A. Waczynski, Y. Wen, S. Wong, J. Yagelowich, and M. Zuray, "Detectors for the James Webb Space Telescope Near-Infrared Spectrograph," *Proc. SPIE, Optical, Infrared, and Millimeter Space Telescopes* **5487**, pp. 710–726, 2004.
- [72] M. J. Uren, D. J. Day, and M. J. Kirton, "1/f and random telegraph noise in silicon metal-oxide-semiconductor field-effect transistors," *Applied Physics Letters* **47**, pp. 1195–1197, 1985.
- [73] J. D. Offenberg, D. J. Fixsen, and J. C. Mather, "Memory-Efficient Up-the-Ramp Processing with Cosmic-Ray Rejection," *The Publications of the Astronomical Society of the Pacific* **117**, pp. 94–103, Jan. 2005.

Appendix: Burst Noise Code

```

pro popcharlm, array, bin, R, ncompletepeaks, peaks, dbtwnpks, $
    plot=plot, stats=stats, chisq=chisq, text=text, $
    nodouble=nodouble, sdest=sdest, midplot=midplot

if n_params() lt 3 then begin
    print, "Syntax - POPCHARLM, array, bin, R, [n, peaks, " + $
        "dbtwnpks, /plot, /stats,"
    print, "    chisq=chisq, /text, /nodouble, /midplot]"
    print, "This file is for a single pixel array of files."
    print, "R is the resolution between double peaks."
    print, "This file attempts to subtract gaussians off " + $
        "data to find other peaks"
    return
endif

if keyword_set(text) then print, ''

;Input darkcharge vs. time data. Do not need itime array because all
;we care about here are signal levels.

peaks=fltarr(10,3) ;array of peak information for each pixel
nsigma=1 ;number of standard deviations to subtract
if keyword_set(sdest) eq 0 then sdest=6 ;estimated standard deviation
multgauss=1.4 ;multiply estimated gaussian by this number
;start the following counters at 0
findingleftovers=0
movepeakover=0
ncompletepeaks=0

;make a histogram of the signal values
h=histogram(array,bin,bin,bin,min=min(array)-bin, max=max(array)+bin)
h=float(h)
numindex=n_elements(h)
x=findgen(temporary(numindex))*bin + min(array)-bin
totalgauss=x
totalgauss(*)=0

;modify data here...
ind=where(h eq 0, count)
;print, ind
if ind(0) eq 0 then begin
    count=count-1

```

```

        if count gt 0 then ind=ind(1:count)
    endif
    if count gt 0 then if ind(count-1) eq n_elements(h)-1 then begin
        count=count-1
        if count gt 0 then ind=ind(0:count-1)
    endif
    if count gt 0 then for i=0,count-1 do begin
        if h[ind(i)-1] gt 0 AND h[ind(i)+1] gt 0 and h[ind(i)] eq 0 then $
            h[ind(i)]=0.5
    endfor

    deleteme=temporary(ind)
    deleteme=temporary(count)
;done modifying data

;*****if doing this again, start here... n will be added to...
DATALEFT:

if n_elements(rememberredh) gt 0 then redh=rememberredh else begin
    redh=h-totalgauss ;for reducing
    ind=where(redh) lt 0
    if ind(0) gt 0 then redh(temporary(ind))=0
endelse
;find local maxs
locmax=fltarr(10)
sizemax=fltarr(10)
wherewevebeen=intarr(n_elements(x))
indgauss=where(totalgauss ge 1)
if indgauss(0) ge 0 then wherewevebeen(temporary(indgauss))=1
n=0
doagain=1
while doagain eq 1 do begin
    if keyword_set(midplot) then begin
        plot, x, redh, psym=10, /ylog, $
        yrange=[1,max(h)];title=maintitle, xtitle=xtit, $
        ;ytitle=yaxis
    endif
    ;find where local max is
    ind=where(redh eq max(redh))
    ;discriminatory method... if we've been here before and
    ;there is no data surrounding it, then it is probably
    ;just a statistical fluctuation and not another peak, so
    ;skip it

```

```

skp=0
if ind(0) eq 0 then if wherewevebeen(ind(0)) eq 1 OR $
    wherewevebeen(ind(0)+1) eq 1 then skp=1
if ind(0) gt 0 AND ind(0) lt n_elements(wherewevebeen)-1 then $
    if wherewevebeen(ind(0)) eq 1 OR $
        wherewevebeen(ind(0)+1) eq 1 or $
        wherewevebeen(ind(0)-1) eq 1 then skp=1
if ind(0) eq n_elements(wherewevebeen)-1 then if $
    wherewevebeen(ind(0)) eq 1 OR $
    wherewevebeen(ind(0)-1) eq 1 then skp=1
if temporary(skp) eq 1 then begin
    if keyword_set(text) then $
        print, "Skipping this potential peak..."
    redh(ind(0))=0
    if n_elements(rememberredh) gt 0 then begin
        if ind(0) eq 0 then if rememberredh(ind(0)+1) $
            le 1 then rememberredh(ind(0))=0
        if ind(0) gt 0 AND ind(0) lt $
            n_elements(wherewevebeen)-1 then $
            if rememberredh(ind(0)-1) le 1 AND $
            rememberredh(ind(0)+1) le 1 then $
            rememberredh(ind(0))=0
        if ind(0) eq n_elements(wherewevebeen)-1 then $
            if rememberredh(ind(0)-1) le 1 then $
            rememberredh(ind(0))=0
    endif
endif else begin
    ;first local max to look at is the first one
    ;found (record in locmax)
    locmax(n)=x(ind(0))
    ;find size of local max (record in sizemax)
    sizemax(n)=redh(ind(0))
    ;new method--first create data for gaussian
    ;associated with lm
    estgauss=sizemax(n)*exp(-((x-locmax(n))/(sdest+1))^2/2)
    ;find indices where estimated gaussian is and set
    ;equal to 1 so we know where we've been
    indgauss=where(estgauss ge 1)
    if indgauss(0) ge 0 then $
        wherewevebeen(temporary(indgauss))=1
        ;then subtract estimated gaussian from data
    redh=redh-estgauss*multgauss
    ;after subtracting gaussian, need to wipe all
    ;data within 1SD of found peak

```

```

ind=where(x ge locmax(n)-nsigma*(sdest+1) AND x le $
locmax(n)+nsigma*(sdest+1))
redh(temporary(ind))=0
;set points that by subtracting became negative
;to zero
ind=where(redh lt 0)
if ind(0) ge 0 then redh(temporary(ind))=0
;iterate to the next local max
if keyword_set(midplot) then begin
oplot, x, estgauss*multgauss;,title=maintitle, $
;xtitle=xtit, ytitle=yaxis
key=get_kbrd(1)
endif
n=n+1
if keyword_set(text) then print, "Potential " + $
strtrim(string(n),1)+"th gaussian."
endelse
;print, "Maximum LEFT: ",max(redh)
;if there are no more local maxs, or can't record
;anymore, abort
if max(redh) lt 1.5 or n ge 10 then doagain=0
endwhile
deleteme=temporary(wherewevebeen)
deleteme=0

if n eq 0 then GOTO, FINISHED

;*****if haven't done this before then numpeaks=n, else
;numpeaks=n-already fit numpeaks
;also, n can be number of peaks to fit this time around. n can be
;redefined, since it's already been through.
numpeaks=n
locmax=reform(temporary(locmax(0:n-1)))
sizemax=reform(temporary(sizemax(0:n-1)))
if keyword_set(text) then print, $
"Number of peaks is "+strtrim(string(n),1)+". "
peaksskipped=intarr(n)

;now put peaks in order to determine if there are zeroes between peaks
;If there are zeroes, then each peak will be fit separately
;without zeroes, they must be fit together. so far this program will
;fit up to 3 peaks simultaneously, but I want to leave room for
;possible double peaks, so let's give it a try

```

```

if numpeaks gt 1 then begin

locmaxint=fix(locmax)
order=sort(locmaxint)
zerobtwn=intarr(n_elements(temporary(locmaxint))-1)
locmax=temporary(locmax(order))
sizemax=temporary(sizemax(temporary(order)))

if keyword_set(text) then print, "Max locations", locmax(0:n-1)
if keyword_set(text) then print, "Max values", sizemax(0:n-1)

n=0
;trying to see if there are any zeroes between
for n=0,numpeaks-2 do begin
    indmin=where(x eq locmax(n))
    indmax=where(x eq locmax(n+1))
    ind=where(h(temporary(indmin):temporary(indmax)) eq 0)
    if ind(0) ge 0 then zerobtwn(n)=1
endfor

endif else begin
    zerobtwn=intarr(1) ;numpeaks gt 1
    zerobtwn(0)=1
endelse
if keyword_set(text) then print, 'zerobtwn: ',zerobtwn

;turn around peaks if lgst peak is at end
if numpeaks gt 1 then begin
if max(sizemax(0:(numpeaks-2)/2)) lt $
    max(sizemax(((numpeaks-2)/2)+1:numpeaks-1)) then begin

locmaxrev=locmax
for i=0,numpeaks-1 do locmaxrev(i)=locmax(numpeaks-1-i)
sizemaxrev=sizemax
for i=0,numpeaks-1 do sizemaxrev(i)=sizemax(numpeaks-1-i)
zerobtwnrev=zerobtwn
for i=0,numpeaks-2 do zerobtwnrev(i)=zerobtwn(numpeaks-2-i)
locmax=temporary(locmaxrev)
sizemax=temporary(sizemaxrev)
zerobtwn=temporary(zerobtwnrev)

if keyword_set(text) then print, $

```

```

        "*****Reducing from largest peak... must reverse*****"
if keyword_set(text) then print, "Max locations", locmax
if keyword_set(text) then print, "Max values", sizemax
if keyword_set(text) then print, 'zerobtwn: ',zerobtwn
endif
endif

if n_elements(rememberredh) gt 0 then redh=temporary(rememberredh) else $
    redh=h-totalgauss
ind=where(redh lt 0)
if ind(0) ge 0 then redh(ind)=0
A=fltarr(3)
doagain=1
numdual=0
revert=0
n=0
m=0
R=1.33 ;Resolution, 1.22 initially:
;this is used for estimating initial gaussian separation
redoskipped=0
lastpeak=0
numberofpeaks=numpeaks

DOSKIPPEDPEAKS:
;jump to here to redo the peaks that were skipped the first time around
if redoskipped eq 1 then begin
    if keyword_set(text) then print, "Redoing skipped peaks..."
    if keyword_set(text) then print, '**peaksskipped**', peaksskipped
endif

for l=0,numberofpeaks-1 do begin
if keyword_set(text) then print, "Going through..", n

if redoskipped eq 1 then begin
    ind=where(peaksskipped eq 1)
    if n_elements(ind) eq 1 then lastpeak=1
    m=ind[0]
    l=fix(m)
endif ;else begin

;if no zero, then do multiple peaks together
;How do I find peak pairs?

morepeaks=1

```

```

startwith=1
if m lt n_elements(zerobtn) and redoskipped eq 0 then begin
;so that if hits last peak single, it can move forward
while morepeaks eq 1 do begin
if zerobtn(m) eq 0 then begin
    startwith=temporary(startwith)+1
    m=m+1 ;iterate through peaks
endif
if startwith eq 3 or n_elements(zerobtn) le m then morepeaks=0 else $
    begin ;max pks tog=3
        if zerobtn(m) eq 1 then morepeaks=0
    endelse
endwhile
endif

if keyword_set(text) then print, 'm ', m
if n_elements(zerobtn) gt m+1 AND redoskipped eq 0 then begin
if zerobtn(m) eq 0 then begin
    tempx=x
    tempredh=redh
    midpt=where(abs(x-(locmax(m)+locmax(m+1))/2) eq $
        min(abs(x-(locmax(m)+locmax(m+1))/2)))
    midpt=midpt(0)
    if keyword_set(text) then print, "Midpoint", x(midpt), $
        " locmax(m) ", locmax(m)
    if locmax(m) gt x(midpt) then begin
        x=x(midpt:n_elements(tempx)-1)
        redh=redh(temporary(midpt):n_elements(tempredh)-1)
    endif else begin
        x=x(0:midpt)
        redh=redh(0:temporary(midpt))
    endelse
endif else begin
    tempx=x
    tempredh=redh
    midpt=where(x gt min([locmax(m),locmax(m+1)]) AND $
        x lt max([locmax(m),locmax(m+1)]) AND redh eq 0)
    midpt=midpt((n_elements(midpt)-1)/2)
    if keyword_set(text) then print, "Midpoint", x(midpt), $
        " locmax(m) ", locmax(m)
    if locmax(m) gt x(midpt) then begin
        if n_elements(tempx)-1 - midpt lt 3 then begin
            x=x(midpt-1:n_elements(tempx)-1)
            redh=redh(temporary(midpt)-1:n_elements(tempredh)-1)
        endif
    endif
endif
endif

```

```

        endif else begin
            x=x(midpt:n_elements(tempx)-1)
            redh=redh(temporary(midpt):n_elements(tempredh)-1)
        endelse
    endif else begin
        if midpt - 0 lt 3 then begin
            x=x(0:midpt+1)
            redh=redh(0:temporary(midpt)+1)
        endif else begin
            x=x(0:midpt)
            redh=redh(0:temporary(midpt))
        endelse
    endelse
endelse
endif
l=l+startwith-1
;iterate l through peaks if more than one so it doesn't try to do the
;same thing twice

;endelse
;now, do each peak or multipeak separately, for some of these peaks
;can be doubles

;here need to be able to start with up to three peaks and adjust
;based upon the fit
;not sure if I want to use an 'if' statment, for then I'll have to do
;the same thing multiple times.  Instead, should I use 'switch'?  Or
;'case'?  Or create miniprogs to handle the switch between cases?

if keyword_set(text) then print, "Plotting data to be fit..."
if keyword_set(midplot) then begin
    plot, x, redh, psym=10, /ylog, yrange=[1,max(h)]
    key=get_kbrd(1)
endif

nrevpks=1 ;number of peaks to revert to...
so=0 ;did I start over? (beginagain)
skippeak=0 ;this is useful when a peak is anomalous and alone

BEGINAGAIN: ;jump to here if want to restart with different ICs
CASE startwith OF
    1: BEGIN ;start with 1 gaussian
        if n_elements(chisq1) gt 0 then deleteme=temporary(chisq1)
        if n_elements(chisq2) gt 0 then deleteme=temporary(chisq2)

```

```

if n_elements(chisq3) gt 0 then deleteme=temporary(chisq3)
if keyword_set(text) then $
    print, "Starting with one peak..."
if so eq 0 then A1=[sizemax(m),locmax(m),sdest]
if keyword_set(text) then print, "A1",A1
A1IC=A1
;*****
if redoskipped eq 1 OR movepeakover eq 1 then begin
;finding if this peak is worth re-fitting.  if
;there is no data here, then skip it
indmax=where(x gt A1(1))
indmin=where(x lt A1(1))
if movepeakover eq 1 then begin
    gt1indmax=where(redh(indmax) le 1)
    gt1indmin=where(redh(indmin) le 1)
    if gt1indmax(0) le 0 then $
        gt1indmax=indmax(0)-1 else $
        gt1indmax=indmax(gt1indmax(0));-1
    if gt1indmin(0) eq -1 then $
        gt1indmin=indmin(0)+1 else $
        gt1indmin=indmin(gt1indmin(n_elements(gt1indmin)-1));+1
    midind=fix((gt1indmin+gt1indmax)/2)
    A1[1]=x(midind)
    A1[0]=redh(midind)
    A1[2]=A1[2]*2./3.
    if keyword_set(text) then $
        print, "Trying new parameters for A: ", A1
    if keyword_set(midplot) then begin
        tmpestgauss=A1[0]*exp(-((x-A1[1])/(A1[2]))^2/2)
        plot, x, redh, psym=10, /ylog, yrange=[1,max(h)]
        oplot, x, temporary(tmpestgauss)
        key=get_kbrd(1)
    endif
endif else begin ;redoskipped
indmax=indmax(0)
indmin=indmin(n_elements(indmin)-1)
if max(redh(temporary(indmin):temporary(indmax))) lt 1 then begin
    skippeak=1
    peaksskipped(1)=peaksskipped(1)+1
    if keyword_set(text) then $
        print, "Permanently skipping this erroneous peak"
    GOTO, DONEFITTING
endif
endif
endelse ;redoskipped

```

```

;*****
endif
indmax=where(x gt A1(1) AND redh eq 0)
indmin=where(x lt A1(1) AND redh eq 0)
if indmax(0) ne -1 then indmax=indmax(0) else $
    indmax=n_elements(redh)-1
if indmin(0) ne -1 then indmin=indmin(n_elements(indmin)-1) $
    else indmin=0
while indmax-indmin+1 le 3 do begin
    if indmax eq n_elements(redh)-1 then $
        indmin=indmin-(4-(indmax-indmin+1))
    if indmin eq 0 then indmax=3
    if indmax lt n_elements(redh)-1 AND indmin gt 0 then begin
        indmin=indmin-1
        indmax=indmax+1
    endif
endwhile
if indmax(0) ne -1 then indmax=indmax(0) else $
    indmax=n_elements(redh)-1
if indmin(0) ne -1 then indmin=indmin(0) else indmin=0
if keyword_set(text) then print, 'min sig', x(indmin), $
    'max sig', x(indmax)
fit1pk, x(indmin:indmax), redh(indmin:indmax), A1, chisq1, $
    status, text=text
;fit1pk fits one gaussian to the data.
if keyword_set(text) then print, "A1 after fit", A1
if keyword_set(text) then print, "data", redh
if keyword_set(text) then print, 'chisq', chisq1
if keyword_set(midplot) then begin
    tmpestgauss=A1[0]*exp(-((x-A1[1])/(A1[2]))^2/2)
    oplot, x, $
    temporary(tmpestgauss);*multgauss;
    key=get_kbrd(1)
endif
if keyword_set(text) then print, $
    "n_elements(redh(indmin:indmax))", $
    n_elements(redh(indmin:indmax))
;check to see if this peak is on top of others...
tgaussind=where(abs(A1(1)-x) eq min(abs(A1(1)-x)))
if keyword_set(text) then print, $
    "totalgauss(temporary(tgaussind(0)))", $
    totalgauss(temporary(tgaussind(0)))
;compare chisq to determine if a good fit
;below, preventing spikey-ness too close to actual data with

```

```

;second to last condition
if chisq1 eq 0 or A1(0) eq 0 or A1(2) eq 0 or A1(1) lt $
  x(indmin) or A1(1) gt x(indmax) or $
  (totalgauss(temporary(tgaussind(0))) gt 1 and $
  A1(2) lt sdest/2) OR $
  (totalgauss(temporary(tgaussind(0))) gt A1(0)) then begin
;if there's only a single peak and it's skipping it, it's
;probably not the proper shape for a gaussian fit. Try
;to move peak over instead.
if movepeakover eq 1 then begin
  movepeakover=0
  skippeak=1
  if keyword_set(text) then $
    print, "Skipping this erroneous peak"
  GOTO, DONEFITTING
endif else begin
  movepeakover=1
  A1=A1IC
  GOTO, BEGINAGAIN
endelse
endif
;if not a good fit, chisq too high, try 2 gaussians
IF chisq1 gt 100 AND n_elements(redh(indmin:indmax)) gt sdest $
  AND (A1(2) gt sdest+1 OR chisq1 gt 500) THEN BEGIN
;need a wide fit in order to need two peaks, otherwise
;overkill
if keyword_set(text) then print, "Trying two peaks..."
;setup ICs
A2=A1
B2=A1
A2(0)=A2(0);*5./6.
B2(0)=B2(0);*5./6.
A2(1)=A2(1)-A2(2)*R;/2.
B2(1)=B2(1)+B2(2)*R;/2.
A2(2)=A2(2)*2./3
B2(2)=B2(2)*2./3
chisq2=chisq1
if keyword_set(text) then print, "A2", A2
if keyword_set(text) then print, "B2", B2
fit2pk, x(indmin:indmax), redh(indmin:indmax), A2, B2, $
  R, chisq2, revert, status, text=text
;fit2pk fits 2 gaussians to data, if revert=1 that says
;this fit is worse than before and to revert to previous
;fit

```

```

if keyword_set(text) then print, "A2", A2
if keyword_set(text) then print, "B2", B2
if keyword_set(text) then print, "Chisq2", chisq2
IF revert eq 0 THEN BEGIN
  IF chisq2 gt 100 AND $
  n_elements(redh(indmin:indmax)) gt 9 THEN BEGIN
  if keyword_set(text) then print, $
    "Chisq still too large... Trying three peaks"
    ;setup ICs
    A3=A1
    B3=A1
    C3=A1
    A3(1)=A3(1)-A3(2)
    C3(1)=C3(1)+C3(2)
    chisq3=chisq2
    fit3pk, x(indmin:indmax), $
      redh(indmin:indmax), A3, B3, C3, R, $
      chisq3, revert, status, erroneous, $
      text=text
    ;fit3pk fits 3 gaussians to data
  IF revert eq 1 or n_elements(erroneous) gt 0 $
    THEN nrevpks=2 ELSE nrevpks=3
  ENDIF else nrevpks=2
  ENDIF ELSE nrevpks=1
  ENDIF ELSE nrevpks=1
END
2: BEGIN ;start with 2 gaussians to fit
  if n_elements(chisq1) gt 0 then deleteme=temporary(chisq1)
  if n_elements(chisq2) gt 0 then deleteme=temporary(chisq2)
  if n_elements(chisq3) gt 0 then deleteme=temporary(chisq3)
  if keyword_set(text) then print, "Starting with two peaks..."
  if so eq 0 then A2=[sizemax(m-1),locmax(m-1),sdest]
  if so eq 0 then B2=[sizemax(m),locmax(m),sdest]
  if keyword_set(text) then print, "A2",A2
  if keyword_set(text) then print, "B2",B2
  IF A2(1) gt B2(1) THEN lgstpk='A' ELSE lgstpk='B'
  A2IC=A2
  B2IC=B2
  indmax=where(x gt A2(1) AND redh eq 0)
  indmin=where(x lt A2(1) AND redh eq 0)
  if indmax(0) ne -1 then indmax=indmax(0) else $
    indmax=n_elements(redh)-1
  if indmin(0) ne -1 then indmin=indmin(0) else indmin=0
  while indmax-indmin+1 le 6 do begin

```

```

        if indmax eq n_elements(redh)-1 then $
            indmin=indmin-(7-(indmax-indmin+1))
        if indmin eq 0 then indmax=6
        if indmax lt n_elements(redh)-1 AND indmin gt 0 then begin
            indmin=indmin-1
            indmax=indmax+1
        endif
    endwhile
    fit2pk, x(indmin:indmax), redh(indmin:indmax), A2, B2, R, $
        chisq2, revert, status, erroneous, text=text
    IF keyword_set(text) then print, "A2",A2
    if keyword_set(text) then print, "B2",B2
    if keyword_set(text) then print, "chisq", chisq2
    if n_elements(erroneous) gt 0 then begin
;this takes care of erroneous peaks
        if keyword_set(text) then print, $
            "***** Starting over without erroneous peak *****"
        if so ne 1 then begin
            if erroneous eq 'A' then $
                peaksskipped(l-1)=peaksskipped(l-1)+1
            if erroneous eq 'B' then $
                peaksskipped(l)=peaksskipped(l)+1
            if keyword_set(text) then print, $
                "Skipping this erroneous peak"
        endif
        if temporary(erroneous) eq 'A' then A1=B2IC else A1=A2IC
        startwith=1
        so=1
        GOTO, BEGINAGAIN
    endif
    IF revert eq 0 THEN BEGIN
;*****revert eq 0
    IF chisq2 gt 100 AND n_elements(redh(indmin:indmax)) $
        gt 9 THEN BEGIN
        if keyword_set(text) then print, $
            "Chisq too large... Trying three peaks"
;setup ICs
        IF lgstpk eq 'A' THEN BEGIN
            A3=A2IC
            B3=A2IC
            C3=B2IC
        ENDIF ELSE BEGIN
            A3=B2IC
            B3=B2IC

```

```

        C3=A2IC
    ENDELSE
    A3(0)=A3(0);*2./3.
    B3(0)=B3(0);*2./3.
    A3(1)=A3(1)-A3(2)*R
    B3(1)=B3(1)+B3(2)*R
    chisq3=chisq2
    fit3pk, x(indmin:indmax), redh(indmin:indmax), $
        A3, B3, C3, R, chisq3, revert, status, $
        erroneous, text=text
    if keyword_set(text) then print, "A3",A3
    if keyword_set(text) then print, "B3",B3
    if keyword_set(text) then print, "C3",C3
    if keyword_set(text) then print, "chisq", chisq3
    IF revert eq 1 or n_elements(erroneous) gt 0 $
        THEN nrevpks=2 ELSE BEGIN
            nrevpks=3
            IF keyword_set(text) THEN print, $
                "Ending with three peaks"
    ENDELSE
ENDIF ELSE BEGIN
    IF ((B2(1)+sqrt(-2*(B2(2))^2.*alog(1/B2(0))))- $
        (A2(1)+sqrt(-2*(A2(2))^2.*alog(1/A2(0)))) LT 4 OR $
        (B2(1)-sqrt(-2*(B2(2))^2.*alog(1/B2(0))))- $
        (A2(1)-sqrt(-2*(A2(2))^2.*alog(1/A2(0)))) LT 4) $
    THEN BEGIN
        if keyword_set(text) then print, $
            (B2(1)+sqrt(-2*(B2(2))^2.*alog(1/B2(0))))- $
            (A2(1)+sqrt(-2*(A2(2))^2.*alog(1/A2(0))))), $
            (B2(1)-sqrt(-2*(B2(2))^2.*alog(1/B2(0))))- $
            (A2(1)-sqrt(-2*(A2(2))^2.*alog(1/A2(0))))
        IF lgstpk eq 'A' THEN $
            A1=[sizemax(m-1),locmax(m-1),sdest] ELSE $
            A1=[sizemax(m),locmax(m),sdest]
        fit1pk, x(indmin:indmax), redh(indmin:indmax), $
            A1, chisq1, status
        IF A1(2) le sdest OR (chisq1 le 200 AND A1(2) $
            le sdest+1) THEN nrevpks=1 ELSE nrevpks=2
        IF keyword_set(text) then print, "A1: ",A1
        if keyword_set(text) then print, "chisquared", $
            chisq1
    ENENDIF ELSE nrevpks=2
ENDIF ELSE
;*****revert eq 0

```

```

ENDIF ELSE BEGIN
  IF lgstpk eq 'A' THEN $
    A1=[sizemax(m-1),locmax(m-1),sdest] ELSE $
    A1=[sizemax(m),locmax(m),sdest]
  fit1pk, x(indmin:indmax), redh(indmin:indmax), A1, $
    chisq1, status
  nrevpks=1
  if keyword_set(text) then print, "Ending with one peak"
ENDELSE
END
3: BEGIN
  if n_elements(chisq1) gt 0 then deleteme=temporary(chisq1)
  if n_elements(chisq2) gt 0 then deleteme=temporary(chisq2)
  if n_elements(chisq3) gt 0 then deleteme=temporary(chisq3)
  if keyword_set(text) then print, "Starting with three peaks..."
  A3=[sizemax(m-2),locmax(m-2),sdest]
  B3=[sizemax(m-1),locmax(m-1),sdest]
  C3=[sizemax(m),locmax(m),sdest]
  if keyword_set(text) then print, "A3",A3
  if keyword_set(text) then print, "B3", B3
  if keyword_set(text) then print, "C3", C3
  A3IC=A3
  B3IC=B3
  C3IC=C3
  CASE max([A3(0),B3(0),C3(0)]) OF
    A3(0): lgstpk='A'
    B3(0): lgstpk='B'
    C3(0): lgstpk='C'
  ENDCASE
  CASE min([A3(0),B3(0),C3(0)]) OF
    A3(0): smstpk='A'
    B3(0): smstpk='B'
    C3(0): smstpk='C'
  ENDCASE
  indmax=where(x gt A3(1) AND redh eq 0)
  indmin=where(x lt A3(1) AND redh eq 0)
  if indmax(0) ne -1 then indmax=indmax(0) else $
    indmax=n_elements(redh)-1
  if indmin(0) ne -1 then indmin=indmin(0) else indmin=0
  while indmax-indmin+1 le 9 do begin
    if indmax eq n_elements(redh)-1 then $
      indmin=indmin-(10-(indmax-indmin+1))
    if indmin eq 0 then indmax=9
    if indmax lt n_elements(redh)-1 AND indmin gt 0 then begin

```

```

        indmin=indmin-1
        indmax=indmax+1
    endif
endwhile
if n_elements(chisq3) gt 0 then print, 'chisq3', chisq3
fit3pk, x(indmin:indmax), redh(indmin:indmax), A3, B3, C3, R, $
    chisq3, revert, status, erroneous, text=text
IF n_elements(erroneous) gt 0 THEN BEGIN
    if keyword_set(text) then print, $
        "***** Starting over without erroneous peak *****"
    startwith=2
    so=1
;since it seems that the peak that ended up erroneous wasn't
;necessarily the correct one... try if more than one erroneous
;peak, revert to IC with lgst two peaks.
;if only one erroneous, remove it and try with fit of good two
    if revert eq 1 then begin
        CASE smstpk OF
            'A': BEGIN
                A2=B3IC & B2=C3IC
            END
            'B': BEGIN
                A2=A3IC & B2=C3IC
            END
            'C': BEGIN
                A2=A3IC & B2=B3IC
            END
        ENDCASE
        deleteme=temporary(erroneous)
    endif else begin
        CASE temporary(erroneous) OF
            'A': BEGIN
                peaksskipped(1-2)=peaksskipped(1-2)+1
                if keyword_set(text) then print, $
                    "Skipping this erroneous peak"
                A2=B3IC & B2=C3IC
            END
            'B': BEGIN
                peaksskipped(1-1)=peaksskipped(1-1)+1
                if keyword_set(text) then print, $
                    "Skipping this erroneous peak"
                A2=A3IC & B2=C3IC
            END
            'C': BEGIN

```

```

        peaksskipped(1)=peaksskipped(1)+1
        if keyword_set(text) then print, $
            "Skipping this erroneous peak"
        A2=A3IC & B2=B3IC
        END
    ENDCASE
ENDELSE
GOTO, BEGINAGAIN
ENDIF
IF revert eq 1 THEN BEGIN
    CASE smstp OF
        'A': BEGIN
            A2=B3IC & B2=C3IC
            END
        'B': BEGIN
            A2=A3IC & B2=C3IC
            END
        'C': BEGIN
            A2=A3IC & B2=B3IC
            END
    ENDCASE
    fit2pk, x(indmin:indmax), redh(indmin:indmax), A2, B2, $
        R, chisq2, revert, status, text=text
    if keyword_set(text) then print, "Chisq2", chisq2
    IF revert eq 1 THEN BEGIN
        if keyword_set(text) then print, $
            "Trying peaks farthest away"
        CASE max([A3(1),B3(1),C3(1)]) OF
            A3(1): lgstloc='A'
            B3(1): lgstloc='B'
            C3(1): lgstloc='C'
        ENDCASE
        CASE min([A3(1),B3(1),C3(1)]) OF
            A3(1): smstloc='A'
            B3(1): smstloc='B'
            C3(1): smstloc='C'
        ENDCASE
        CASE smstloc OF
            'A': A2=A3IC
            'B': A2=B3IC
            'C': A2=C3IC
        ENDCASE
        CASE lgstloc OF
            'A': B2=A3IC

```

```

        'B': B2=B3IC
        'C': B2=C3IC
    ENDCASE
    fit2pk, x(indmin:indmax), redh(indmin:indmax), $
        A2, B2, R, chisq2, revert, status, text=text
    if keyword_set(text) then print, "Chisq2", chisq2
    IF revert eq 1 then begin
        CASE lgstpk OF
            'A': A1=A3IC
            'B': A1=B3IC
            'C': A1=C3IC
        ENDCASE
        fit1pk, x(indmin:indmax), $
            redh(indmin:indmax), A1, chisq1, $
            status, text=text
        nrevpks=1
    ENDIF ELSE nrevpks=2
    ENDIF ELSE nrevpks=2
    ENDIF ELSE nrevpks=3
    if keyword_set(text) then print, "Ended with " + $
        strtrim(string(nrevpks),1)+" peaks."
    END
ENDCASE

;need to replace x proper here...
DONEYFITTING:
if n_elements(tempx) gt 0 then begin
    x=temporary(tempx)
    redh=temporary(tempredh)
    if keyword_Set(text) then print, $
        "Putting all the original data back..."
endif
movepeakover=0

if redoskipped eq 1 then begin
    case nrevpks of
        3: begin
            ind=where(abs(x-A3(1)) eq min(abs(x-A3(1))))
            if max(totalgauss(ind(0)-1:ind(0)+1)) gt 1 then skippeak=1
            ind=where(abs(x-B3(1)) eq min(abs(x-B3(1))))
            if max(totalgauss(ind(0)-1:ind(0)+1)) gt 1 then skippeak=1
            ind=where(abs(x-C3(1)) eq min(abs(x-C3(1))))
            if max(totalgauss(ind(0)-1:ind(0)+1)) gt 1 then skippeak=1
        end
    end
end

```

```

2: begin
  ind=where(abs(x-A2(1)) eq min(abs(x-A2(1))))
  if max(totalgauss(ind(0)-1:ind(0)+1)) gt 1 then skippeak=1
  ind=where(abs(x-B2(1)) eq min(abs(x-B2(1))))
  if max(totalgauss(ind(0)-1:ind(0)+1)) gt 1 then skippeak=1
  end
1: begin
  ind=where(abs(x-A1(1)) eq min(abs(x-A1(1))))
  if max(totalgauss(ind(0)-1:ind(0)+1)) gt 1 then skippeak=1
  end
endcase
if keyword_set(text) then print,"totalgauss at peak " + $
  strtrim(string(totalgauss(ind(0))),1)+' , data height '+$
  strtrim(string(redh(ind(0))),1)
if skippeak eq 1 and keyword_set(text) then print, $
  "This peak may be unnecessary.  Skipping..."
endif

if ncompletepeaks+n le 9 AND skippeak eq 0 then begin
  estgauss(*)=0
  case nrevpks of
    3: begin
      peaklocation=[A3(1),B3(1),C3(1)]
      stddevofpks=[A3(2),B3(2),C3(2)]
      pksz=[A3(0),B3(0),C3(0)]
      switch 1 of
        n+ncompletepeaks le 7: begin
          estgauss=estgauss+C3(0)*exp(-((x-C3(1))/C3(2))^2/2)
          peaks(n+ncompletepeaks,*)=C3
          n=n+1
          end
        n+ncompletepeaks le 8: begin
          estgauss=estgauss+B3(0)*exp(-((x-B3(1))/B3(2))^2/2)
          peaks(n+ncompletepeaks,*)=B3
          n=n+1
          end
        n+ncompletepeaks le 9: begin
          estgauss=estgauss+A3(0)*exp(-((x-A3(1))/A3(2))^2/2)
          peaks(n+ncompletepeaks,*)=A3
          n=n+1
          end
      endswitch
    end
  2: begin

```

```

    peaklocation=[A2(1),B2(1)]
    stddevofpks=[A2(2),B2(2)]
    pksz=[A2(0),B2(0)]
    switch 1 of
        n+ncompletepeaks le 8: begin
            estgauss=estgauss+B2(0)*exp(-((x-B2(1))/B2(2))^2/2)
            peaks(n+ncompletepeaks,*)=B2
            n=n+1
            end
        n+ncompletepeaks le 9: begin
            estgauss=estgauss+A2(0)*exp(-((x-A2(1))/A2(2))^2/2)
            peaks(n+ncompletepeaks,*)=A2
            n=n+1
            end
    endswitch
end
1: begin
    peaklocation=[A1(1)]
    stddevofpks=[A1(2)]
    pksz=[A1(0)]
    case 1 of
        n+ncompletepeaks le 9: begin
            estgauss=estgauss+A1(0)*exp(-((x-A1(1))/A1(2))^2/2)
            peaks(n+ncompletepeaks,*)=A1
            n=n+1
            end
    endcase
end
endcase
minpeak=peaklocation[where(peaklocation eq min(peaklocation))]
minpeak=minpeak[0]
maxpeak=peaklocation[where(peaklocation eq max(peaklocation))]
maxpeak=maxpeak[0]
;*****
deleteme=where(peaksskipped eq 1)
if deleteme(0) ne -1 then doest=0 else begin
    if n_elements(zerotwn) eq m then doest=1 else begin
        if zerotwn(m) eq 1 then doest=1 else doest=0
    endelse
endelse
if keyword_set(midplot) then begin
    plot, x, redh, psym=10, /ylog, yrange=[1,max(h)]
endif
;ALWAYS SUBTRACT GAUSSIANS!!!

```

```

if keyword_set(text) then print, 'Subtracting gaussians...'
    ;find where estgauss is lt 1. Then find what the data is
    ;one index outside. if data is lt 1, then eliminate it.
    ;end on minus side...
for i=0,nrevpks-1 do begin
    A=reform(peaks(ncompletepeaks+n-i-1,*))
    ind=where(x lt (A(1)-sqrt(-2*(A(2))^2.*alog(1/A(0))))))
    indn=ind(n_elements(ind)-1)
    if indn eq -1 OR indn eq 0 then elimneg=0 else $
        if min(redh(indn-1:indn)) le 1 then elimneg=1 $
        else elimneg=0
    ;end on plus side...
    ind=where(x gt (A(1)+sqrt(-2*(A(2))^2.*alog(1/A(0))))))
    indp=ind(0)
    if indp eq n_elements(redh)-1 OR indp eq -1 then $
        elimpos=0 else $
            if min(redh(indp:indp+1)) le 1 then elimpos=1 $
            else elimpos=0
    if temporary(elimpos) eq 1 then begin
        if keyword_set(text) then print, $
            "Eliminating positive data"
        redh(min(where(x ge A(1))):temporary(indp))=0
    endif
    if temporary(elimneg) eq 1 then begin
        if keyword_set(text) then print, $
            "Eliminating negative data"
        redh(temporary(indn):max(where(x le A(1))))=0
    endif
endifor
    estgauss=estgauss*multgauss
    redh=redh-estgauss
    ind=where(redh lt 0)
    if ind(0) ge 0 then redh(temporary(ind))=0
if keyword_set(midplot) then begin
    oplot, x, estgauss*multgauss
    key=get_kbrd(1)
endif
totalgauss=totalgauss+estgauss
endif
if lastpeak eq 1 then l=numpeaks-1
m=m+1 ;to iterate forward so as not to repeat peaks
endfor ; l

ncompletepeaks=n+ncompletepeaks

```

```

;here, check to see if there's data left... perhaps if we do this,
;we don't need skipped peaks...

if max(redh) gt 1.5 AND findingleftovers eq 0 then begin
    rememberredh=redh
    findingleftovers=1
    GOTO, DATALEFT
endif

;if dataleft then GOTO, DATALEFT

FINISHED:

;redefine the following to take up much less memory after it's not
;needed anymore
redh=0
locmax=0
sizemax=0
zerobtwn=0
;redefine above...

finalplot=ncompletepeaks-1
if keyword_set(plot) then begin
plot, x, h, psym=10, yrange=[1,max(h)]
sumofall=fltarr(n_elements(h))
for k=0,finalplot do begin
oplot, x, peaks(k,0)*exp(-((x-peaks(k,1))/peaks(k,2))^2/2)
endfor
oplot, x, totalgauss/multgauss, linestyle=2, thick=2
endif ;keyword_set(plot)

if keyword_set(stats) then print, peaks(0:finalplot,*)
if ncompletepeaks ge 2 then $
    dbtwnpks=max(peaks(0:ncompletepeaks-1,1))-
    min(peaks(0:ncompletepeaks-1,1)) else dbtwnpks=0
if keyword_set(text) then print, "Number of peaks", ncompletepeaks
end

```